National Institute of Standards and Technology
Technology Administration, U.S. Department of Commerce

NIST Technical Note 1546

Measurements to Support Modulated-Signal Radio Transmissions for the Public-Safety Sector

K.A. Remley
G. Koepke
C.L. Holloway
C. Grosvenor
D. Camell
J. Ladbury
R.T. Johnk
D. Novotny
W.F. Young
G. Hough
M.D. McKinley
Y. Becquet
J. Korsnes

NIST Technical Note 1546

Measurements to Support Broadband Modulated-Signal Radio Transmissions for the Public-Safety Sector

K.A. Remley
G. Koepke
C.L. Holloway
C. Grosvenor
D. Camell
J. Ladbury
R.T. Johnk[1]
D. Novotny
W.F. Young
G. Hough[2]
M.D. McKinley[3]
Y. Becquet[4]
J. Korsnes[4]

Electronics and Electrical Engineering Laboratory
National Institute of Standards and Technology
325 Broadway
Boulder, CO 80305

1. Institute for Telecommunication Sciences, Boulder, CO
2. Fire Department of New York City, NY
3. Georgia Institute of Technology, Atlanta, GA
4. Chalmers University of Technology, Gothenburg, Sweden

June 2008

U.S. Department of Commerce
Carlos M. Gutierrez, Secretary

National Institute of Standards and Technology
James Turner, Deputy Director

Certain commercial entities, equipment, or materials may be identified in this document in order to describe an experimental procedure or concept adequately. Such identification does not imply recommendation or endorsement by the National Institute of Standards and Technology, nor does it imply that the entities, materials, or equipment are necessarily the best available for the purpose.

National Institute of Standards and Technology Technical Note 1546
Natl. Inst. Stand. Technol. Tech. Note 1546, 256 pages (June 2008)
CODEN: NTNOEF

U.S. Government Printing Office
Washington: 2008

For sale by the Superintendent of Documents, U.S. Government Printing Office
Internet bookstore: gpo.gov Phone: 202-512-1800 Fax: 202-512-2250
Mail: Stop SSOP, Washington, DC 20402-0001

Contents

Executive Summary

This is the fifth in a series of NIST Technical Notes (TN) on propagation and detection of radio signals in large building structures. This series has been developed to support improved radio communications for the public-safety community in difficult radio environments. The first, second, and third NIST Technical Notes (NIST TN 1540, 1541, and 1542) described experiments that measured received signal strength in structures before, during, and after implosion. The fourth, NIST Technical Note 1545, describes a series of signal-strength measurements carried out in 14 large public buildings. The first four Technical Notes have created a large, public-domain data set describing the attenuation of radio signals in various building types for the public safety and cellular telephone bands. The present document augments this work by providing additional data that are relevant to modulated-signal communication measurement and simulation for the public-safety sector. We describe measurements of three large public buildings and one subterranean tunnel.

Wireless communication using wideband digitally modulated signals propagating into and out of large buildings and other structures is complicated by several factors, including the strong attenuation of radio signals caused by losses in the building materials, scattering from structural features (multipath), and waveguiding effects of corridors and tunnels. Understanding the losses and their variability, decay times for reflected signals, the frequency-selective behavior of the channel, and the combined effect these have on broadband digitally modulated signals can help system engineers assess various technologies. This work can also help in designing and verifying network simulations and ultimately will help with standards development.

Our in-depth study of four structures presented here includes several types of data. As in TNs 1540 through 1542 and TN 1545, we collected single-frequency, received-power data measured over a continuous path in the various structures. These data were collected at frequencies near public safety and cell phone bands as well as industrial, scientific, and medical (ISM) and wireless local-area network (LAN) bands (approximately 50 MHz, 150 MHz, 225 MHz, 450 MHz, 900 MHz, and 1.8 GHz). We carried radio transmitters similar to those used by first responders throughout the structures while recording the received signal at a fixed receive site. From this we determined the field strength variability throughout the structures.

We also measured excess path loss at selected locations within each structure. From the excess path loss we calculated the RMS time-delay spread. The excess path loss provides the relative received signal strength over the frequency bands of 300 MHz to 1 GHz and 1 GHz to 18 GHz. The time-delay spread gives an indication of the level of multipath interference encountered during the signal transmission.

Our third set of tests involved measuring the distortion across the passband of a digitally modulated signal. We measured the spectra associated with broadband digitally modulated OFDM signals at frequencies of 2.4 GHz and 4.95 GHz, and from this we evaluated the common wireless-system figure of merit error vector magnitude (EVM), which indicates the level of distortion in the received symbols. This set of tests was designed to investigate the differences between wireless reception in the unlicensed

frequency bands near 2.4 GHz and those proposed for use in the new public-safety frequency band covering 4.91 GHz to 4.96 GHz.

The collection of data presented here shows a number of propagation effects relevant to transmission of broadband modulated signals in public-safety and emergency-responder environments. Some effects were common to all environments, such as the attenuation of higher frequencies when they impinge upon structural materials. Some of them were unique to a specific environment; for example, the intense frequency-selective distortion and multipath across the signal's modulation bandwidth in an oil refinery. From the data, we were able to classify distinct types of propagation channels depending on the distance and type of obstructions between the transmitter and receiver. These include the unobstructed, direct-path channel; the Rayleigh, flat-fading channel; the wideband fading channel; simple building penetration, where material attenuation is observed; and waveguide-below-cutoff propagation. Each effect is illustrated by measurements.

We provide some interpretation of the large body of measurement data presented here. However, we anticipate that engineers, systems designers, academics, and standards organizations will find more information in these data than can be described in one document. Hopefully this work will contribute to our goal of improved wireless communications for emergency responders.

Measurements to Support Broadband Radio Communications for the Public-Safety Sector

Kate A. Remley, Galen Koepke, Christopher L. Holloway, Chriss Grosvenor, Dennis Camell, John Ladbury, Robert T. Johnk,[1] David Novotny, William F. Young, George Hough,[2] Michael D. McKinley,[3] Yann Becquet,[4] John Korsnes[4]

Electromagnetics Division
National Institute of Standards and Technology
325 Broadway, Boulder, CO 80305

1. Institute for Telecommunication Sciences, Boulder, CO
2. Fire Department of New York City, NY
3. Georgia Institute of Technology, Atlanta, GA
4. Chalmers University of Technology, Gothenburg, Sweden

Abstract *We report on measurements of parameters used to characterize broadband wireless technologies proposed for use by emergency responders (firefighters, police, and emergency medical personnel) and other public-safety personnel. We designed a collection of experiments in various large structures in an effort to quantify radio-signal attenuation, the level of multipath, and the amount of frequency-selective distortion. We also monitored the distortion introduced into digitally modulated signals under the orthogonal frequency division multiplexing access protocol. This report summarizes the experiments, performed in four large building structures. We describe the experiments and the measurement systems, and then show primary results of the data we collected in each of the four structures. Finally, we discuss some of the interesting propagation effects we observed and discuss how they may be classified into different propagation channel types. The complete sets of measured data are presented in the appendices.*

Key words: *attenuation; broadband radio communications; building penetration; digital modulation; emergency responders; error vector magnitude; excess path loss; received power; time-delay spread; wireless signals; wireless system measurements; wireless telecommunications; vector network analyzer; vector signal analyzer; ultrawideband signals.*

1. Introduction

To aid in the development of standards that support reliable wireless communications for first responders, the Department of Justice, through the Community-Oriented Policing Services (COPS) program, and the Department of Homeland Security Office of Standards are supporting the National Institute of Standards and Technology (NIST) in acquiring data on radiowave propagation in key emergency responder and public-safety environments. In past work by NIST [1-3],

measurements were gathered in buildings scheduled for implosion to simulate collapsed-building environments. The focus of current work is to study penetration radio waves into large buildings where difficult radio reception is often encountered.

A companion NIST Technical Note, TN 1545 [4], reports on measurements of received-signal strength for single-frequency excitation in several large public buildings. A spectrum analyzer was used to measure the relative signal strength as a portable transmitter was carried throughout the buildings. All measurements were reported relative to a line-of-sight reference signal level measured outside the building of interest. Frequencies included bands near licensed public-safety bands and cell phone bands including 49 MHz, 160 MHz, 225 MHz, 450 MHz, 900 MHz, 1.8 GHz, and a limited set of data at 2.4 GHz and 4.95 GHz. Statistical descriptions of single-frequency signal attenuation data are reported in TN 1545.

In this report, we focus on additional parameters relevant to propagation of modulated signals. We conducted a number of tests in environments that are notoriously difficult in terms of radio reception for emergency responders. Where possible, we tried to find locations similar to those described in the SAFECOM Statement of Requirements (SoR), second revision [5]. Specifically, we conducted tests at an apartment building to simulate the residential apartment fire scenario (Section 3.3), and at an oil refinery to simulate the chemical plant explosion communications scenario (Section 3.5). We also carried out tests down a long corridor of an office building typical of many commercial facilities such as industrial plants, universities, offices, and schools. Finally, we carried out a limited set of tests in a subterranean tunnel to simulate subways, utility tunnels, and parking garages, among others.

In each location, several types of tests were carried out that are relevant to wireless communication systems that utilize digital modulation. We measured received power over a continuous path in each structure at single frequencies near public safety frequency bands. We conducted this testing with a high-dynamic-range communications receiver that enabled measurement of even very weak signals at various frequencies. We also carried out ultrawideband (UWB) measurements using synthetic-pulse techniques to assess the time-delay spread of the multipath in the propagation environments and the excess path loss over a wide frequency band at selected locations in each structure.

Finally, we measured broadband digitally modulated signals at both 2.4 GHz and 4.95 GHz using the 802.11g orthogonal-frequency-division-multiplexing (OFDM) protocol. In these tests, we recorded the bandpass spectra of each signal and measured the error vector magnitude (EVM), which describes the level of distortion to the demodulated information-carrying symbols. Currently, the 2.4 GHz unlicensed frequency band is sometimes used by responders to transmit broadband data such as images and video. The 4.95 GHz band is licensed to the public safety community and may also be used for broadband data transfer.

Much work has been published describing measurement characterization of the propagation environment with respect to loss, delay spread, and/or EVM. Most of these publications (e.g., reference [6] and references cited therein) describe measurements intended to simulate communications via cellular telephone or other wireless systems that rely on a fixed base station whose antenna is positioned high above the ground and a mobile user located at ground level. Few publications describe measurements that

simulate point-to-point radio-communication scenarios (e.g., reference [7] and references cited therein), such as those required in many emergency-responder scenarios.

In addition to supplying standards-development organizations with real-world data, one of the goals of this program is to provide measurement data that may be useful for verification of network simulations of emergency responder radio links. These types of simulations are being developed by NIST, among others. We anticipate these data may also be used directly by system designers, researchers, and by end users, including public-safety practitioners.

This document is organized as follows. In Section 2, we discuss the instrumentation, calibrations, and post-processing methods we used to collect the various data. In Sections 3 through 6, we provide the measured data collected at each of the four large structures: an apartment building, the long corridor of an office building, an oil refinery, and a subterranean tunnel. Section 7 summarizes the propagation effects noted and draws some conclusions on the types of propagation channels seen in the four structures. The Appendices at the end of the document contain all of the measured data.

Occasionally product names are specified solely for completeness of description, but such identification constitutes no endorsement by the National Institute of Standards and Technology. Other products may work as well or better.

2. Measurements for Modulated-Signal Path Characterization

2.1 Overview

Our in-depth study of the four structures included collecting several types of data relevant to wireless system designers and engineers. These include a large body of single-frequency received-power data collected at frequencies of interest to the public safety community, as well as received-power data collected over a very broad frequency band at selected points in the propagation environment. From the broad-spectrum measurements, we determined the excess path loss, and from this we calculated time-delay spread, a figure of merit that describes the time it takes for reflections in a received signal to die out. Finally, we collected bandpass spectra measurements and error vector magnitude (EVM) data associated with OFDM 802.11a/g signals at 2.4 GHz and 4.95 GHz. EVM is a figure of merit that describes the level of distortion in received, demodulated symbols in a digitally modulated signal.

The instrumentation, measurement methods, and calibrations for these measurements are described below. In most cases, these techniques were extensions of laboratory-based methods developed in prior years in the NIST Electromagnetics Division.

2.2 Narrowband Received-Power Measurements Using a Calibrated Narrowband Communications Receiver

As in Technical Notes 1540 through 1542 and 1545, we collected single-frequency received-power data measured over a continuous path in the various structures. These data were collected at frequencies near public safety and cell phone bands as well as unlicensed industrial, scientific, and medical (ISM) bands (approximately 50 MHz, 150 MHz, 225 MHz, 450 MHz, 900 MHz, and 1.8 GHz).

For this study, we carried radio transmitters throughout the structures while recording the received signal at a fixed receive site, as illustrated in Fig. 2.2-1(a). The radios we used were similar to those used by first responders (Fig. 2.2-1(b)), except that they were placed in ruggedized cases and were modified to transmit continuously.

For the receiver (Fig. 2.2-1(c)), we used a narrowband communications receiver. This instrument, when combined with NIST-developed post-processing techniques, provides a high-dynamic-range measurement system that is affordable for most public safety organizations. Part of our intent was to demonstrate a user-friendly system that could be utilized by public-safety organizations to assess their own unique propagation environments.

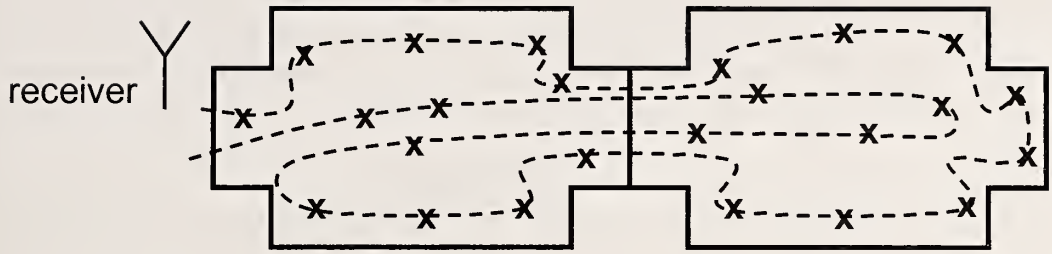

(a)

(b)

(c)

Figure 2.2-1: Illustration of the narrowband received-power measurements. (a) A radio transmitter was carried throughout the building on a continuous path, and the signal strength was recorded by the receiver. (b) The radio transceivers used in the tests were placed in protective cases with additional batteries and modified for continuous transmission. (c) The receiver consisted of a commercially available communications receiver, followed by post-processing steps to determine the received-signal level.

The use and calibration of the communications receiver is described in more detail in other publications [8] but is briefly summarized here for convenience. The system, shown in block diagram form in Fig. 2.2-2(a), is based on a common communications receiver and a personal computer (PC) sound card. The receiver is set to its "upper sideband" mode and is tuned to a frequency slightly below the carrier. In this way, the receiver acts as a frequency downconverter (Fig. 2.2-2(b)), transforming the RF signal to baseband (audio) frequencies. The baseband signal is digitized using the sound card and is then post-processed and graphically displayed, letting the operator know whether a radio signal is present and what the level of that signal is.

We may observe the upper and lower sidebands of the down-converted signal by setting the receiver's center frequency to approximately the middle of its intermediate-frequency (IF) passband. For example, a signal with a 100 MHz carrier frequency may be measured by a receiver with a 3 kHz passband by tuning the receiver to 99.9985 MHz. In this case, the receiver will display the 100 MHz signal at 1.5 kHz (see Fig. 2.2-2(c)).

The communications receiver has an automatic-gain-control (AGC) circuit whose function is to control the receiver gain to produce a constant-output-level signal regardless of the input power. The AGC circuit ensures the receiver circuitry operates in its optimal range. For the receiver we used, the AGC is active only for signals above a certain power threshold, and does not modify weak signals (on the order of P_{rec} less than −90 dBm).

The purpose of the AGC circuit is to ensure the receiver will demodulate as high-level of a signal as possible without overdriving the front end. It does this by altering the received-signal level to fit the best range for the demodulator. However, for received-power measurements the signal-level information is exactly what we are trying to determine. Hence, we need to undo the effects of the AGC modification of the signal level. To extract the signal-level information from the AGC-modified received signal, we monitor the DC voltage level that corresponds to the feedback of the AGC circuit. This voltage is directly related to the received-signal power and may be used to compensate for the AGC. We measure the DC voltage at the AGC jack on the back panel of the receiver with a digital multimeter having a recording feature. By synchronizing the recorded signal with the recorded AGC levels, we may determine the received signal's level during post-processing.

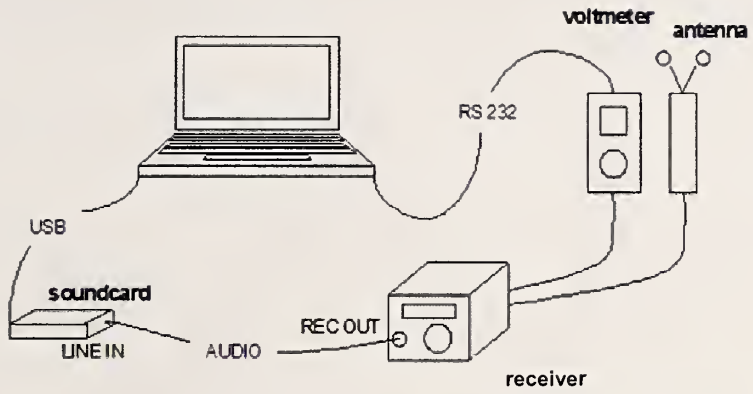

(a)

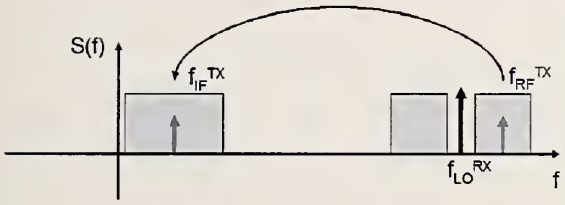

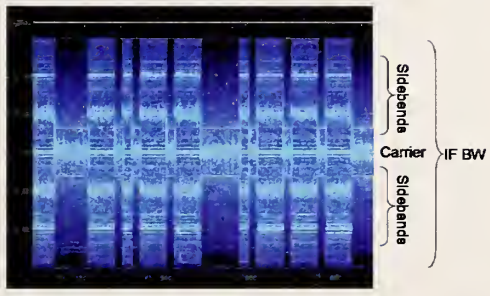

(b) (c)

Figure 2.2-2: (a) Set-up used to calibrate a communication receiver to display received signal strength. The receiver down-converts the signal to baseband frequencies, as shown in (b), and the sound card digitizes the baseband signal. A DC voltmeter monitors the automatic-gain-control setting on the receiver. The AGC data are used in post-processing to determine the signal's actual level. Graphic (c) shows a recorded, down-converted signal with time on the *x*-axis and frequency on the *y*-axis. The stripe at the center corresponds to the carrier frequency, and the bands on either side correspond to the FM sidebands. In this case the received signal is in Morse code.

Once the post-processing steps are carried out, the average received signal power for each location in a building may be measured. Note that the received power depends on the antenna and cabling used with the receiver. However, these effects may be calibrated out to display system-independent electric field level. In the measurements described here, we typically used a biconical, omnidirectional antenna for frequencies below 1 GHz. A typical received-power plot is shown in Fig. 2.2-3, where we see the received electric field (proportional to the power) versus time, averaged over one-second increments for a received-power measurement in a hotel structure. Structural features are noted on the graph as the transmitter is carried throughout the building.

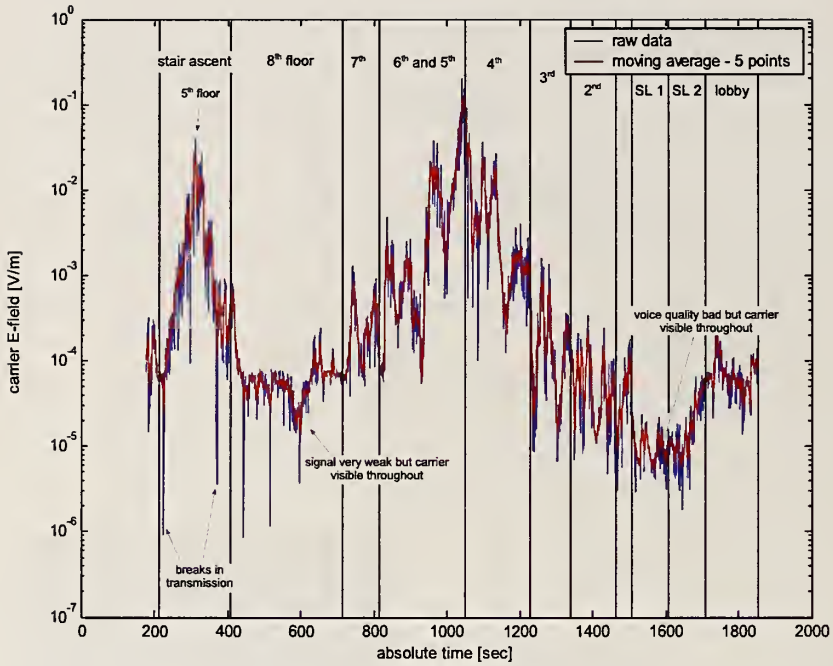

Figure 2.2-3: Electric field strengths measured during an 867 MHz building walk-through of a hotel. The vertical marker lines represent boundaries in time between different sections of the walk. The curve represents a five-point moving average of the measured calibrated data (from [6]).

The communications receiver allows us to determine the range of received power values that can be expected for a given structure. If antenna characteristics are known, these levels can be calibrated to absolute electric field strength, enabling easy comparison of measurements from different measurement systems. In the following sections, we instead report on the received-signal level relative to a reference line-of-sight measurement. Similar to the spectrum analyzer data collected in TNs 1540 through 1543 and 1545, these data can then be processed in terms of mean and standard deviation to provide channel models for network simulations. Because data are collected continuously, signal levels can easily be associated with features in the propagation environment. Some advantages of the communications receiver over the spectrum analyzer are its increased dynamic range; that is, we can detect weaker signals with this system. Also, our receiver system has a lower cost compared to that of a spectrum analyzer.

2.3 Wideband Excess-Path-Loss Measurements and Time-Delay Spread

2.3.1 VNA-based measurement system

We studied excess path loss over a wide frequency band at selected locations within each structure. The wideband excess-path-loss measurements provide measurements of received signal strength relative to a direct-path signal for a wide frequency band of 25 MHz to 18 GHz. These measurements complement the narrowband, continuously recorded received power measured with the communications receiver by providing the received power over a wide range of frequencies but at only a few locations. Note that we use the phrase "excess path loss" in the context of the vector-network-analyzer (VNA)-based measurements. Technically we are measuring received signal power, not path loss. Graphs of path loss would have positive ordinates and increase with distance. However, the phrase "excess path loss" has a specific meaning in the measurement community and will be used throughout this report. Time-delay spread was calculated from the excess path loss data in post processing. Root-mean-square (RMS) delay spread is a figure of merit that gives an indication of the level of multipath interference encountered during the signal transmission.

For the wideband measurements, we used a synthetic-pulse, ultrawideband system based on a VNA developed at NIST [9]. Figure 2.2-4 is a representative diagram of the measurement system. Here the system is shown collecting a line-of-sight reference measurement. In practice, the transmitting and receiving antennas may be separated by significant distances, although they must remain tethered together by the fiber-optic link. While directional horn antennas are shown in Fig. 2.2-4, omnidirectional antennas were also used in our measurements, offering insight into antenna systems most often used in public-safety applications.

In the synthetic-pulse system, the VNA acts as both transmitter and receiver. The transmitting section of the VNA sweeps over a wide range of frequencies, but at a single frequency at a time. The transmitted signal is amplified and fed to a transmitting antenna, as shown in the figure. The received signal is picked up over the air by the receiving antenna and sent back to the transmitter via a fiber-optic cable. The fiber-optic cable phase locks the received signal to the transmitted signal, enabling reconstruction of the time-domain waveform associated with the received signal in post-processing. Because the wideband transmitted signal corresponds to a short-duration pulse in the time domain, this system lets us measure transmitted signal, modified by the propagation path, including losses and multipath reflections that the narrow pulse experiences as it travels from the transmitter to the receiver.

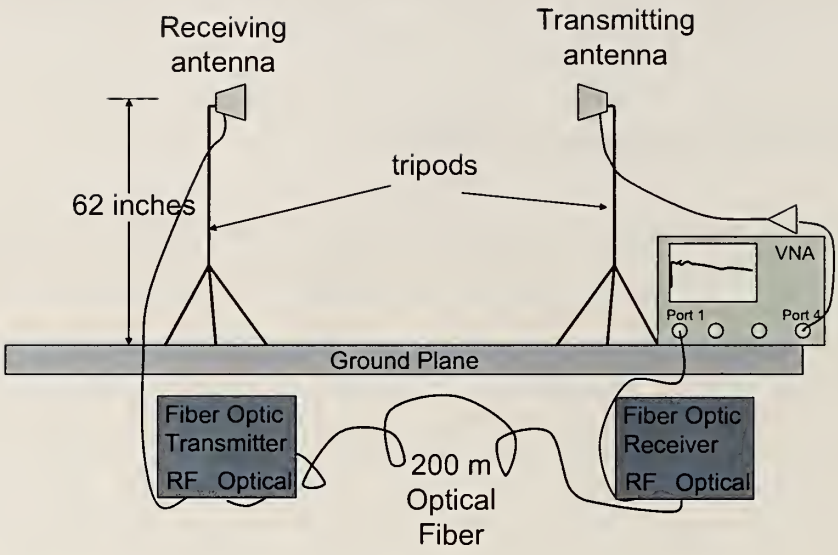

Figure 2.2-4: Ultrawideband synthetic-pulse measurement system based on a vector network analyzer. Frequency-domain measurements, synchronized by the optical fiber link, are transformed to the time domain in post-processing. This enables determination of excess path loss, time-delay spread, and other figures of merit important in characterizing broadband modulated-signal transmissions.

The vector network analyzer is first calibrated by use of standard techniques, where known impedance standards are measured. Then a reference measurement is conducted where the transmitting and receiving antennas are placed close enough together that environmental effects are negligible. This reference measurement enables us to correct for the response of the fiber-optic system, amplifiers, or any other electronics used in the measurement. The frequency response of the antennas is measured separately in the laboratory environment at NIST and is deconvolved in a post-processing step.

Once the measurements have been made, one additional post-processing step is carried out on the raw VNA measurements to provide clean frequency-domain and time-domain representations. Our optical links add a large amplitude oscillation to the measured signal. Because this oscillation occurs at a low frequency, we are able to suppress it by applying a high-pass filter, as shown in Fig. 2.2-5.

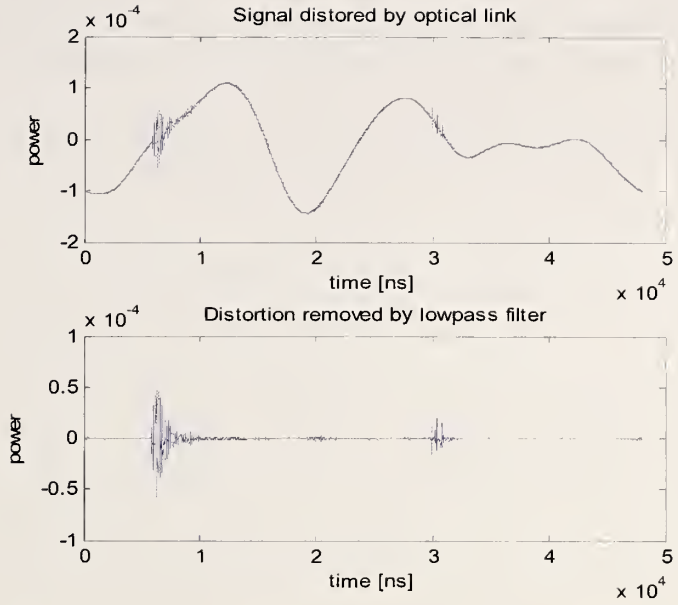

Figure 2.2-5: Low-frequency oscillations introduced by the optical link (top) are removed by use of a high-pass filter in post-processing (bottom). This enables us to clearly discern the measured data; here an initial pulse is received at approximately 5 ns, followed by a reflected pulse at approximately 30 ns.

2.3.2 Excess path loss

Excess path loss is typically understood to be the loss seen to exceed that measured in a free-space environment [10]. In order to obtain the measured free-space loss with our system, we begin by taking a reference measurement at a specified distance. The measurement includes environmental effects, so we use time-domain gating to obtain the free-space path loss. We use the total energy of the pulse response as our reference. Figures 2.2-6(a) and (b) show the time- and frequency-domain responses for a 3 m reference measurement using a pair of dual-ridged-guide (DRG) antennas. In Fig. 2.2-6(a), the time-domain reference is shown with all environmental effects. The time-domain reference is gated from 2 ns to 32 ns to isolate the antenna response. The frequency-domain responses for the 3 m reference are shown in Fig. 2.2-6(b). The noisier black trace shows the reference including environmental effects and the smoother red trace shows the frequency-domain response of the isolated antennas. The environmental effects cause the hashy noise seen in the black trace. The gated response is what we would see if the antenna were measured in a free-space environment.

The measured signal (not the reference) is also gated, but not for the same reasons. We want to see the measured signal's interaction with the environment, so we gate the signal at a place where the signal is no longer visible above the system noise. We choose a gate length that includes all of the important signal data. For example, for

the signal in Fig. 2.2-6(a), we would gate the signal from approximately 10 ns to 40 ns. By gating out the remaining noise we obtain a better signal-to-noise ratio. This is not critical in propagation measurements such as those presented here, but is important in measurements where the signal levels are fairly low.

For the VNA measurements, the excess path loss (EPL) is therefore defined as the ratio of the measured signal to the free-space reference:

$$EPL = \frac{S_{21\,(\text{gated signal})}}{S_{21\,(\text{gated reference})}}. \qquad (2.3\text{-}1)$$

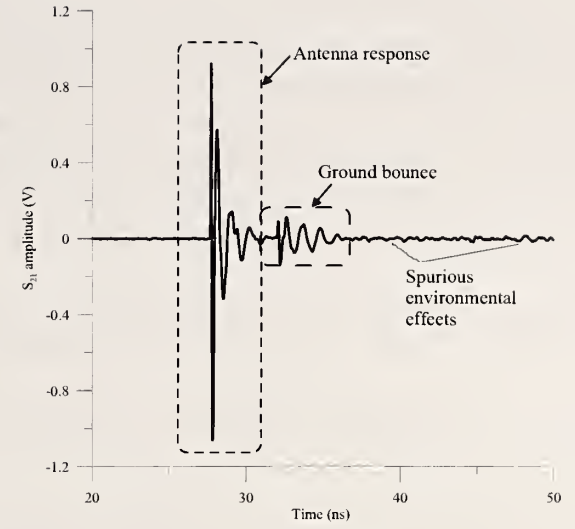

(a)

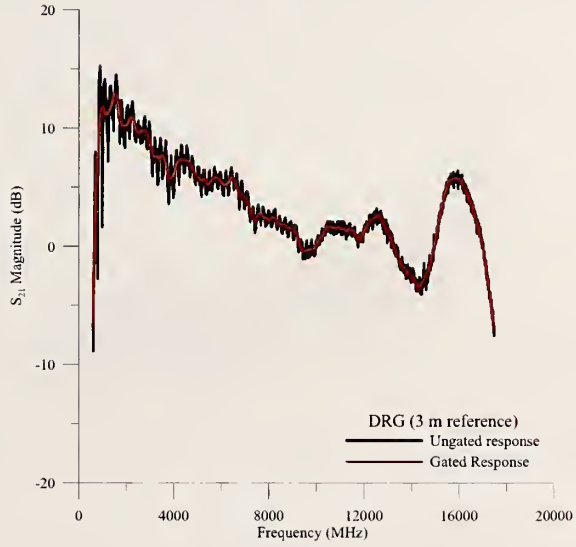

(b)

Figure 2.2-6: (a) Time-domain waveform for a DRG 3 m reference measurement. The waveform shows the antenna response, the ground-bounce response and the spurious environmental effects. (b) The frequency-domain response for both the ungated response (noisy black trace), which includes all environmental effects, and the gated response (smoother red trace), which includes only the antenna response.

2.3.3 RMS delay spread

Root-mean-square (RMS) delay spread is calculated from the power-delay profile of a measured signal [11-13]. Figure 2.2-7 shows the power-delay profile for a typical building propagation measurement. The peak level usually occurs when the signal arrives at the receiving antenna, although sometimes we see the signal build up

gradually to the peak value and then fall off. A common rule of thumb is to calculate the RMS delay spread by use of signals at least 10 dB above the noise floor of the measurement. For typical measurements, we define the maximum dynamic range to be about 40 dB below the peak value. However, for the measurement shown in Figure 2.2-7, we extended the window down to 70 dB below the peak value, because the RMS delay spread does not change appreciably due to the almost constant slope of the power decay curve. Note that the dynamic range value may change for low signal levels.

The following equation is used to define the RMS delay spread, σ_τ:

$$\sigma_\tau = \sqrt{\overline{\tau^2} - \left(\overline{\tau}\right)^2} \,. \qquad (2.3\text{-}2)$$

In (2.3-2), $\overline{\tau}$ is defined as the average of the power-delay profile in the defined dynamic range, and $\overline{\tau^2}$ is the variance of the power-delay profile.

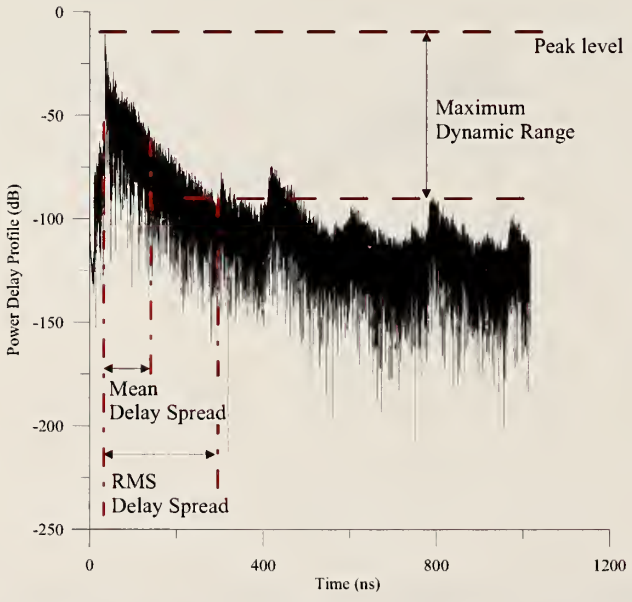

Figure 2.2-7: Power-delay profile for a building propagation measurement. The important parameters for a measured propagation signal are the peak level, the maximum dynamic range, the mean delay spread, and the RMS delay spread.

2.3.4 Measurement set-up

For the measurements reported in this document, the instrument was set up with the following parameters. The initial output power was set to −15 dBm to −13 dBm. The gain of the amplifier and the optical link and the system losses ensured that the power level at the receiving port was not more than 0 dBm. An intermediate-frequency (IF) averaging bandwidth of around 1 kHz was used to average the received signal. We

typically used 6401 points per frequency band and chose the number of bands recorded in each measurement to avoid aliasing of the signal. For these measurements, the high-band measurements (750 MHz to 18 GHz, using directional DRG antennas) were taken by measuring 48003 points for a total of three bands. Only one band was required for the low-frequency measurements (25 MHz to 1.4 GHz with omnidirectional antennas). The dwell time was approximately 25 μs per point.

2.4 Error Vector Magnitude Measurements

2.4.1 Error vector magnitude for OFDM channels

Our third set of tests involved measuring the waveforms of bandpass modulated signals and, from these, calculating EVM, which is a commonly used wireless-system figure of merit. EVM gives an indication of the distortion introduced into a digitally modulated signal as it passes through a propagation channel. To find EVM, the signal is first demodulated to find the in-phase and quadrature-phase voltage levels that correspond to the received symbols. We then normalize and compare the measured voltages to their ideal values. The algorithm we used to find EVM was built into the receiver.

The modulated signal we used as excitation was based on the OFDM transmission scheme, as specified by the IEEE 802.11a™-1999 standard [14-16]. OFDM is used in wireless local-area networks (WLANs), in dedicated short-range communication (DSRC) systems for tracking and observing loads in commercial vehicles [17], and in the public-safety band at 4.95 GHz. In the latter, OFDM signals are often transmitted in a 10 MHz wide channel using the 802.11j standard, instead of the 20 MHz wide channel utilized in 802.11a. The demodulator that we had was able to measure only the 802.11a standard, and this is what we report on in the following sections.

In the OFDM scheme, data are encoded onto 52 frequency-multiplexed subcarriers. For strong received signals, data are transmitted at a high data rate, maximally 54 megabits per second (Mbps). As the received signal strength decreases, the data rate decreases to compensate for the increase in noise. Note that both attenuation in the propagation environment and an increase in undesired interference will cause a reduction in data rate. In the tests reported on here, we force the signal generator to transmit either a slow-data-rate quadrature-phase-shift-keyed (QPSK) or a high-data-rate 64-quadrature-amplitude-modulated (64QAM) signal. This lets us assess the impact on EVM of a given channel when different modulation schemes are used. In some environments reported here, we were limited by the dynamic range of the receiver.

As mentioned above, EVM describes the difference between the ideal value of a demodulated symbol and the measured value. To aid in visualizing the demodulated signals, constellation diagrams are often used to represent digital symbols. In a constellation diagram, each symbol is represented by a unique magnitude and phase.

The magnitude and phase corresponding to each symbol are plotted in terms of real and imaginary components.

Figure 2.4-1 shows three constellation diagrams for a 16QAM signal, which has 16 symbols that modulate the radio-frequency (RF) carrier in both magnitude and phase. In each case, *I* and *Q* represent the in-phase (0 degree relative phase) and quadrature (90 degree relative phase) voltage values of each symbol. This gives each symbol a resulting magnitude and phase.

Figure 2.4-1(a) represents a measured set of symbols. Scattered dots on this diagram represent the effect of small errors in the measured symbols. Figure 2.4-1(b) represents the ideal constellation. The units of the in-phase and quadrature axes are dimensionless integers. A normalization (Fig. 2.4-1(c)) may be carried out to compare the differences between the measured and ideal symbols, as in reference [18]. The magnitude of the vector difference between the ideal and measured symbol is how EVM gets its name. Mathematically, this can be expressed as

$$EVM_{\mathrm{RMS}} = \left[\frac{\frac{1}{N}\sum_{r=1}^{N} | S_{\mathrm{ideal},r} - S_{\mathrm{meas},r} |^2}{\frac{1}{N}\sum_{r=1}^{N} | S_{\mathrm{ideal},r} |^2} \right]^{\frac{1}{2}}, \qquad (2.4\text{-}1)$$

where $S_{\mathrm{meas},r}$ is the normalized r^{th} symbol in a stream of measured symbols, $S_{\mathrm{ideal},r}$ is the ideal normalized constellation point for the r^{th} symbol, and N is the number of unique symbols in the constellation. The fractional form of EVM given in eq. (2.4-1) is often represented as a percentage.

2.4.2 Measurement set-up

For the EVM measurements described in the following sections, a vector signal generator was used to create the digitally modulated signals. The signal generator was mounted on a rolling cart and moved through the various propagation environments.

We used a vector signal analyzer (VSA) to receive the signals. The VSA maintains the relative phase of the measured frequency components and enables laboratory-grade measurements of distortion in digitally modulated signals. For the measurements presented here, the effects of the instrument itself were calibrated out by use of an internal calibration routine in the instrument. The VSA was adjusted for minimum received-signal distortion before each set of measurements. This entailed performing an internal calibration followed by a range adjustment under line-of-sight conditions.

Due to the limited dynamic range of the vector signal analyzer, it was necessary in some cases to use a directional horn antenna to optimize the received signal even though this set-up would probably not be utilized in a response scenario. Thus, some of the measurements that follow may be regarded as an optimized experiment.

We carried out these measurements in frequency bands around 2.4 GHz and 4.95 GHz to investigate the differences in transmission between existing wireless systems in the unlicensed 2.4 GHz industrial/scientific/medical (ISM) frequency band (which is sometimes used by public-safety organizations) and systems proposed for use in the new licensed public-safety frequency band covering 4.94 GHz to 4.99 GHz.

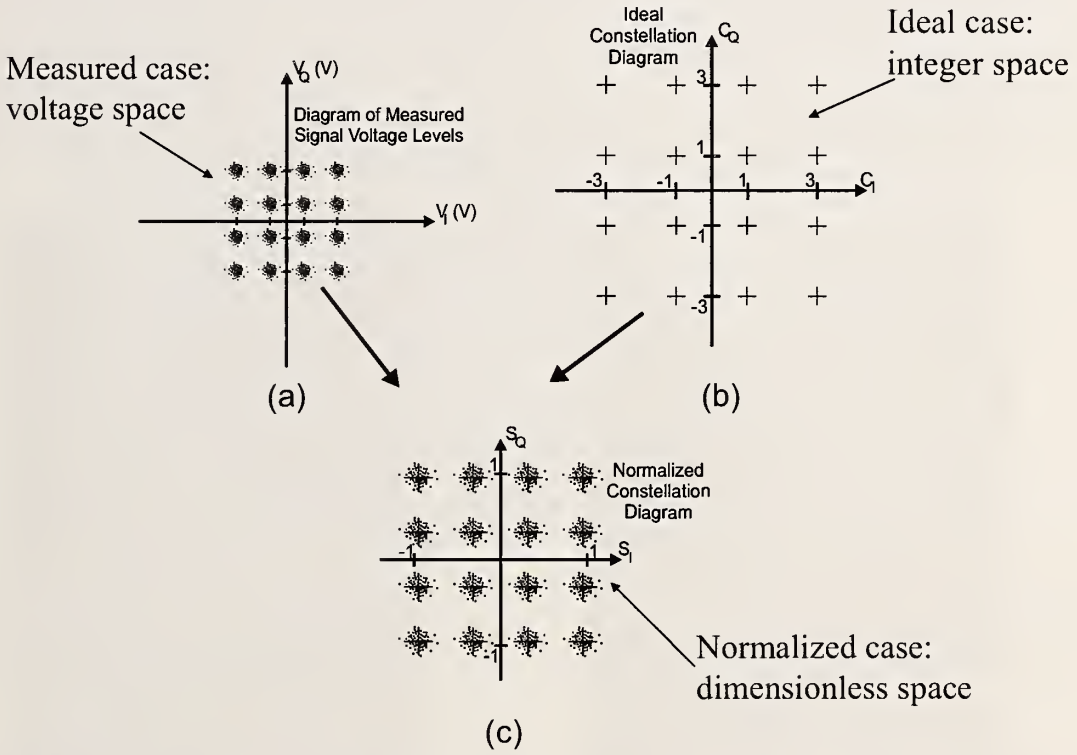

Figure 2.4-1: Calculation of EVM for a 16QAM signal. (a) Demodulated symbols containing distortion and (b) ideal symbol values at discrete constellation-diagram locations. These two are normalized in (c) so that they can be compared prior to calculating the EVM. This enables finding a consistent value of EVM across multiple modulation schemes. From reference [18].

3. Apartment Building Measurements

3.1 Overview

We carried out the various propagation measurements described in Section 2 at an 11-story apartment building located in Boulder, Colorado in October of 2007. As can be seen in Figure 3.1-1, the building is constructed of reinforced concrete, steel, and brick with standard interior finish materials. The building was fully furnished and occupied during the experiments. Measurements were performed during daytime hours, so people were moving throughout the building during the experiments.

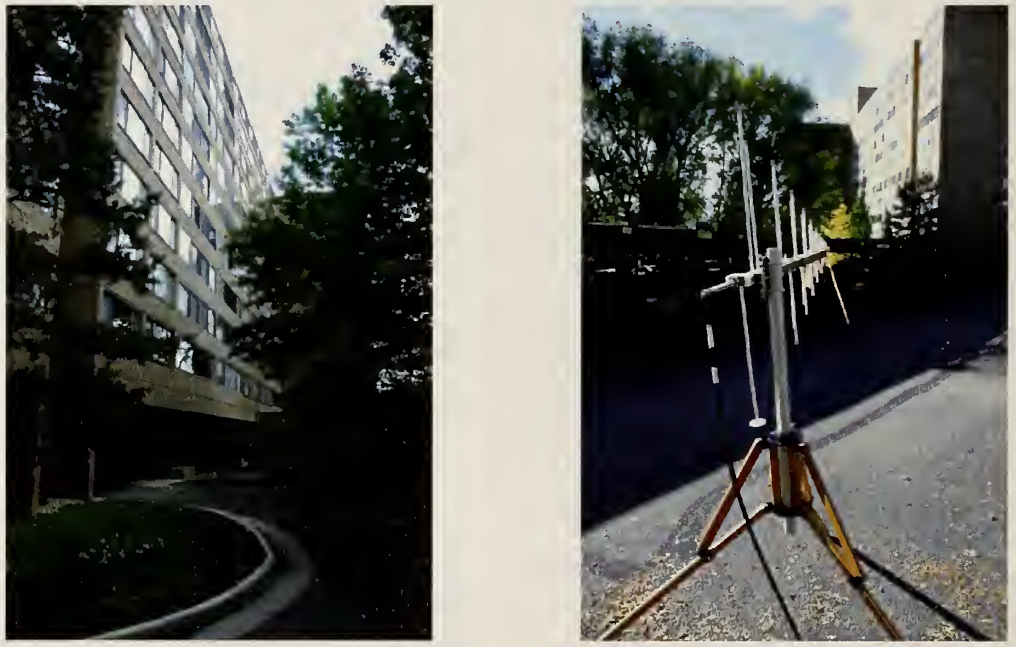

(a) (b)

Figure 3.1-1: Views of the 11-story, concrete and steel apartment building where the NIST measurements were made. (a) Near receiver site 1 (east side of building). (b) Near receiver site 2 (north side of building). The NIST directional antenna is seen in the foreground.

The layout of the apartment building is shown in Figure 3.1-2, with a simplified schematic in Figure 3.1-3. The building floor plan is T-shaped, with two elevators near the junction of the T. This apartment building has several features in common with the building described in the Apartment Fire Scenario of the SAFECOM SoR [5], including concrete construction, stairwells at the ends of the hallways, apartments off a main corridor with outside-facing windows, and the need for single- or two-wall radiowave penetration. The Apartment Fire Scenario deals with a fire response on the second floor of such an apartment building.

To simulate the fire response scenario, we carried out narrowband received-power measurements throughout the building, entering an apartment on the second and seventh floors. Excess path loss, time-delay spread, and EVM were measured at selected points on the second and seventh floors only.

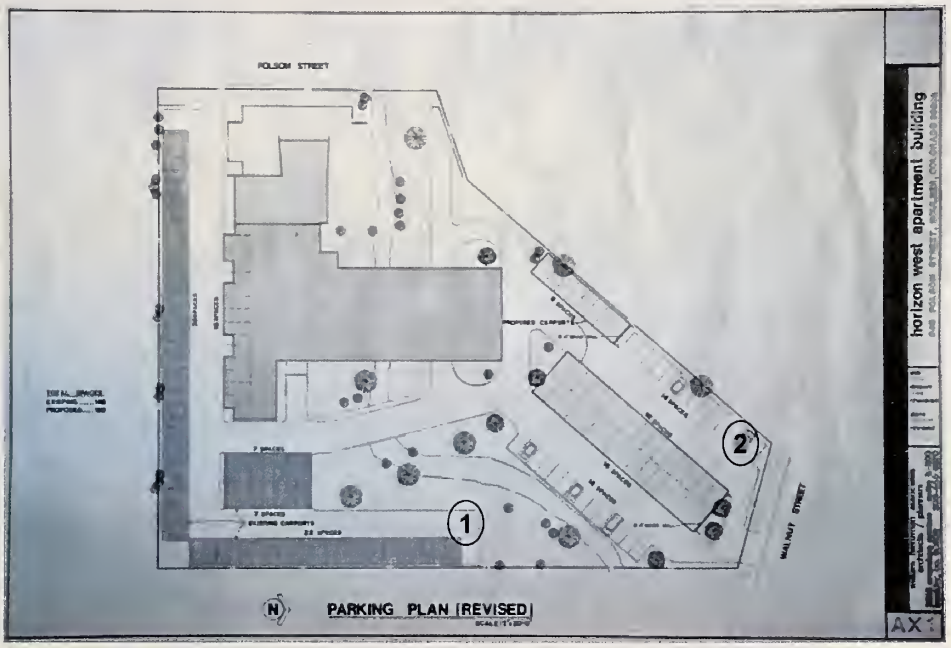

Figure 3.1-2: Layout of the apartment building lot, including parking areas. The building itself is the shaded, T-shaped structure in the center, and the hatched structures are metallic carports. The two sites where the NIST measurements were made are shown by the circled numbers.

One of the receiver sites (depending on the experiment, the single-frequency receiver, vector network analyzer, or vector signal analyzer) was located outside the building on the ground level approximately 60 m away, as shown in Figures 3.1-2 and 3.1-3. For the single-frequency received-power measurements, a second receiver site was set up north of the building approximately 80 m away. These locations were chosen to mimic those of a command vehicle responding to a fire at that location.

In the following sections, we describe the various experiments we conducted to study narrowband received power (using the single-frequency receiver), excess path loss and RMS delay spread (using the vector network analyzer), and modulated-signal response and EVM (using the vector signal analyzer). Selected data sets are presented to highlight significant aspects of signal propagation in this environment. The complete sets of data are included in the appendices at the end of the report.

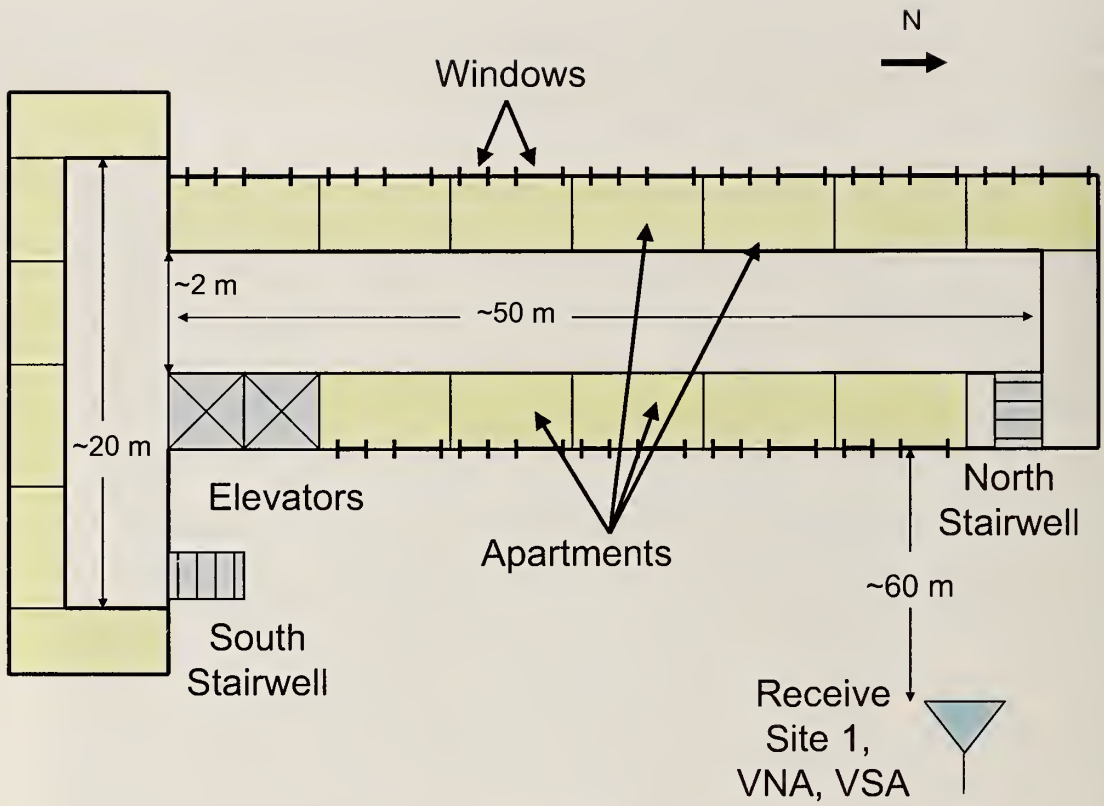

Figure 3.1-3: Layout of a single floor of the 11-story apartment building studied by NIST. A T-shaped corridor is lined with apartments that face the outside of the building. Each apartment has at least two large windows to the exterior. NIST equipment was positioned on the ground floor approximately 60 m from the building. An additional receiver site was located approximately 80 m north of the building. The drawing is not to scale, but critical dimensions are noted. Even though marked "receive site," for the VNA measurements, the transmitting antenna was placed there.

3.2 Narrowband Received-Power Measurements

For the narrowband received-power experiments, two fixed receiver sites (as described above) were assembled. Photos from receiver site 2 are shown in Figure 3.2-1. Measurements were performed with omnidirectional receiving antennas polarized in the vertical direction, as shown in Figure 3.2-2.

Figure 3.2-3 shows the path taken by the handheld transmitters as they were carried through the top 10 floors of the apartment building. We entered each floor from the stairwell, proceeded along the path noted in Figure 3.2-3, and exited through the opposite stairwell. Additionally, on the second and seventh floors, we entered apartments, walked through, and exited again. The apartment on the second floor faced the receiver sites, while the apartment on the seventh floor was on the opposite side of the building. As the received signals were recorded, the location of the transmitter in the building was also recorded and is marked on the graphs of the measured data. Figure

3.2-4(a) shows a photograph of the hallway, and Figure 3.2-4(b) shows the types of transmitters that were used in the test.

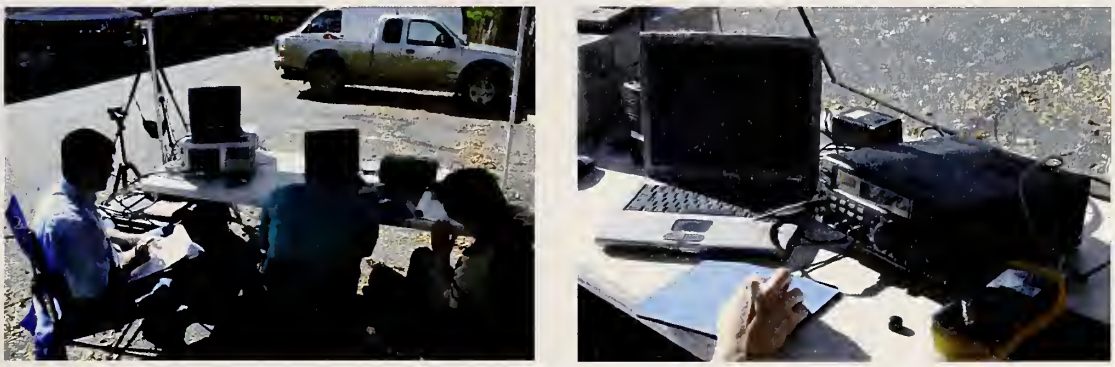

(a) (b)

Figure 3.2-1: Receiver site 2, showing equipment used for narrowband received-power measurements. (a) The spectrum analyzer on the left side of the table was used for received-power measurements described in NIST Technical Note 1545, receiver on left. (b) Receiver set-up showing communications receiver in center, voltmeter on right. The voltmeter measures the AGC voltage that is subsequently used to calibrate the measurement.

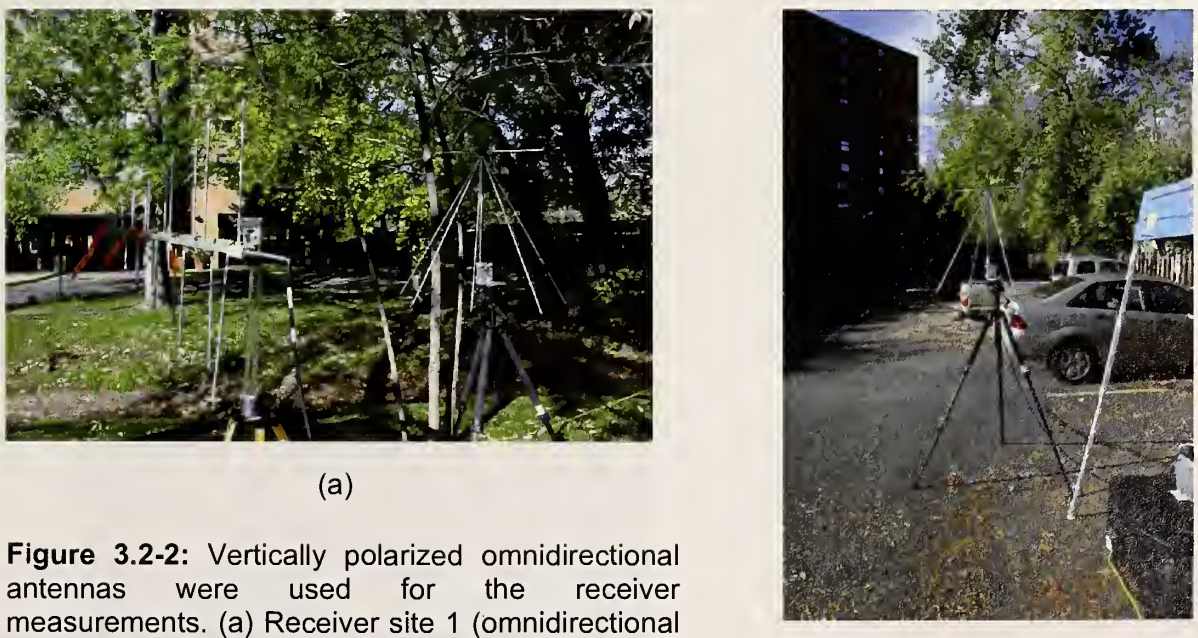

(a) (b)

Figure 3.2-2: Vertically polarized omnidirectional antennas were used for the receiver measurements. (a) Receiver site 1 (omnidirectional antenna is on the right). (b) Receiver site 2.

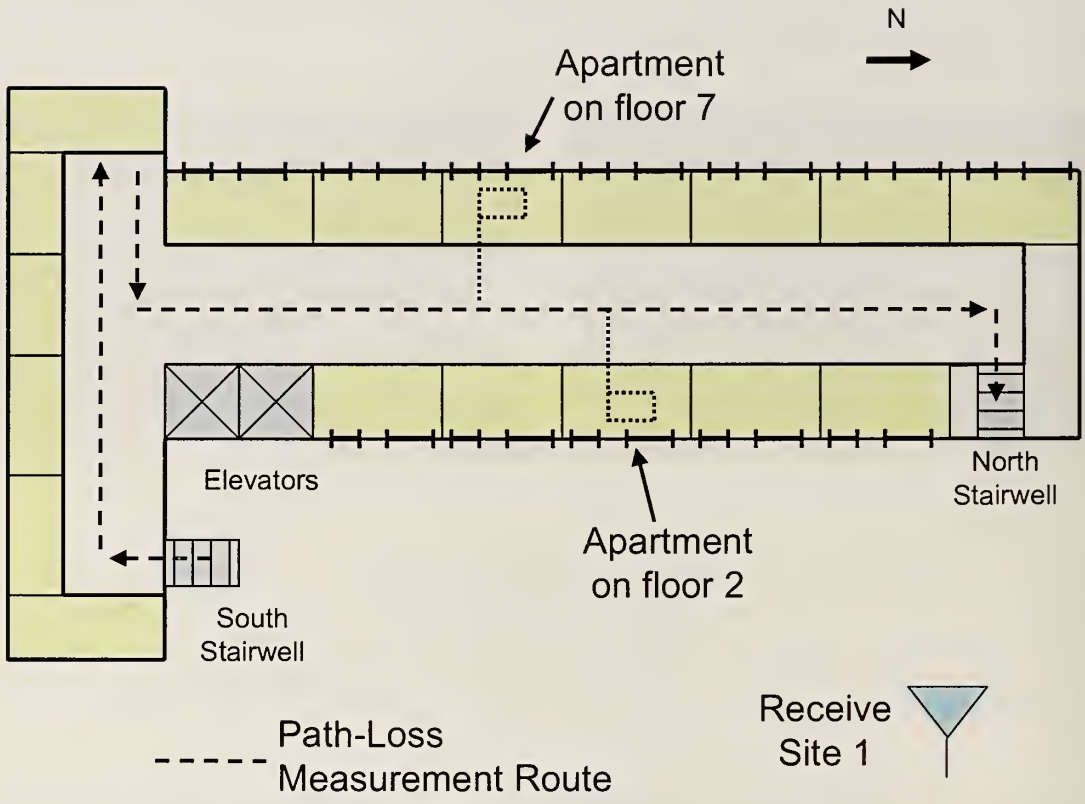

Figure 3.2-3: The dashed line shows the route taken on each of the top 10 floors of the apartment building during the single-frequency received-power measurements. Measurements continued up the stairwells. Dotted lines show the approximate path taken into apartments on the second and seventh floors. A second receiver site was located approximately 80 m to the north of the building.

(a)

(b)

Figure 3.2-4: (a) Carrying a transmitter down a hallway in the apartment building. (b) Set of transmitters used in the narrowband received-power measurements.

Figures 3.2-5(a) and (b) show a representative set of receiver data covering the top 10 floors of the apartment building for a carrier frequency of 908 MHz recorded at the two receiver sites shown in Figures 3.1-2 and 3.1-3. The complete set of data recorded at receiver sites 1 and 2 appears in Appendix A. In each plot, vertical lines marked with an "L" and a number represent the transmitter entering the various floors of the building from the stairwells on either end. The path zigzags up through the building; that is, if the third floor was entered from the south stairwell, then the fourth floor was entered through the north stairwell. The locations of the apartments on the second and seventh floors are also noted on the graphs.

Figure 3.2-5 shows that in general, the signal levels were strongest in the stairwells, which are relatively weakly shielded. The levels dropped significantly when the transmitters moved behind the elevators. When the transmitters were carried through the apartments on the second and seventh floors, the signal levels changed significantly as well. At receiver site 1, directly across from the window of the second-floor apartment, the signal level increased, while it decreased when the transmitter entered the seventh-floor apartment on the opposite side of the building. At receiver site 2, the signal levels dropped when the transmitter entered either apartment.

This example set of data illustrates the wide range of signal levels that may be encountered by radio systems when building penetration is involved. Many of the level changes can be explained by simple deduction based on the physical environment. While narrowband received power data such as this are vital for an adequate understanding of the attenuation due to building penetration, when wideband modulation is used, multipath and frequency selectivity in the channel can affect building penetration as well. These aspects of signal propagation are discussed in the following sections.

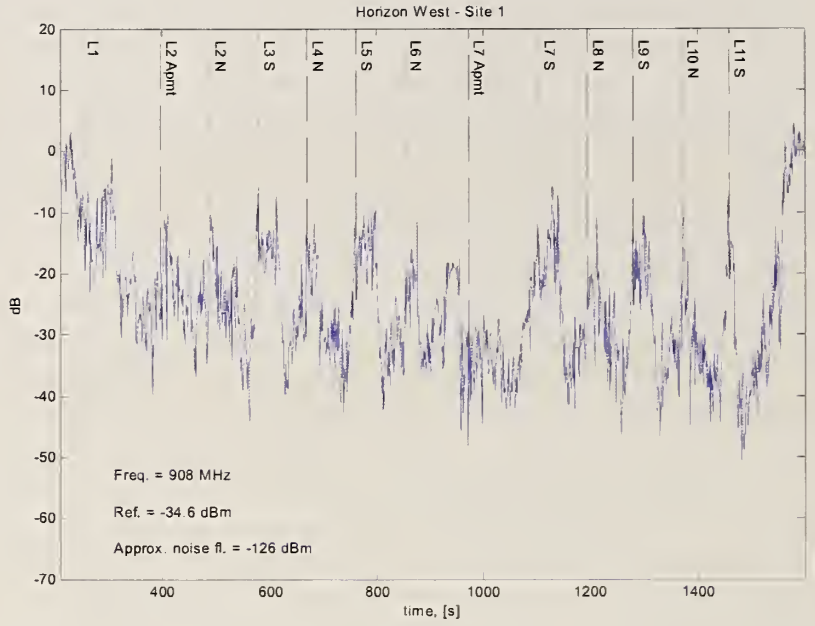

(a)

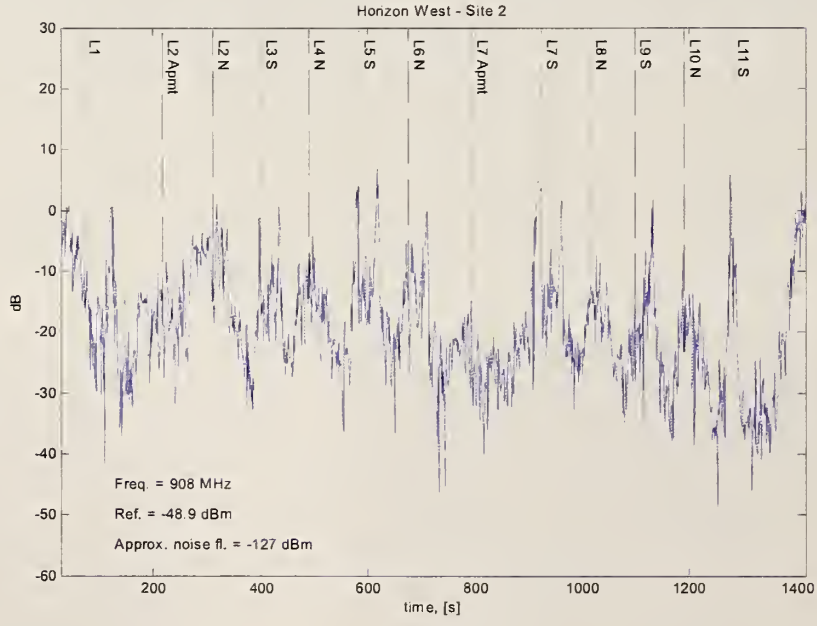

(b)

Figure 3.2-5: Received-power data for the top 10 floors of an apartment building as measured by a narrowband communications receiver at (a) receiver site 1 and (b) receiver site 2. The carrier frequency was 908 MHz. The received signal levels are referred to a line-of-sight reference signal, whose level is noted on each graph. The locations of the stairwells at the north and south ends of the buildings are noted by the vertical dashed lines on each graph, as are the locations of the apartments on the second and seventh floors.

3.3 Excess Path Loss and RMS Delay Spread

We next carried out measurements at the apartment building using the VNA-based synthetic-pulse measurement system described in Section 2.3. Figure 3.3-1 shows photographs of the transmitter site set-up. Only site 1 was used. Because of the time required for each measurement (up to two or three minutes, depending on the number of frequency points acquired), and because of the necessity of linking the transmitting and receiving sections with a fiber-optic link, we restricted our data collection to selected points on the second and seventh floors. Again, we chose the second floor because this is studied in the SAFECOM SoR Apartment Fire Scenario.

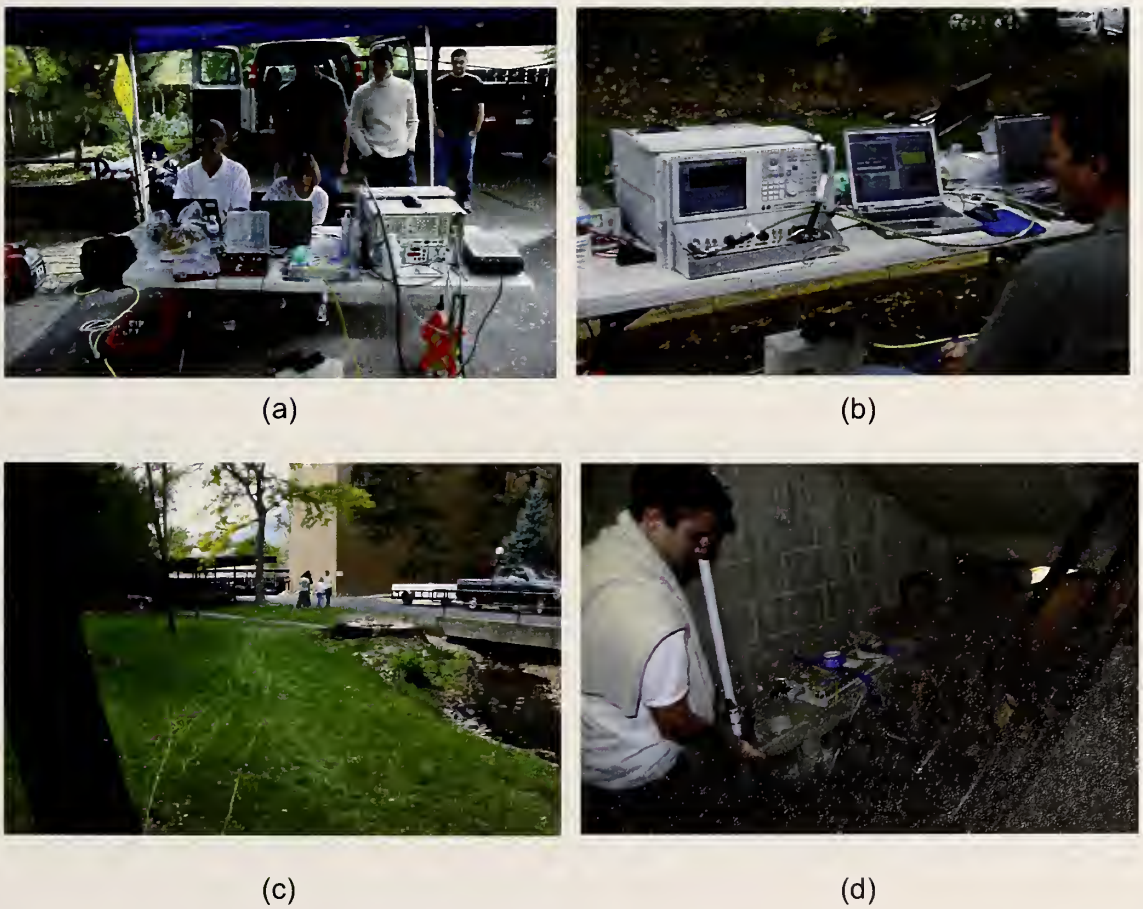

(a) (b)

(c) (d)

Figure 3.3-1: Set-up of the synthetic-pulse, ultrawideband measurement system at receiver site 1. (a) Equipment included the optical-fiber link (far right on table), the vector network analyzer (to the left of the link), and a computer for data acquisition. (b) Vector network analyzer and laptop. (c) Optical fiber cable was tethered to the receiving antenna as it was carried through the building, as shown in a stairwell in (d).

Measurements were made at points approximately every five meters along both corridors of the apartment building, as shown in Fig. 3.3-2. We collected data covering

two frequency bands. For the lower frequency band (25 MHz to 1.4 GHz), we used omnidirectional antennas, as would be used by most emergency response companies. For the higher frequency band (750 MHz to 18 GHz) it was necessary to use directional horn antennas in order to have sufficient signal strength at the higher frequencies. The omnidirectional antennas we used are shown in Figure 3.2-2(a) and (b).

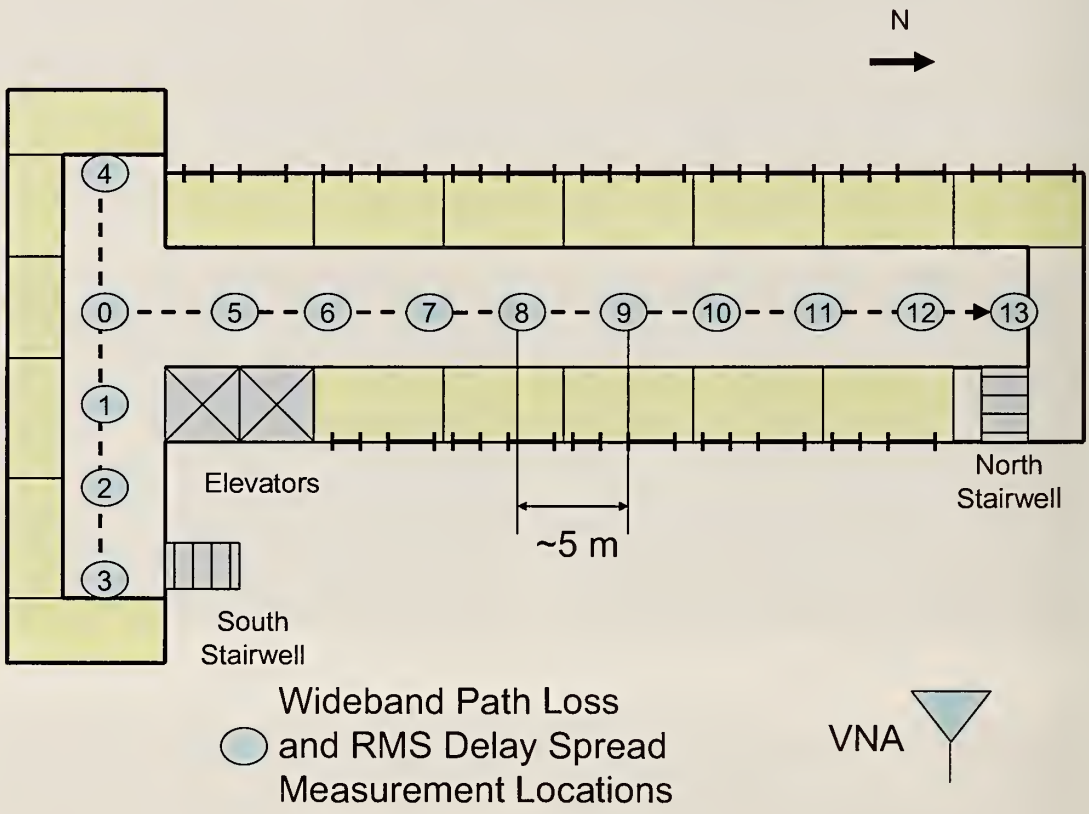

Figure 3.3-2: Positions along the apartment building corridor where synthetic pulse measurements were made. Measurements were carried out on the second and seventh floors. The transmitting antenna was located outside and the receiving antenna was moved along the floors.

Figure 3.3-3 shows a summary of the wideband excess path loss data covering a frequency range of 1 GHz to 18 GHz. These curves, too small to be easily interpreted, are shown simply to give a feeling for how the signal levels change with floor and with frequency. The complete sets of measured data are provided in Appendix E. The top black curve represents the data collected on the second floor, the middle red curve represents the data from the seventh floor, and the bottom blue curve is the noise floor of the measurement system.

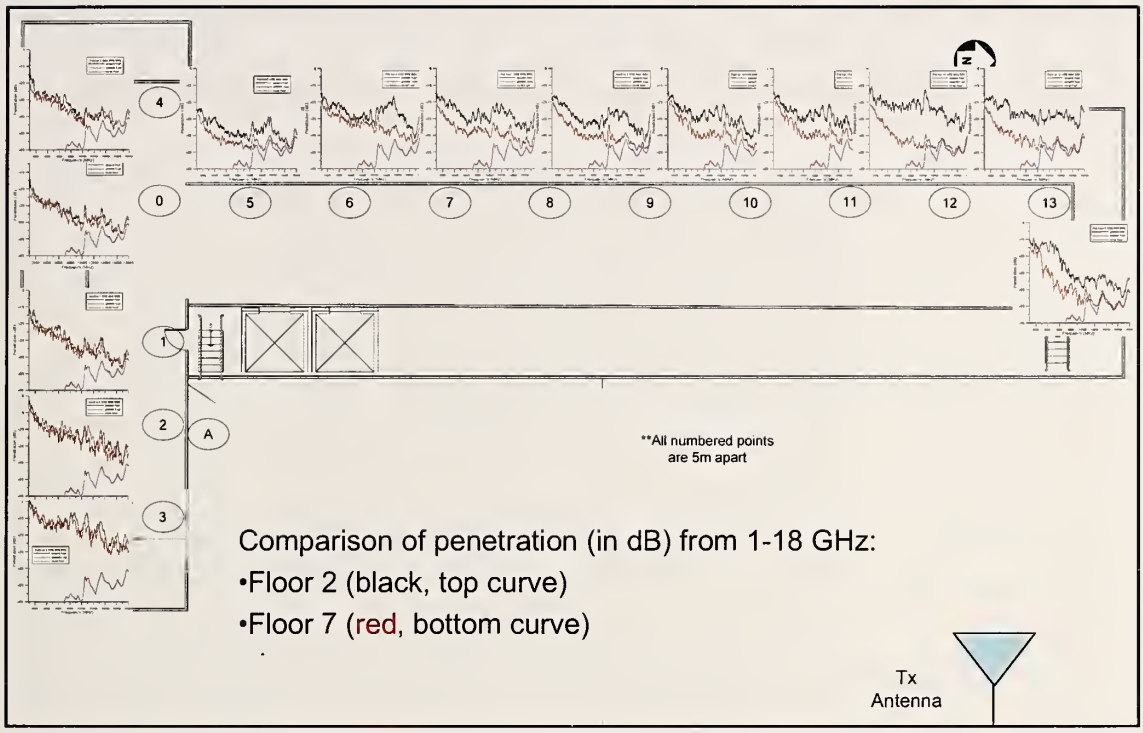

Figure 3.3-3: Summary of VNA-based synthetic-pulse data collected on the second and seventh floors of an 11-story apartment building. The top line is data from the second floor, the middle line is from the seventh floor, and the bottom line represents the noise floor of the measurement system. The point labeled "TX Antenna" represents the location of the VNA at receiver site 1. Note that the placement of the south stairwell and elevators is incorrect on this figure. The complete set of data, enlarged, is in given Appendix E.

Figure 3.3-3 clearly shows that along the main hallway, the signals received from the seventh floor are noticeably weaker than those from the second floor, in particular at the higher frequencies. The locations where the receiver is positioned behind the elevators have universally weak signals relative to those with a less-obstructed path. The data also indicate that lower frequencies penetrate the building better than higher frequencies. This may have some bearing on the use of the 4.9 GHz frequency band for public-safety use at an emergency site.

The RMS delay spread values calculated from the VNA measurements are presented below in Tables 3.3-1 through 3.3-4. On the second floor, the delay spread ranges from 28.2 ns at position 3 to 71.2 ns at position 6 for the lower frequency band using omnidirectional antennas, and from 15.3 ns (position 3) to 48.2 ns (position 5) in the higher frequency band using horn antennas. Position 3 is nearest to the receiver site, and so very little multipath is seen. Positions 5 and 6 are behind the elevator and so an increased level of multipath is seen for these locations.

These same trends are seen on the seventh floor. For the lower frequency band, the RMS delay spread ranged from 33.2 ns at position 3 to 82.4 ns at position 13. For the higher frequency band, the RMS delay spread ranged from 14.5 ns at position 3 to

44.2 ns at position 5. This indicates that the signals are experiencing a similar level of multipath on both floors.

Table 3.3-1. RMS delay spread calculated from excess path loss measurements on the second floor for the lower frequency band.

Floor 2, 300 MHz to 1 GHz, Omnidirectional Antennas

Position	RMS Delay Spread (ns)	Initial Tau* (ns)	Stop Time** (ns)
0	49.2	248.6	900
1	38.7	216.7	1000
2	35.8	151.1	800
3	28.2	121.4	800
4	48.8	278.2	1000
5	59.1	254.7	1000
6	71.2	225.4	1000
7	62.9	215.2	1000
8	61.6	211.4	1000
9	56.7	200.7	1000
10	58.6	190.8	1000
11	54.3	189.0	1000
12	60.9	185.4	1000
13	62.9	182.8	1000

* Initial tau is when the signal appears in the measurement window
** The calculation was stopped when the signal level dropped 40 dB below highest level

Table 3.3-2. RMS delay spread calculated from excess path loss measurements on the second floor for the higher frequency band.

Floor 2, 1 GHz to 18 GHz, Directional Antennas

Position	RMS Delay Spread (ns)	Initial Tau* (ns)	Stop Time** (ns)
0	24.1	219.2	600
1	21.4	207.9	600
2	16.7	188.6	600
3	15.3	184.4	700
4	24.9	227.1	700
5	48.2	200.9	800
6	30.7	191.0	800
7	36.3	182.6	800
8	31.2	174.1	800
9	30.4	167.7	800
10	31.7	161.7	800
11	39.4	155.9	800
12	38.0	153.9	800
13	20.8	154.3	800

* Initial tau is when the signal appears in the measurement window
** The calculation was stopped when the signal level dropped 40 dB below highest level

Table 3.3-3. RMS delay spread calculated from excess path loss measurements on the seventh floor for the lower frequency band.

Floor 7, 300 MHz to 1 GHz, Omnidirectional Antennas

Position	RMS Delay Spread (ns)	Initial Tau* (ns)	Stop Time** (ns)
0	47.2	268.7	1000
1	36.4	250.5	1000
2	37.7	233.6	1000
3	33.2	225.3	1000
4	49.9	285.7	1000
5	59.9	287.9	1000
6	70.9	250.3	1000
7	77.5	238.0	1000
8	70.1	221.2	1000
9	66.5	209.7	1000
10	69.1	204.2	1000
11	65.5	208.2	1000
12	67.5	228.7	1000
13	82.4	195.6	1000

* Initial tau is when the signal appears in the measurement window
** The calculation was stopped when the signal level dropped 40 dB below highest level

Table 3.3-4. RMS delay spread calculated from excess path loss measurements on the seventh floor for the higher frequency band.

Floor 7, 1 GHz to 18 GHz, Directional Antennas

Position	RMS Delay Spread (ns)	Initial Tau* (ns)	Stop Time** (ns)
0	32.4	226.3	800
1	23.7	214.8	800
2	24.3	198.4	800
3	14.5	189.5	800
4	35.9	245.2	800
5	44.2	211.4	800
6	37.4	201.4	800
7	40.8	193.2	800
8	38.8	184.7	800
9	30.5	178.4	800
10	31.0	172.2	800
11	34.8	169.3	800
12	36.8	166.1	800
13			

* Initial tau is when the signal appears in the measurement window
** The calculation was stopped when the signal level dropped 40 dB below highest level

3.4 Error Vector Magnitude and Modulated-Signal Spectra

Finally, we investigated the transmission of wideband digitally modulated signals into the apartment building using the error vector magnitude metric, described in Section 2.4. We also measured the spectra of the digitally modulated signals and the multisine signals designed to simulate them. The excitation was a QPSK-modulated OFDM signal having a bandwidth of 20 MHz.

For these measurements, we used the vector-signal-analyzer-based measurement set-up described in Section 2.4. Because of the length of time required to perform these measurements (on the order of minutes), data were again collected at only selected locations. We used the same locations on the second and seventh floors where the UWB measurements of Section 3.3 were made. Photographs of the measurement set-up at receiver site 1 and the cart containing the transmitting equipment are shown in Figures 3.4-1(a) and (b).

(a) (b)

Figure 3.4-1: Measurement set-up for the vector-signal analyzer measurements of wideband digitally modulated signals. (a) At receiver site 1, the VSA can be seen at the back of the van on the right side. A computer was used for data acquisition. (b) The transmitter was moved through the hallways on a rolling cart. A vector signal generator is on top of the cart, power amplifiers are on the bottom of the cart, and an omnidirectional antenna can be seen at the corner of the cart.

Figure 3.4-2(a) shows the measured EVM data for the second floor and Figure 3.4-2(b) for the seventh floor. The top set of numbers on each plot corresponds to carrier frequencies of 2.4 GHz and the bottom numbers are for 4.95 GHz. In all cases the EVM is quite high. However it is clear that the higher carrier frequency results in a higher EVM for both floors.

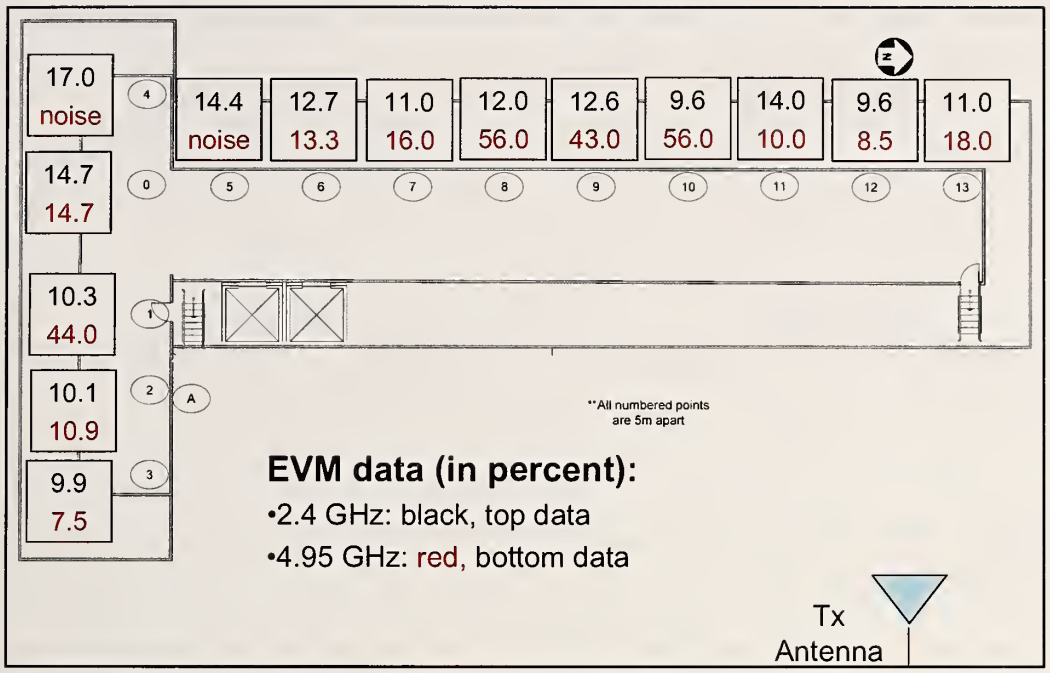

(a)

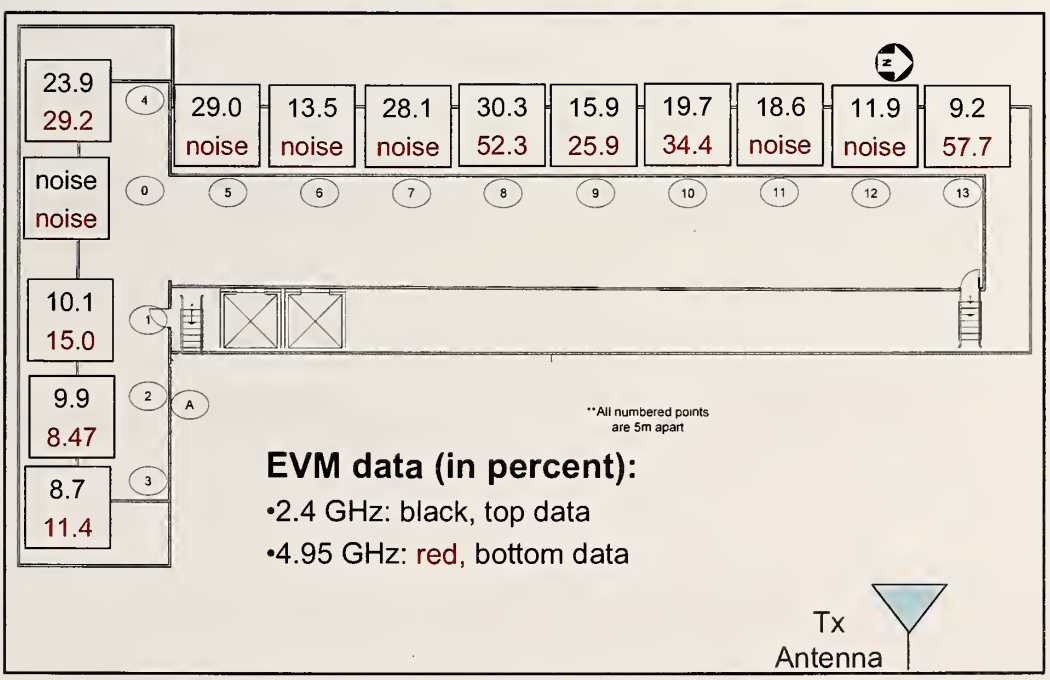

(b)

Figure 3.4-2: EVM data for OFDM signals using QPSK modulation at selected points on (a) the second floor and (b) the seventh floor of an 11-story apartment building. Carrier frequencies of 2.4 GHz and 4.95 GHz were used. Percentage values of EVM are defined in (2.4-1).

Figures 3.4-3 and 3.4-4 show the magnitude spectrum of the received signals at positions 2 and 8, respectively. Figures 3.4-3(a) and 3.4-4(a) show measurements made on the second floor for the two different carrier frequencies (2.412 GHz and 4.95 GHz). Figures 3.4-3(b) and 3.4-4(b) show measurements on the seventh floor.

Position 2 has a relatively direct path to the receiver. These signals show less frequency-selective distortion, but the 4.95 GHz carrier is clearly received at a lower level, even though the transmitters had the same nominal output power and we used the same transmitting and receiving antennas.

Position 8 shows the effects of signal attenuation and reflection from the elevators and other building materials, so the received signal is relatively weak. We see frequency-selective distortion to the signal; that is, some frequency components of the received signals are subject to higher interference levels than others. This is commonly seen in broadband-modulated-signal transmissions where building penetration and propagation are involved, and is an additional factor that must be considered for robust deployment of broadband systems. The complete set of VSA data in the apartment building is given in Appendix I.

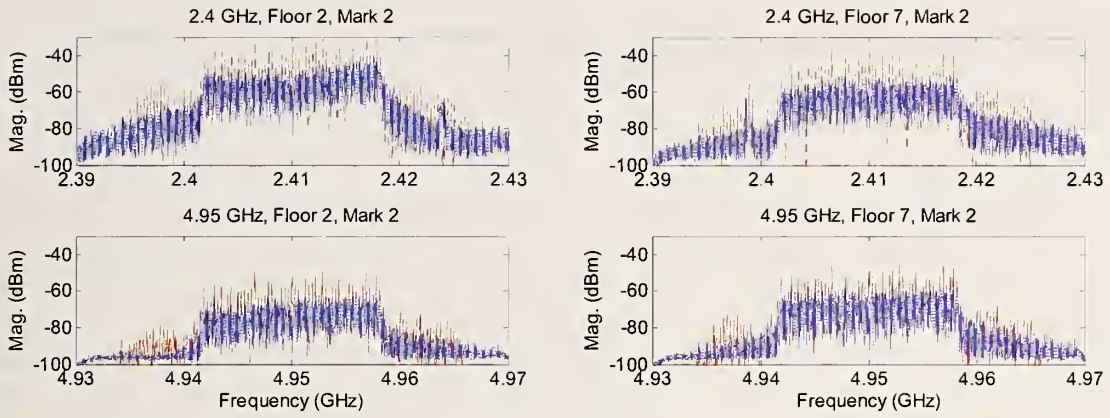

(a) (b)

Figure 3.4-3: Amplitude spectrum of VSA-measured wideband modulated signals for carrier frequencies of 2.41 GHz (top) and 4.95 GHz (bottom) at position 2 (see Figure 3-4.2). (a) Second floor. (b) Seventh floor. The solid blue lines are the QPSK-modulated signals, and the dashed red lines are the multisine signals designed to simulate them. Most of the received signals exhibit a small amount of frequency-selective distortion, with the 4.95 GHz signals having lower overall received signal strength.

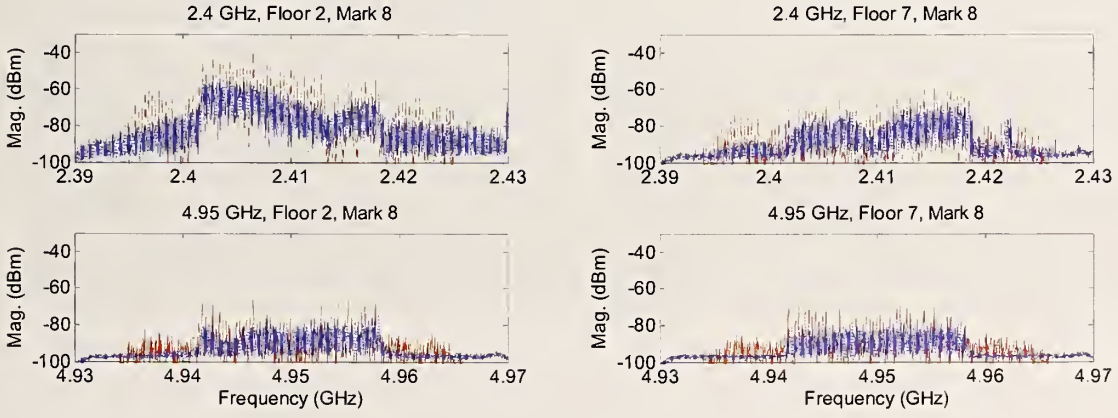

(a) (b)

Figure 3.4.4: Amplitude spectrum of VSA-measured wideband modulated signals for carrier frequencies of 2.41 GHz (top) and 4.95 GHz (bottom) at position 8 (see Figure 3-4.2). (a) Second floor. (b) Seventh floor. The solid blue lines are the QPSK-modulated signals, and the dashed red lines are the multisine signals designed to simulate them. Again we see a high level of frequency-selective distortion. As well, the 4.95 GHz signals again have lower overall received signal strength.

4. Office Corridor Measurements

4.1 Overview

We again carried out the three types of propagation measurements described in Section 2 (narrowband received power, excess path loss/RMS delay spread, and modulated signal/EVM measurements). This time the location was a corridor on level three, Building 1 of the Department of Commerce Laboratory complex that houses NIST in Boulder, Colorado. The building is constructed of reinforced concrete and consists of four stories. However, the building is built into the side of a hill, and as a result, not all four floors exist throughout the structure. As well, some locations in the building are below ground level. Measurements were performed during daytime hours with people moving throughout the building during the experiments.

The layout of the corridor is shown in Figure 4.1-1 and a photograph of the corridor is shown in Figure 4.1-2. There is no building structure above or below the part of corridor denoted by points A and B. For locations beyond the hallway junction (marked C and D), there are floors above and below the corridor.

We used two receiver sites for the narrowband received-power measurements, the wideband excess-path-loss measurements, and the RMS delay spread, as shown in Figure 4.1-3. One of the receiver sites was located at the end of the corridor, around a corner on a loading dock (marked "Wing 4" in Figure 4.1-1). This receiver site, shown in Figure 4.1-3(a), enabled a study of propagation in the corridor under non-line-of-sight conditions. The second receiver site was located outside the building approximately 60 m from the end of the corridor (marked "Wing 6" in Figure 4.1-1). This receiver site is shown in Figures 4.1-3(b) through (d). At this site we studied both non-line-of-sight propagation and building penetration in a position where emergency-response equipment may be located. The EVM measurements were carried out only under non-line-of-sight conditions, that is, at the first receiver site described above.

In the following sections, we describe the various measurements we conducted of narrowband received power (using the single-frequency receiver), excess path loss and RMS delay spread (using the vector network analyzer), and modulated-signal response and EVM (using the vector signal analyzer). Selected data sets are presented to highlight significant aspects of signal propagation in this environment. The complete sets of data are included at the end of the report in Appendices B, E, and I.

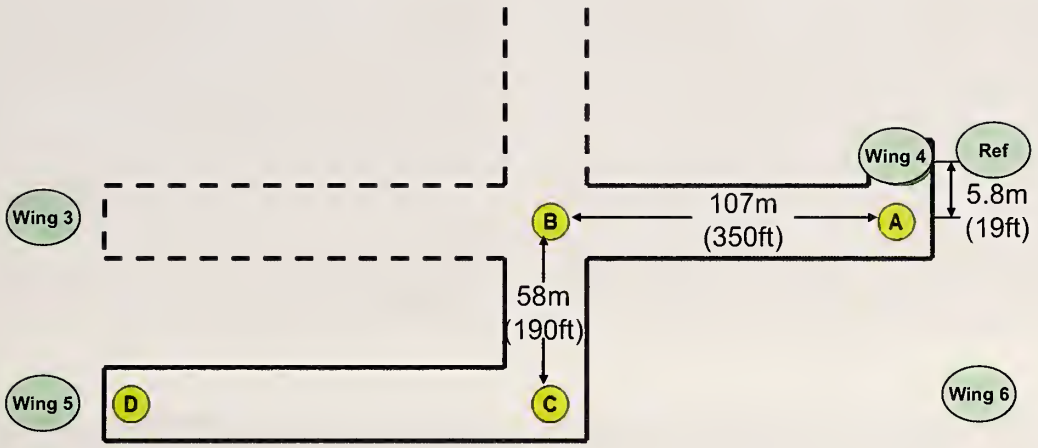

Figure 4.1-1: Layout of office corridor. One receiver site was located at the point marked "Wing 4." This was inside the building but in a non-line-of-sight location from the transmitter, except at point A. The other receiver site was located outside the building at the end of Wing 6, and is marked "Wing 6." Distances are approximate.

(a) (b)

Figure 4.1-2: Photographs of the office corridor where NIST measurements were made. (a) Looking from the indoor receiver site toward the junction. The corridor consists of cinderblock walls with wooden doors to offices. Each office has a window to the outside. (b) The junction, where the transmitter either went straight or turned left.

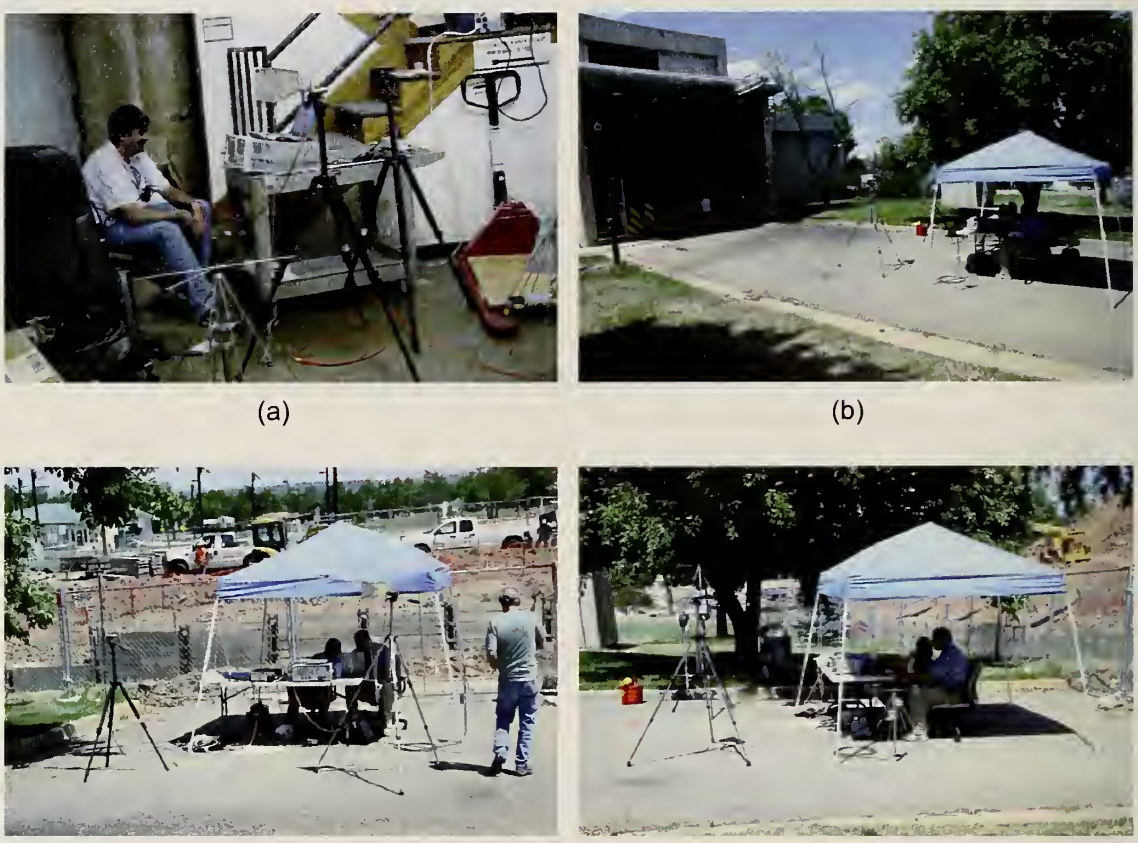

(a) (b)

(c) (d)

Figure 4.1-3: Photographs of the two receiver sites. (a) Indoor, non-line-of-sight location at the end of Wing 4. (b) Outdoor location at the end of Wing 6. (c) and (d) show the omnidirectional (left in (c)) and directional (right in (c)) antennas used in the measurements.

4.2 Narrowband Received-Power Measurements

For the narrowband received-power experiments, the two fixed receiver sites (as described above) were assembled. During this experiment, transmitters were carried through the laboratory corridors along two different paths, illustrated in the top and bottom plots of Fig. 4.2-1. Measurements were performed with the receiving antennas polarized in the vertical direction. As the received signals were recorded, the location of the transmitter in the corridor was also recorded and is marked on the graphs of the measured data.

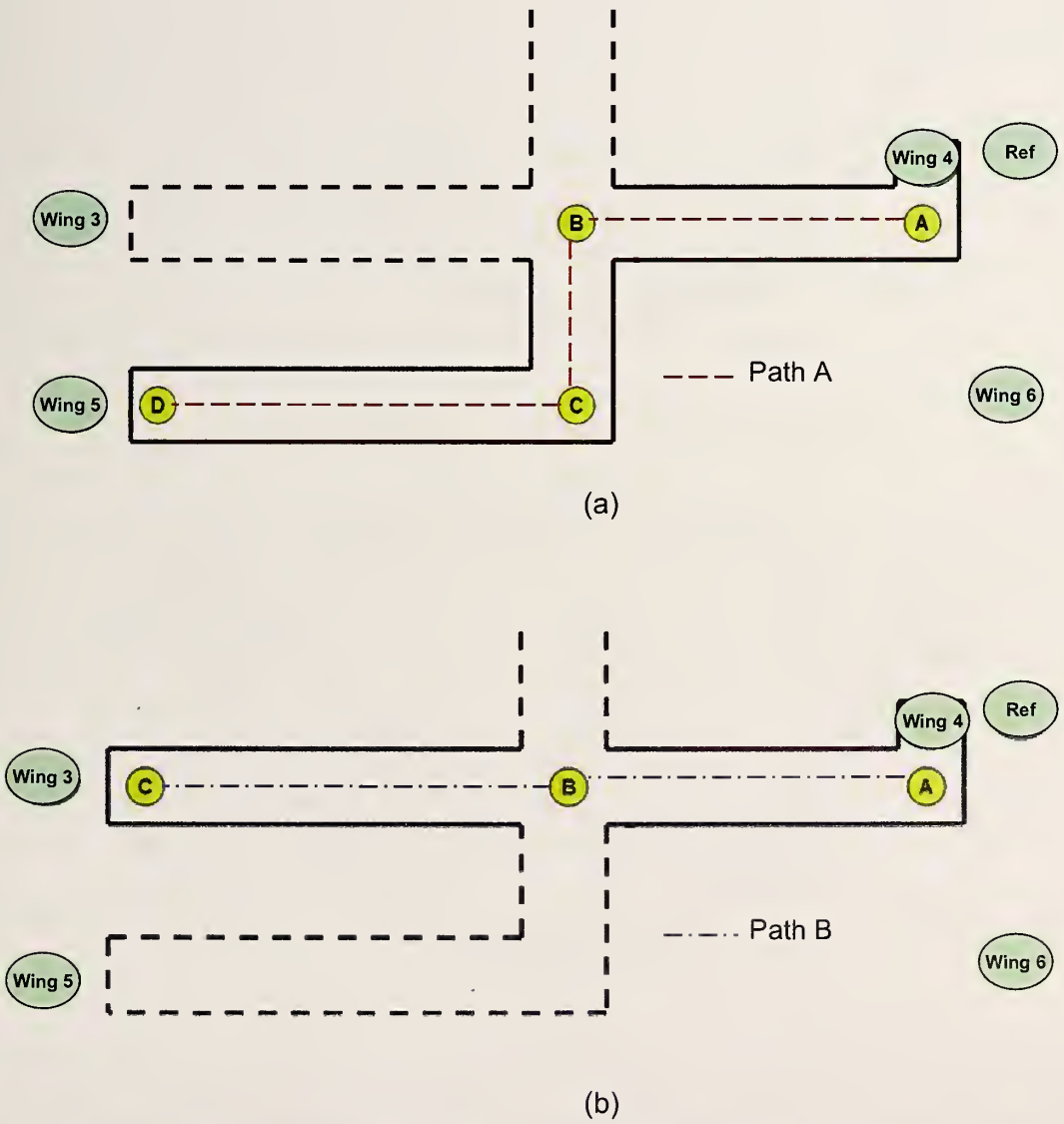

Figure 4.2-1: Two paths taken by the handheld transmitters in the office corridor. The path in (a) jogged over to a second, different corridor between points C and D. The path in (b) was straight.

Figure 4.2-2 shows a representative data set for a carrier frequency of 439.25 MHz collected at (a) receiver site one (located inside the building but non-line-of-sight, marked "Wing 4" in Figure 4.2-1) and (b) receiver site two (outside the building, marked "Wing 6" in Figure 4.2-1). The transmitter was carried along Path A and returned along the same path, so the first and second half results in each graph should theoretically be mirror images of each other. The fact that they are not may be due to a number of factors, including the different levels of shielding of the body on the outbound and return trips and the radiation pattern of the antennas that may be affected by the transmitter cases.

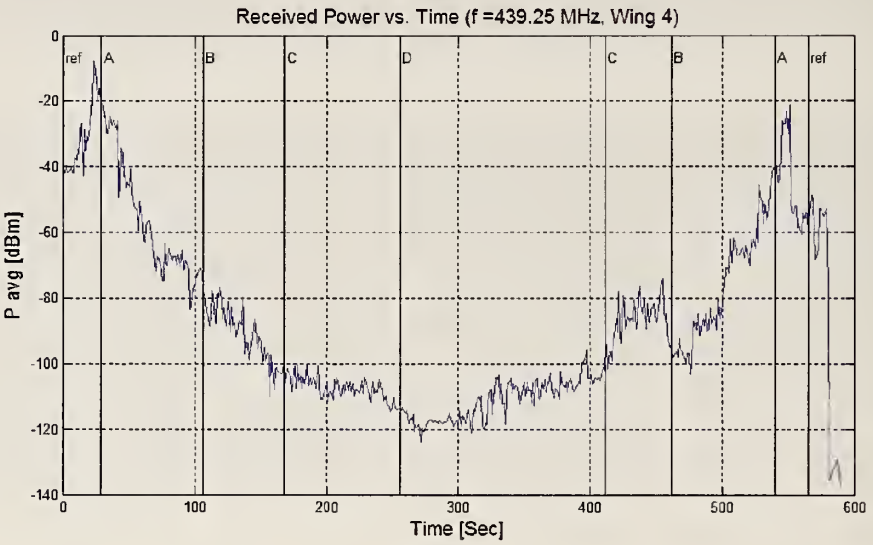

(a)

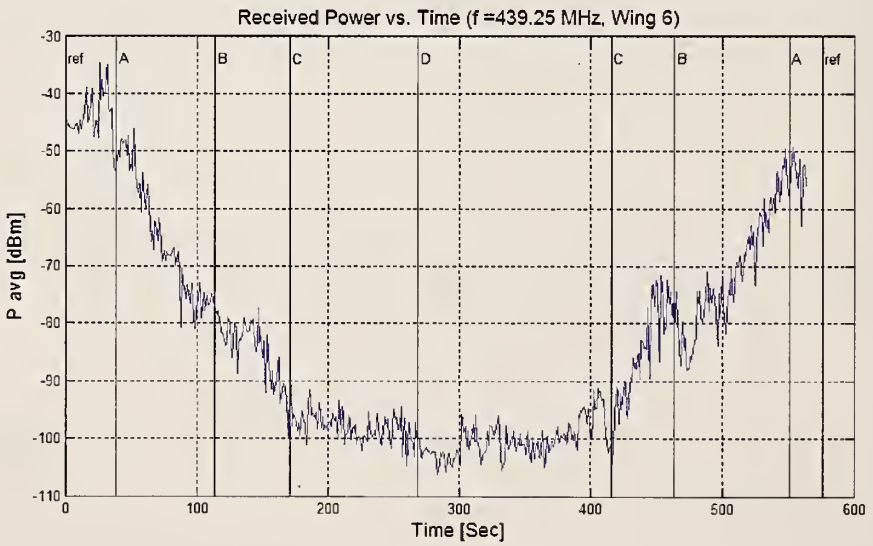

(b)

Figure 4.2-2: Received-power data for a carrier frequency of 439.25 MHz along Path A. (a) Receiver site one at the end of Wing 4. (b) Receiver site two at the end of Wing 6. The corridors denoted by the vertical lines have different propagation characteristics, indicated by the different slopes in the received-power curves.

Figure 4.2-3 shows received power data at the same carrier frequency for Path B. The top graph (a) corresponds to receiver site one and the bottom graph (b) to receiver site two. Once the transmitter passes the corridor junction, the received signal is quite weak, clearly showing the attenuation introduced by the junction.

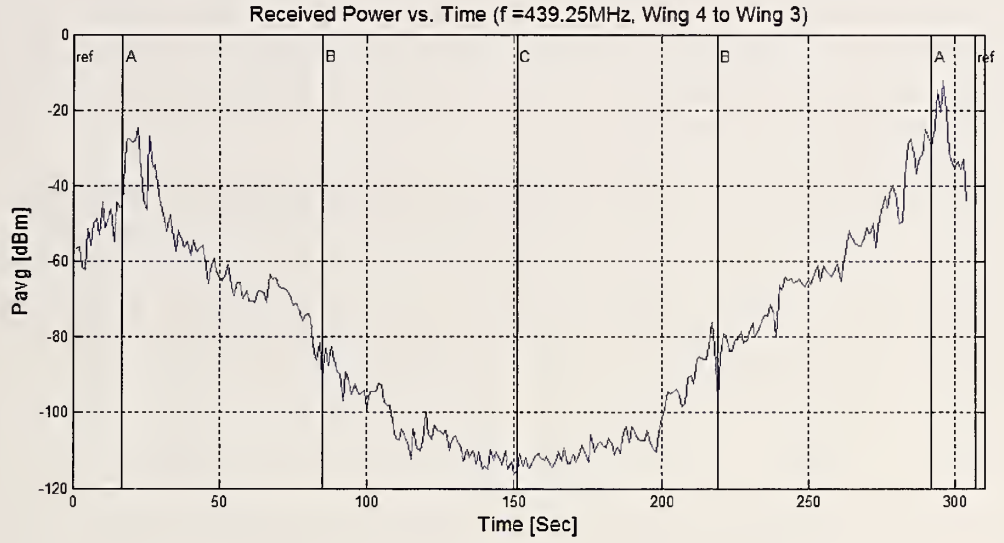

(a)

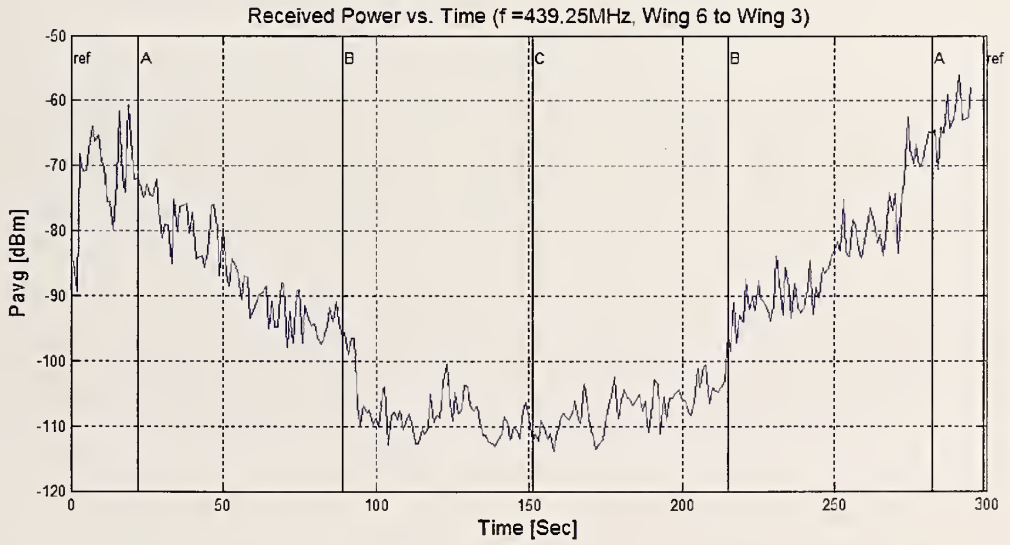

(b)

Figure 4.2-3: Received-power data for a carrier frequency of 439.25 MHz along Path B. (a) Receiver site one at the end of Wing 4. (b) Receiver site two at the end of Wing 6. Abrupt signal attenuation is introduced at the junction of the corridors, even though the path was straight.

Figures 4.2-2 and 4.2-3 show similar received-power profiles for both receiver sites, with receiver site two having an overall greater received power, since this path includes building penetration. Figures 4.2-2 and 4.2-3 also show a rapid decrease in signal strength between points A and B, probably due to the corridor acting as a waveguide below its cut-off frequency. Signals whose wavelengths are longer than the physical dimension of a waveguide rapidly attenuate when they are launched into the waveguide. We see this to an even greater extent for a carrier frequency of 162 MHz, shown in Figure 4.2-4. This effect is more pronounced at receiver site one since most of the signal's energy propagates only along the corridor. At receiver site two, the signal may also propagate to the receiver though windows. We will discuss the waveguide-below-cutoff effect in more detail in Section 6.

Figure 4.3-3 also shows that once the transmitter passes the corridor junction at point B, the signal level is quite low and decreases at a slower rate than before. The fact that the slope of the received power graph does not change more dramatically once the corner is turned (as it theoretically should) may be due to penetration through walls of the lower-frequency signals. The full set of received power data can be found in Appendix B.

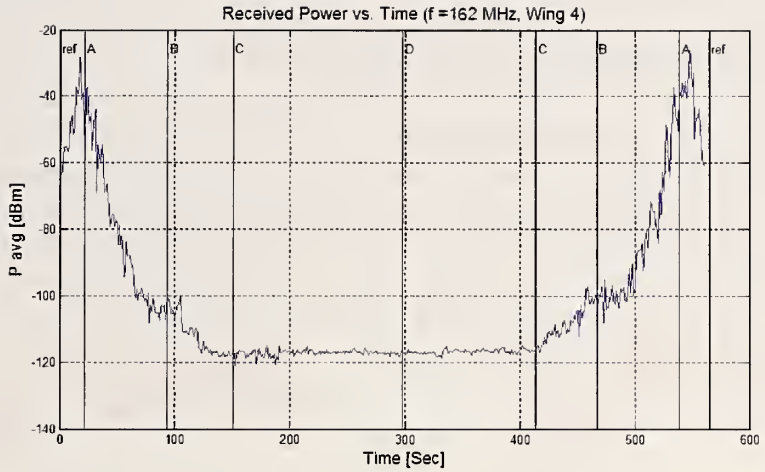

(a)

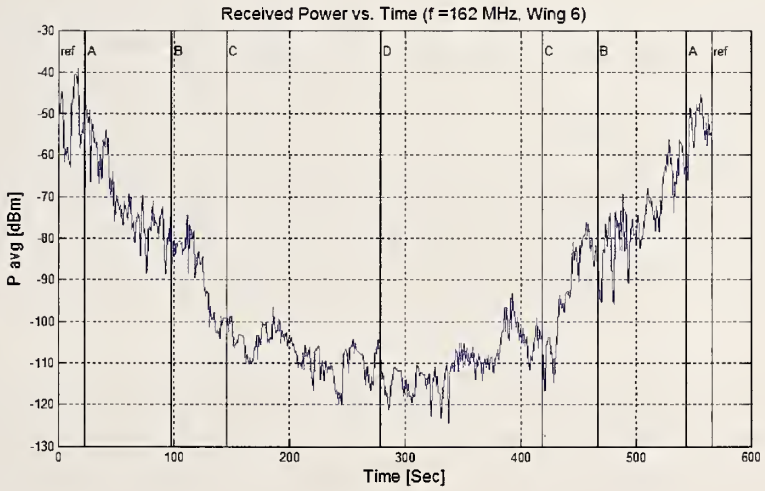

(b)

Figure 4.2-4: Illustration of the waveguiding effect experienced by lower carrier frequencies in the office corridor. The rapid attenuation between points A and B as the transmitter and receiver separate in (a) is minimized in (b) since the signals may take additional paths in the case of building penetration.

4.3 Excess Path Loss and RMS Delay Spread

We next carried out measurements in the office corridor using the VNA-based synthetic-pulse measurement system described in Section 2.3. Measurements were made at points approximately every 15.25 meters (50 feet) along the corridor of the office building, as shown in Figure 4.3-1. The transmitting antenna was located either at site one at the end of Wing 4 or at site two, outside the building by the end of Wing 6, as shown earlier in Figure 4.1-3. The receiving antenna was moved along the corridor to the locations marked in Figure 4.3-1.

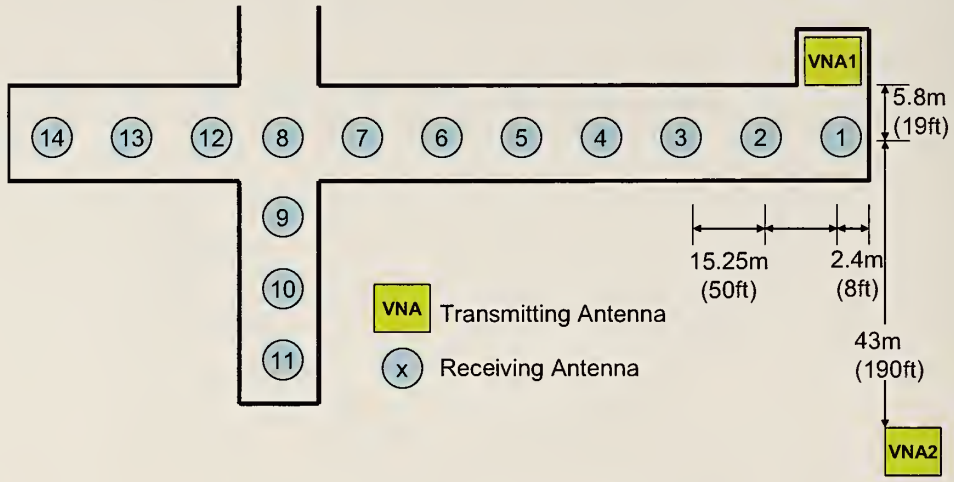

Figure 4.3-1: Layout of the synthetic-pulse ultra-wideband (UWB) VNA measurements in an office corridor. VNA1 is the location of the transmitting antenna placed inside the building, but non-line-of-sight with the receiving antenna. VNA2 is the location of the transmitting antenna outside the building for a second set of measurements.

We collected data covering two frequency bands. For the lower frequency band (25 MHz to 1.4 GHz), we used omnidirectional antennas, as would be used by most emergency response companies. For the higher frequency band (750 MHz to 18 GHz) we used both omnidirectional antennas and a set of directional horn antennas. The horn antennas minimized the reception of multipath by focusing the main lobe of the antenna toward the maximum received signal. This effect is illustrated in the RMS delay spread figures below. Both sets of antennas are shown in Figure 4.1-3.

Figure 4.3-2 shows representative lower-frequency measurement data when the VNA is located at site 1. In (a), the transmitting and receiving antennas are near each other, while in (b) the receiving antenna has moved down the corridor approximately 75 meters. At 1 GHz, the signal is roughly 25 dB lower down the corridor than it was in a line-of-sight condition, similar to what we saw with the receiver. Note the significant attenuation in the lower frequencies down the corridor, again illustrating the low-frequency waveguide-attenuation effect described in the previous section.

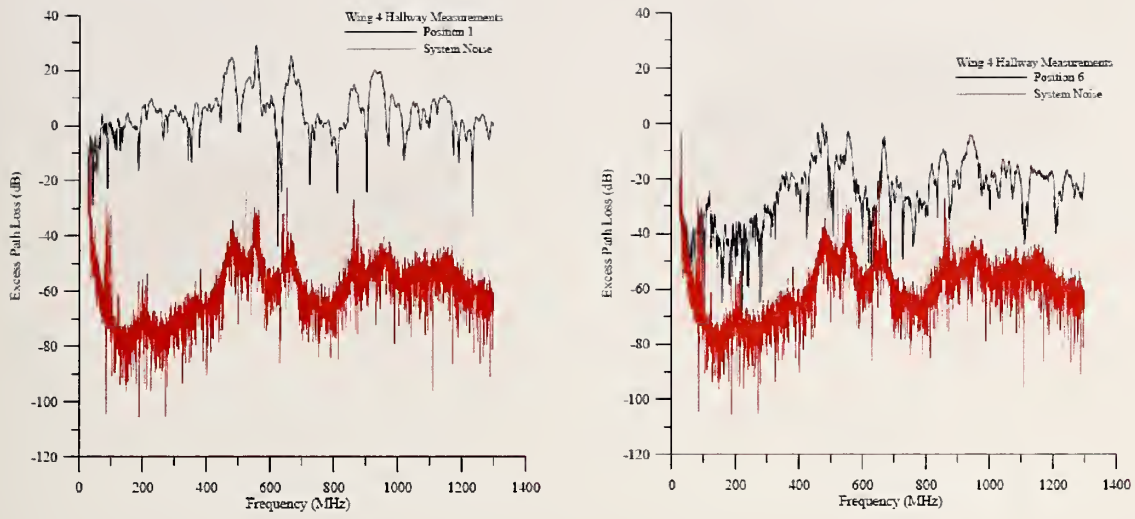

(a) (b)

Figure 4.3-2: Representative low-frequency (25 MHz to 1.4 GHz) data at position 1 (a) and position 6 (b) in the corridor when the receiving antenna was at site one. The top curve is the received signal and the bottom curve is the measurement system noise. In addition to overall decrease in signal level in (b), the frequencies below approximately 400 MHz are additionally reduced due to the corridor's waveguide-attenuation effect.

Figure 4.3-3 shows a significant reduction in signal strength at the junction of the corridors for the frequency band 750 MHz to 18 GHz. This is seen in the lower frequency band as well. The graph in (a) shows a relatively strong signal at position 8. In (b), the receiving antenna has turned the corner to position 9, and the signal level has dropped significantly. This is for the case where the transmitting antenna is located at the end of Wing 4 in a non-line-of-sight condition.

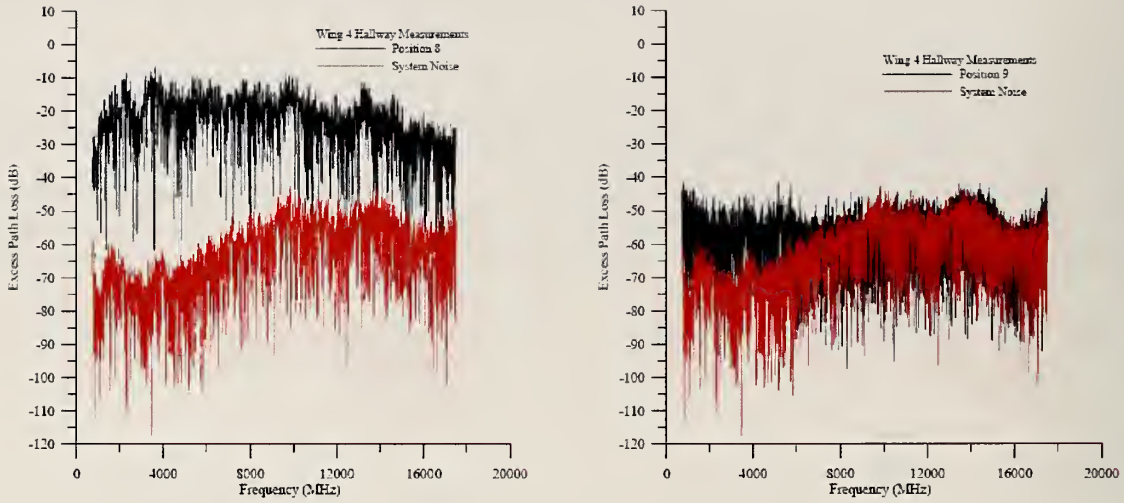

(a) (b)

Figure 4.3-3: A significant reduction in signal strength was seen across all frequencies from 750 MHz to 18 GHz when the receiving antenna turned the corner (positions 8 and 9) and the transmitting antenna was located inside the building. The transmitting antenna was at site 1. Similar results were seen for the lower frequency band.

Very different effects are seen for the case involving building penetration; that is, when the transmitting antenna is located outside the building at the end of Wing 6 at site 2. Figures 4.3-4(a) and (b) show a much lower received signal strength for both positions 8 (end of first corridor) and 9 (around the corner). The signals at higher frequencies are lower than the system noise at both locations 8 and 9. However, for the lower frequencies, turning the corner inside the building has little effect on the received signal level. While the overall signal levels are lower, corridor effects play a less-significant role in the propagation environment when building penetration can be achieved through multiple paths. The complete data sets for excess path loss appear in Appendix E.

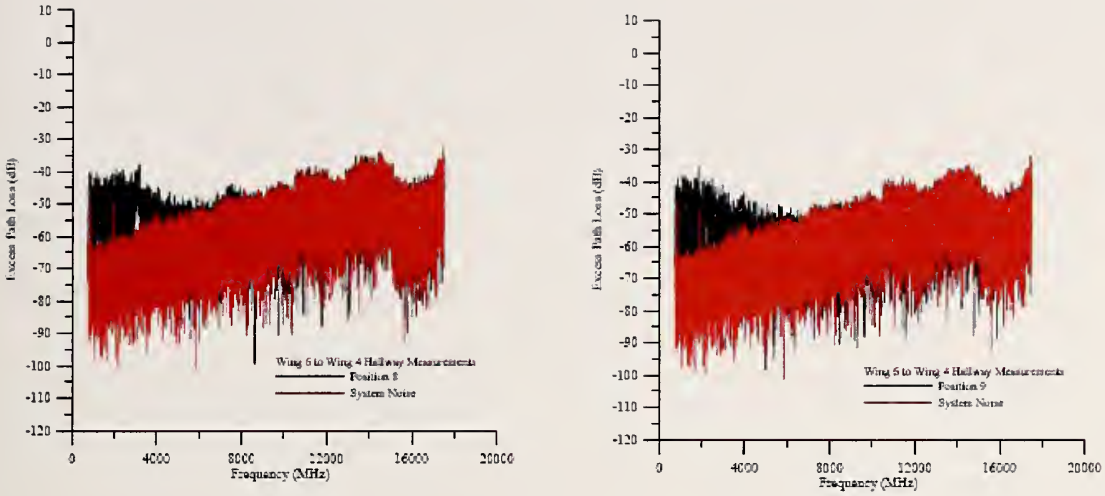

(a) (b)

Figure 4.3-4: When the transmitting antenna was located outside the building, there was little change in the excess path loss as the receiving antenna moved from position 8 in the junction (a) to position 9 around the corner (b). The overall signal level was lower than for the case where the transmitting antenna was inside the building. Most of the high-frequency signals were below the noise floor of the measurement system.

The RMS delay spread calculated from the VNA measurements is summarized in Figures 4.3-5 and 4.3-6. Three different measurement configurations are shown covering different frequency ranges and antenna types. Figure 4.3-5 is the case where the transmitting antenna was inside the building at site 1 and Figure 4.3-6 is when it was outside at site 2. We were unable to calculate reliable RMS delay spread numbers past point 8 at the junction of the corridors, due to low received-signal levels.

These data reflect the qualitative discussion above on corridor propagation effects. For example, the RMS delay spread is more significant at lower frequencies for indoor propagation (transmitter site 1), where the waveguide-attenuation effect is strong. Also, for the lower frequencies, the RMS delay spread increases significantly as the receiving antenna is moved down the corridor.

For the higher-frequency bands, the variation in RMS delay spread as the receiving antenna moves down the corridor is not as significant as for the lower-frequency bands. When the transmitting antenna is inside, the use of a directional antenna decreases the RMS delay spread as well as its variation as the antennas are separated from each other. When the transmitting antenna is outside, the directional antenna provides an RMS delay spread shorter than that of the omnidirectional antenna.

Note that in some cases the signals at the higher frequencies were close to the noise floor. For this reason, we did not calculate RMS delay spread at points above 8. However, in the building penetration case, noise may still have had an impact on the RMS delay spread calculations, for example, see Figure 4.3-4(a). However, the RMS calculations below do show the trends clearly.

It is interesting to note that the lower-frequency band has a shorter RMS delay spread than the higher-frequency band when the transmitting antenna is outside and the receiving antenna is nearest to the transmitting antenna. This implies that when the penetration path dominates (as opposed to the corridor waveguide), the reflections at lower frequencies die out relatively quickly. It is only as we proceed down the corridor that the lower-frequency RMS delay spread becomes significant.

RMS Delay Spread (ns) for Indoor Transmit Antenna:

•Omnidirectional Antenna 25 MHz to 1.4 GHz: green, top data

•Omnidirectional Antenna 750 MHz to 18 GHz: red, middle data

•Directional Antenna 750 MHz to 18 GHz: blue, bottom data

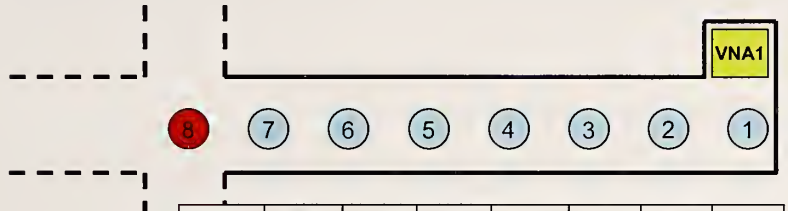

P8	P7	P6	P5	P4	P3	P2	P1
134.7	89.3	84.4	98.0	93.1	76.4	55.9	27.9
21.3	30.9	25.6	26.9	22.9	22.2	23.6	14.4
19.6	20.4	18.6	18.0	17.5	16.6	16.7	8.8

Figure 4.3-5: RMS delay spread for measurements made with the transmitting antenna inside the building at site 1.

RMS Delay Spread (ns) for Outdoor Transmit Antenna:

•Omnidirectional Antenna 25 MHz to 1.4 GHz: green, top data

•Omnidirectional Antenna 750 MHz to 18 GHz: red, middle data

•Directional Antenna 750 MHz to 18 GHz: blue, bottom data

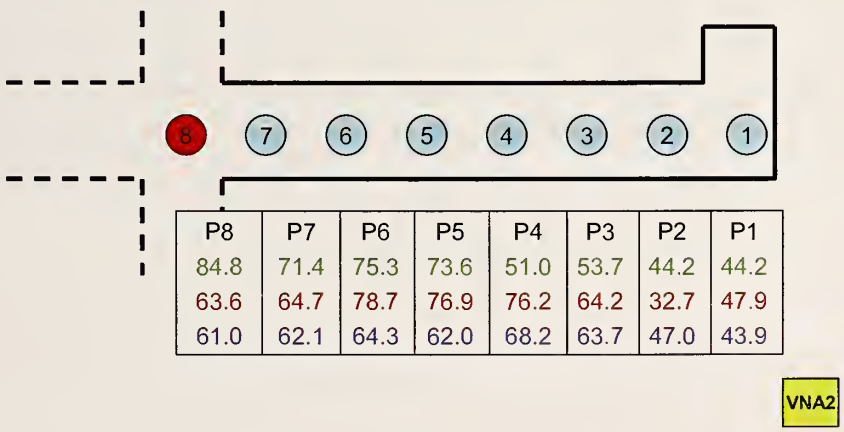

P8	P7	P6	P5	P4	P3	P2	P1
84.8	71.4	75.3	73.6	51.0	53.7	44.2	44.2
63.6	64.7	78.7	76.9	76.2	64.2	32.7	47.9
61.0	62.1	64.3	62.0	68.2	63.7	47.0	43.9

Figure 4.3-6: RMS delay spread for measurements made with the transmitting antenna outside the building at site 2.

4.4 Error Vector Magnitude and Modulated-Signal Spectra

Finally, we investigate the transmission of digitally modulated signals in the corridor. We carried out measurements of the error vector magnitude associated with the received digitally modulated signal. We also measured the spectra of the digitally modulated signals and multisine signals that were designed to simulate them. The excitation was a QPSK-modulated OFDM signal having a bandwidth of 20 MHz, and the carrier frequencies were 2.412 GHz and 4.95 GHz.

For these measurements, we used the vector-signal-analyzer-based measurement set-up described in Section 2.4. We used both omnidirectional whip antennas and directional dual-ridge-guide antennas. We made measurements at the same locations where the UWB measurements of Section 4.3 were made, as shown in Figure 4.3-1.

Figure 4.4-1 shows the measured EVM results in the corridor for the directional antenna when the receiver was located inside the building but in a non-line-of-sight condition. We had to use the directional antenna in order to have sufficient gain for a VSA measurement, even though we connected a power amplifier to the vector signal generator. Real-time sampling used in the VSA measurement limits its dynamic range. The top set of numbers in the plot corresponds to a carrier frequency of 2.412 GHz, and the bottom numbers are for 4.95 GHz.

The EVM values are lower for the 2.412 GHz carrier frequency, but significantly so only at points beyond about halfway down the corridor (P4 = 50 m). Note also that reception for both signals is all but lost before we reach the junction at P8 (110 m) even though they were quite strong at P1.

EVM (in percent):

•2.412 GHz: green, top data

•4.95 GHz: red, bottom data

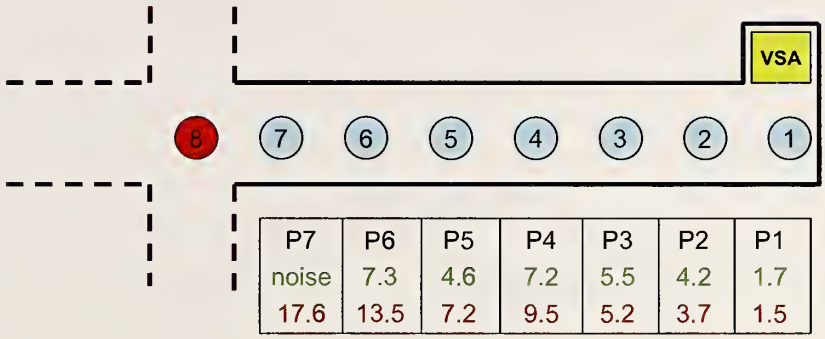

P7	P6	P5	P4	P3	P2	P1
noise	7.3	4.6	7.2	5.5	4.2	1.7
17.6	13.5	7.2	9.5	5.2	3.7	1.5

Figure 4.4-1: Error vector magnitude in percent for locations in the corridor as the transmitter moves away from the receiver (the vector signal analyzer).

Figure 4.4-2 shows the magnitude spectrum of the received signal at position 6 in the corridor for the two different carrier frequencies. Both the digitally modulated signals (solid line) and multisines designed to simulate them (dashed line) are shown. Measurements were made with directional antennas. We see mild frequency-selective distortion to the 2.4 GHz signal, while the 4.95 GHz signal remains fairly constant. As mentioned previously, frequency selectivity is a common effect in broadband-modulated-signal transmissions. As we saw in the apartment building study, the received levels of the 4.95 GHz signals are somewhat lower than those of the 2.4 GHz signals. This effect is quantified in NIST TN 1545 [4].

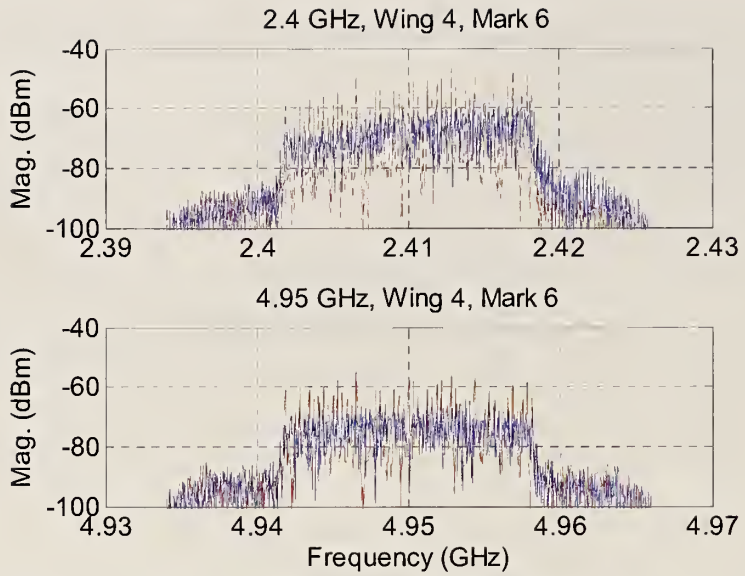

Figure 4.4-2: Digitally modulated OFDM QPSK-modulated signal (blue, solid line) and multisine signal (red, dashed line) at point 6 in the corridor. The 2.4 GHz plot (top) shows a mildly frequency-selective channel, while the 4.95 GHz signal remains fairly constant.

Figure 4.4-3 compares measurements at 4.95 GHz made with the omnidirectional whip antenna to those made with the directional horn antenna. These measurements were made with the transmitting antenna at position 4 and the receiving antenna at site 1. As mentioned above, we had to use the horn antenna in our EVM measurements in order to achieve adequate signal levels. In practice, emergency responders do not typically use these types of antennas. We compare the two types of antennas at 4.95 GHz and see that the signal level is approximately 5 dB higher with the directional antennas, and that the received signal shows slightly less frequency-selective distortion. The complete set of VSA spectral data taken in the corridor are given in Appendix I.

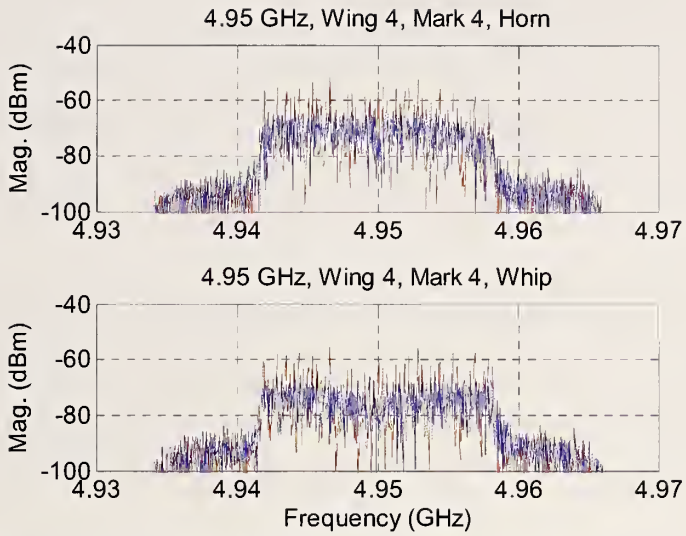

Figure 4.4-3: Digitally modulated OFDM signal (solid, blue line) and multisine (red, dashed line) for a carrier frequency of 4.95 GHz. The measurements in the top graph were made with horn antennas and those in the lower graph were made with omnidirectional antennas.

5. Oil Refinery Measurements

5.1 Overview

NIST carried out measurements at a large oil refinery in Commerce City, Colorado in March of 2007. As with the measurements at the apartment building, we chose this facility to simulate the chemical plant explosion scenario in the SAFECOM statement of requirements.

The refinery is an outdoor facility covering many hectares with intricate piping systems. Figure 5.1-1 shows photos of the refinery complex, including an aerial view of the entire facility in 5.1-1(a). We carried out tests primarily in the dense piping complex located under the lower roadway in the photo, also shown in 5.1-1(b). The complex is several hundred meters long, as can be seen in the photos. In certain areas, the dense piping overhead forms a tunnel-like structure, 5.1-1(c)-(d), which can be a barrier to radio communications.

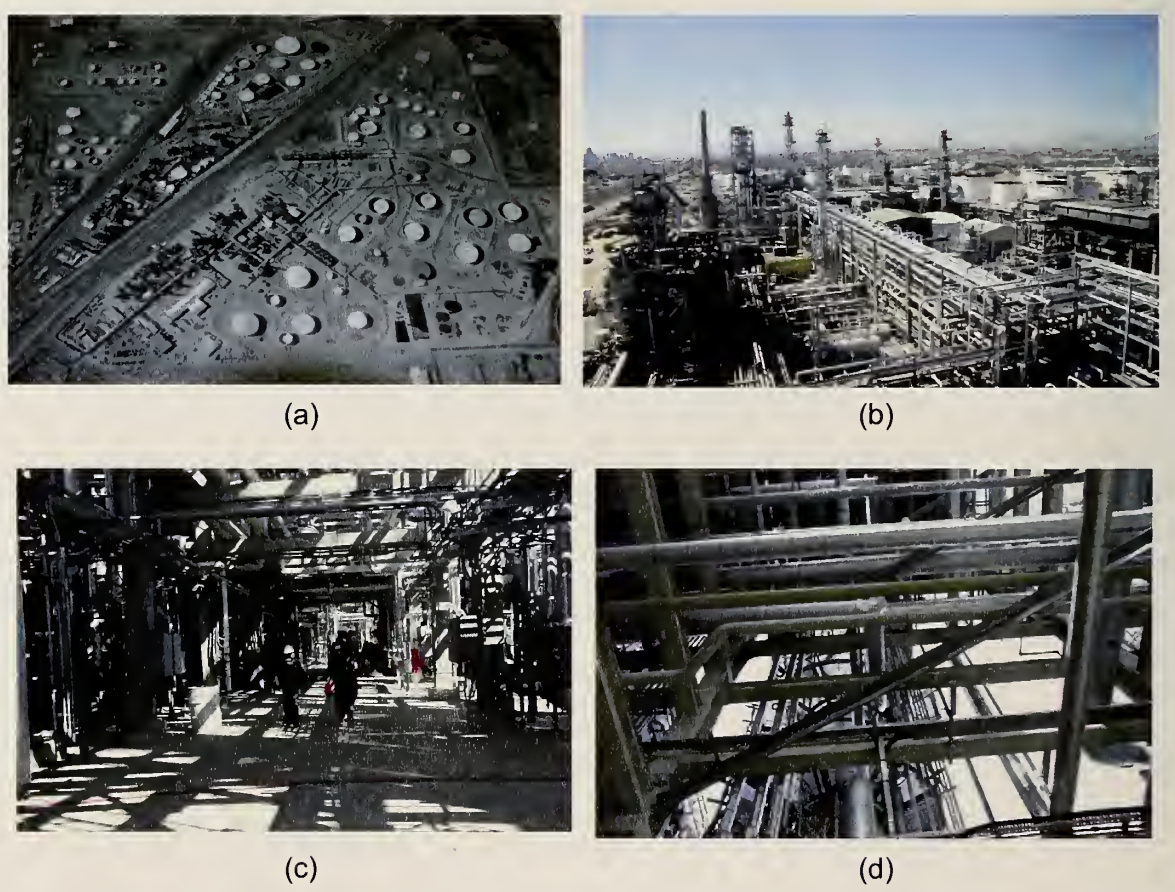

(a) (b)

(c) (d)

Figure 5.1-1: Oil refinery in Commerce City, Colorado. (a) Aerial view showing the piping complex (left center, see Figure 5.2-1 for an enlarged view) and storage tanks (circular structures). Received-power measurements were made while walking through the former and driving around the latter. (b) View from tower of the piping complex. (c) Dense piping essentially forms an outdoor tunnel in some areas. (d) Looking upward into the piping complex from the ground.

We again conducted three types of tests: (a) narrowband received power measurements using a calibrated communications receiver, (b) wideband excess path loss measurements using a synthetic pulse system based on a vector network analyzer, and (c) modulated-signal measurements using a vector signal analyzer.

5.2 Narrowband Received-Power Measurements

Measurements were made with the receiver system described in Section 2.1. One fixed receiver site was utilized on the south side of the refinery complex (see Figures 5.2-1 and 5.2-2(a)), approximately 30 m from the piping structures. The receiving equipment was placed in a van made available for NIST use by the Institute for Telecommunication Sciences (ITS), a sister Department of Commerce organization at the Boulder Labs Site. The antennas were mounted on a mast on top of the van, as shown in Figure 5.2-2(a).

The green dashed line in Figure 5.2-1 represents the path where the transmitters were carried by foot through the refinery. The path wound through the center of the processing section. Dense piping exists in this area, both to the side and overhead. Tunnel-like corridors through the piping are approximately five meters in width. In some cases, the corridors were tall enough for vehicles to pass underneath. In other cases, only pedestrians were allowed. In most cases, the piping extended several stories into the air. Figure 5.2-2(b) shows NIST personnel carrying a portable transmitter through the dense piping.

Figure 5.2-1: Path taken through the complex in measurements of narrowband received power. Portable transmitters were carried along the path shown by the green dashed line, and the received signals were measured at the location marked "RX1." At point 9, NIST staff climbed approximately 30 m up a tower.

(a) (b)

Figure 5.2-2: Narrowband received-power measurements at the oil refinery. (a) The receiver was located inside a van with antennas top-mounted on a mast approximately 7.5 m above the ground. (b) NIST personnel carried portable transmitters throughout the complex along the path shown in Figure 5.2-1.

A second set of tests was carried out around a cluster of large metal storage tanks on the perimeter of the facility. This area was much more open, consisting of one- to two-story storage tanks spaced several hundred meters apart. This set of tests was conducted from a vehicle, with the transmitting antennas placed on the roof of the vehicle. Figure 5.2-3 shows NIST staff conducting measurements while driving through the refinery.

Figure 5.2-3: NIST staff collecting measurement data while driving around the perimeter of the facility among the large storage tanks.

Measurements were performed with the receiving antennas polarized in the vertical direction. As the received signals were recorded, the location of the transmitters in the refinery complex was also recorded, and these locations are marked on the graphs.

Figures 5.2-4(a)–(c) show a few sets of representative receiver data gathered while the receivers were carried by foot through the facility. We see a limited amount of the waveguide effect described in previous sections for a carrier frequency of 50 MHz, Figure 5.2-4(a). That is, received signal levels decrease rapidly as the observer moves from a nearby line-of-sight location at position 4 to a line-of-sight position deep inside the piping structure at position 5. Little difference is seen between the data collected at the higher frequencies inside the facility ((b) and (c) in Figure 5.2-4).

Little difference between frequencies is seen in the graphs where the transmitters were driven around the storage tanks (Figure 5.2-5), although the carrier frequency of 1830 MHz does show an overall lower received signal level. The complete set of data is given in Appendix C.

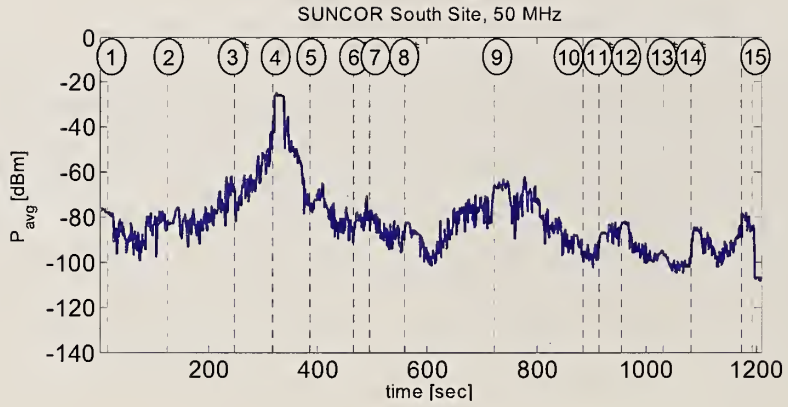

(a)

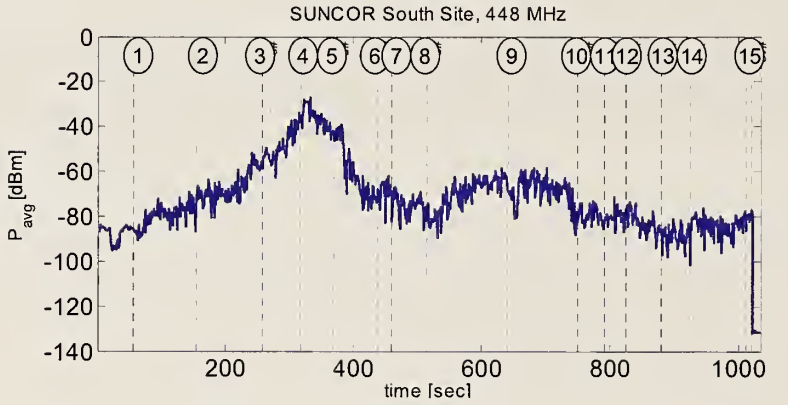

(b)

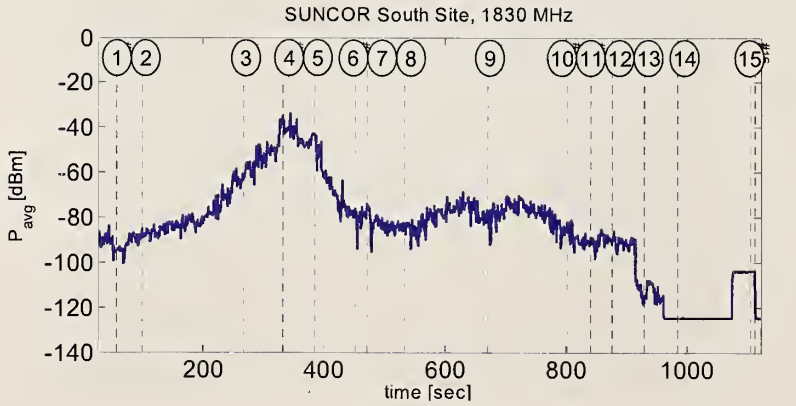

(c)

Figure 5.2-4: Received-power measurements collected as transmitters were carried by foot throughout an oil refinery complex for carrier frequencies of (a) 50 MHz, (b) 448 MHz, and (c) 1830 MHz. Point 4 is nearest to the receiver. Point 9 is located at the top of a tall tower.

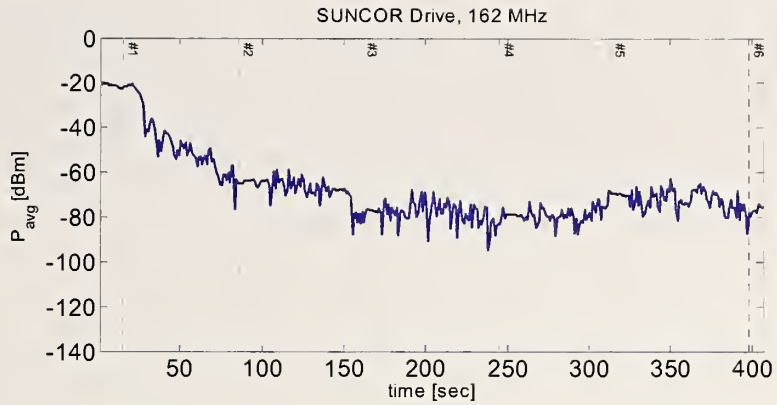

(a)

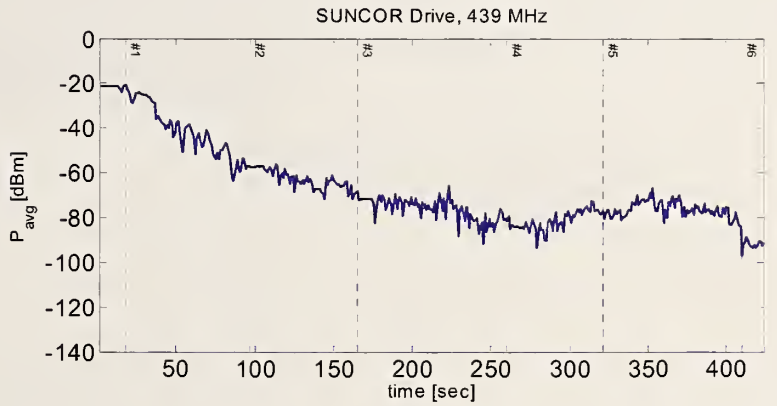

(b)

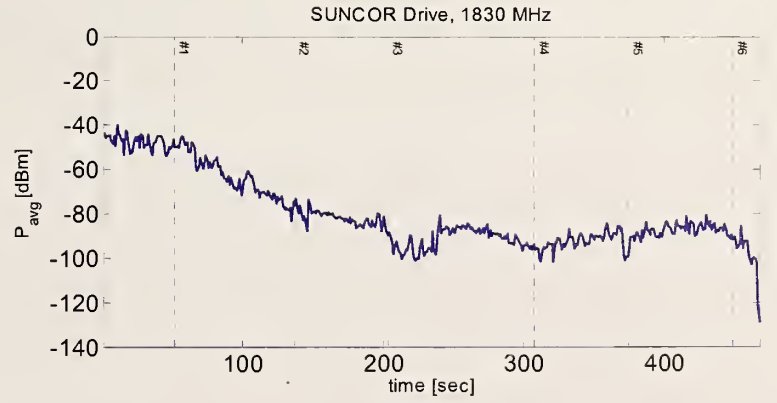

(c)

Figure 5.2-5: Received power as transmitters were driven around the perimeter of the facility at carrier frequencies of (a) 162 MHz, (b) 439 MHz, and (c) 1830 MHz. Little difference is seen between the different frequencies, except for an overall lower level at the 1830 MHz carrier.

5.3 Excess Path Loss and RMS Delay Spread

We next carried out measurements at specific locations in the oil refinery using the UWB synthetic-pulse, VNA-based measurement system described in Section 2.3. These points were located in an area of very dense piping in the facility. We rolled the receiving antenna along the path on a mobile cart. The VNA was again located in the mobile ITS test van. The vertically polarized transmitting antenna was located on top of this van. The layout of the test points is shown in Fig. 5.3-1, and the receiver location is denoted by "ITS van."

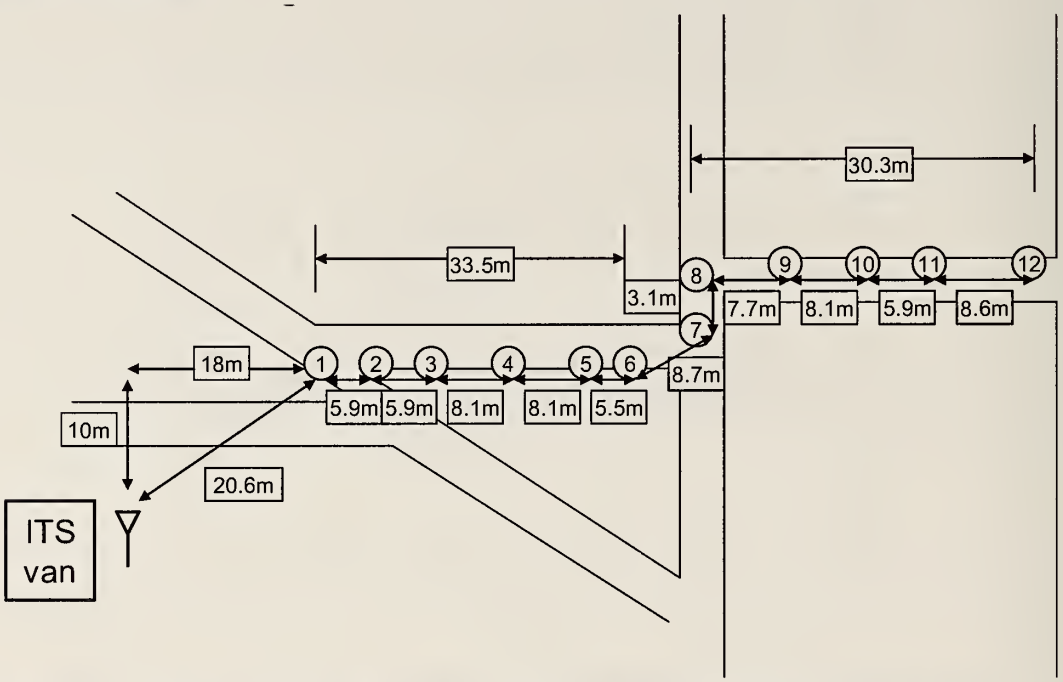

Figure 5.3-1: Layout of the test points for the synthetic-pulse measurements in the oil refinery complex. The test points were located under dense overhead piping and metallic structures, in most cases several stories high.

We collected data covering two frequency bands. For the lower frequency band (25 MHz to 1.2 GHz), we used omnidirectional antennas that would be used by most emergency response companies. For the higher frequency band (1 GHz to 18 GHz) we used both omnidirectional antennas and a set of directional dual-ridge-guide (DRG) antennas. The DRG antennas minimized the reception of multipath by focusing the main lobe of the antenna toward the maximum received signal. The photo in Figure 5.2-2(a) shows the omnidirectional antenna mounted on the mast.

We discuss a few representative data sets of the UWB measurements. Figure 5.3-2 shows excess path loss for frequencies between 25 MHz and 1.2 GHz at position 2 (near the opening of the piping), position 6 (several meters within the piping), and position 13 (deep within the piping). Because measurements were made outdoors in an operational facility, we see increased signal levels at commonly used frequency bands such as the 400 MHz two-way radio band, the 800 MHz cell phone band, and the 900 MHz ISM band. There is also a strong signal component at frequencies around

200 MHz, which may correspond to machine noise arising from the pumps and other heavy machinery at the facility.

We see the effects of strong reflections even at the opening of the piping structure (Figure 5.3-2(a)), shown by the deep nulls and peaks in the spectrum. Figure 5.3-2(b) shows the same wideband fading, but also shows increased attenuation at the lower frequencies, again due to the waveguiding of the structure. The attenuation at most frequencies between position 2 and position 13 (Figure 5.3-2(c)) is approximately 30 dB.

Figure 5.3-3 shows excess path loss for frequencies between 1 GHz and 18 GHz at positions 2, 6, and 13 along the same path. At position 2, shown in Figure 5.3-3(a), the spectrum corresponding to the lower frequencies is quite flat. Once the transmitting antenna is within the piping corridor, the spectrum starts to show some frequency dependence in the form of nulls and peaks caused by strong reflections, as shown in Figure 5.3-3(b). Then, as the transmitting antenna turns the corner and proceeds even further down the piping corridor, the signal drops off rapidly and is almost in the noise at position 13, Figure 5.3-3(c). The higher frequency bands show greater attenuation with distance than do the lower frequency bands. The complete set of UWB excess-path-loss data is given in Appendix F.

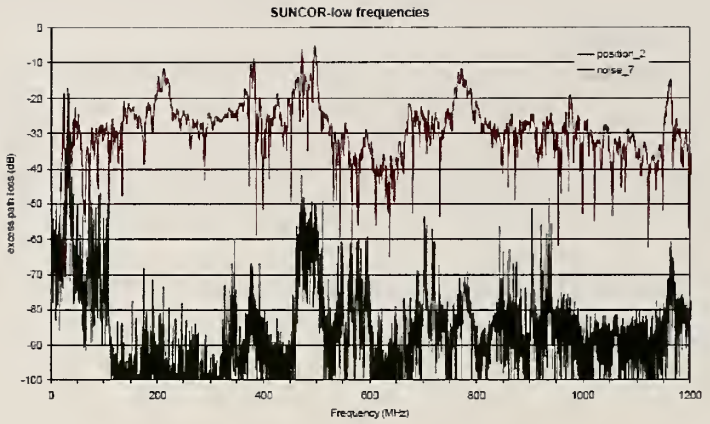

(a)

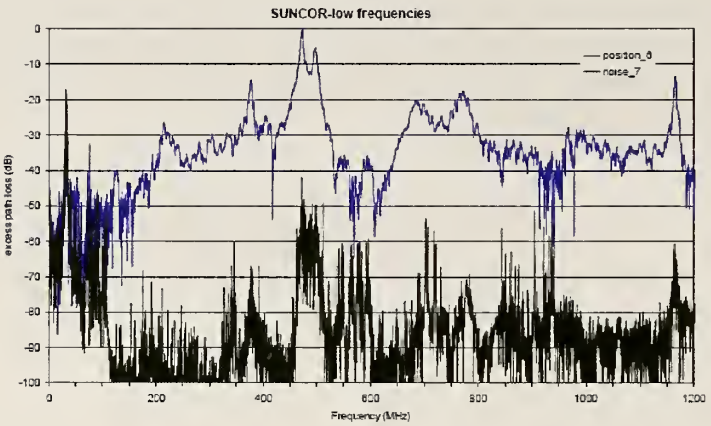

(b)

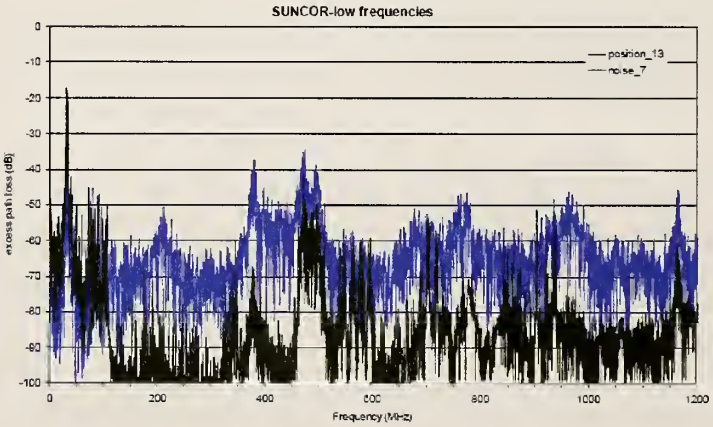

(c)

Figure 5.3-2: Excess-path-loss measurements at an oil refinery at (a) position 2, (b) position 6, and (c) position 13 for frequencies from 25 MHz to 1.2 GHz. The path was located outdoors but under dense piping several stories high.

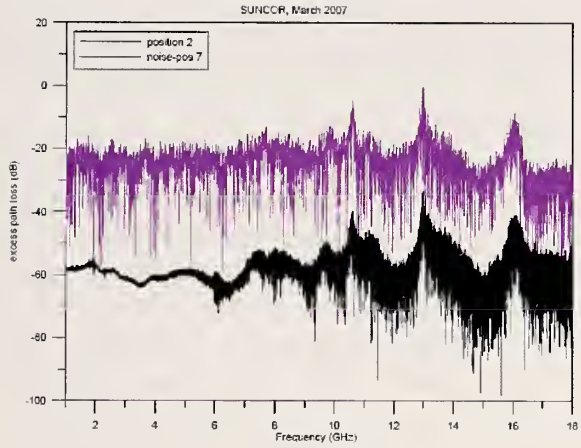

(a)

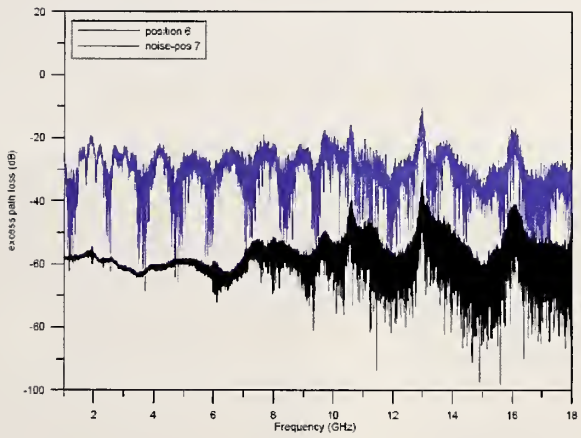

(b)

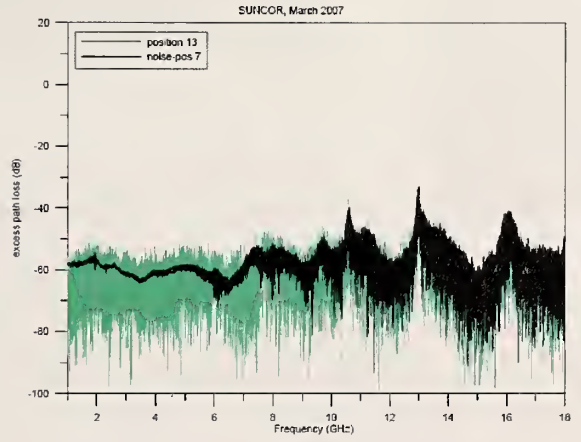

(c)

Figure 5.3.3: Excess-path-loss measurements at an oil refinery at (a) position 2, (b) position 6, and (c) position 13 for frequencies from 1 GHz to 18 GHz. The path was located outdoors but under dense piping several stories high. Attenuation is approximately 40 dB between 1 and 5 GHz when the receiver moved from position 2 to position 13, and is even greater at the higher frequencies.

The RMS delay spread calculated from the VNA measurements is summarized in Fig. 5.3-4. The delay spread remains relatively constant for positions 1 through 7 and 8 through 12. Beyond position 12, the signal is so weak that meaningful RMS delay spread values cannot be obtained.

The delay spread averages around 40 ns for both frequency bands for positions 1 through 7. When the transmitting antenna moves around the corner to position 8, we see a significant increase in RMS delay spread, to approximately 140 ns for the lower frequencies and to approximately 80 ns for the higher frequencies. At position 8, the path is completely non-line-of-sight. The lower RMS delay spread at the higher frequencies may be due to the use of directional antennas in that frequency band. Or, the pipes that cause the multiple reflections may be better reflectors at lower frequencies.

Note that the signals at the higher frequencies were close to the noise floor when the transmitter and receiver were separated by a great distance. This may have an effect on the accuracy of the RMS delay spread calculation at these points. However, the curves presented in Figure 5.3-4 show the trends clearly.

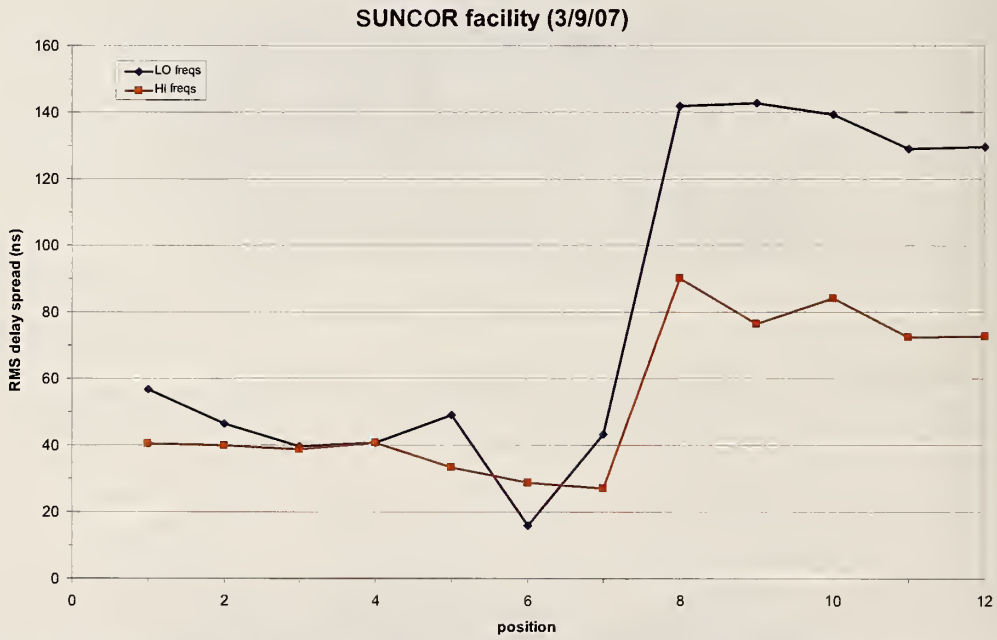

Figure 5.3-4: Summary of RMS delay spread calculated from the excess path loss measurements made with the VNA. The dark blue curve with diamonds corresponds to the lower-frequency band (25 MHz to 1.2 GHz). The orange curve with squares corresponds to the higher-frequency band (1 GHz to 18 GHz).

5.4 Error Vector Magnitude and Modulated-Signal Spectra

We carried out measurements of digitally modulated signals and multisine signals that were designed to simulate the modulated signals in the oil refinery as well. For these measurements, we used excitations that included both QPSK-modulated and 64-QAM-modulated OFDM signals. In each case, these signals had a bandwidth of 20 MHz, and we conducted measurements using carrier frequencies of both 2.41 GHz and 4.95 GHz.

For these measurements, we used the vector-signal-analyzer-based measurement set-up described in Section 2.4. We made measurements at positions 1 through 12 where the UWB measurements of Section 5.3 were made, as shown in Figure 5.3-1. This path is along an alley in the oil refinery complex where large numbers of metal pipes run alongside and overhead, often two or more stories high. Figures 5.4-1(a) and (b) show photographs of the transmitter, consisting of a vector signal generator, power amplifier, and omnidirectional antenna mounted on a cart. The VSA receiver was located in the ITS van discussed in prior sections.

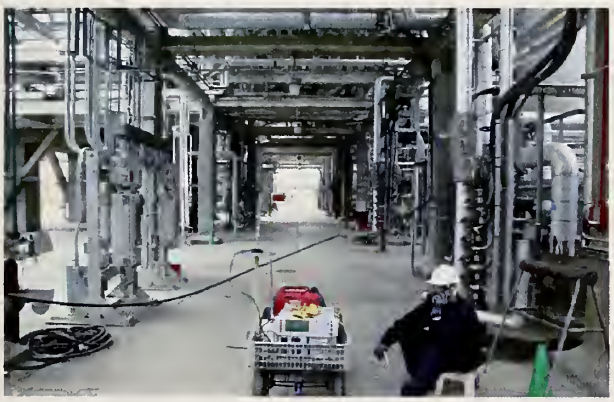

(a)

(b)

Figure 5.4-1: Modulated-signal transmitting unit on mobile cart (a) inside and (b) outside the dense piping in the facility.

Figure 5.4-2 shows EVM measurements made along the piping corridor when the receiver was at the location marked "ITS van." In each case, we took the average of three EVM measurements. The top two rows correspond to a carrier frequency of 2.41 GHz and the bottom two rows are for 4.95 GHz. We studied two different digital modulations for the OFDM signal: QPSK and 64 QAM, as noted on the figure.

The EVM values are comparable for both carrier frequencies, but the 2.41 GHz signal could be received when the transmitter was located deeper in the piping complex. The type of modulation used had little effect on the overall EVM value.

EVM for QPSK and 64QAM modulation at 2.41 GHz and 4.95 GHz

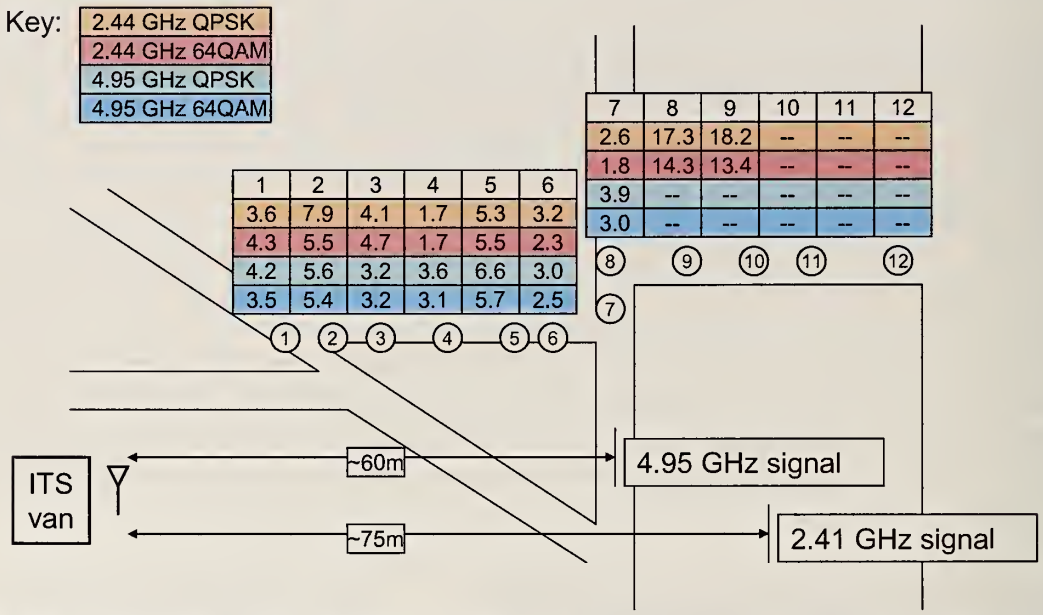

Figure 5.4-2: Measured EVM values (in percent) at locations surrounded by metallic piping in the oil refinery. The lower carrier frequency could be received from deeper within the complex, and the modulation format made little difference in the EVM numbers.

The EVM values are lower for the 2.41 GHz carrier frequency, but not significantly lower, except when the signal level approaches the receiver noise floor near the corridor junction.

Figure 5.4-3 shows measured bandpass spectra for the digitally modulated signals and for multisine signals designed to simulate them at position 2 shown above. The measurements were made by saving the VSA traces to data files. These measurements were collected at the same time that the EVM data were collected. Omnidirectional antennas were used, as shown in Figure 5.4-1.

At position 2, the transmitter has just entered into the metallic piping structure and there is still a good line of sight between the transmitter and receiver. Still, the figure shows a good deal of frequency-selective distortion, indicated by the deep nulls across the pass band. The signal with the 2.41 GHz carrier is more strongly affected than the one with the 4.95 GHz carrier. This may be due to the physical dimensions of objects within the piping structure.

At position 2, the levels of signals at both carrier frequencies are similar. There appears not to be much difference between the QPSK and 64-QAM modulation schemes with respect to spectral distortion, even though the latter is strongly amplitude modulated. At 4.95 GHz, however, both the QPSK and the 64-QAM signal diverge more from their respective multisines compared to the 2.41 GHz signals.

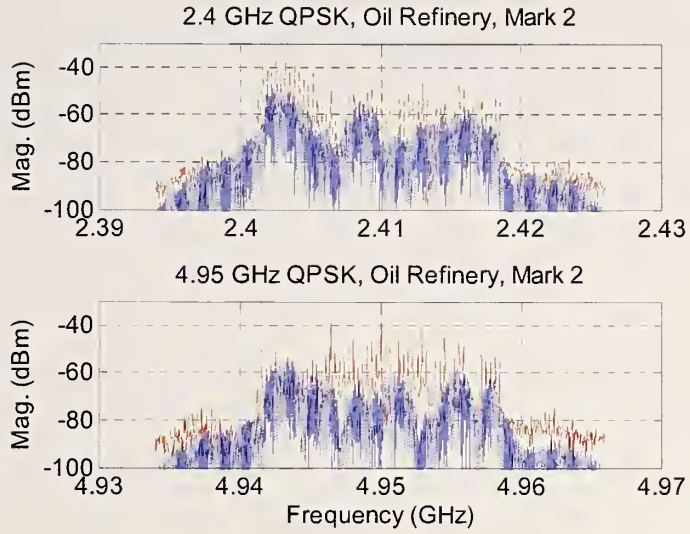

(a)

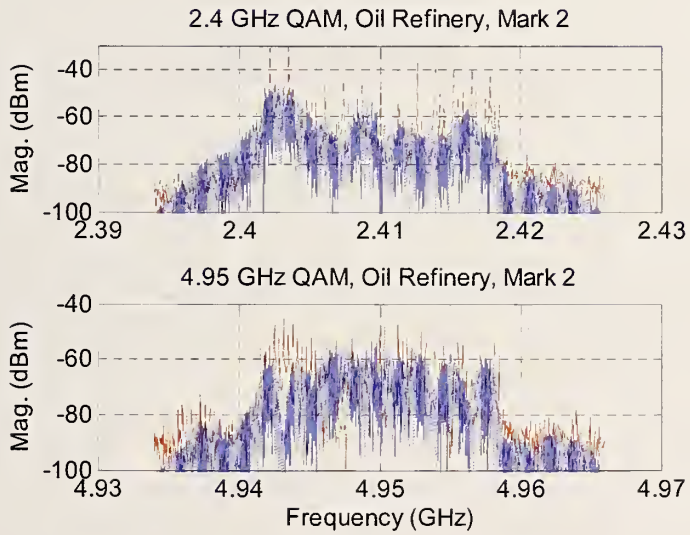

(b)

Figure 5.4-3: Bandpass spectra of a digitally modulated OFDM signal (solid, blue trace) and a multisine signal (dashed, red trace) at position 2 in the oil refinery. (a) QPSK modulation. (b) 64-QAM digital modulation. The broad nulls indicate a frequency-selective channel that similarly affects the spectra for both modulations. At position 2, the 2.41 GHz and 4.95 GHz signals had similar amplitude levels.

Figure 5.4-4 shows the bandpass spectra at position 8. Here we again see the frequency-selective distortion, but also a greater attenuation of the 4.95 GHz with respect to the 2.41 GHz signal. The received signals at the two carrier frequencies were approximately equal until position 8, when the 4.95 GHz signal is greatly reduced. We saw similar behavior for the measurements made using the UWB system. In this case, the digitally modulated signals and the multisines track well.

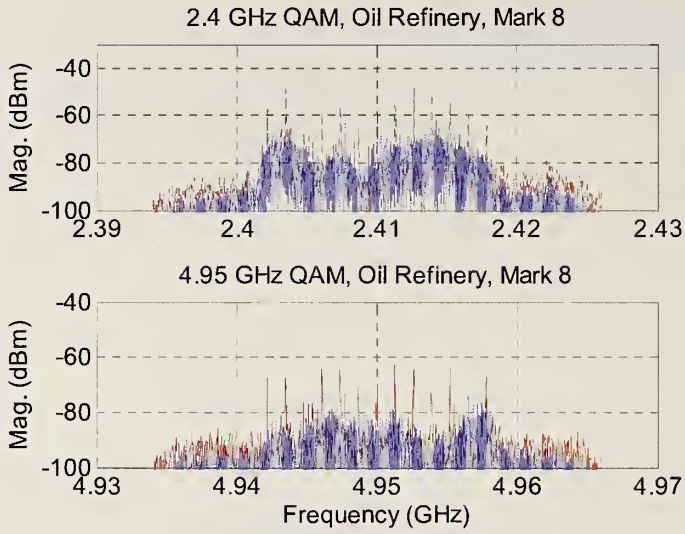

Figure 5.4-4: Bandpass spectra measured with the vector signal analyzer and showing the received 64-QAM digitally modulated OFDM signal at carrier frequencies of 2.41 GHz (top) and 4.95 GHz (bottom). The dashed red lines correspond to multisine signals designed to simulate the modulated signal. The deep nulls in the spectra correspond to a severely frequency-selective channel. The 4.95 GHz signal suffered more attenuation as the transmitter and receiver were separated.

The VSA measurements show significant distortion to the received broadband modulated signals as soon as the transmitter enters the piping complex. While the overall signal levels are sufficient for most radio receivers, the in-band distortion would make reception difficult except in the main piping corridor (positions 1 through 7). Deeper into the structure, both signals are still strongly distorted, but the 4.95 GHz signals are more strongly attenuated as well. The complete set of data appears in Appendix K.

6. Subterranean Tunnel Measurements

6.1 Overview

As part of a large, multi-agency field test of ad-hoc radio networks for public-safety applications, we conducted radio-propagation tests in tunnels at Black Diamond Mines Regional Park near Antioch, California. While the focus of this work was to study the reliability of wireless telemetry and control of Urban Search and Rescue robots in tunnels and other weak-signal environments, we also conducted propagation measurements relevant to designers of emergency responder communication systems.

The tests were conducted March 19–21, 2007. We measured only narrowband and excess path loss. From the latter, we calculated the RMS delay spread in two different tunnel environments. The Black Diamond Mines are part of an old silica mine complex that was used early in the 1900s to extract pure sand for glass production. As such, the walls of the mine shafts are rough and consist of sandy material.

Two tunnels were studied, the Hazel-Atlas North (called "Hazel-Atlas" below) and Hazel-Atlas South (called "Greathouse" below). The tunnels are located beneath a mountain and are joined together deep inside, as shown in Figure 6.1-1. The dimensions of the Hazel-Atlas tunnel varied from approximately 1.9 m (6', 3") x 1.9 m to as much as 2.6 m (8', 5") x 2.4 m (8', 0"). The dimensions of the Greathouse tunnel were somewhat bigger, up to approximately 3 m square in places. The Hazel-Atlas tunnel contained railroad tracks spaced 61 cm (24") apart. Both tunnels consisted of a straight section followed by a right-angle turn around a corner, as shown in Figure 6.1-1.

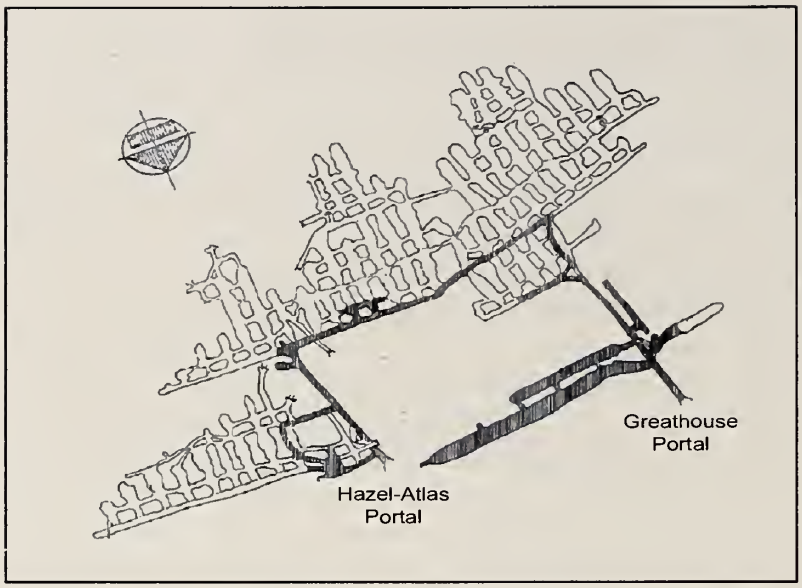

Figure 6.1-1: Overview of the Hazel-Atlas mine tunnel complex. The network of mines is located deep within a mountain. The dark-shaded areas are accessible. We studied the mine tunnels starting from the Hazel-Atlas Portal and the Greathouse Portal.

Figure 6.1-2 shows photographs of the Hazel-Atlas mine tunnel, including (a) the portal (opening) of the Hazel-Atlas mine; (b) just inside the portal, where our antennas were placed; (c) approaching the right-angle turn shown in Figure 6.1-1; and (d) past the turn. The photos show the rough, rocky walls in the tunnels, some with wooden shoring, and the railroad tracks.

(a)

(b)

(c)

(d)

Figure 6.1-2: Views from outside (a) and inside (b) through (d) the Hazel-Atlas mine tunnel.

Figure 6.1-3 shows photos inside the Greathouse tunnel. Our antennas were placed several meters inside the tunnel near a room called the "Greathouse," shown to the left of the main shaft in a shaded area of Figure 6.1-1. Equipment was set up in the Greathouse, as shown in Figure 6.1-3(a), while the antennas were set up in the tunnel. Figure 6.1-3(b) shows measurement staff aligning directional antennas for the UWB measurements.

(a) (b)

Figure 6.1-3: Measurement set-up in the Greathouse mine tunnel. The instrumentation was located in the Greathouse room, while the antennas were placed in the mine tunnel proper.

6.2 Narrowband Received-Power Measurements

We carried out single-frequency measurements in both the Hazel-Atlas and Greathouse tunnels using the receiver system described in Section 2.2. The receiving antenna was located just outside the portal for the former, and inside but near the portal entrance for the latter. We used omnidirectional discone antennas for the receiving antenna. The paths we took are illustrated by dashed lines in Figures 6.2-1(a) and (b).

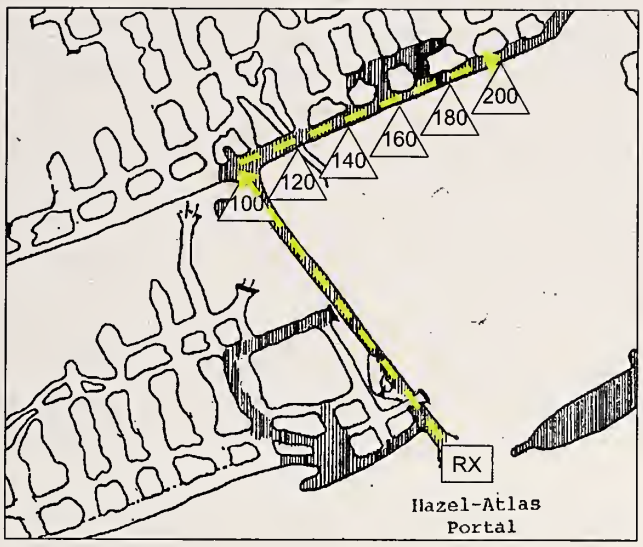

(a)

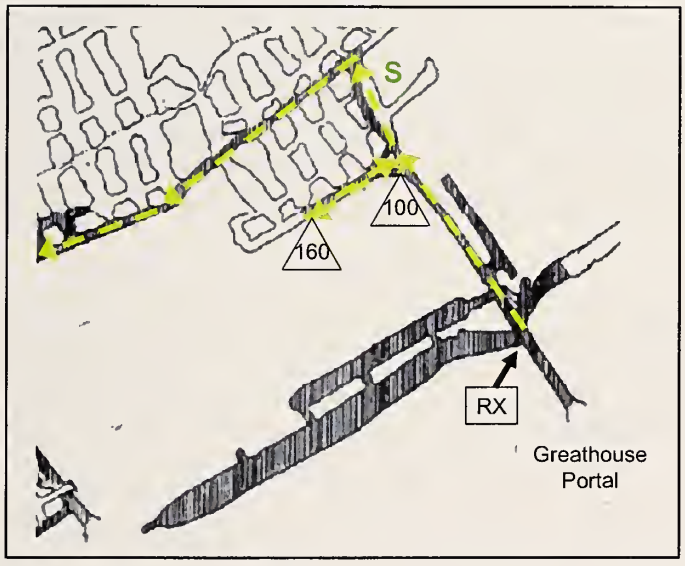

(b)

Figure 6.2-1: Layout of the (a) Hazel-Atlas and (b) Greathouse mine tunnels at Black Diamond Mines Regional Park. The triangles indicate approximate distance in meters from the tunnel entrance. The receivers were positioned at the points marked "RX." The dashed lines denote the walk-through paths we took for narrowband received-power measurements.

Figures 6.2-2 (a) through (c) show representative measured received-power data from the Hazel-Atlas mine tunnel at frequencies of 50 MHz, 162 MHz, and 448 MHz. Figures 6.2-3 (a) through (c) show similar results for the Greathouse tunnel. The full set of data can be found in Appendix D. The transmitters were carried into each tunnel

approximately 100 m, around a corner, and then deeper into the mine. For the Hazel-Atlas mine, we went another 100 m. For the Greathouse tunnel, the distance was much farther, but the final distance was not measured. The transmitters were then carried back out along the same path. This is the reason why the left and right halves of the graphs look similar. The reason why the first and second half results in each graph are not mirror images of each other may be due to a number of factors, including the different levels of shielding of the body on the outbound and return trips and the radiation pattern of the antennas when mounted in their cases.

We see that in all cases the signals propagate deeper into the tunnel at the higher frequencies. This is because the mine exhibits significant waveguiding effects. As discussed in Sections 4 and 5, waveguides readily propagate signals for frequencies above their "cut-off frequency," the frequency below which electromagnetic modes cannot be supported. At frequencies below cut-off, waveguides strongly attenuate signals.

The cut-off frequency for each tunnel waveguide depends on its physical dimensions and the wavelength of the excitation signals, as well as the tunnel surface material, surface roughness, and flatness of the floor. In Figures 6.2-2 and 6.2-3, the most significant waveguiding effects occur before the turn at the end of the main tunnel (refer to Fig. 6.2-1). In the Hazel-Atlas tunnel, once the corner has been turned, the signal level drops significantly. Just past the corner, an increase in the signal level occurs where propagation through an airshaft provided an alternate route to the receiver. In the Greathouse tunnel, we again see classic waveguiding effects up to the corner. Beyond this there are routes for the signal to take to the receiver other than through the main tunnel, for example, a stairwell marked by an S on Fig. 6.2-1(b).

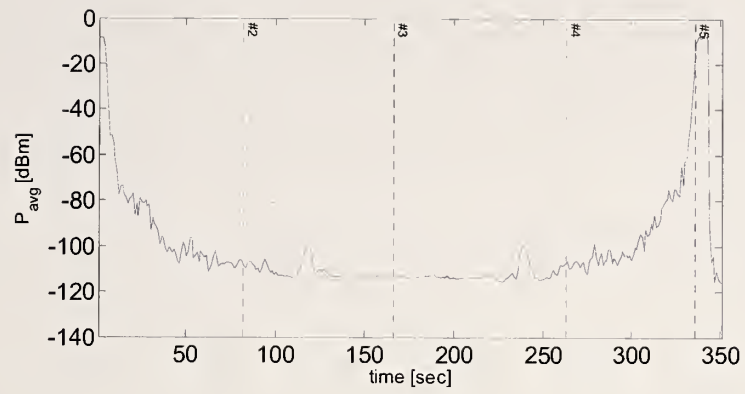

(a)

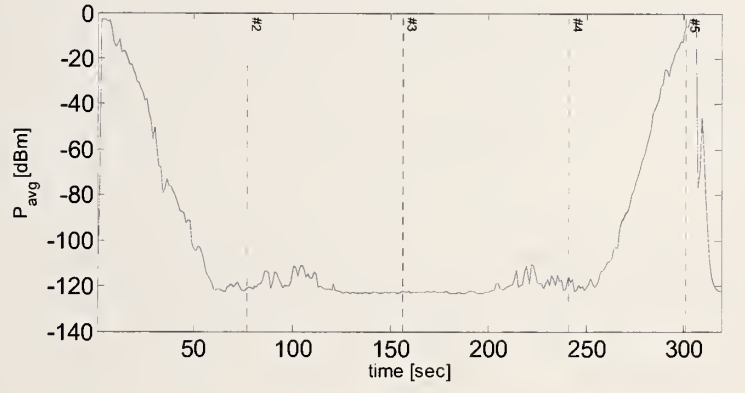

(b)

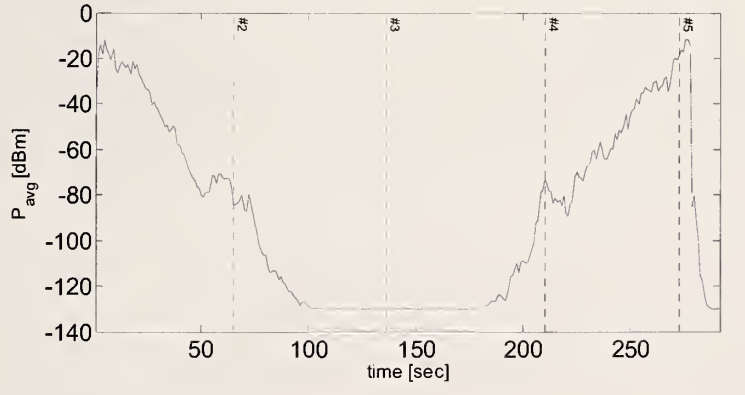

(c)

Figure 6.2-2: Received-power data in the Hazel-Atlas mine for three carrier frequencies: (a) 50 MHz, (b) 162 MHz, (c) 448 MHz. The transmitters were carried into the tunnel and then back out, so the left and right halves of the graphs should be mirror images. In each case, the first and third vertical dashed lines correspond to the turn at 100 m, and the second dashed line represents the end point at 200 m, shown in Fig. 6.2-1(a). The higher frequencies show less attenuation deeper into the tunnel, in agreement with waveguide-below-cutoff models for tunnels of these dimensions.

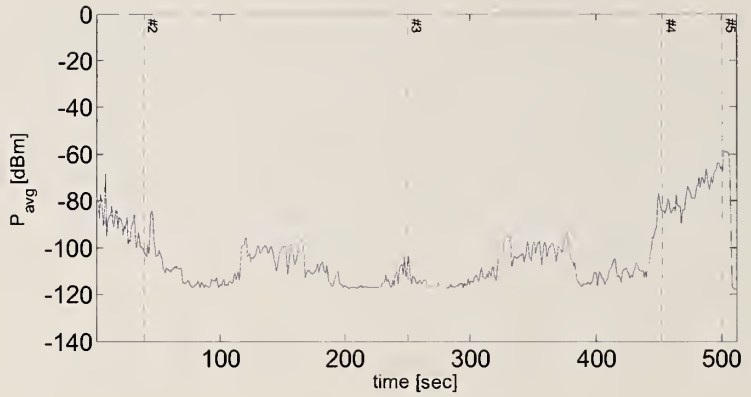

(a)

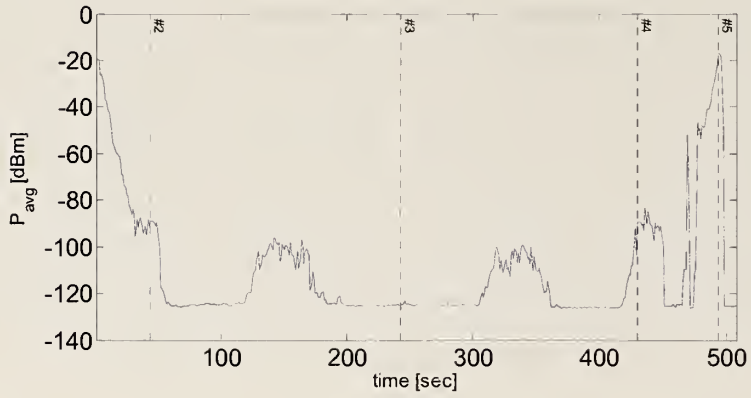

(b)

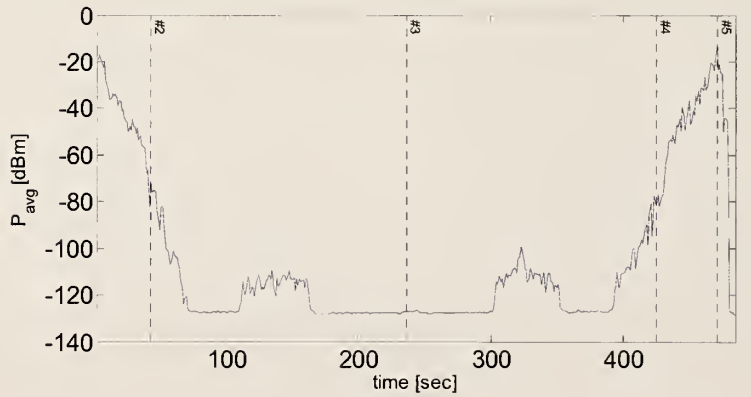

(c)

Figure 6.2-3: Received-power data in the Greathouse mine for three carrier frequencies: (a) 50 MHz, (b) 162 MHz, (c) 448 MHz. In each case, the first and third vertical dashed lines correspond to a turn at approximately 100 m, and the second dashed line represents the end point as shown in Fig. 6.2-1(b). The higher signals between the turn and the end point correspond to a stairwell that provided an almost line-of-sight path between the transmitter and receiver.

To study the extent of waveguiding in these tunnels, we implemented an analytical model that simulates signal propagation in tunnel environments having various physical parameters [19, 20]. Briefly, the model assumes a dominant EH11mode in a lossy rectangular waveguide with the specific attenuation α in decibels/meter expressed for vertical polarization as

$$\alpha = \alpha_{\text{TUNNEL}} + \alpha_{\text{ROUGHNESS}} + \alpha_{\text{TILT}}, \tag{6.1}$$

where

$$\alpha_{\text{TUNNEL}} = 4.343\lambda^2\left(\frac{1}{a^3\sqrt{\varepsilon_R - 1}} + \frac{\varepsilon_R}{b^3\sqrt{\varepsilon_R - 1}}\right), \tag{6.2a}$$

$$\alpha_{\text{ROUGHNESS}} = 4.343\pi^2 h^2 \lambda\left(\frac{1}{a^4} + \frac{1}{b^4}\right), \tag{6.2b}$$

$$\alpha_{\text{TILT}} = 4.343\frac{\pi^2\theta^2}{\lambda}, \tag{6.2c}$$

with λ the wavelength, *a* the width of the tunnel, *b* the height of the tunnel, and h is the roughness, all in meters. Other parameters include ε_R, the dielectric constant of the rock walls, and θ, the angle of the tunnel tilt in degrees.

We set the parameters of the model to approximate the Hazel-Atlas tunnel, given below in Table 6.2-1. This model works well only for frequencies where the signal wavelength is not much longer than the dimensions of the tunnel. Hence, we show results for 448 MHz only. Figures 6.2-4(a) and 6.2-4(b) show representative results of these models for the Hazel-Atlas and Greathouse tunnels, respectively. The good agreement between the measured and modeled data led us to conclude that waveguiding plays a significant role in radio propagation in these tunnels, as it did to a lesser extent in the hallway corridor discussed in Section 4 and the oil refinery in Section 5.

Table 6.2-1. Parameters used in tunnel model.

Parameter	Value
Width	2 m
Height	2 m
Wall roughness	0.3
ε_r	6
tilt	1 degree

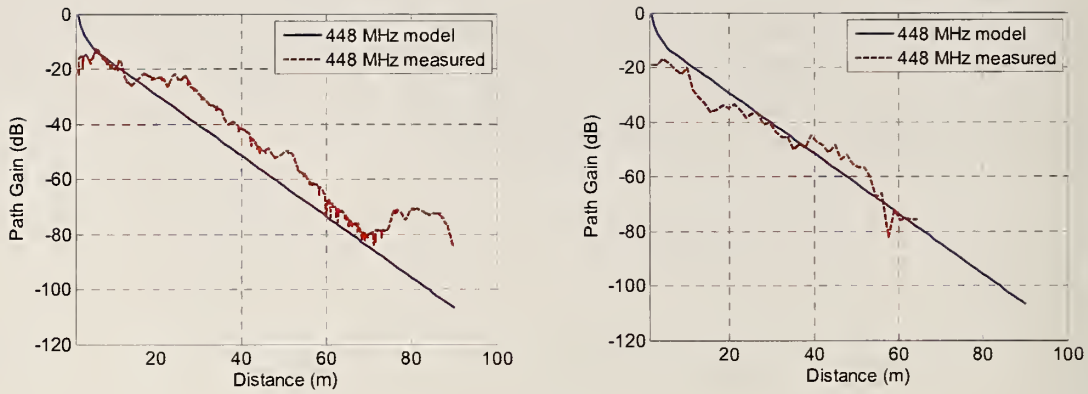

(a) (b)

Figure 6.2-4: Comparison of measured and modeled data for (a) the Hazel-Atlas tunnel and (b) the Greathouse tunnel. The carrier frequency is 448 MHz. The modeled data simulates waveguide propagation for a waveguide whose physical parameters approximate those of the tunnels. The good agreement between the slopes of the two curves indicates that significant waveguide propagation was occurring in these tunnels.

As discussed in references [19, 20], the frequency-dependent behavior of the tunnel leads to a "sweet spot" in frequency. Below the sweet spot, signals do not propagate well, due to the effect of waveguide-below-cutoff attenuation. Above the sweet spot, loss mechanisms again dominate and signals do not propagate well. We simulated this combined effect using the method described in reference [19]. The results are shown in Figure 6.2-5.

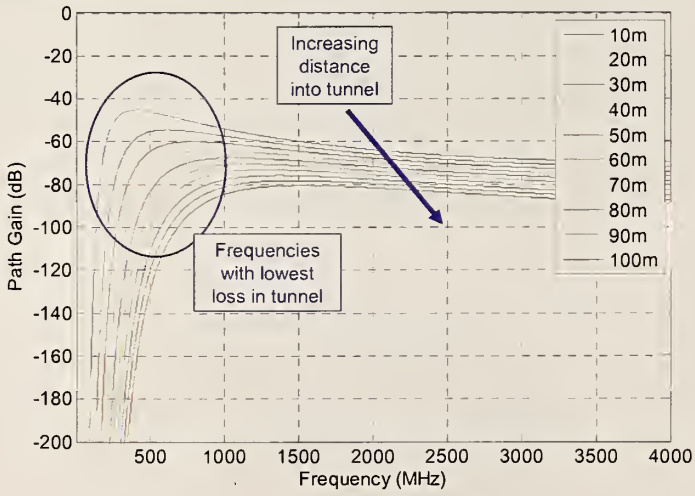

Figure 6.2-5: Path gain versus frequency for various distances in a tunnel having similar physical characteristics as the Hazel-Atlas tunnel. Frequencies around approximately 400 MHz to 1 GHz propagate better than either lower or higher carrier frequencies.

Figure 6.2-5 shows that, theoretically, frequencies above around 400 MHz but below 1 GHz propagate with the least attenuation in the tunnel. We will see in the UWB

measurements given below that the measured lower-frequency limit is closer to approximately 500 MHz (see Figure 6.3-2(b)).

6.3 Excess Path Loss and RMS Delay Spread

We next carried out measurements in the two tunnels using the ultrawideband VNA-based measurement system described in Section 2.3. We positioned the transmitting antenna in the same locations as the receivers used in the narrowband received-power measurements above. The transmitting antenna positions and receiver test points are shown in Figs. 6.3-1(a) and (b). For frequencies from 25 MHz to 1.6 GHz, we used omnidirectional discone antennas, and for frequencies from 1 GHz to 18 GHz, we used directional, dual-ridge guide antennas. We increased the separation between them by 10 m for each measurement.

Figures 6.3-2 (a)–(c) show representative excess path loss curves from 25 MHz to 1.6 GHz in the Hazel-Atlas tunnel. The full set of data from the mines can be found in Appendix H. In Figure 6.3-2, the transmitting antenna was located at the portal to the tunnel, while the receiving antenna was located 10 m, 70 m, and 110 m into the tunnel. The 110 m position was around the corner and as a result, no line-of-sight condition existed.

A comparison of Figures 6.3-2(a) and (b) clearly shows that the low frequencies are attenuated more significantly than the higher frequencies as the receiving antenna moves deeper into the tunnel. This indicates the waveguide-below-cutoff attenuation described in Section 6.2. Also, the attenuation is much less frequency dependent once the waveguide cut-off frequency has been exceeded. Once no line-of-sight condition exists (Figure 6.3-2(c)), the received signal falls into the noise.

Figures 6.3-2(a)–(c) show an interesting effect: Railroad tracks spaced approximately 24 inches apart run the length of this tunnel. The wavelength of the frequency corresponding to this separation is 492 MHz, close to the spike in frequency at about 475 MHz seen in each of the graphs. The effect may be related to the tracks, or it may be a spurious signal from some other source.

Figures 6.3-3(a)–(b) show excess path loss in the Greathouse tunnel for frequencies from 1 GHz to 18 GHz. At 27 m, the higher frequencies in Fig. 6.3-3(a) show deep nulls, indicating frequency-dependent interference. Deep nulls occur at other frequencies as the transmitter moves deeper into the mine. Local features in the tunnels such as rock outcroppings and doorways may be the cause of the signal-level variations in certain areas. Fig. 6.3-3(b) shows the signal once the receiving antenna moves around the corner. Here we see that the signal is still above the noise floor, but is greatly attenuated.

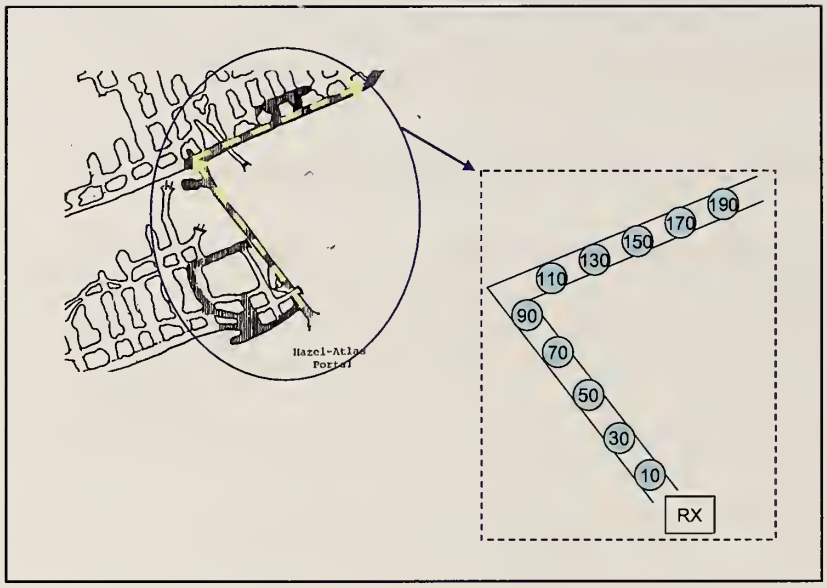

(a)

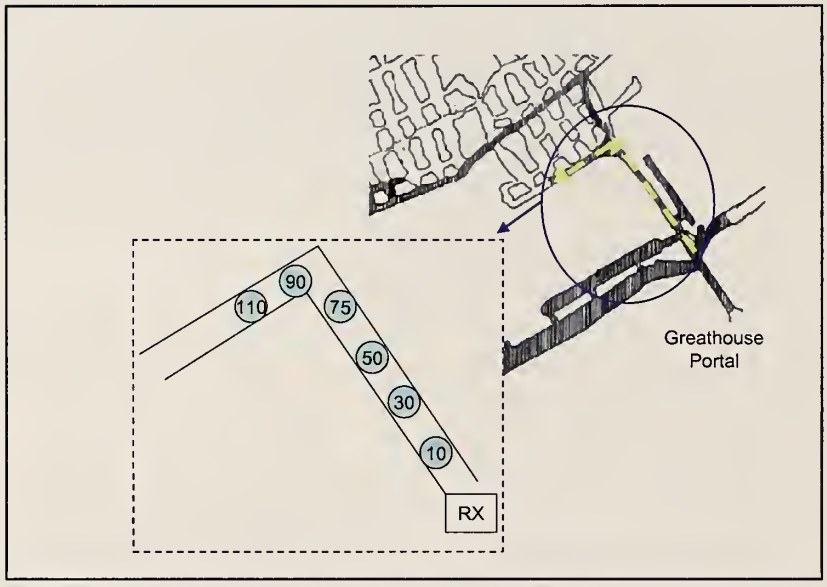

(b)

Figure 6.3-1: Layout of mine tunnels. Insets indicate where UWB measurements were performed. Distances marked on the insets are in meters. (a) Hazel-Atlas tunnel. (b) Greathouse tunnel.

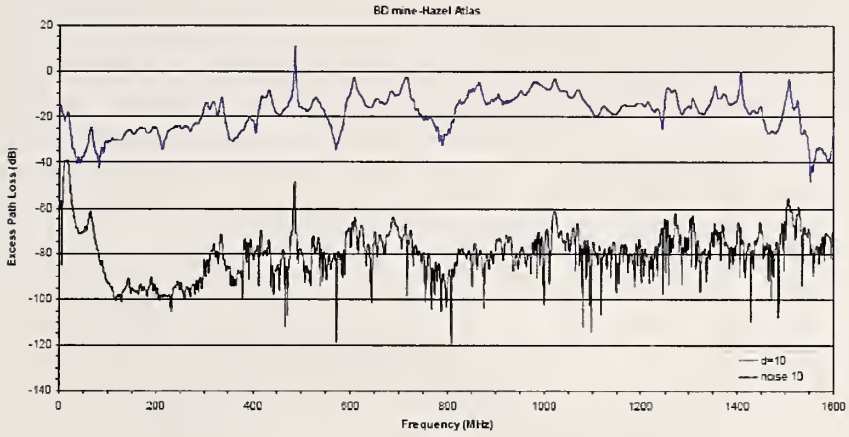

(a)

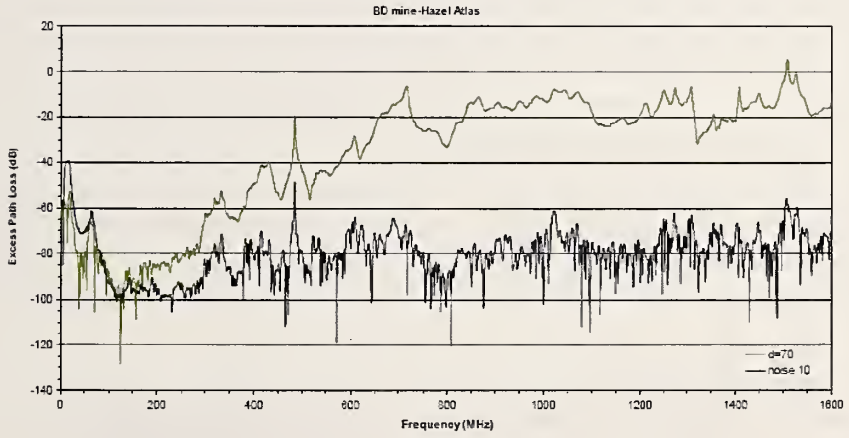

(b)

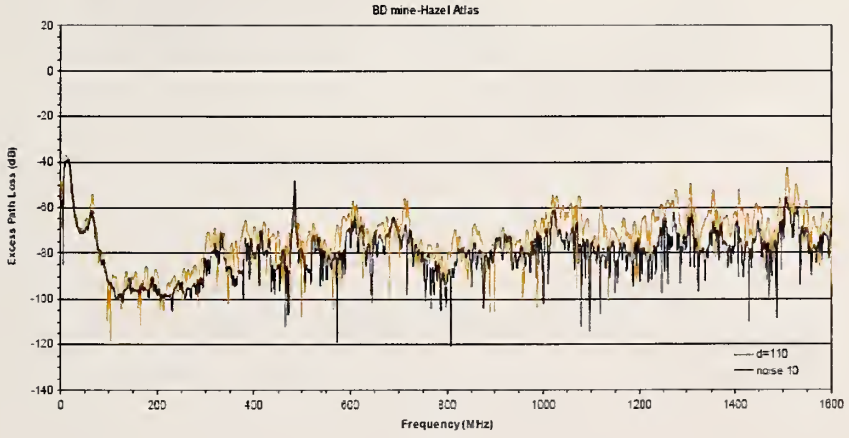

(c)

Figure 6.3-2: UWB excess-path-loss measurements in the Hazel-Atlas tunnel from 25 MHz to 1.6 GHz at distances of (a) 10 m, (b) 70 m, and (c) 110 m into the tunnel. Significant low-frequency attenuation occurs between (a) near the entrance of the tunnel and (b), deep inside. In (c), the receiving antenna is around a corner, and no line-of-sight path exists.

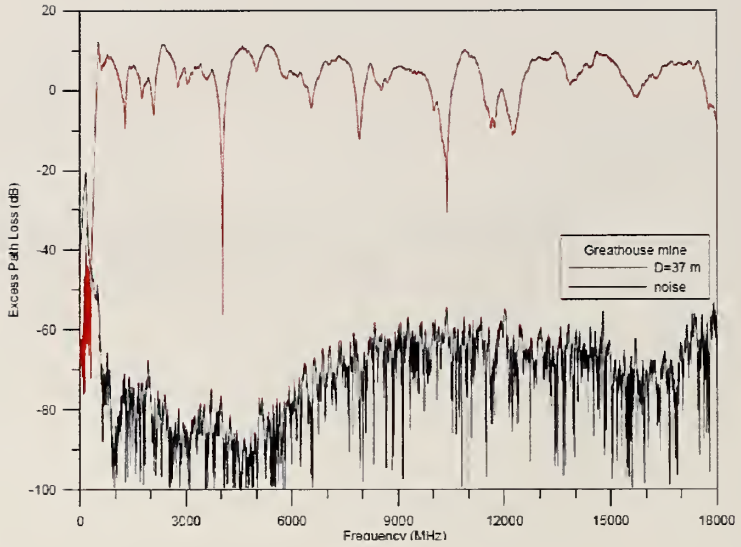

(a)

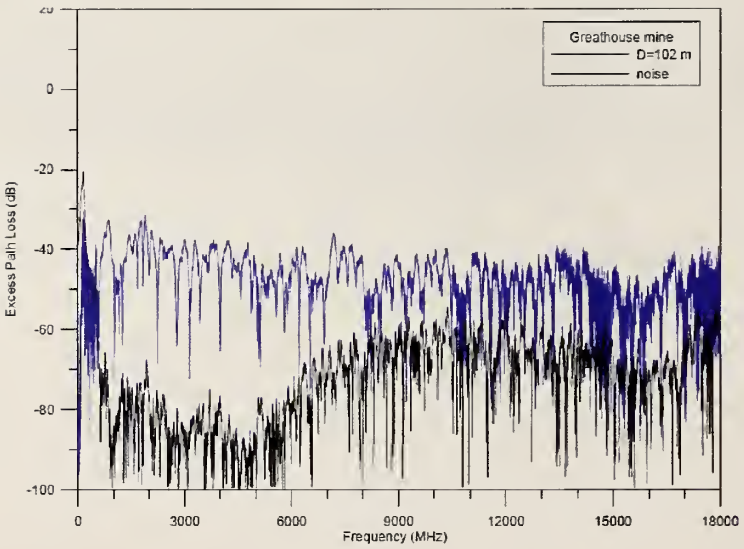

(b)

Figure 6.3-3: Excess-path-loss measurements in the Greathouse tunnel for frequencies from 1 GHz to 18 GHz. Separation between transmitter and receiver is (a) 37 m and (b) 102 m. Deep nulls in frequency are seen in (a). In (b), the receiving antenna is around a corner and no line-of-sight path exists. The received signal is above the noise floor, but is greatly attenuated.

Finally, we present the RMS delay spread for the mine tunnels in Tables 6.3-1 and 6.3-2. We see that the delay spreads are longest for low frequencies before the turn in the tunnel. This coincides with the waveguide-below-cutoff region. The delay spread decreases after the corner is turned. The shortest delay spreads are found by use of the directional antennas.

Table 6.3-1. RMS delay Spread, mean delay, and stop time for the RMS delay spread calculation for the Hazel-Atlas mine tunnel. **Left Table:** Frequencies from 25 MHz to 1.6 GHz measured with omnidirectional discone antennas. **Right Table:** Frequencies from 1 GHz to 18 GHz measured with directional dual-ridge-guide horn antennas. The gray-shaded areas represent a NLOS propagation condition.

Distance (m)	RMS Delay Spread (ns)	Mean Delay (ns)	Stop Time For RMS (ns)
0	31.0	15.5	2000
40	25.3	13.1	1000
20	18.5	18.4	1000
30	15.9	11.2	500
40	17.0	12.7	500
50	15.5	8.6	500
60	19.7	11.7	500
70	17.2	11.1	500
80	15.2	8.2	500
90	15.2	10.5	500
100	15.7	21.8	450
110	x	x	x

Distance (m)	RMS Delay Spread (ns)	Mean Delay (ns)	Stop Time For RMS (ns)
0	14.4	5.4	700
40	17.6	5.8	700
20	7.6	2.1	700
30	15.0	5.0	700
40	11.5	3.6	700
50	13.1	4.4	700
60	20.6	17.1	700
70	11.1	3.0	700
80	10.5	2.3	700
90	8.4	2.2	700
100	9.6	17.8	500
110	7.5	29.1	500

Table 6.3-2. RMS delay spread, mean delay, and stop time for the RMS delay spread calculation for the Greathouse mine tunnel. **Left Table:** Frequencies from 25 MHz to 1.6 GHz. **Right Table:** Frequencies from 1 GHz to 18 GHz. The gray-shaded areas represent a NLOS condition.

Distance (m)	RMS Delay Spread (ns)	Mean Delay (ns)	Stop Time For RMS (ns)
7	22.7	11.4	1000
17	14.3	8.4	1000
27	15.2	6.3	700
37	17.6	7.2	650
47	21	7.1	650
57	18.1	6.1	800
67	23.1	5.7	800
72	29.5	6.0	800
77	4.6	3.6	350
82	14.2	44.5	350
102	10.0	13.3	350
107	19.8	31.6	350

Distance (m)	RMS Delay Spread (ns)	Mean Delay (ns)	Stop Time For RMS (ns)
7	3.2	1.3	300
17	5.0	1.3	700
27	3.8	1.3	700
37	4.0	1.2	700
47	19.3	3.5	800
57	7.3	1.3	800
67	11.6	2.2	1000
72	6.4	1.4	1000
77	7.3	1.4	800
82	3.8	2.3	600
102	3.7	3.7	500
107	4.1	3.8	500

7. Discussion

7.1 Classification of Channel Types

The measurements described in Sections 3 through 6 illustrate a number of propagation effects. Some are common to all environments; some of them are unique to a specific environment. By observing a selected number of key features from the graphs, we are able to classify distinct propagation environments ("channels") depending on the distance and type of obstruction between the transmitter and receiver [21]. The primary features we observe to make our classifications include (1) the RMS delay spread; (2) the frequency response over the entire frequency range (e.g., excess path loss over 1 to 18 GHz); (3) the amount and structure of frequency-selective distortion over the modulation bandwidth (e.g., the spectrum over 4.95 GHz ± 10 MHz); (4) the low-frequency response (e.g., below 1 GHz). We illustrate several types of channel classifications and the key features of each.

7.1.1 AWGN channel

When the path between transmitter and receiver contains few obstructions and the distance between them is not too great, the frequency response over the channel is typically flat. Technically, this means that transmission channel impairments occur primarily due to noise in the instrumentation (often called average white Gaussian noise (AWGN) [21]). As signals get weaker, the channel degrades because the amplitude level of the noise floor of the measurement instrument approaches that of the signal.

We saw very few examples of this since our intent was to study propagation that included building penetration and multipath environments.

7.1.2 Rayleigh flat-fading channel

A second type of propagation channel can exist when there is no line of sight between the transmitter and receiver but there are multiple paths to the receiver that still provide approximately equal received signal levels at the receiver. These are called Rayleigh "flat-fading" channels because the statistical distribution of the received signal components follows a Rayleigh distribution [21].

In this type of channel, the level of multipath distortion is approximately equal across the modulation bandwidth of the signal even though the level of distortion may change significantly across a wider frequency range. Generally, this means that the difference between the times when the multipath signal components are received is smaller than the data symbol period. As a result, deep fading will not occur within the modulation bandwidth of the excitation. Because all of the received signal components arrive on non-line-of-sight paths, the phase relationship between them is random, and the received signal takes on a noise-like structure.

This is a common propagation channel in environments where emergency responders are deployed in, for example, most building penetration situations. Multiple paths from transmitter to receiver exist through windows, doors, and walls, but there is no direct path or single strong multipath component. Examples of this type of propagation can be seen in our UWB measurements, where no line-of-sight path existed, for example, in the office corridor after the receiver turned the corner (Figs. 4.3-3(a) and (b)), and when signals penetrated from outside to inside the office building (Figs. 4.3-4(a) and (b)). The frequency dependence of the noise-like signal in Fig. 4.3-4 is discussed below in Section 7.1.4.

7.1.3 Rician fading channel

In some cases, there is a line-of-sight signal component or one very strong multipath component accompanied by weaker multipath signal components. In this case, the frequency response of the channel has characteristics of both the AWGN channel and the Rayleigh channel. This hybrid case is called "Rician fading," because of the distribution of received signal components [21]. The standard deviation of a Rician-distributed received signal depends on the ratio of the direct (or strong, reflected) signal component level to the level of the weaker multipath components.

We saw this type of propagation primarily in corridors when a line-of-sight path existed. Reflections off the walls cause a limited amount of multipath, but the main received signal component is direct line-of-sight or one single reflection. An example is shown in the tunnels (Figure 6.3-2), where the received signal in the main corridor (before the receiving antenna turned the corner) did have nulls due to multipath fading, but it did not look noisy.

7.1.4 Simple building attenuation

A variation on the Rayleigh propagation channel occurs when signals propagating in a non-line-of-sight, flat-fading channel penetrate through some type of building material that has a frequency dependence of its own. For example, the radio signal may be incident on the wall of a windowed building and may penetrate one or two walls before encountering the receiver. Building materials typically exhibit a slowly varying frequency dependent attenuation, changing on the order of decibels over several decades of frequency, rather than the deep nulls associated with multipath propagation. In simple building attenuation, the RMS delay spread will not be much different from that of the Rayleigh channel, but the overall frequency response will be affected.

Because the non-flat frequency response is mainly due to attenuation through the building materials (as opposed to multipath), the roll-off is generally gradual and monotonic with frequency. Examples of this can be seen in the UWB measurements of the apartment building (Fig. 3-3.3) and when the transmitted signal penetrated the office corridor from outside (Fig. 4.3.4). The VSA measurements show these effects as well. For example, in the apartment building, we saw greater attenuation of the 4.95 GHz

signal but only a small amount of frequency-selective distortion across the channel (see Fig. 3.4-3).

7.1.5 Waveguide below cut-off propagation

A fifth type of propagation channel may exist when signals are constrained to travel through a corridor or tunnel and the dimensions of the tunnel are on the order of the wavelength of the signal. If no other propagation path exists, waveguide-below-cutoff attenuation can reduce signal levels dramatically even when a line-of-sight condition exists between transmitter and receiver. The channel may be either fast-fading (Rayleigh) or wideband-fading (described below) when waveguide-below-cutoff propagation effects occur; the key is that the lower frequencies are attenuated.

We noted this type of propagation several times during our measurements, most notably in the subterranean tunnels (Figs. 6.2-2 and 6.2-3 show the receiver measurements and 6.3-2 shows the UWB measurements). We implemented a model to demonstrate that the measured attenuation with distance follows a waveguide-below-cutoff roll-off and found good agreement (Figs. 6.2-4 and 6.2-5). Using this model, we were also able to predict the optimal frequencies for transmission in tunnel environments (Fig. 6.2-5). This was verified through UWB measurement (Fig. 6.3-2).

Interestingly, we also noticed the waveguide-below-cutoff effect in a number of other propagation environments, such as the office corridor (Fig. 4.2-2 for the receiver and Fig. 4.3-2(b) for the UWB system) and the oil refinery (Fig. 5.2-4(a) for the receiver and, to a lesser extent, Fig. 5.3-2(b) for the UWB system).

7.1.6 Wideband-fading channel

In multipath channels—either with a line-of-sight component (Rician) or without (Rayleigh)—when the RMS delay spread approaches the time-scale of the transmitted signal's data rate, frequency-selective distortion across the modulation bandwidth may occur. Distinguishing this type of "wideband-fading" propagation channel [21] from the flat-fading channel is easiest when we look at either (a) the RMS delay spread relative to the data rate or (b) the VSA spectra. When we see frequency-selective distortion (nulls and peaks) within the modulation bandwidth of the excitation, we are dealing with a wideband fading channel.

Examples of wideband fading include the first several points measured in the oil refinery (Fig. 5.3-3(b) and Fig. 5.4-3), and the subterranean tunnel (Fig. 6.3-2(a)). The VSA clearly shows frequency-selective distortion across the modulation bandwidth when this type of multipath occurs. Examples include Fig. 4.4-2 (top) in the office corridor and Figs. 5.4-3 and 5.4-4 of the oil refinery. Other indicators of this type of strong multipath propagation included an increase in RMS delay spread and EVM.

7.1.7 Site-specific physical effects

We also noted a number of site-specific physical effects that had a predictable yet significant effect on received signals. A number of these were apparent in the apartment building. For example, looking at the receiver measurements in Figs. 3.2-5 and 3.2-6, the elevators, stairwells, and even the apartments that we entered could all be identified by their relative received signal levels. From these graphs, and from the increase in RMS delay spread (Tables 3.3-1 and 3.3-2) and EVM (Fig. 3.4-2), we were also able to determine that the floor number had a pronounced effect on the overall received signal level, with higher floors related to weaker received signal strength.

In the tunnels, one of the more interesting physical-environment effects was that of the railroad track embedded in the ground of the Hazel-Atlas tunnel. The spacing of the tracks corresponded to an electrical wavelength whose corresponding frequency had an increased received-signal level. It is possible that the track was acting as a transmission line (see Figs. 6.3-2(a)-(c)).

The VSA study comparing the EVM and received-signal spectra for the carrier frequencies of 2.4 GHz and 4.95 GHz showed that the 4.95 GHz signal was more prone to high EVM, lower received signal strength, and a greater level of frequency-selective distortion. Examples include Figs. 3.4-2, 3.4-3, and 3.4-4 for the apartment building, Figs. 4.4-1 and 4.4-2 for the office corridor, and Figs. 5.4-2 and 5.4-4 for the oil refinery. We saw no strong dependence on modulation type when we studied QPSK versus 64-QAM modulation in the oil refinery (Fig. 5.4-3).

Finally, we conducted several sets of measurements comparing both omnidirectional antennas and directional antennas. As expected, when the directional antennas were used, received signal strength was generally higher (Fig. 4.4-3 shows an example from the office corridor) and RMS delay spread lower (Figs. 4.3-5 and 4.3-6 illustrate this effect in the corridor).

7.2 Classifying Propagation in the Different Structures

Finally, we draw some conclusions about the different types of propagation channel with respect to the individual structures based on analysis of selected features of the measured data. Using tables and graphs, we summarize some of the key features of measured data from previous sections of the report to clearly illustrate our conclusions.

7.2.1 Apartment building

In the apartment building, we measured short RMS delays (on the order of tens of nanoseconds, as shown below in Table 7.2-1). The environment consisted entirely of NLOS propagation paths as the signals penetrated through the outside walls of the structure and at least one interior wall. The excess path delay measurements presented nearly monotonic roll-off in frequency (summarized in Figure 7.2-1).

The VSA measurements (summarized below in Figures 7.2-2(a) and (b)) show that the channel is generally flat. However, some frequency-selective distortion does occur, primarily when the transmitter is behind the elevators or stairwell doors. Note that because the modulated-signal measurements were made using OFDM excitation, the multipath does not disrupt the ability of the receiver to demodulate the signal except when the signal level becomes very weak. This was shown by the EVM graphs in Figure 3.4-2. We see weaker signals both for the 4.95 GHz carrier frequency and for signals transmitted from the seventh floor.

These observations tell us we are dealing with simple building penetration, where a multipath environment (flat- or wideband-fading) is combined with attenuation due to building materials.

Table 7.2-1: RMS delay spread at the apartment building (ns). Lower-frequency measurements using omnidirectional antennas, higher-frequency measurements using directional antennas.

Position	Floor 2, 0.3-1.0 GHz	Floor 7, 0.3-1.0 GHz	Floor 2, 1-18 GHz	Floor 7, 1-18 GHz
0	49.2	47.2	24.1	32.4
1	38.7	36.4	21.4	23.7
2	35.8	37.7	16.7	24.3
3	28.2	33.2	15.3	14.5
4	48.8	49.9	24.9	35.9
5	59.1	59.9	48.2	44.2
6	71.2	70.9	30.7	37.4
7	62.9	77.5	36.3	40.8
8	61.6	70.1	31.2	38.8
9	56.7	66.5	30.4	30.5
10	58.6	69.1	31.7	31.0
11	54.3	65.5	39.4	34.8
12	60.9	67.5	38.0	36.8
13	62.9	82.4	20.8	154.3

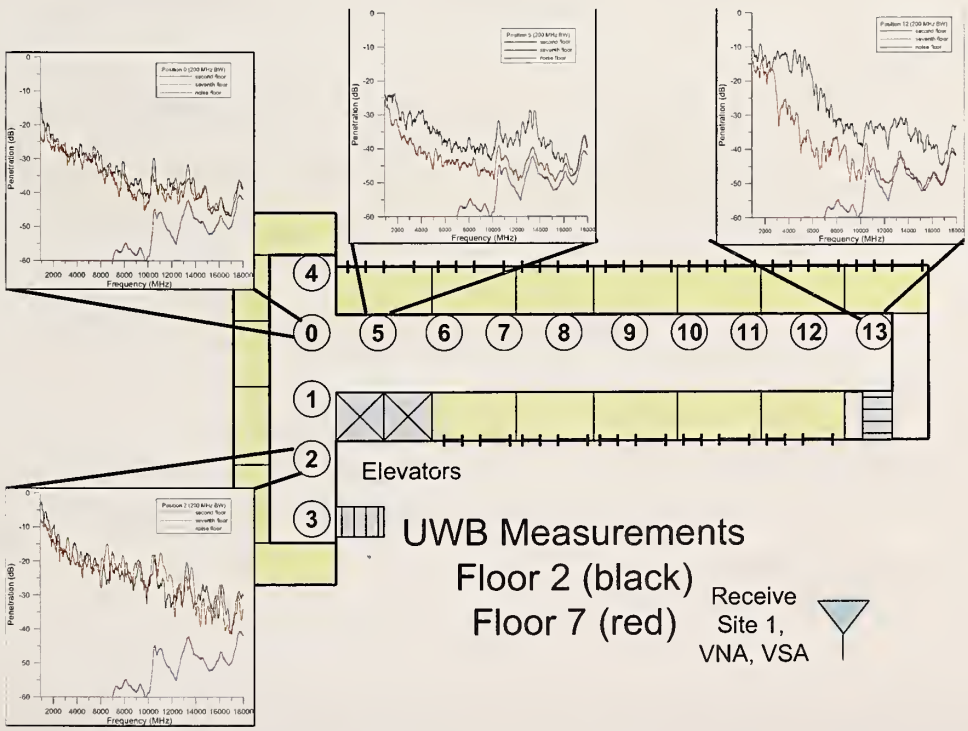

Figure 7.2-1: Excess path loss on floors two (top curves, black) and seven (bottom curves, red) of the apartment building for frequencies from 1 to 18 GHz.

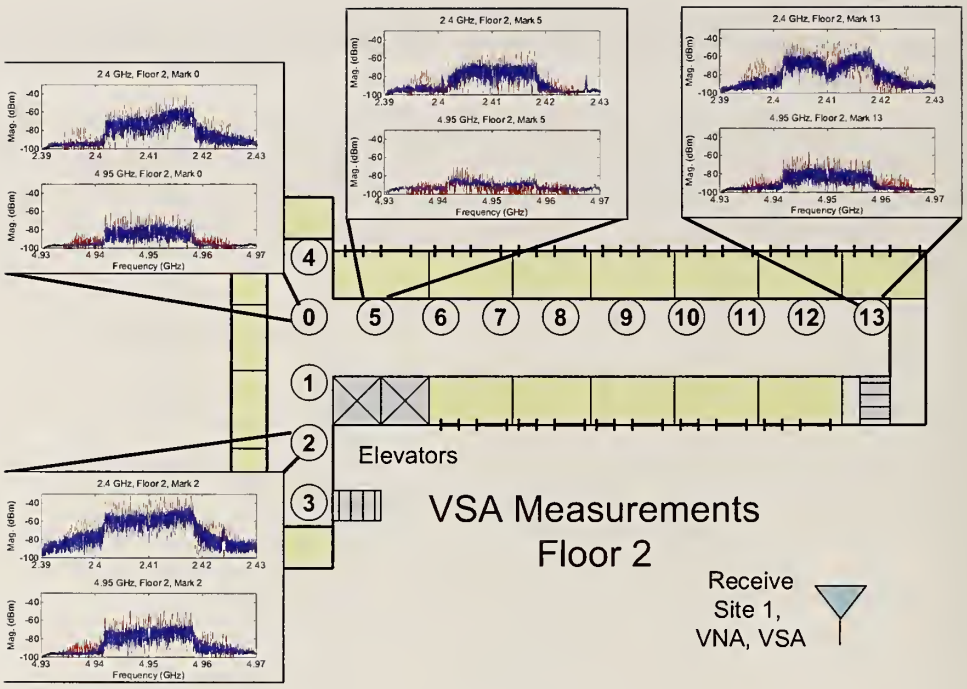

(a)

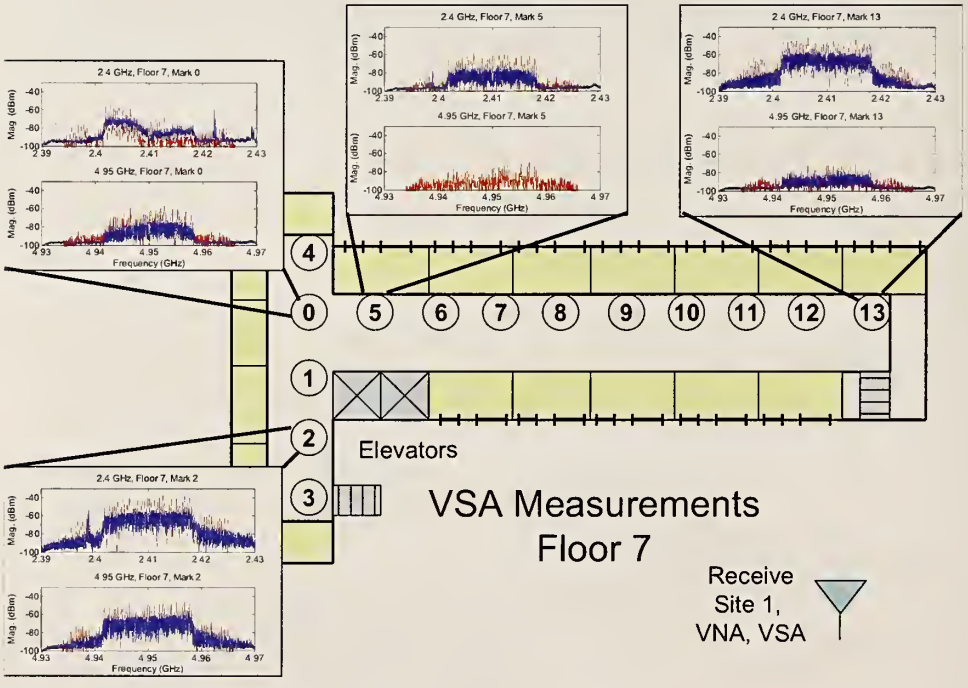

(b)

Figure 7.2-2: Measured spectra across the modulation bandwidth in the apartment building. (a) Second floor. (b) Seventh floor. Top graphs are for a carrier frequency of 2.4 GHz and bottom graphs are for a carrier frequency of 4.95 GHz.

7.2.2 Office corridor

The office corridor contained two different propagation scenarios: one where the transmitter and receiver were both located inside the building, and one where the transmitter was outside, some distance from the building, and the receiver was inside. These present different propagation scenarios and will be analyzed separately.

The RMS delay spread when the transmitter and receiver were both inside is repeated below in Figure 7.2-3. We see short delay times for measurements with carrier frequencies between 1 and 18 GHz, and longer delay times below 1 GHz. The excess path loss measurements (summarized in Figure 7.2-4) show relatively little frequency dependency at the higher frequencies, but a significant roll-off as one moves down the corridor for the lower frequencies. Thus, we deduce that the corridor served as a waveguide below cutoff at the lower frequencies and that we had a flat-fading channel at the higher frequencies. Before the turn in the corridor, signal levels are much higher, and multipath interference has distinct nodes. After the turn, the multipath more closely resembles noise.

Position 1 is one of the only measurements we did that has a line-of-sight component. This position behaves more or less like an AWGN channel.

RMS Delay Spread (ns) for Indoor Transmit Antenna:

•Omnidirectional Antenna 25 MHz – 1.4 GHz: green, top data

•Omnidirectional Antenna 750 MHz – 18 GHz: red, middle data

•Directional Antenna 750 MHz – 18 GHz: blue, bottom data

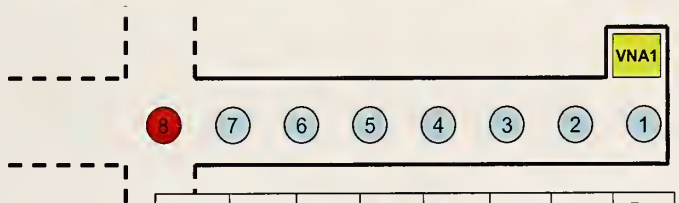

P8	P7	P6	P5	P4	P3	P2	P1
134.7	89.3	84.4	98.0	93.1	76.4	55.9	27.9
21.3	30.9	25.6	26.9	22.9	22.2	23.6	14.4
19.6	20.4	18.6	18.0	17.5	16.6	16.7	8.8

Figure 7.2-3: Summary of the RMS delay spread measured in the office corridor for different frequency bands and different antenna types. The transmitter and receiver were both inside the building.

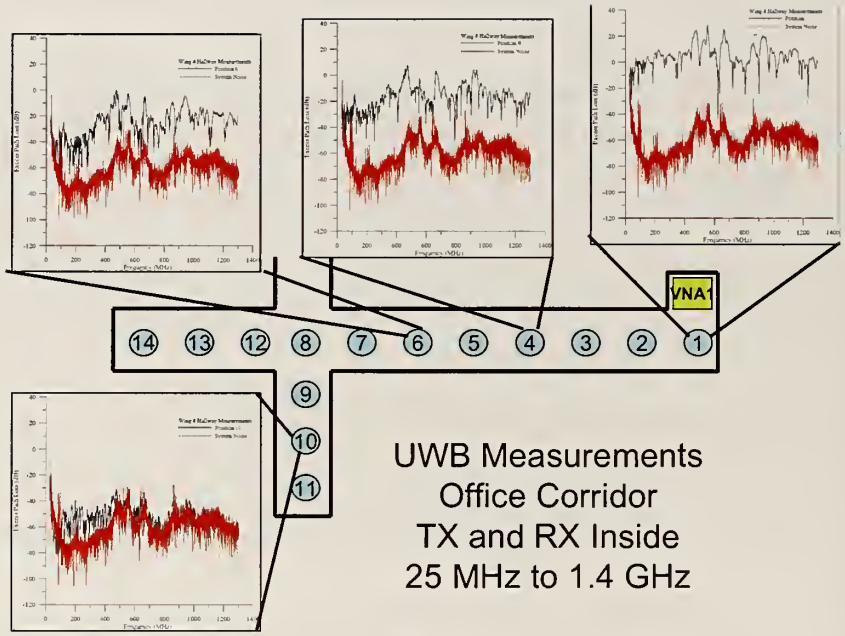

(a)

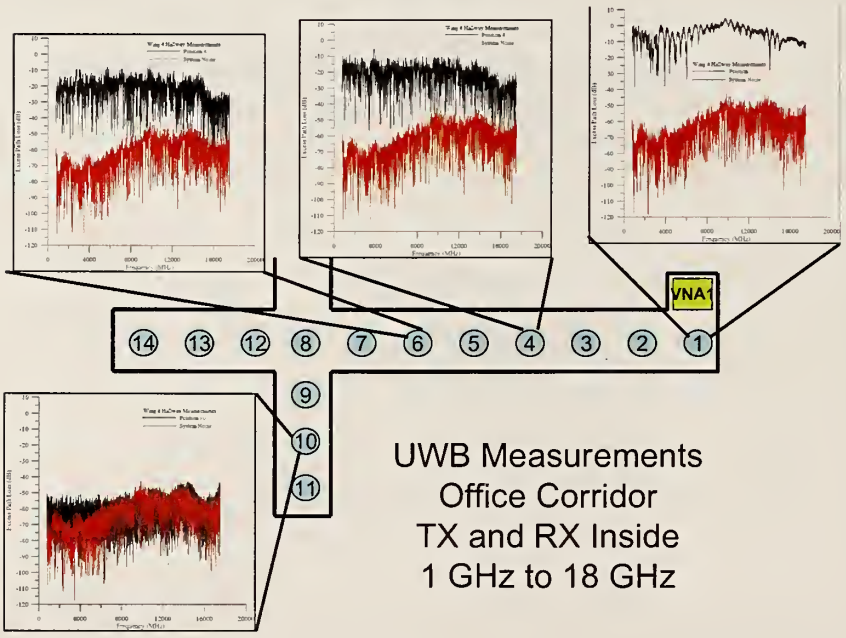

(b)

Figure 7.2-4: Summary of the wideband excess path loss measurements in the office corridor. (a) Carrier frequencies from 25 MHz to 1.4 GHz and (b) 1 GHz to 18 GHz.

Figures 7.2-5(a) and (b) summarize the VSA measurements when the transmitter and receiver are both located inside the building. We see a small amount of frequency-dependent distortion across the modulation bandwidth at some positions. This indicates that in general the corridor can be represented by a flat fading channel, but in some positions it becomes a wideband fading channel.

When the transmitter was outside the corridor and the receiver was inside, the RMS delay spread (repeated below in Figure 7.2-6 from Section 4.3) showed a much smaller dependence on frequency or antenna type, as compared to the delay spreads when the transmitter and receiver were both inside.

Also, the excess path loss (summarized below in Figures 7.2-7(a) and (b)) does not exhibit the waveguide-below-cutoff frequency dependence at the lower frequencies, as in the case where both transmitter and receiver are inside. For most corridor locations in the lower frequency band (7.2-7(a)), the received signal level follows the measured noise floor, indicating a flat-fading channel. In the higher frequency band (7.2-7(b)), the frequency response does start to roll off at around 4 GHz, indicating attenuation due to material parameters. Thus, this channel may be classified as simple building penetration. Note that no VSA measurements were made of the corridor with this transmitter and receiver arrangement.

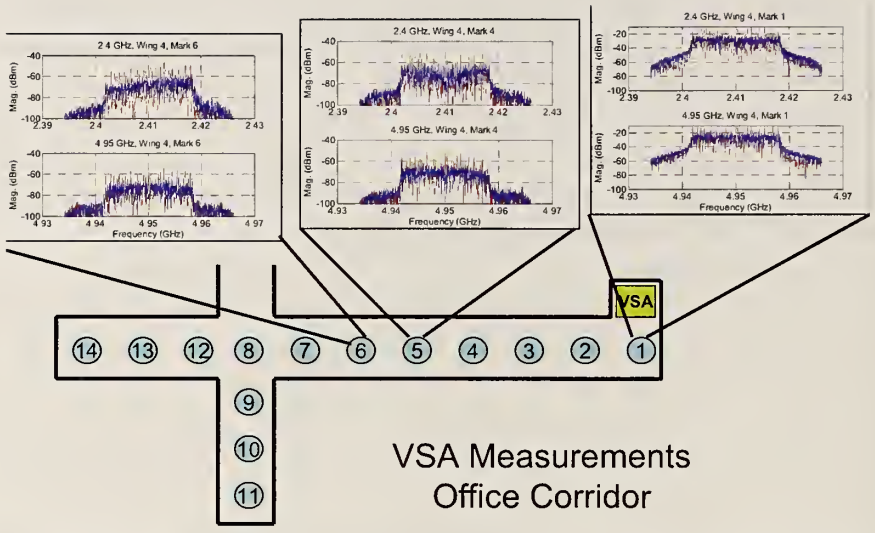

Figure 7.2-5: Summary of the VSA measurements of the spectra of the modulated signal at different locations in the office corridor. The carrier frequency is 2.4 GHz in the top graphs and 4.95 GHz in the bottom graphs.

RMS Delay Spread (ns) for Outdoor Transmit Antenna:

•Omnidirectional Antenna 25 MHz to 1.4 GHz: green, top data

•Omnidirectional Antenna 750 MHz to 18 GHz: red, middle data

•Directional Antenna 750 MHz to 18 GHz: blue, bottom data

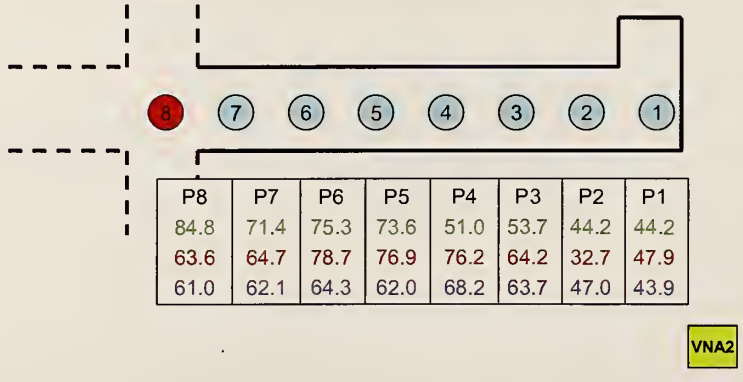

P8	P7	P6	P5	P4	P3	P2	P1
84.8	71.4	75.3	73.6	51.0	53.7	44.2	44.2
63.6	64.7	78.7	76.9	76.2	64.2	32.7	47.9
61.0	62.1	64.3	62.0	68.2	63.7	47.0	43.9

Figure 7.2-6: Summary of the RMS delay spread measured in the office corridor for different frequency bands and different antenna types. The transmitting antenna is outside the building and receiving antenna is inside of the building.

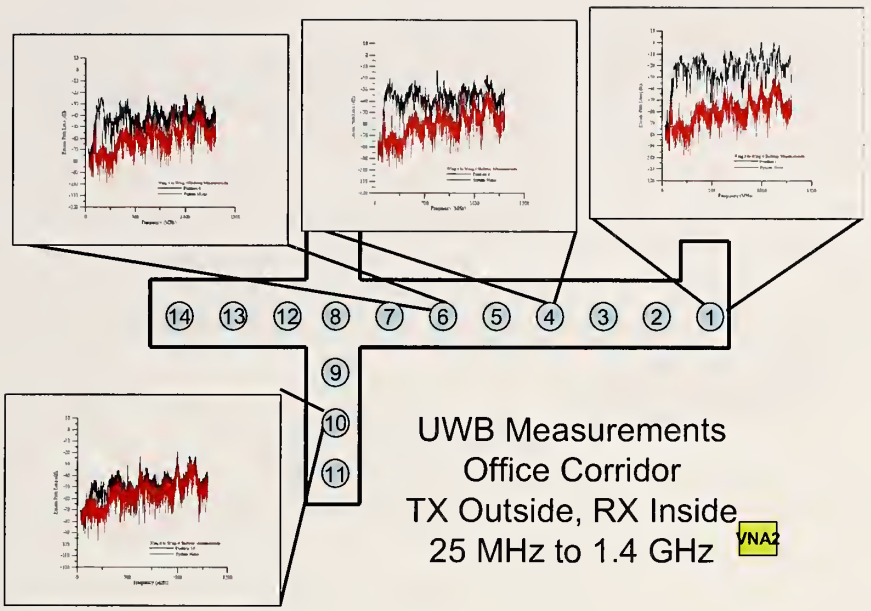

(a)

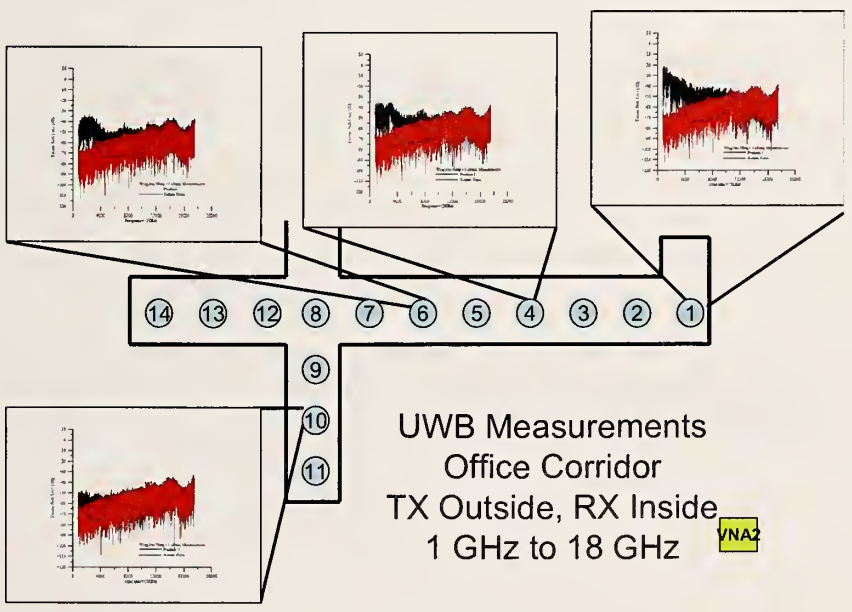

(b)

Figure 7.2-7: Excess-path-loss measurements of the office corridor when the transmitter is outside the building and the receiver is inside. Carrier frequencies from (a) 25 MHz to 1.4 GHz and (b) 1 GHz to 18 GHz.

7.2.3 Oil refinery

We next consider the oil refinery. We were able to identify two distinct propagation channels in this environment. The RMS delay spread, summarized below in Figure 7.2-8 clearly indicates the two types of channels. First, between points 2 and 6, the overhead piping created a tunnel-like environment with significant multipath. In this environment, we see distinct resonant structure in the excess path loss measurements of Figure 7.2-9, as well as some low-frequency attenuation due to waveguiding effects (we also saw this effect in the single-frequency measurements). The VSA measurements in Figure 7.2-10 show frequency-selective distortion. Thus, for this region we have a channel that can be described by both wideband fading with a direct path and waveguide-below-cutoff effects.

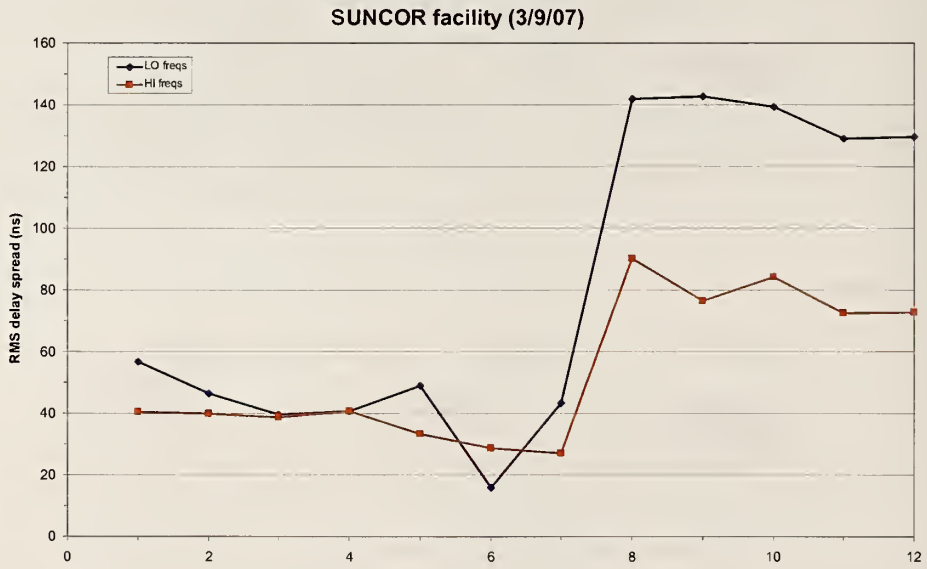

Figure 7.2-8: Summary of the RMS delay spread in the oil refinery at test points 1 to 12. The higher blue curve represents frequencies from 25 MHz to 1.2 GHz and the lower orange curve represents frequencies from 1 GHz to 18 GHz.

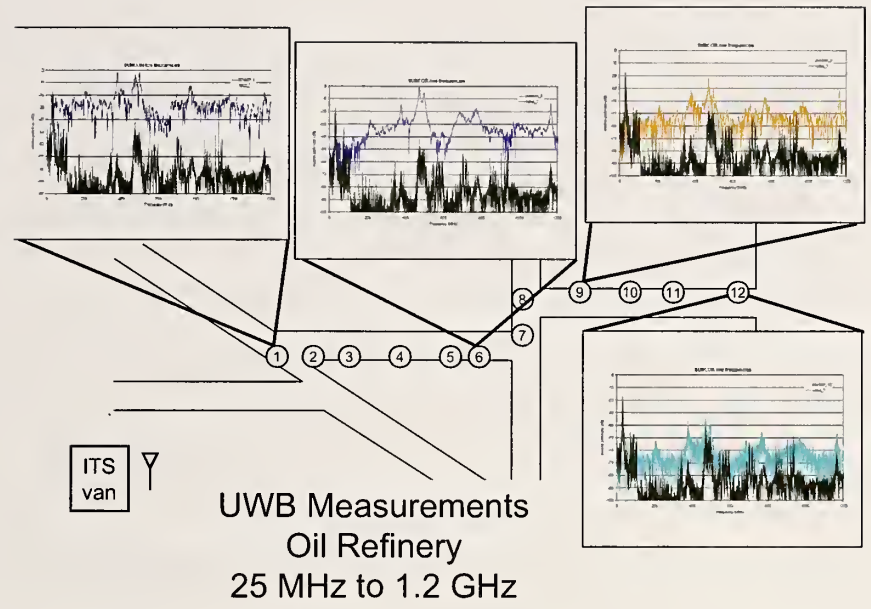

(a)

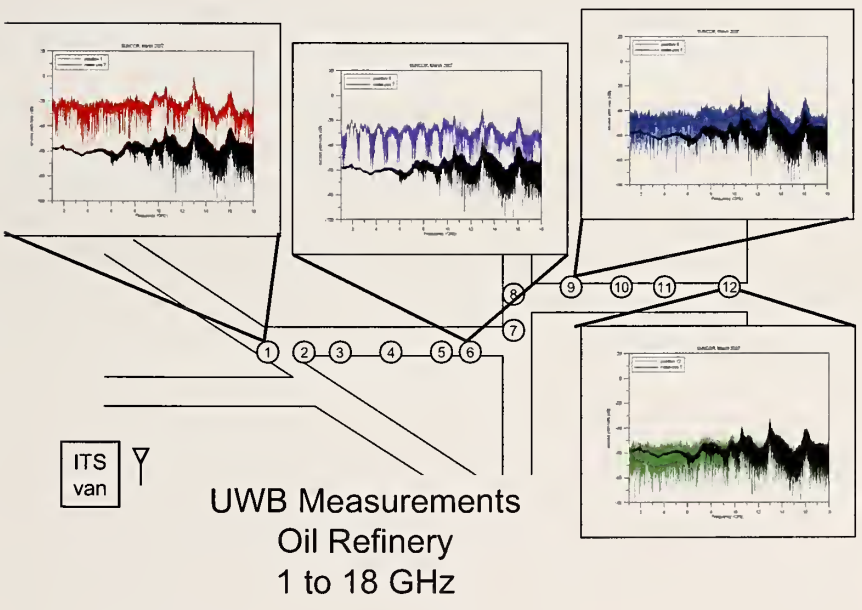

(b)

Figure 7.2-9: Summary of the excess-path-loss measurements in the oil refinery. Carrier frequencies from (a) 25 MHz to 1.2 GHz and (b) 1 GHz to 18 GHz.

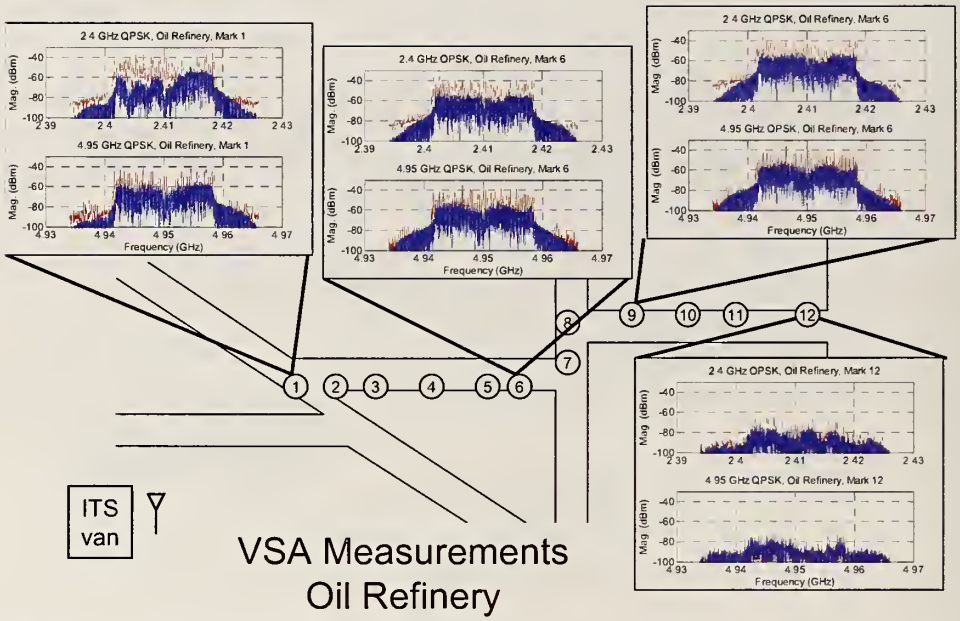

Figure 7.2-9: Summary of the VSA measurements of the spectra of the modulated signal at different locations in the oil refinery. Top graphs represent measurements made at a carrier frequency of 2.4 GHz and bottom graphs are for a carrier frequency of 4.95 GHz.

The second type of propagation channel was identified for points 7 and higher in the NLOS region. Here we see no material- or waveguide-related trends in the excess path loss plots, nor do we see any resonant-like behavior there. However, we do see significant frequency-selective distortion in the VSA measurements, significantly longer RMS delay spreads, and much lower signal levels. This channel could be classified as a simple, highly attenuated, NLOS wideband fading channel.

7.2.4 Subterranean tunnel

Finally, we examine the measured data from the subterranean tunnels in order to classify the propagation channel. Table 7.2-2 shows that the RMS delay spread for frequencies 25 MHz to 1.6 GHz is longer at the lower frequencies as the distance increases. The excess path loss measurements shown Figures 7.2-10 (Hazel-Atlas) and 7.2-11 (Greathouse), respectively, show a definite low-frequency roll-off as the bend in either tunnel is approached. These features indicated waveguide-below-cutoff behavior in the tunnel.

At frequencies higher than the waveguide-cutoff frequency, the low-frequency response of the measured signal follows that of the noise floor with some multipath-induced nulls appearing deeper in the tunnel. Once the corner is turned, the signal essentially drops into the noise of the receiver. Thus, we can classify the channel over the lower frequency band as flat-fading with waveguide-below-cutoff behavior.

The RMS delay spread for frequencies from 1 GHz to 18 GHz are shorter than for the low frequencies, increasing as we approach the bend, then dropping off again once the turn is completed. The excess path loss graphs show definite multipath structure in the tunnels before the corner is turned, but overall the response is flat. Once the corner is turned, the signals have a more uniform, noisy appearance. We classify the high-frequency channel as a wideband fading channel with a line-of-sight component in the tunnel before the corner, and flat fading once the corner is turned.

Table 7.2-2: Summary of RMS delay spread calculated from excess-path-loss measurements for the subterranean tunnels. The columns represent the two tunnels and the different antennas/frequency bands measured in each tunnel. The gray shaded areas represent NLOS propagation condition.

Distance (m)	Hazel-Atlas omni antenna (ns)	Hazel-Atlas directional antenna (ns)	Distance (m)	Greathouse omni antenna (ns)	Greathouse directional antenna (ns)
0	---	--	7	22.7	3.2
10	14.3	5.0	17	14.3	5.0
20	15.2	3.8	27	15.2	3.8
30	17.6	4.0	37	17.6	4.0
40	21	19.3	47	21	19.3
50	18.1	7.3	57	18.1	7.3
60	23.1	11.6	67	23.1	11.6
70	29.5	6.4	72	29.5	6.4
80	4.6	7.3	77	4.6	7.3
90	14.2	3.8	82	14.2	3.8
100	10.0	3.7	102	10.0	3.7
110	19.8	4.1	107	19.8	4.1

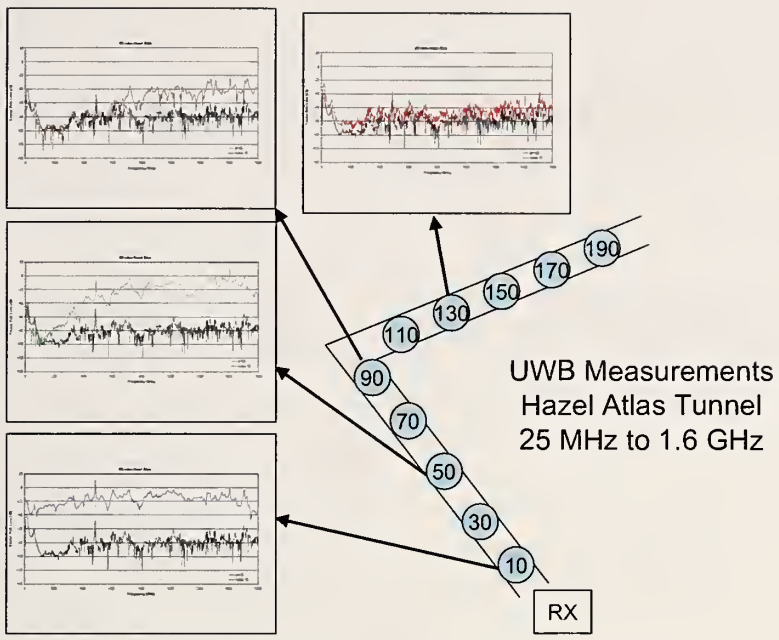

(a)

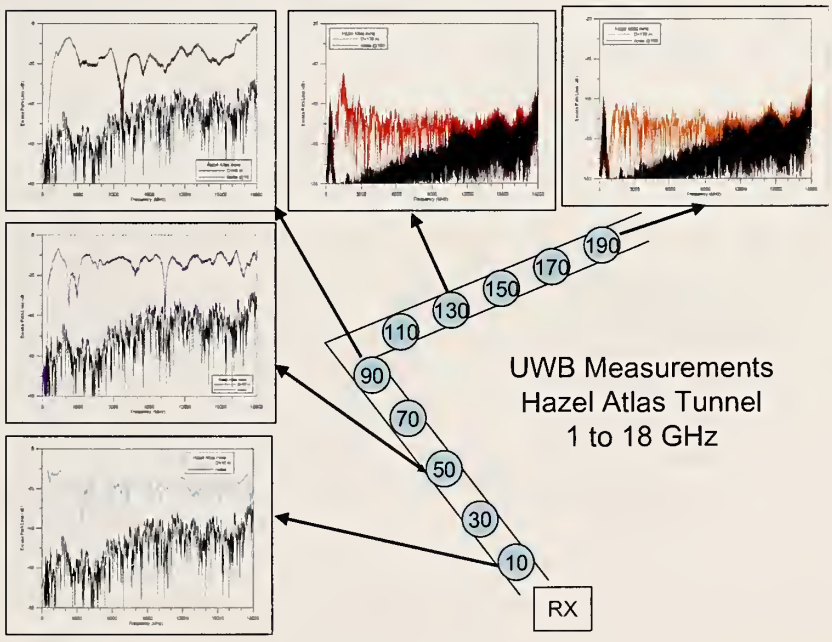

(b)

Figure 7.2-8: Summary of the excess-path-loss measurements in the Hazel-Atlas tunnel. Carrier frequencies from (a) 25 MHz to 1.2 GHz and (b) 1 GHz to 18 GHz.

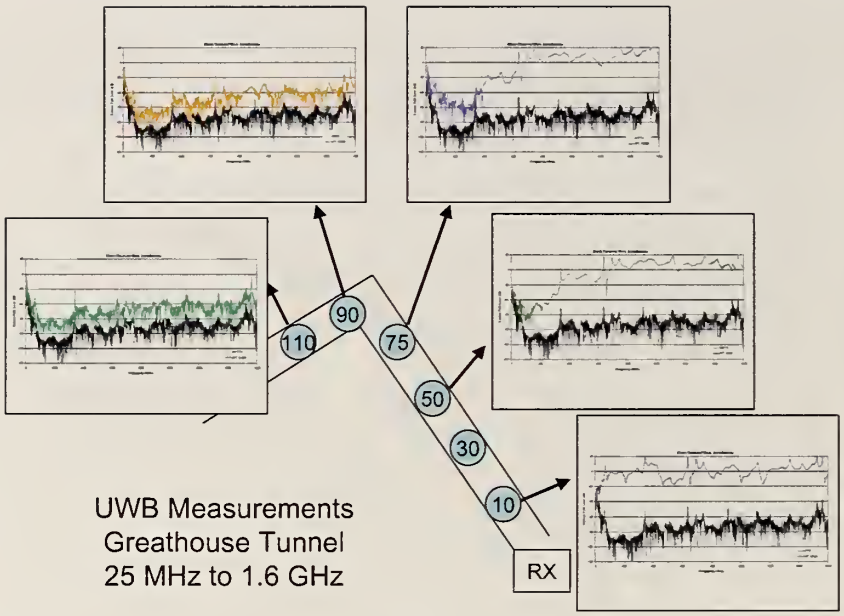

(a)

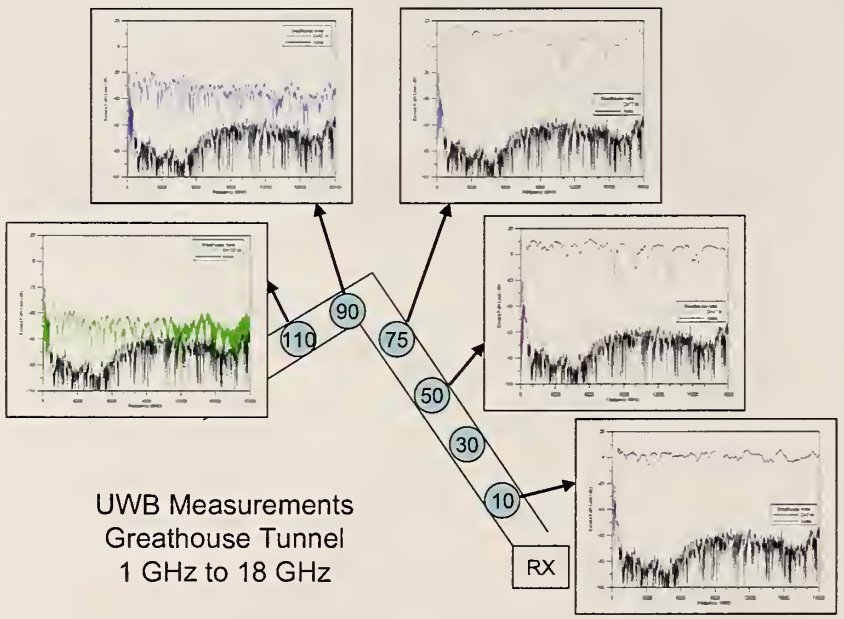

(b)

Figure 7.2-8: Summary of the wideband excess path loss measurements in the Greathouse tunnel. Carrier frequencies from (a) 25 MHz to 1.2 GHz and (b) 1 GHz to 18 GHz.

8. Conclusion

We studied radiowave propagation in four different environments of interest to the public-safety community: an 11-story apartment building, a hallway corridor in an office building, an oil refinery, and a subterranean tunnel. Our study focused on measurements of quantities of interest in design, testing, and standards development for broadband, modulated-signal transmissions. These measurements included detailed, single-frequency received-power measurements throughout the structures; ultrawideband excess path-loss measurements at specific locations in each structure; and measurements of digitally modulated signals under the OFDM protocol at carrier frequencies of 2.4 GHz and 4.95 GHz. From the wideband path-loss measurements, we calculated RMS delay spread. From the collected data, we were able to classify the various environments in terms of types of propagation channels.

These tests show that a number of factors can define the propagation environment and that certain effects are common to environments that superficially appear quite different from each other. For certain propagation channels such as simple building penetration, signal strength measurements may be sufficient to characterize the environment. In cases where multipath reflections, waveguiding effects, and other non-line-of-sight conditions exist, measurements that cover multiple frequencies and metrics can offer additional insight. In any case, we hope that having a large body of well-characterized measurement data for a number of different propagation environments can facilitate development of technically sound standards and radio systems for the first responder community.

The authors acknowledge the support of the Department of Justice Community-Oriented Policing Services (COPS) program, the NIST Office of Law Enforcement Standards (OLES), in particular Dereck Orr, Project Manager for the Public Safety Communication Systems project. Work on the subterranean tunnels was funded in part by the Department of Homeland Security Office of Standards, Bert Coursey, Director. We are grateful for the expert advice from our colleagues at the Institute for Telecommunication Sciences (ITS), part of the National Telecommunications and Information Administration, in particular Rob Stafford, John Ewan, Andy Thiessen, and Jeff Bratcher.

We also acknowledge the assistance of the management and tenants of Horizon West Apartments in Boulder, CO; Teresa Maraia of ITS for finding appropriate frequencies for use in the government frequency bands; the NIST Interference Committee for enabling our measurements in Wing 4 of the Boulder Labs Campus; and Tricia Toussaint from Suncor Oil Refinery in Commerce City, CO for extensive help during our measurements at the facility. Finally, we thank Frederick Remley for help with photographs used in the report.

9. References

[1] C.L. Holloway, G. Koepke, D. Camell, K.A. Remley, D.F. Williams, S.A. Schima, S. Canales, D.T. Tamura, "Propagation and Detection of Radio Signals Before, During, and After the Implosion of a 13-Story Apartment Building," *Natl. Inst. Stand. Technol. Note 1540*, May 2005.

[2] C.L. Holloway, G. Koepke, D. Camell, K.A. Remley, D.F. Williams, S.A. Schima, S. Canales, D.T. Tamura, "Propagation and Detection of Radio Signals Before, During, and After the Implosion of a Large Sports Stadium (Veterans' Stadium in Philadelphia)," *Natl. Inst. Stand. Technol. Note 1541*, October 2005.

[3] C.L. Holloway, G. Koepke, D. Camell, K.A. Remley, S.A. Schima, M. McKinley, R.T. Johnk, "Propagation and Detection of Radio Signals Before, During, and After the Implosion of a Large Convention Center," *Natl. Inst. Stand. Technol. Note 1542*, June 2006.

[4] C.L. Holloway, W.F. Young, G. Koepke, K.A. Remley, D. Camell, Y. Becquet, "Attenuation of Radio Wave Signals Coupled Into Twelve Large Building Structures," *Natl. Inst. Stand. Technol. Note 1545*, April 2008.

[5] SAFECOM Statement of Requirements, vol. 1, version 1.2, http://www.safecomprogram.gov/NR/rdonlyres/8930E37C-C672-48BA-8C1B-83784D855C1E/0/SoR1_v12_10182006.pdf . Section 3.3 discusses the residential fire, and Section 3.5 the explosion at the chemical plant.

[6] P. Papazian, "Basic transmission loss and delay spread measurements for frequencies between 430 and 5750 MHz," *IEEE Trans. Antennas Prop.*, 53(2): 694-701, Feb. 2005.

[7] J.R. Hampton, N.M. Merheb, W.L. Lain, D.E. Paunil, R.M. Shurfor, And W.T. Kasch, "Urban propagation measurements for ground based communication in the military UHF band," *IEEE Trans. Antennas Prop.*, 54(2): 644-654, Feb. 2006.

[8] M. Rütschlin, K. A. Remley, R. T. Johnk, D. F. Williams, G. Koepke, C. Holloway, A. MacFarlane, and M. Worrell, "Measurement of weak signals using a communications receiver system," *Proc. Intl. Symp. Advanced Radio Tech.*, Boulder, CO, March 2005, pp. 199-204.

[9] B. Davis, C. Grosvenor, R.T. Johnk, D. Novotny, J. Baker-Jarvis, M. Janezic, "Complex permittivity of planar building materials measured with an ultra-wideband free-field antenna measurement system," *Natl. Inst. Stand. Technol. J. Res.,* 112(1):67-73, Jan.-Feb., 2007.

[10] M. Riback, J. Medbo, J. Berg, F. Harryson, H. Asplund, "Carrier frequency effects on path loss," *Proc. 63rd IEEE Vehic. Technol. Conf.*, Vol. 6, pp. 2717-2721, 2006.

[11] J.C.-I. Chuang, "The effects of time delay spread on portable radio communications channels with digital modulation," *IEEE J. Selected Areas in Comm.*, SAC-5(5): 879-889, June 1987.

[12] Y. Oda, R. Tsuchihashi, K. Tsuenekawa, M. Hata, "Measured path loss and multipath propagation characteristics in UHF and microwave frequency bands for urban mobile communications," *Proc. 53rd IEEE Vehic. Technol. Conf.*, Vol. 1, pp. 337-341, May 2001.

[13] J.A. Wepman, J.R. Hoffman, L.H. Loew, "Impulse Response Measurements in the 1850-1990 MHz Band in Large Outdoor Cells", *NTIA Report 94-309*, June 1994.

[14] IEEE Standard for Wireless LAN Medium Access Control (MAC) and Physical Layer (PHY) Specifications: High-Speed Physical Layer in the 5 GHz Band, *IEEE Standard 802.11a™-1999*.

[15] IEEE Standard for Wireless LAN Medium Access Control (MAC) and Physical Layer (PHY) Specifications: Higher-Speed Physical Layer Extension in the 2.4 GHz Band, *IEEE Standard 802.11b-1999*.

[16] These standards are identified solely for completeness of description, but such identification does not constitute an endorsement by the National Institute of Standards and Technology. Other products may work as well or better.

[17] www.leearmstrong.com/DSRCHome/DSRCHomeset.htm

[18] M.D. McKinley, K.A. Remley, M. Myslinski, J.S. Kenney, D. Schreurs, B. Nauwelaers, "EVM calculation for broadband modulated signals," *64th ARFTG Conf. Dig.*, Orlando, FL, Dec. 2004, pp. 45-52.

[19] A. G. Emslie, R. L. Lagace, and P. F. Strong, "Theory of the propagation of UHF radio waves in coal mine tunnels," *IEEE Trans. Antennas Prop.*, 23(2): 192-205, Mar. 1975.

[20] M. Rak and P. Pechac, "UHF propagation in caves and subterranean galleries," *IEEE Trans. Antennas Prop.*, 55(4): 1134-1138, Apr. 2007.

[21] S.R. Saunders and A. Aragon-Zavala, *Antennas and Propagation for Wireless Communication Systems*, 2nd. Ed., John Wiley and Sons, Ltd., 2007.

Appendix A: Single-Frequency Received-Power Data Collected Using a Calibrated Communications Receiver: Apartment Building

The following pages contain the complete set of measured data for the apartment building (described in Section 3.2).

Single-Frequency Received-Power Data: 11-Story Apartment Building

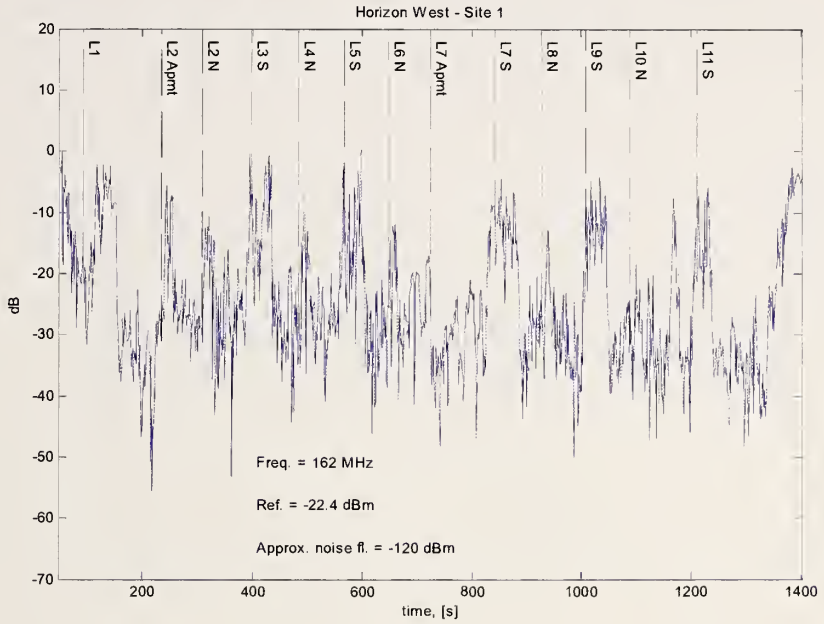

(a)

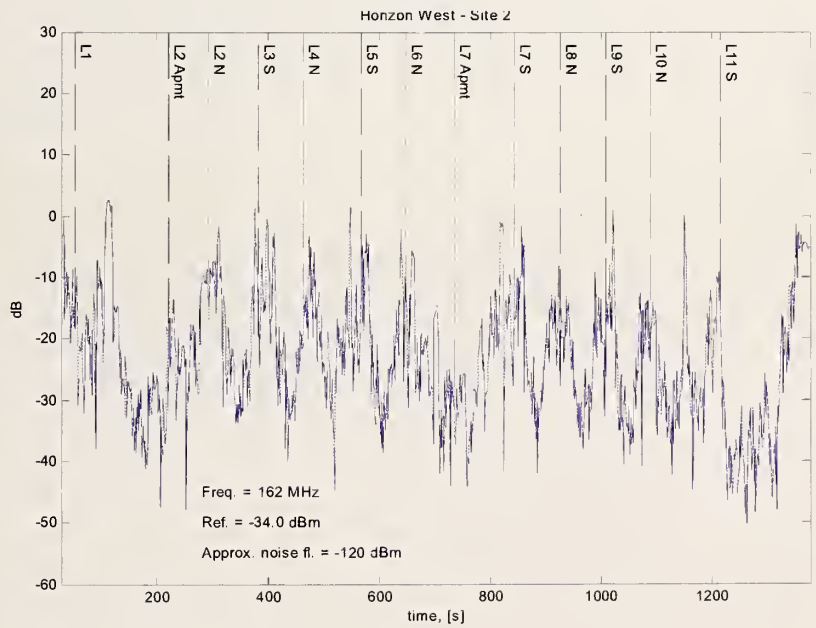

(b)

Figure A.1: Received-power data for the top 10 floors of an apartment building for a transmitter carrier frequency of 162 MHz, measured by a narrowband communications receiver. (a) Site 1. (b) Site 2. The received signal levels are referred to a line-of-sight reference signal, whose level is noted on each graph.

Single-Frequency Received-Power Data: 11-Story Apartment Building

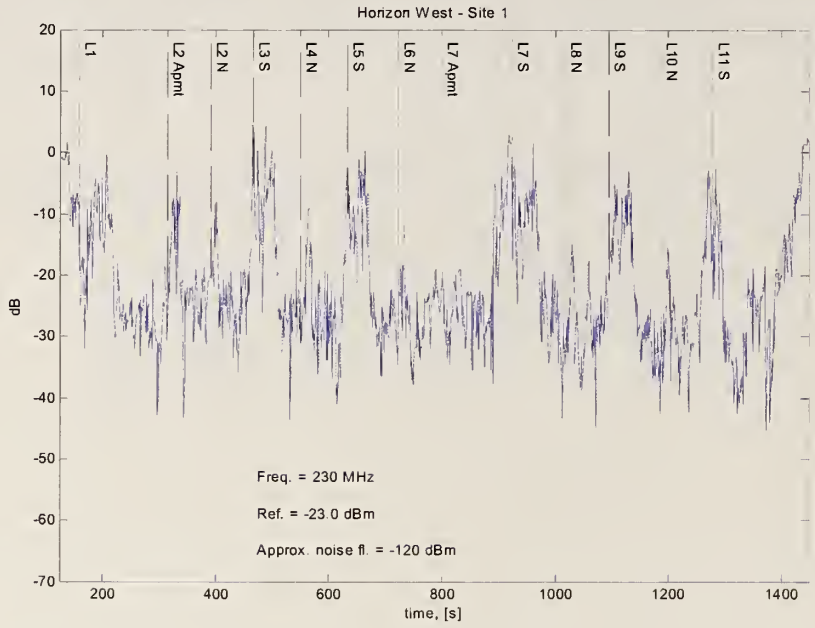

(a)

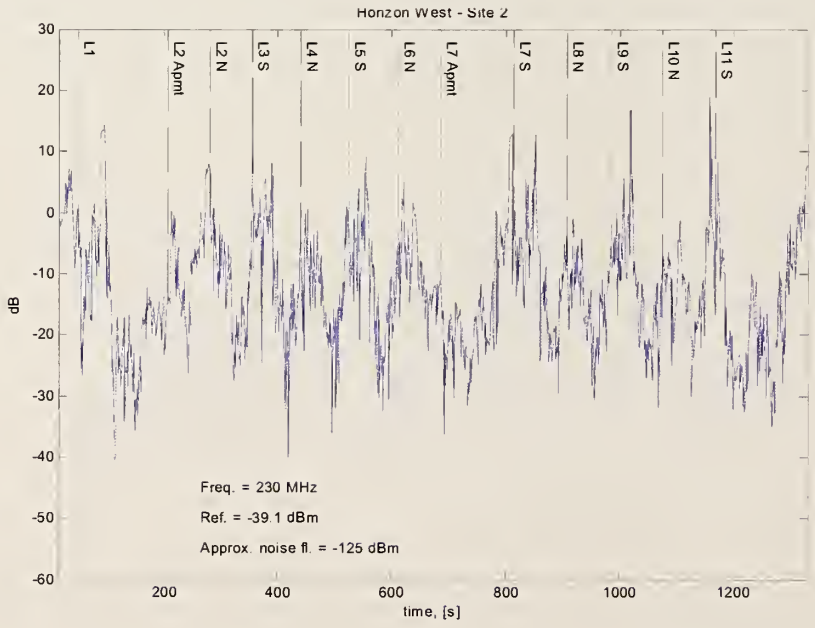

(b)

Figure A.2: Received-power data for the top 10 floors of an apartment building for a transmitter carrier frequency of 230 MHz, measured by a narrowband communications receiver. (a) Site 1. (b) Site 2. The received signal levels are referred to a line-of-sight reference signal, whose level is noted on each graph.

Single-Frequency Received-Power Data: 11-Story Apartment Building

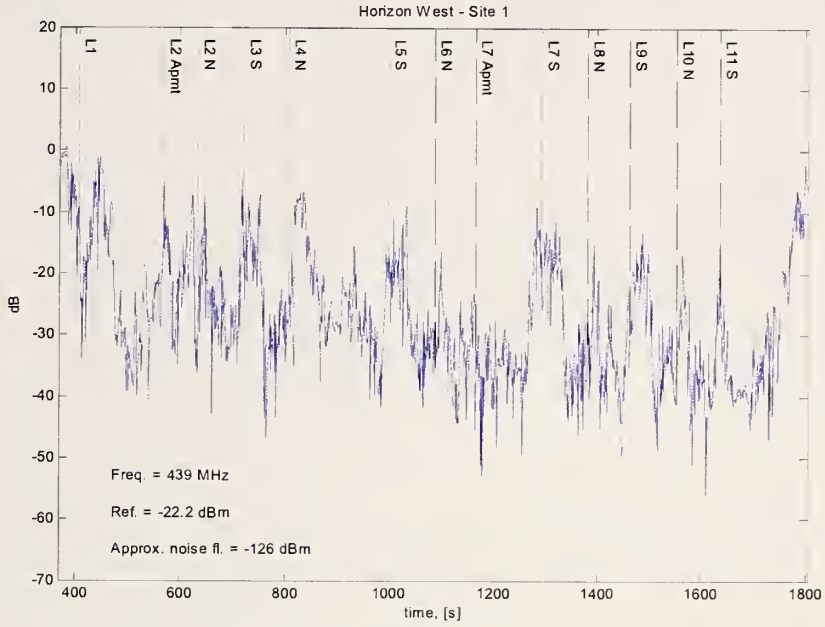

(a)

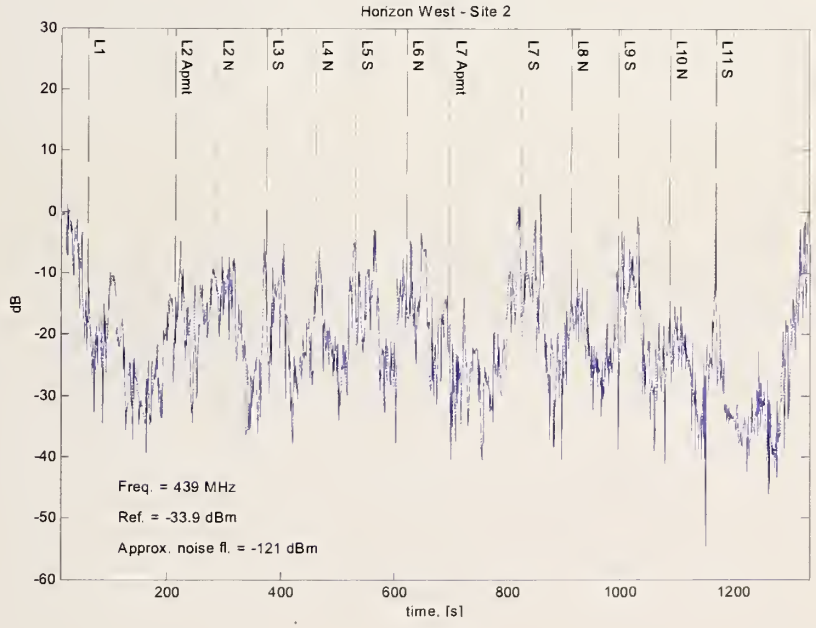

(b)

Figure A.3: Received-power data for the top 10 floors of an apartment building for a transmitter carrier frequency of 439 MHz, measured by a narrowband communications receiver. (a) Site 1. (b) Site 2. The received signal levels are referred to a line-of-sight reference signal, whose level is noted on each graph.

Single-Frequency Received-Power Data: 11-Story Apartment Building

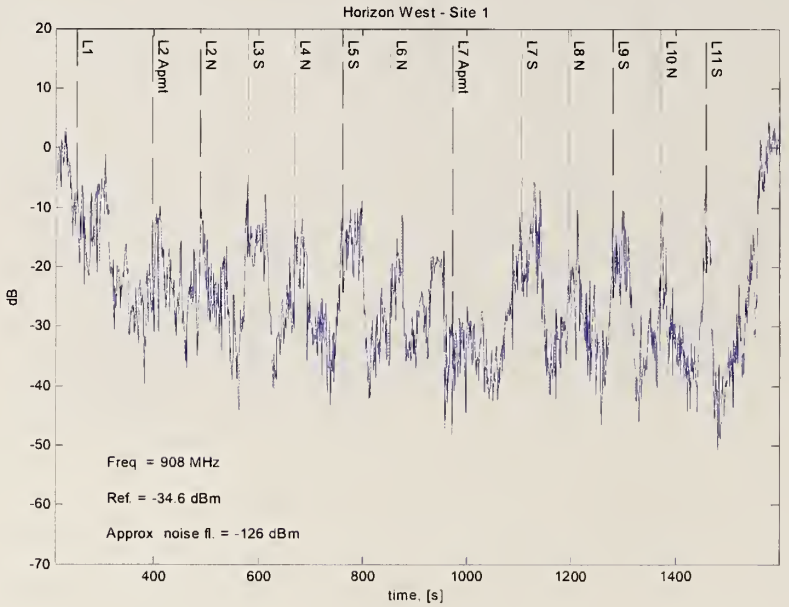

(a)

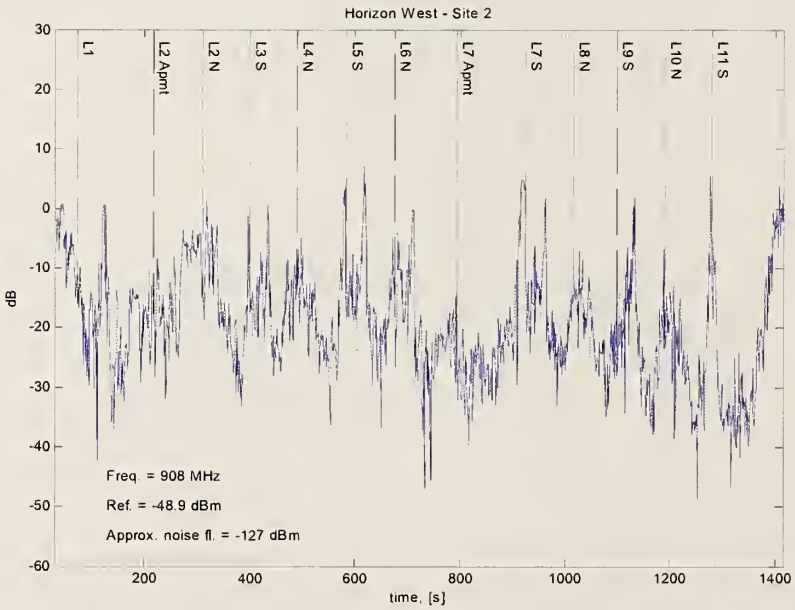

(b)

Figure A.4: Received-power data for the top 10 floors of an apartment building for a transmitter carrier frequency of 908 MHz, measured by a narrowband communications receiver. (a) Site 1. (b) Site 2. The received signal levels are referred to a line-of-sight reference signal, whose level is noted on each graph.

Single-Frequency Received-Power Data: 11-Story Apartment Building

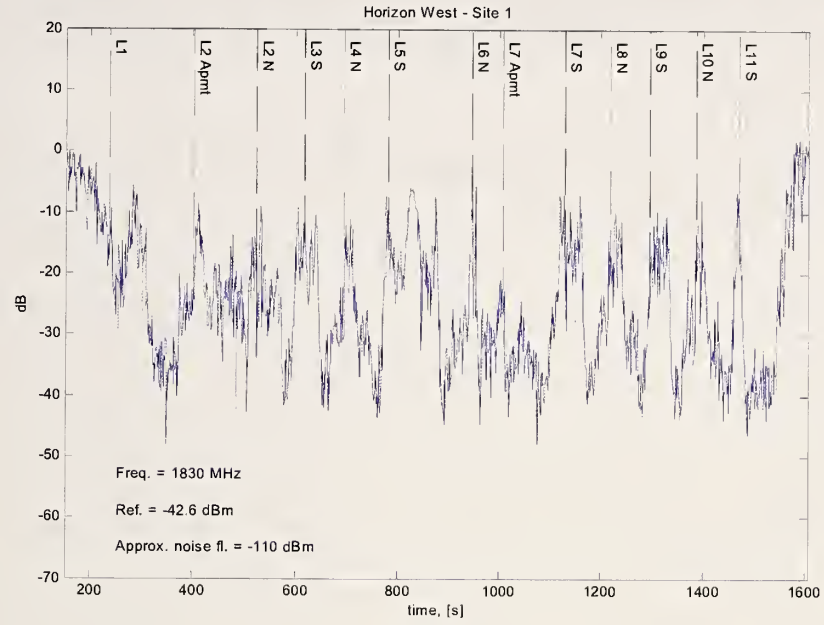

(a)

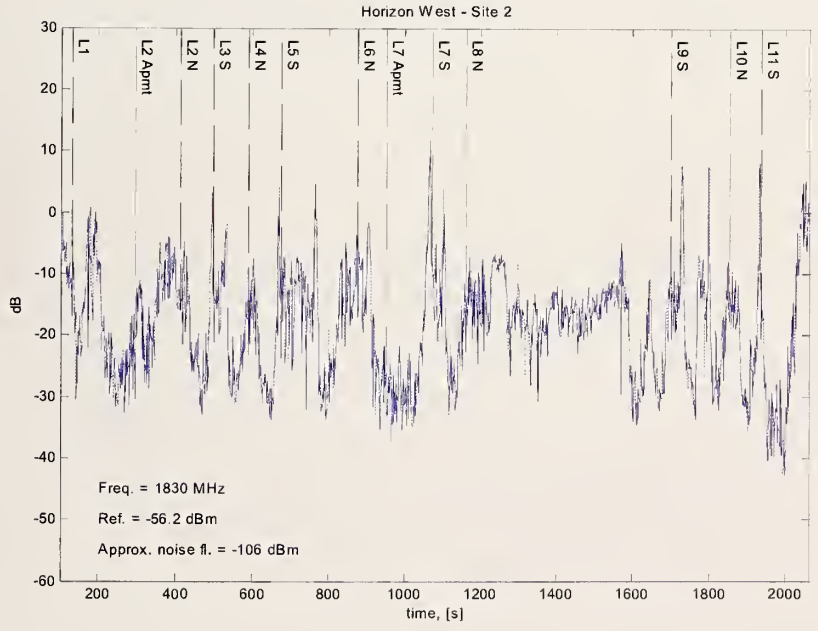

(b)

Figure A.5: Received-power data for the top 10 floors of an apartment building for a transmitter carrier frequency of 1830 MHz, measured by a narrowband communications receiver. (a) Site 1. (b) Site 2. The received signal levels are referred to a line-of-sight reference signal, whose level is noted on each graph.

Appendix B: Single-Frequency Received-Power Data Collected Using a Calibrated Communications Receiver: Office Corridor

The following pages contain the complete set of measured data for the office corridor (described in Section 4.2).

Single-Frequency Received-Power Data: Office Hallway Corridor

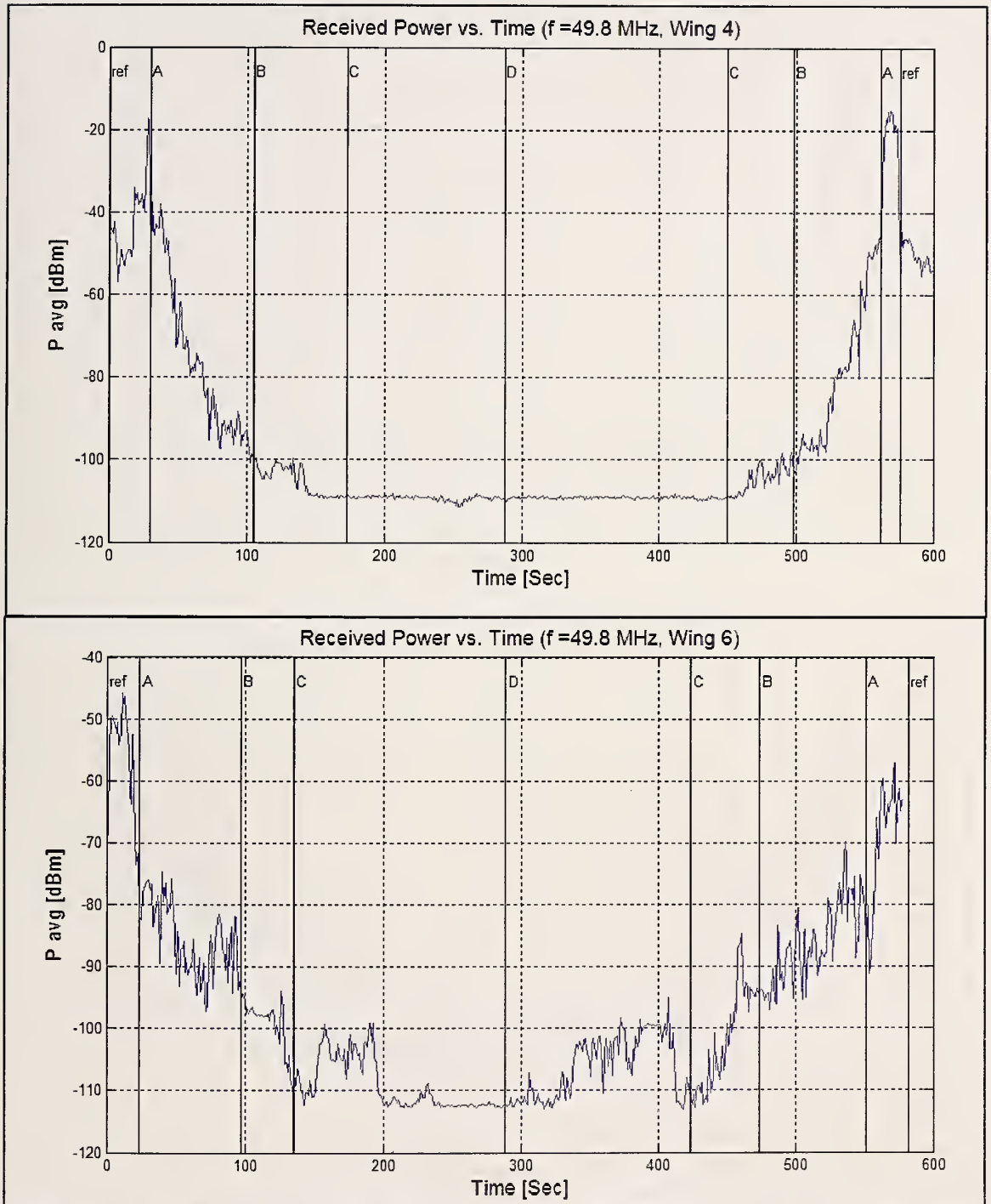

Figure B.1: Received-power data at a carrier frequency of 49.8 MHz. The transmitter was carried from A down a corridor to B, around a corner to C, continued along a third corridor to D and then was returned along the same path. **Top:** Indoor measurement, non-line-of-sight. **Bottom:** Measurement that includes building penetration.

Single-Frequency Received-Power Data: Office Hallway Corridor

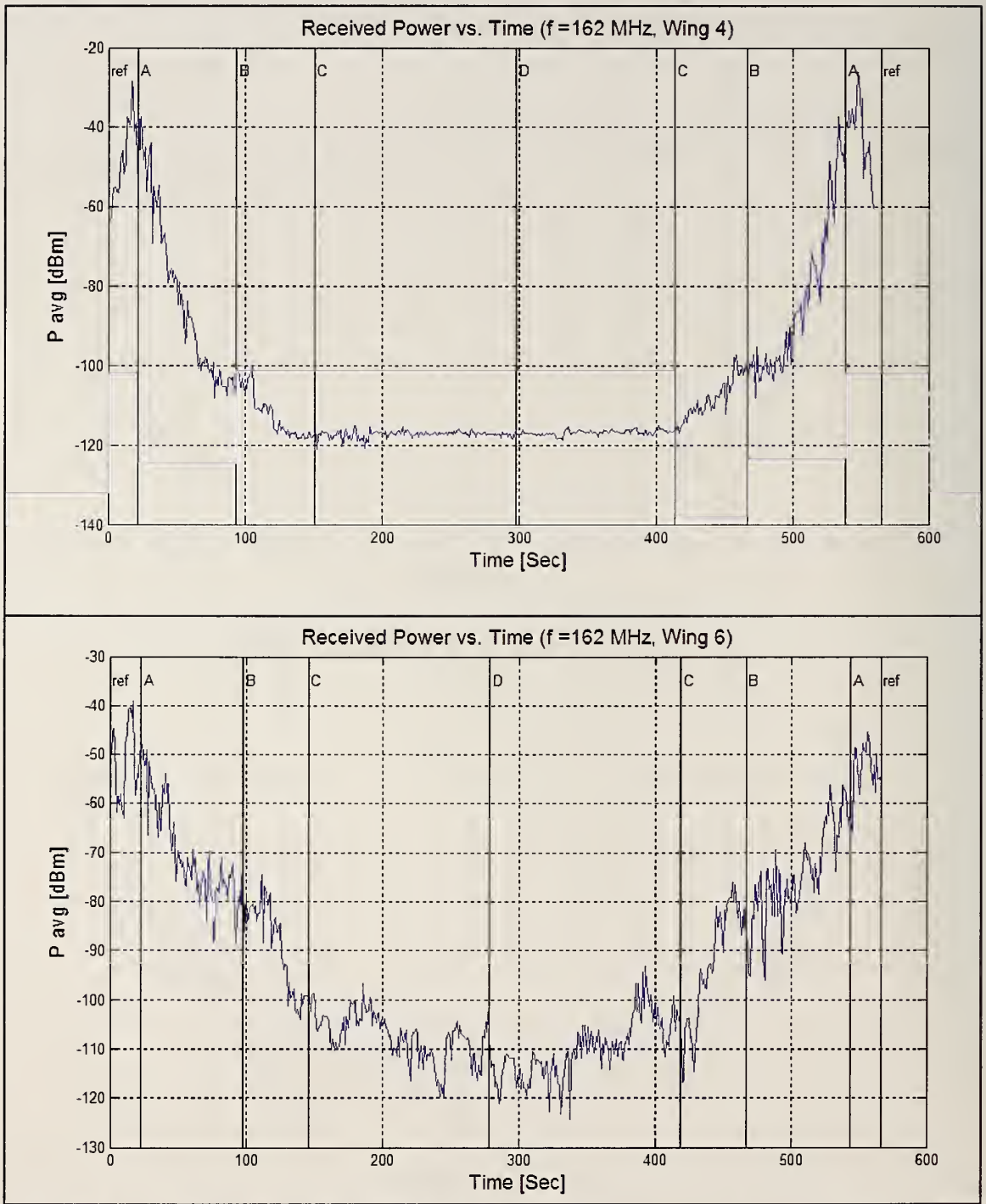

Figure B.2: Received-power data at a carrier frequency of 162.075 MHz. The transmitter was carried from A down a corridor to B, around a corner to C, continued along a third corridor to D and then was returned along the same path. Top: Indoor measurement, non-line-of-sight. Bottom: Measurement that includes building penetration.

Single-Frequency Received-Power Data: Office Hallway Corridor

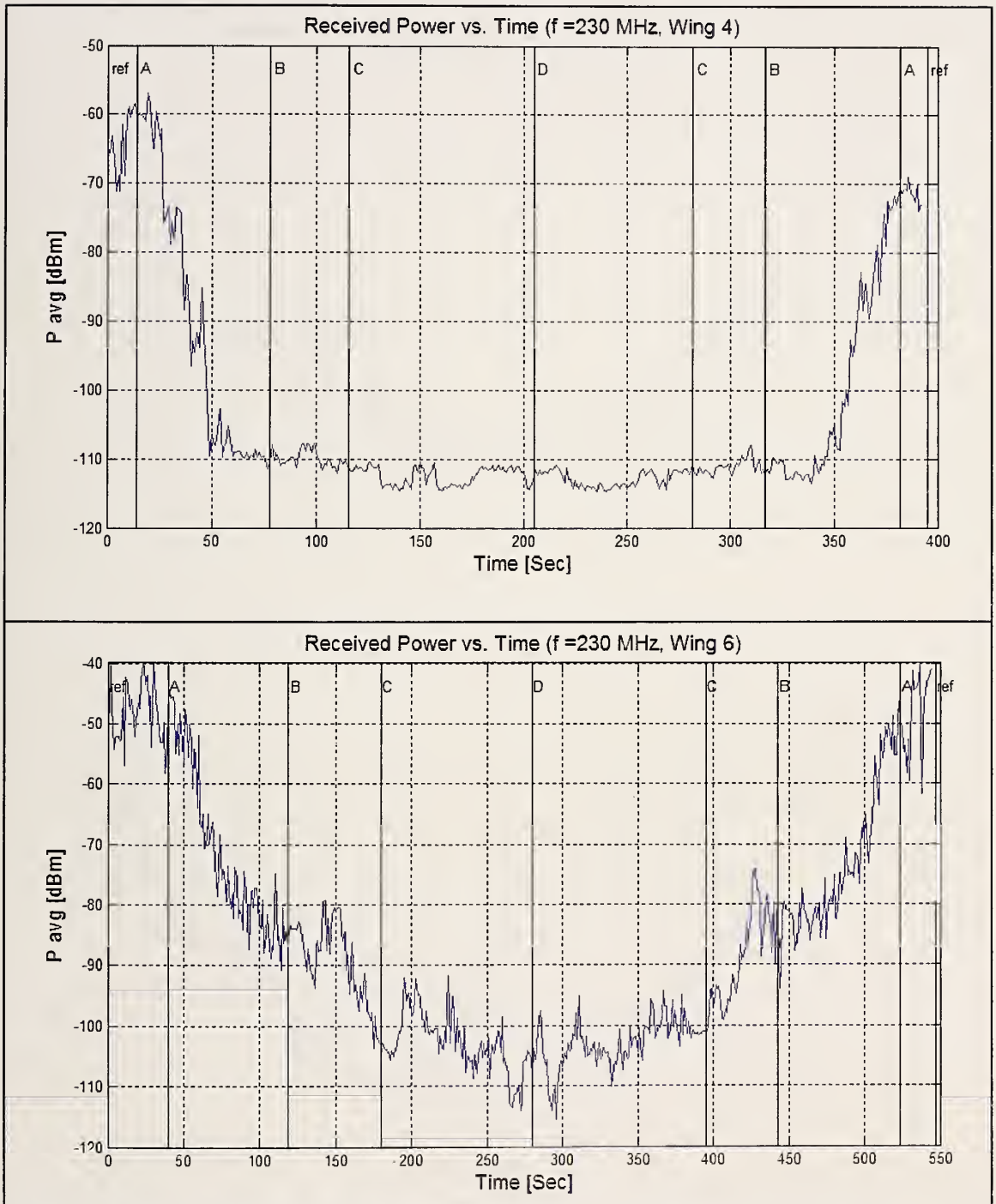

Figure B.3: Received-power data at a carrier frequency of 230.0 MHz. The transmitter was carried from A down a corridor to B, around a corner to C, continued along a third corridor to D and then was returned along the same path. Top: Indoor measurement, non-line-of-sight. Bottom: Measurement that includes building penetration.

Single-Frequency Received-Power Data: Office Hallway Corridor

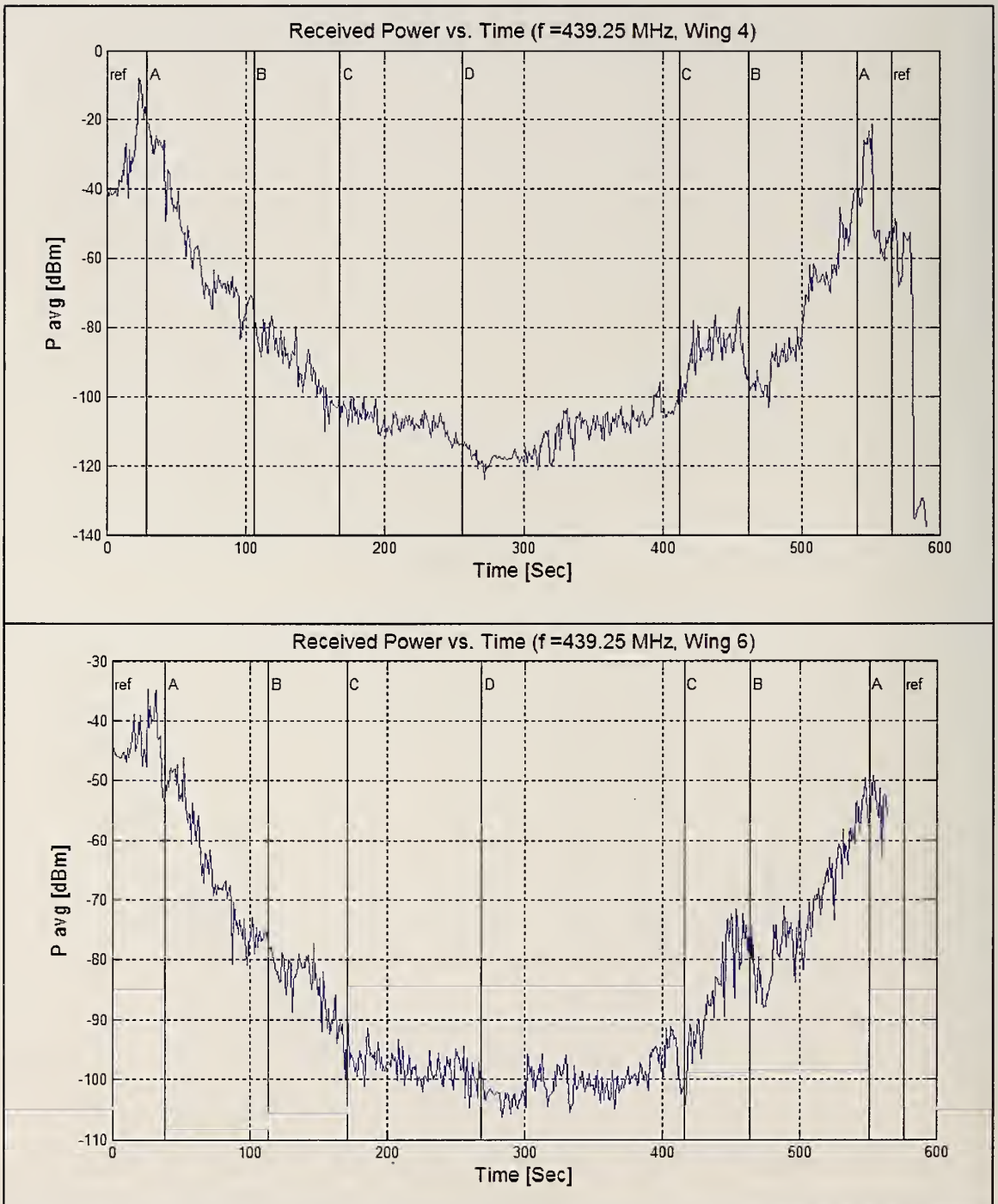

Figure B.4: Received-power data at a carrier frequency of 439.25 MHz. The transmitter was carried from A down a corridor to B, around a corner to C, continued along a third corridor to D and then was returned along the same path. Top: Indoor measurement, non-line-of-sight. Bottom: Measurement that includes building penetration.

Single-Frequency Received-Power Data: Office Hallway Corridor

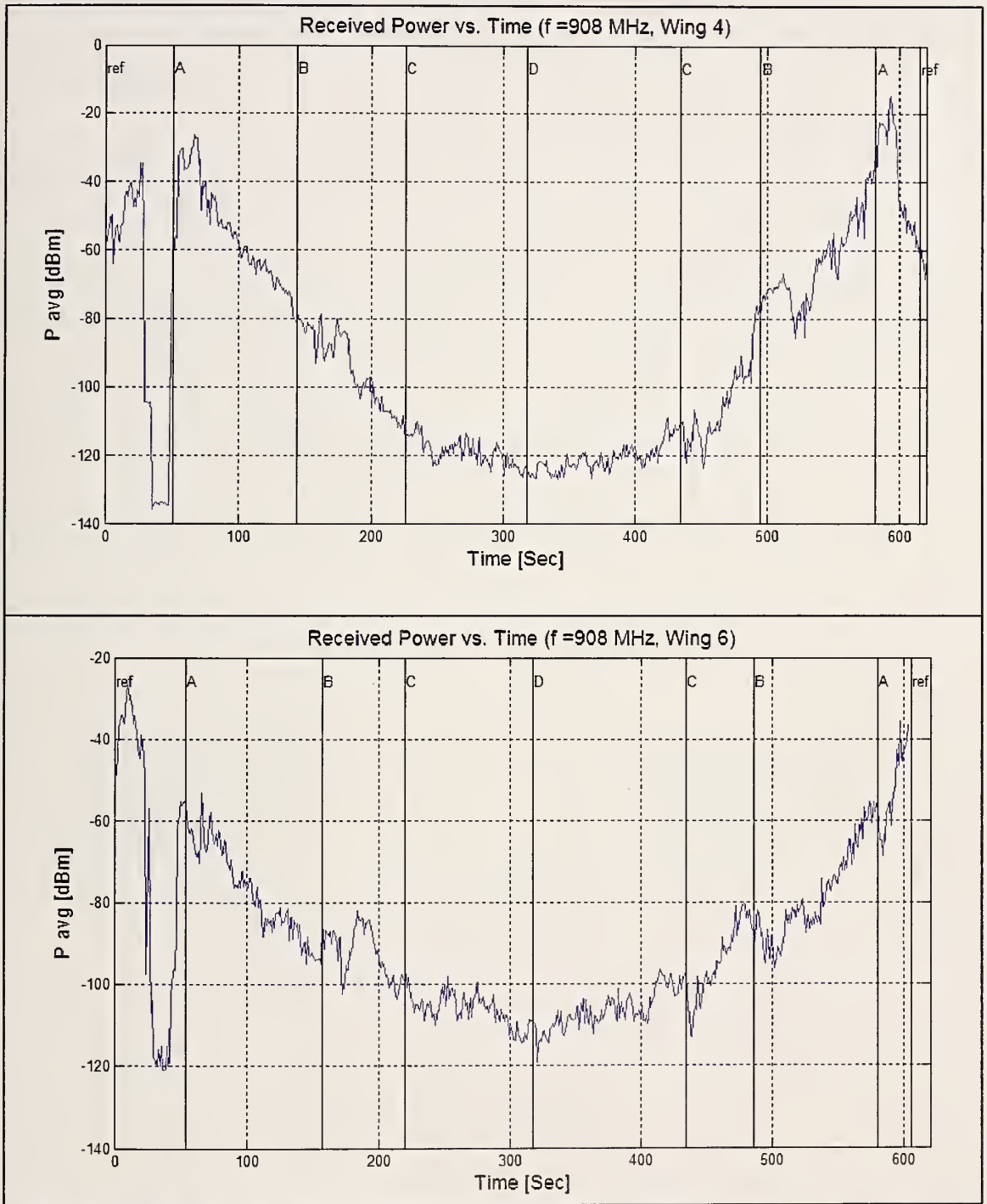

Figure B.5: Received-power data at a carrier frequency of 908.0 MHz. The transmitter was carried from A down a corridor to B, around a corner to C, continued along a third corridor to D and then was returned along the same path. Top: Indoor measurement, non-line-of-sight. Bottom: Measurement that includes building penetration.

Single-Frequency Received-Power Data: Office Hallway Corridor

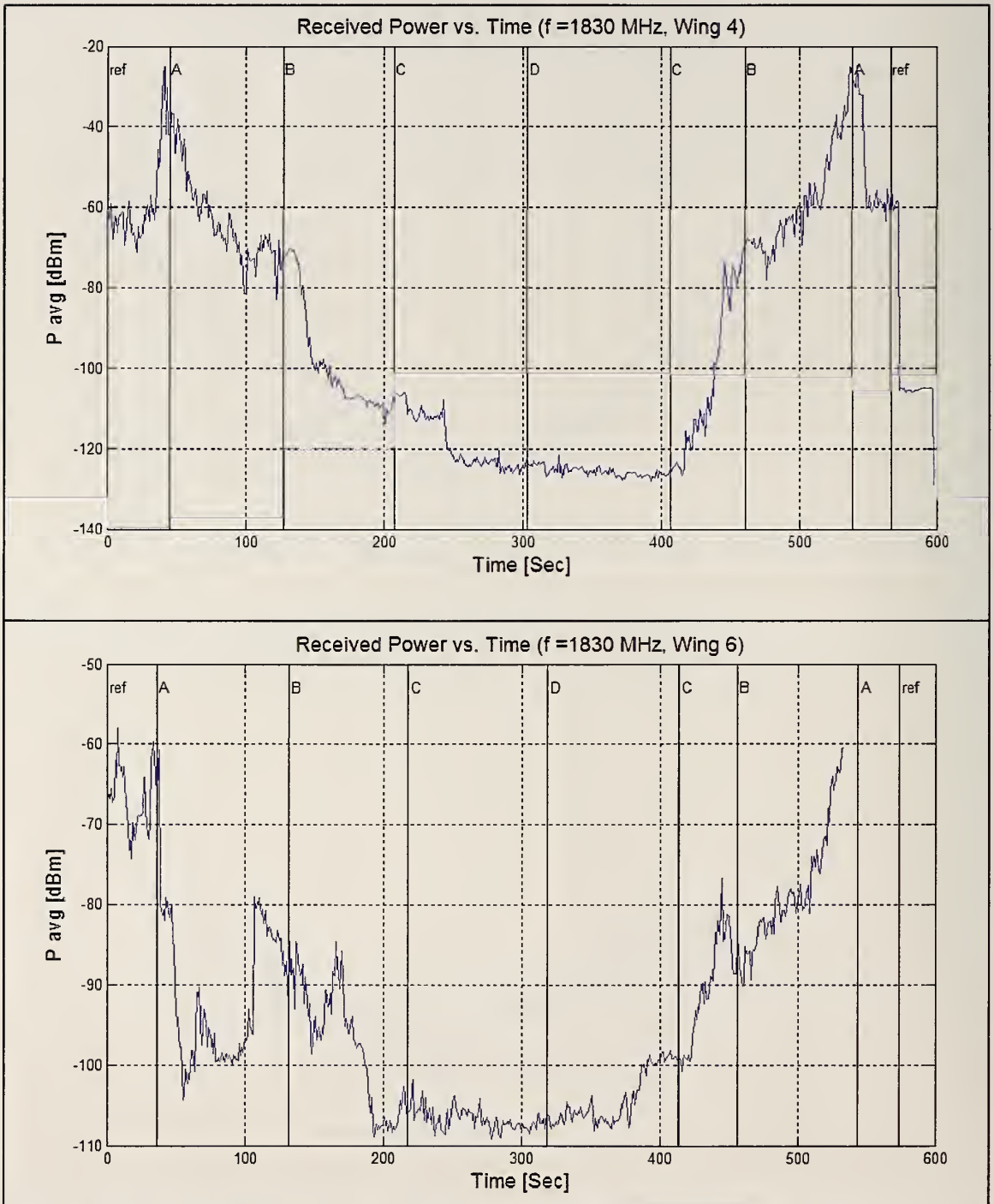

Figure B.6: Received-power data at a carrier frequency of 1830 MHz. The transmitter was carried from A down a corridor to B, around a corner to C, continued along a third corridor to D and then was returned along the same path. Top: Indoor measurement, non-line-of-sight. Bottom: Measurement that includes building penetration.

Appendix C: Single-Frequency Received-Power Data Collected Using a Calibrated Communications Receiver: Oil Refinery

The following pages contain the complete set of measured data for the oil refinery (described in Section 5.2).

Single-Frequency Received-Power Data: Oil Refinery

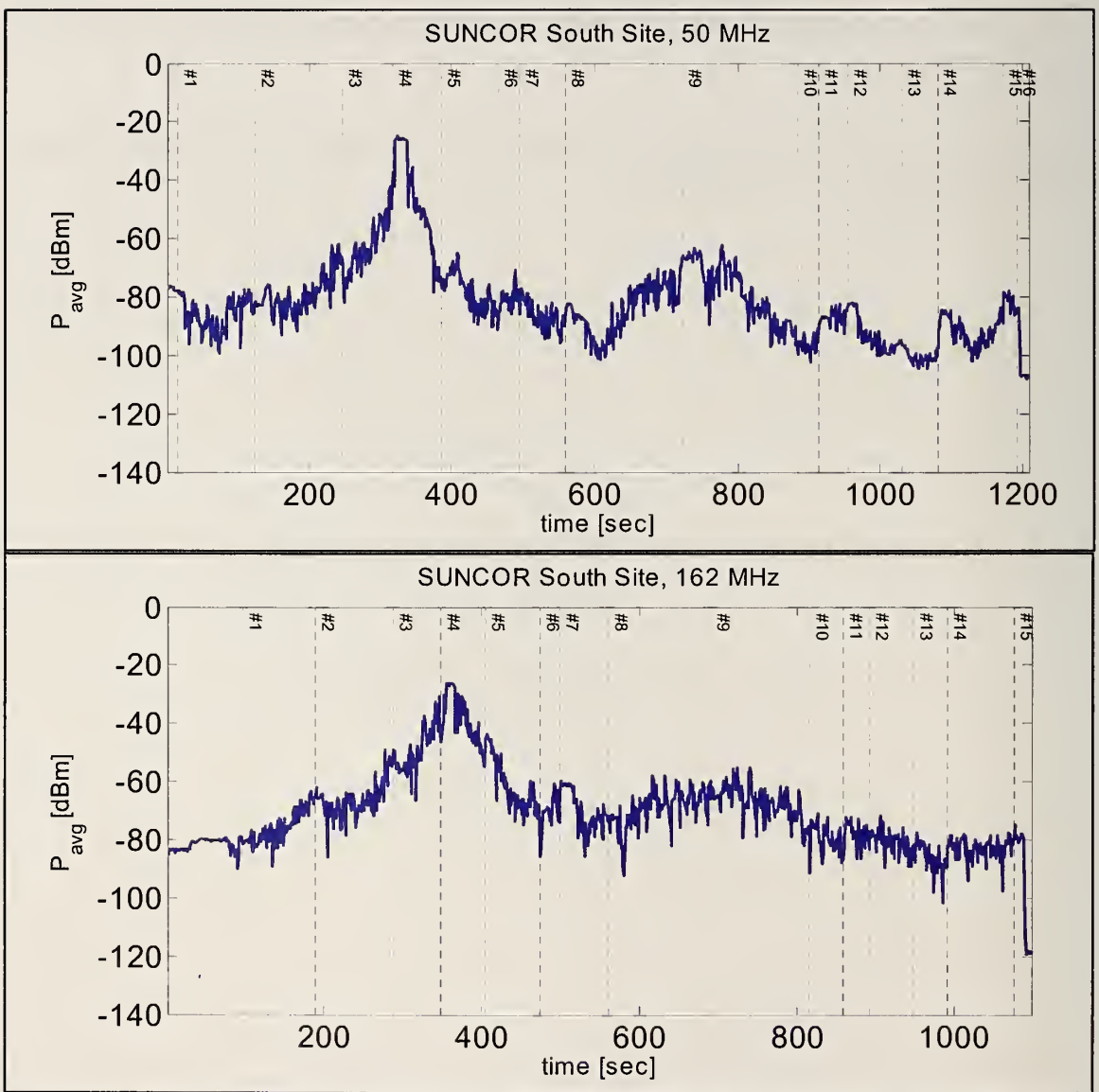

Figure C.1: Received-power data for carrier frequencies of 49 MHz (top) and 162 MHz (bottom). The path, winding through the oil refinery complex, is shown in Figure 5.2-1.

Single-Frequency Received-Power Data: Oil Refinery

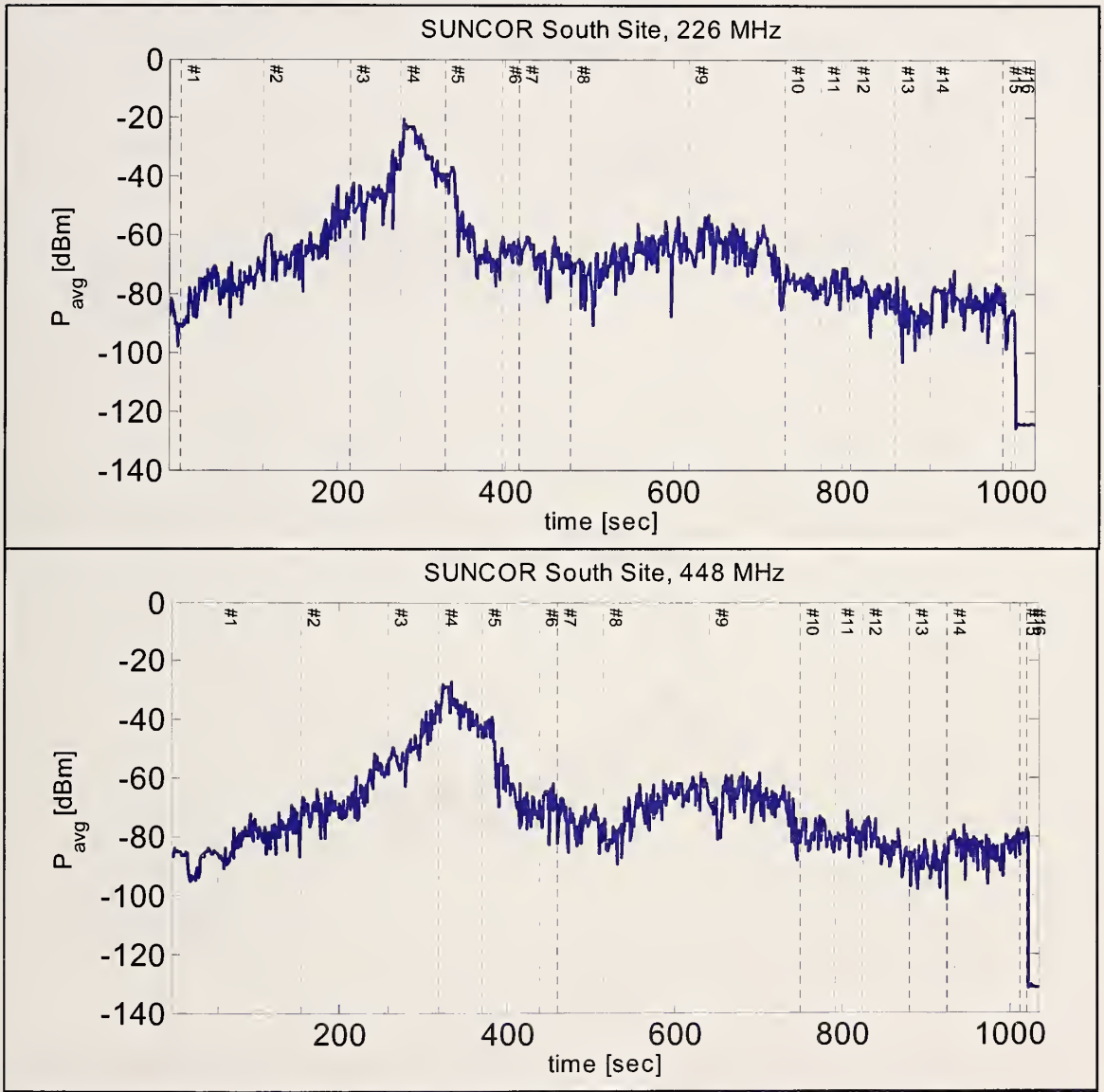

Figure C.2: Received-power data for carrier frequencies of 226 MHz (top) and 448 MHz (bottom). The path, winding through the oil refinery complex, is shown in Figure 5.2-1.

Single-Frequency Received-Power Data: Oil Refinery

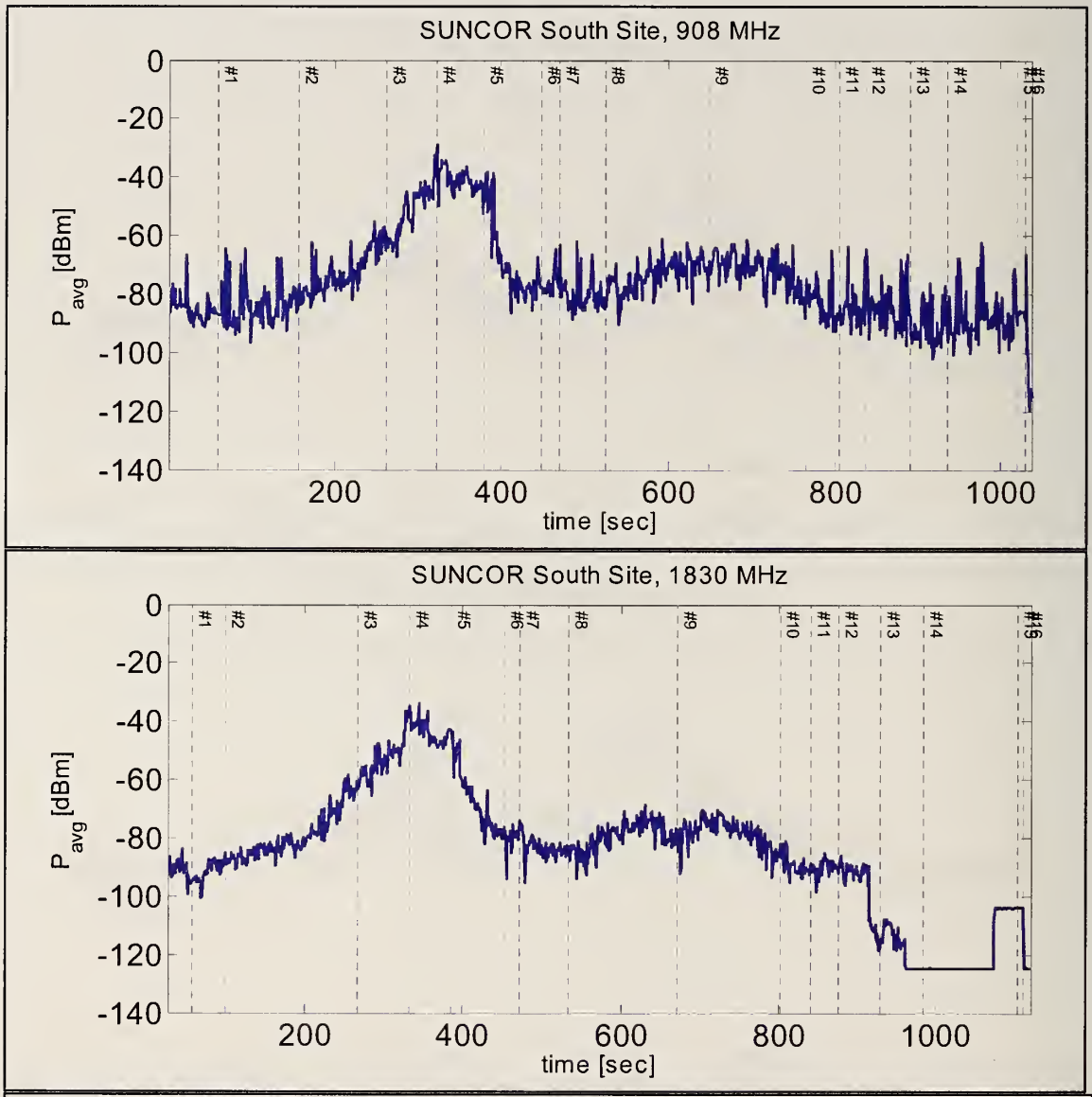

Figure C.3: Received-power data for carrier frequencies of 908 MHz (top) and 1830 MHz (bottom). The path, winding through the oil refinery complex, is shown in Figure 5.2-1.

Single-Frequency Received-Power Data: Oil Refinery

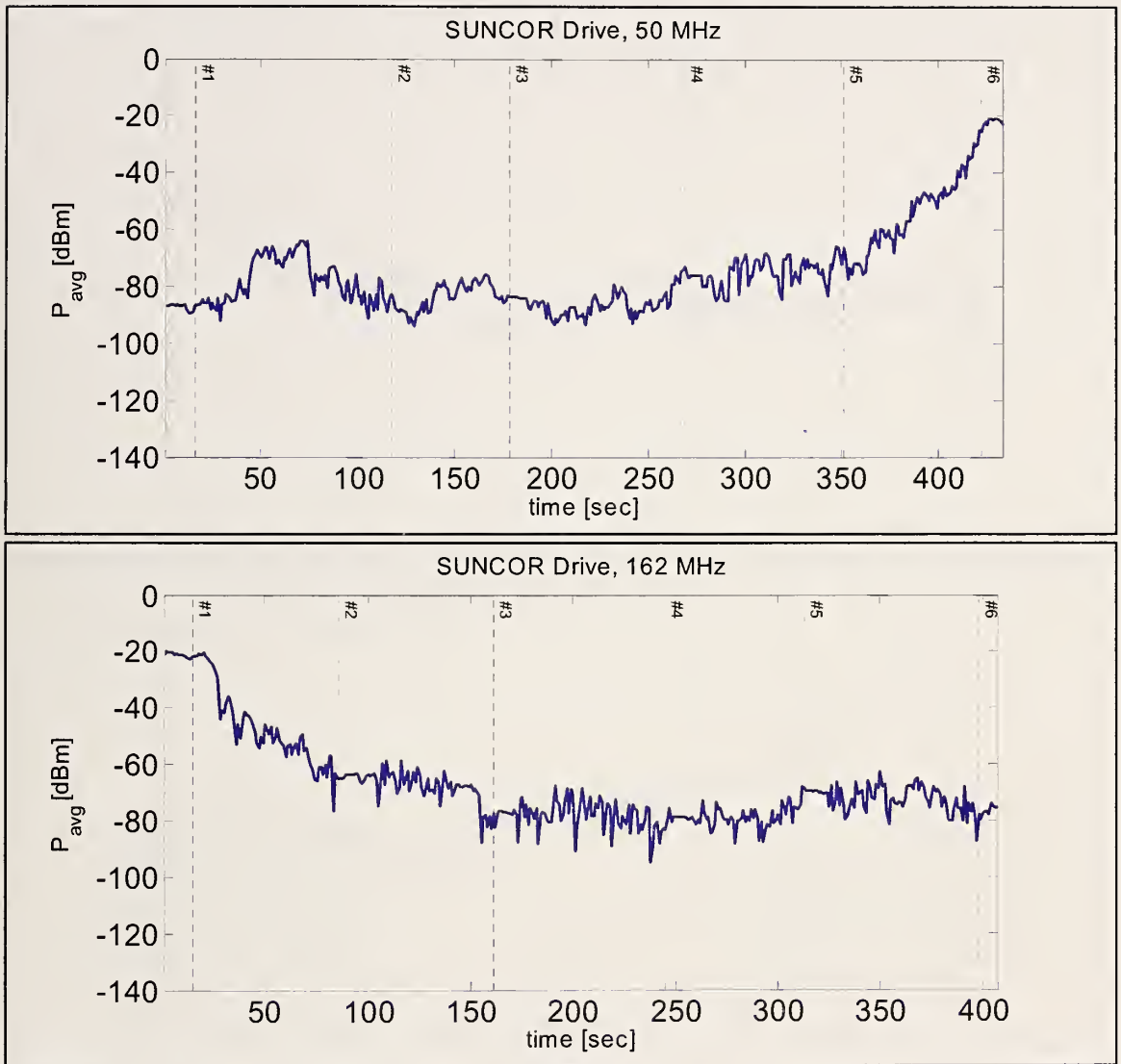

Figure C.4: Received-power data for carrier frequencies of 49 MHz (top) and 162 MHz (bottom). The path covered a drive around the perimeter of the refinery. The top figure was in one direction and the bottom figure was in the opposite direction.

Single-Frequency Received-Power Data: Oil Refinery

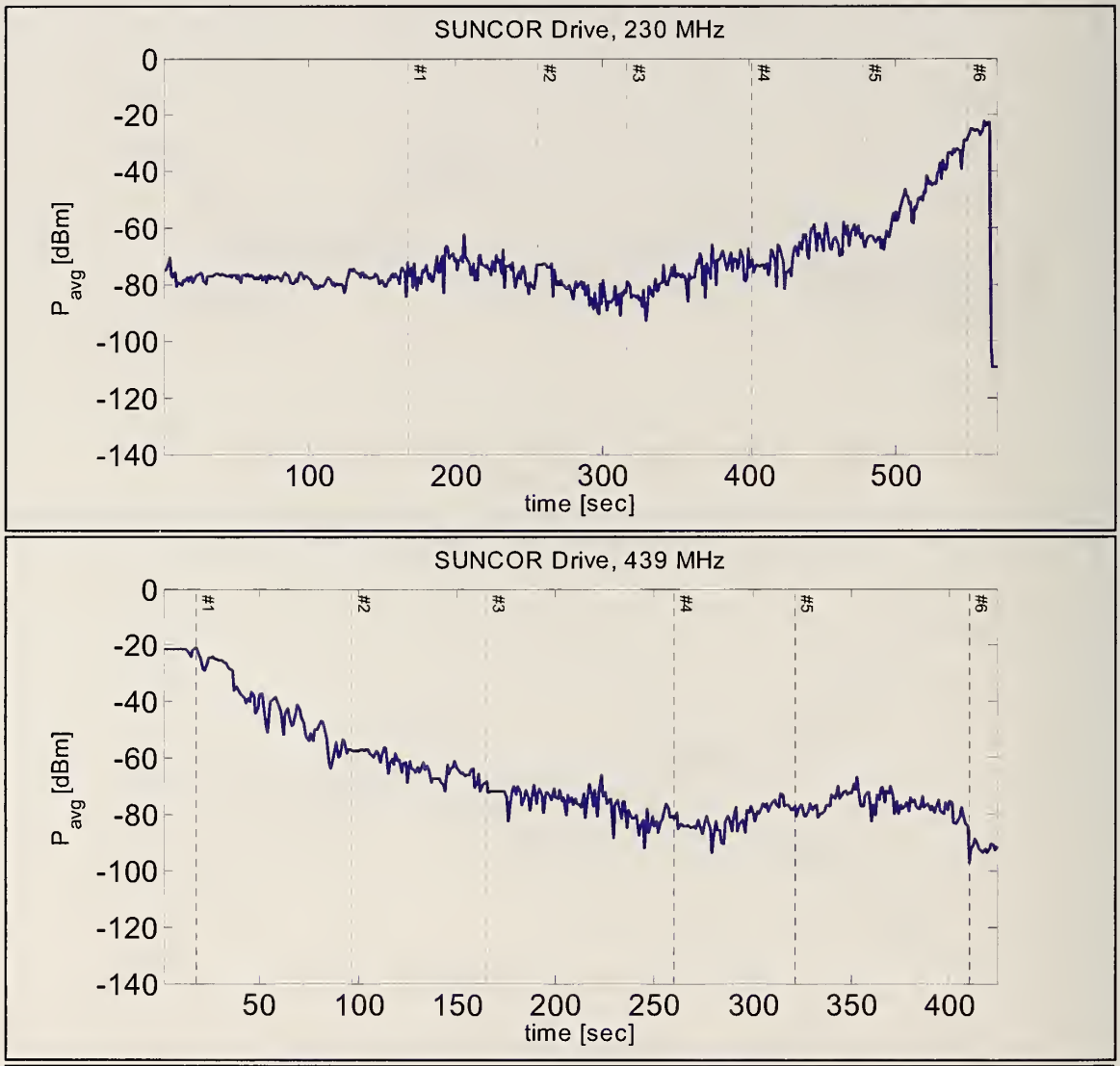

Figure C.5: Received-power data for carrier frequencies of 230 MHz (top) and 439 MHz (bottom). The path covered a drive around the perimeter of the refinery. The top figure was in one direction and the bottom figure was in the opposite direction.

Single-Frequency Received-Power Data: Oil Refinery

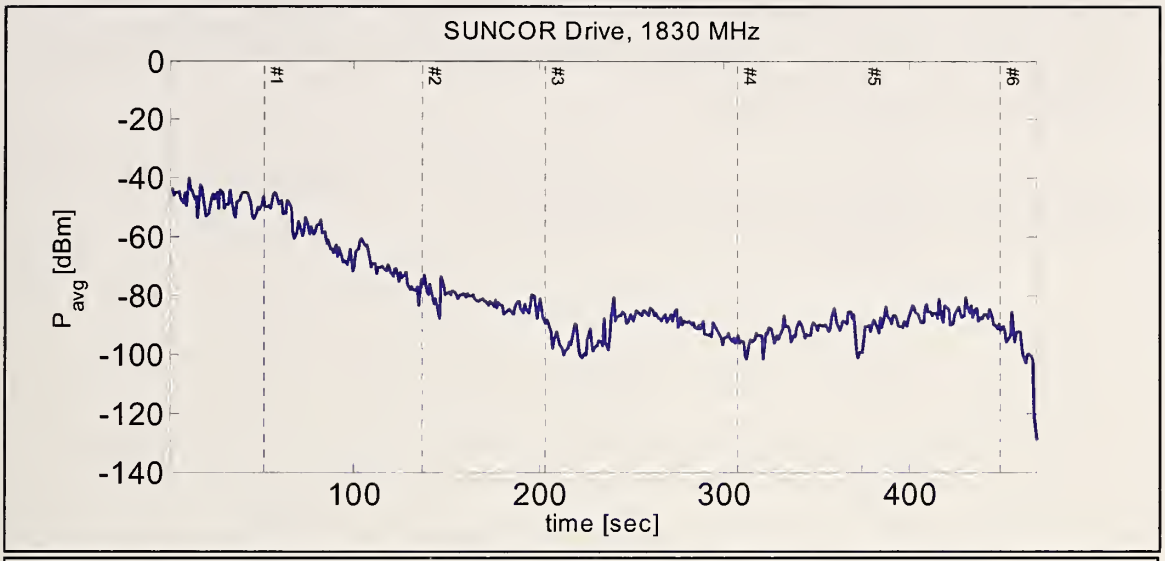

Figure C.6: Received-power data for a carrier frequency of 1830 MHz. The path covered a drive around the perimeter of the refinery. The 900 MHz data was corrupted and is not reported here.

Appendix D: Single-Frequency Received-Power Data Collected Using a Calibrated Communications Receiver: Subterranean Tunnels

The following pages contain the complete set of measured data for the subterranean tunnels (described in Section 6.2).

Single-Frequency Received-Power Data: Subterranean Tunnels

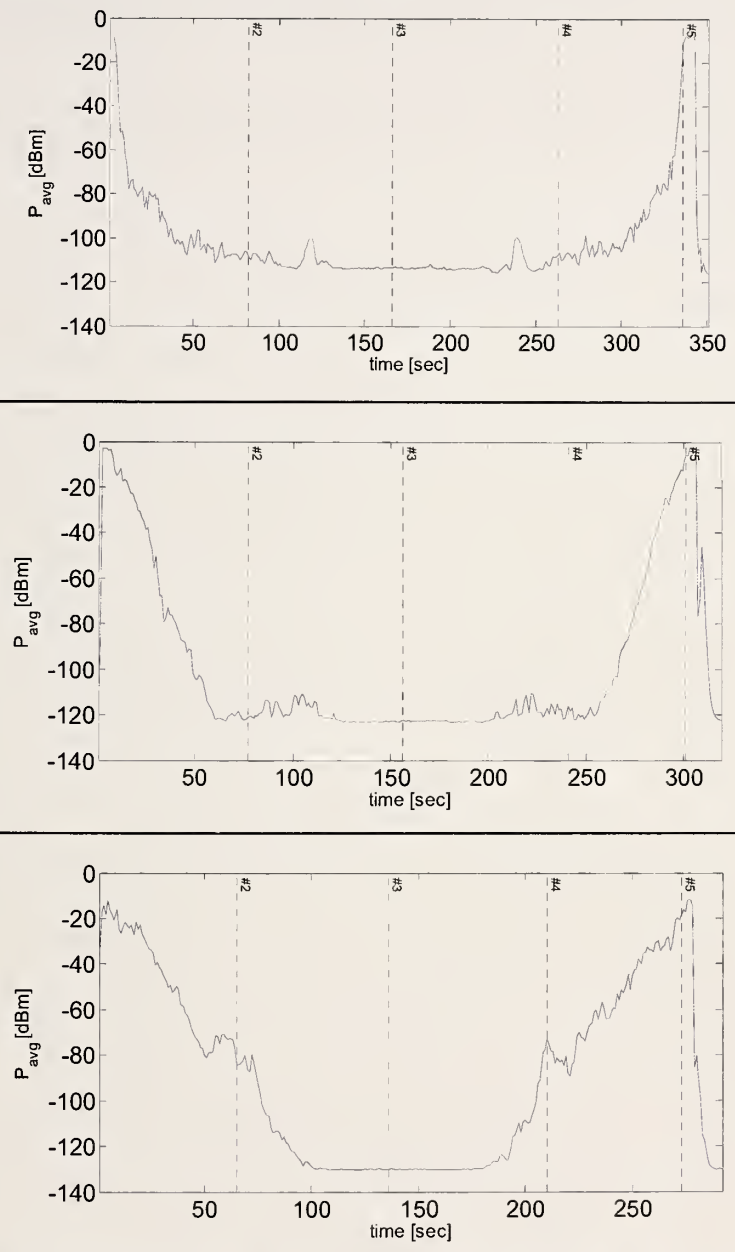

Figure D.1: Received-power data in the Hazel-Atlas mine for three carrier frequencies: Top: 50 MHz. Middle: 162 MHz. Bottom: 448 MHz. The transmitters were carried into the tunnel and then back out, so the left and right halves of the graphs are mirror images. In each case the first and third vertical dashed lines correspond to the turn at 100 m, and the second dashed line represents the end point at 200 m.

Single-Frequency Received-Power Data: Subterranean Tunnels

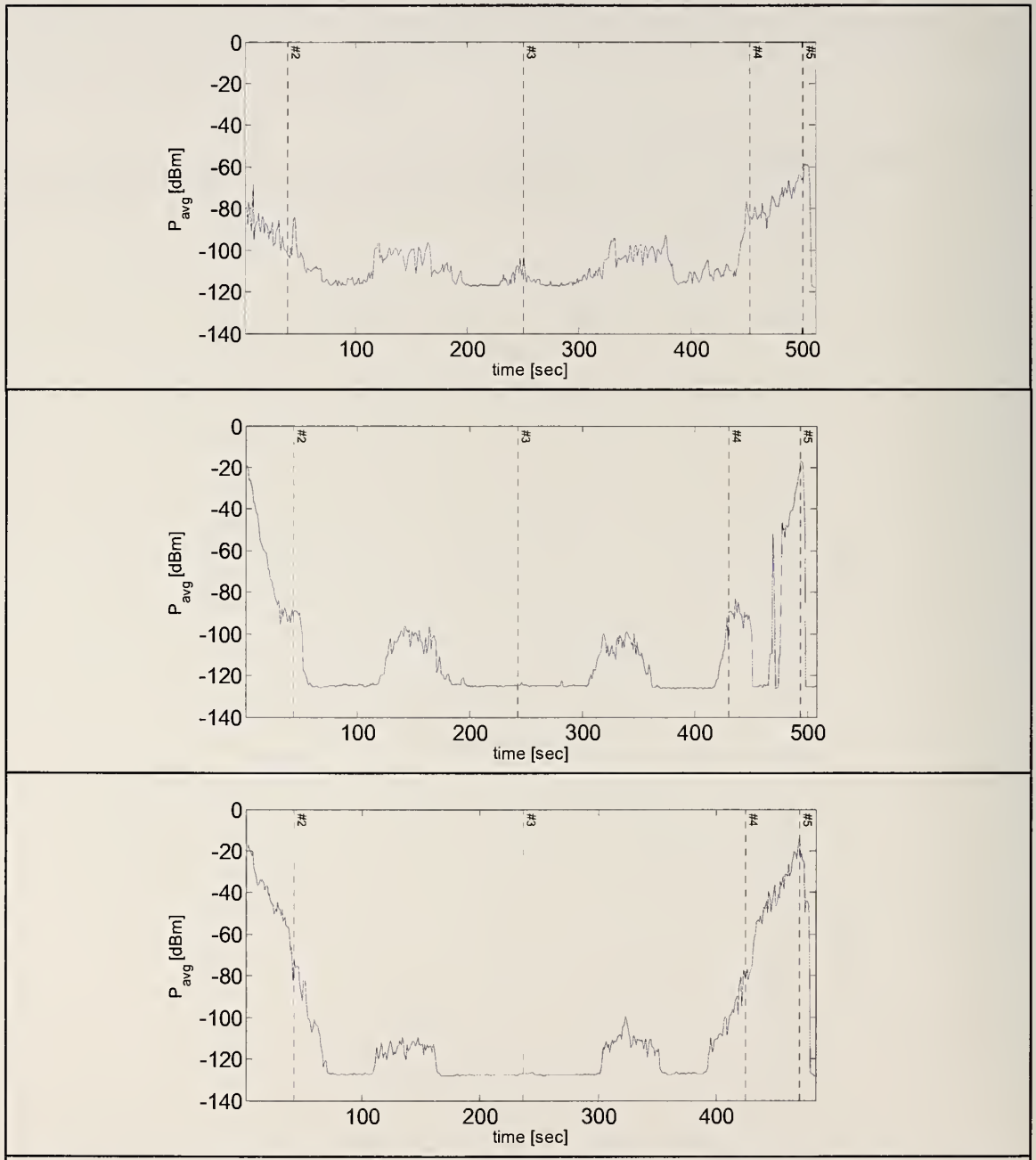

Figure D.2: Received-power data in the Greathouse mine for three carrier frequencies: Top: 50 MHz. Middle: 162 MHz. Bottom: 448 MHz. The transmitters were carried into the tunnel and then back out, so the left and right halves of the graphs are mirror images. In each case the first and third vertical dashed lines correspond to the turn at 100 m, and the second dashed line represents the end point shown in Figure 6.2-1(b).

Appendix E: Wideband Excess Path Loss Measured With a Synthetic-Pulse Vector-Network-Analyzer-Based System: Apartment Building

The following pages contain the complete set of measured data for the apartment building (described in Section 3.3).

Wideband Excess Path Loss: Apartment Building

Layout of apartment building and positions where synthetic pulse measurements were made.

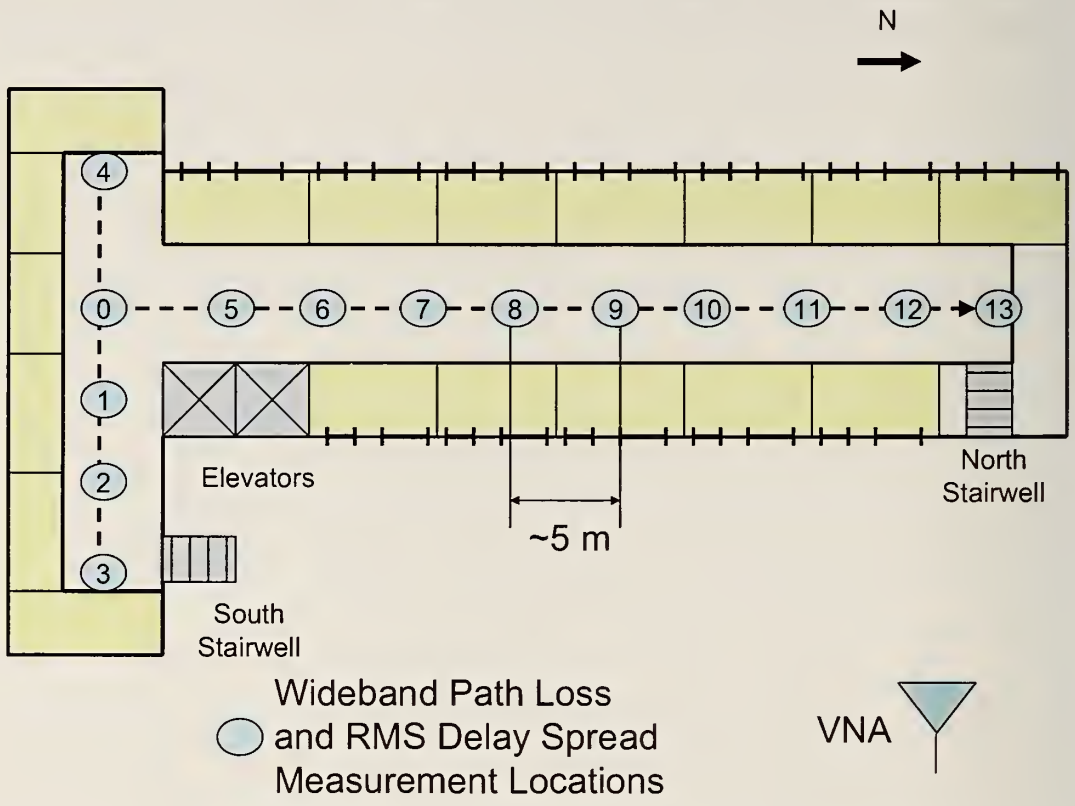

Wideband Excess Path Loss: Apartment Building

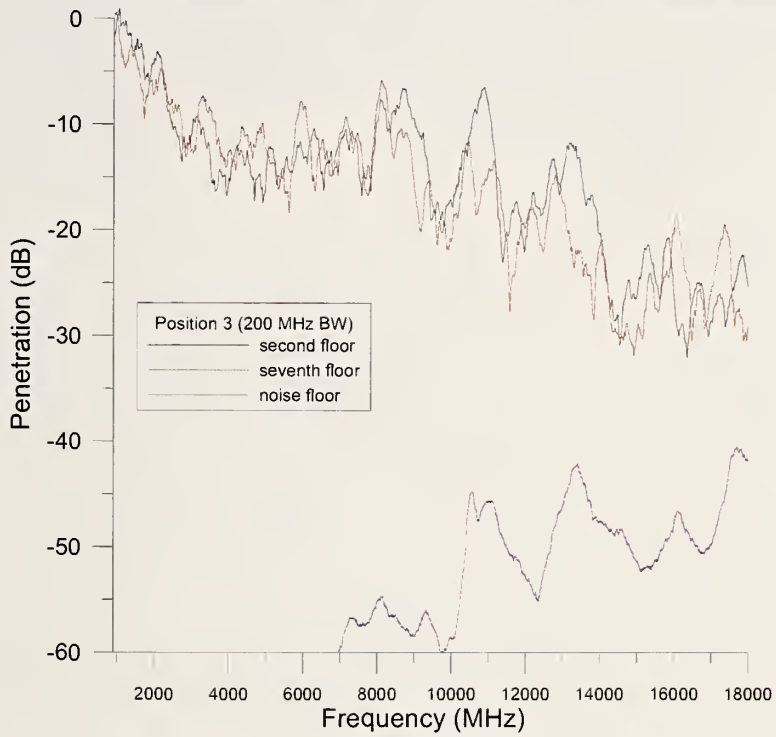

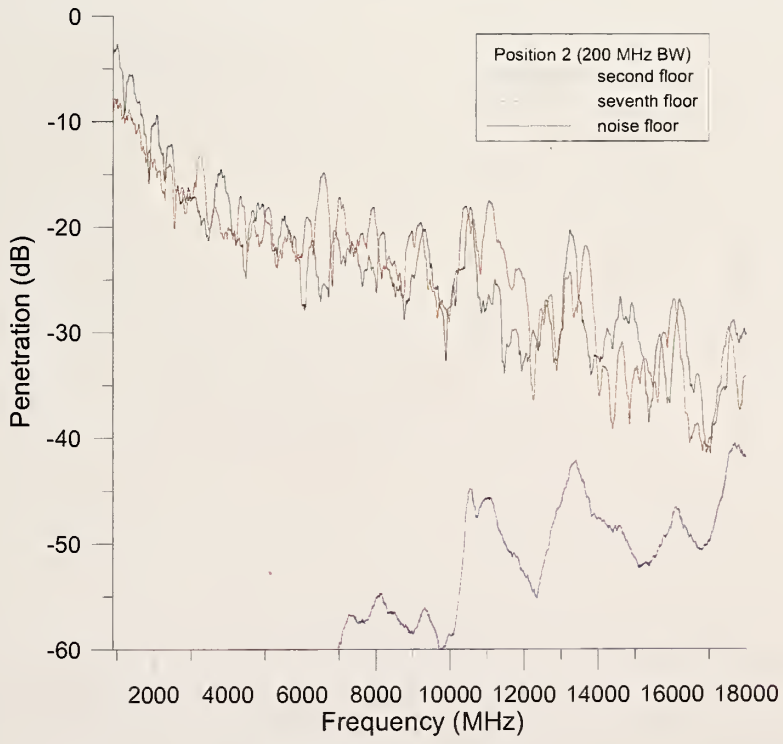

Figure E.1: Excess path loss from 1 GHz to 18 GHz in an 11-story apartment building at locations 3 and 2 on the second (black) and seventh (red) floors. The blue line at the lower part of the graph represents the noise floor.

Wideband Excess Path Loss: Apartment Building

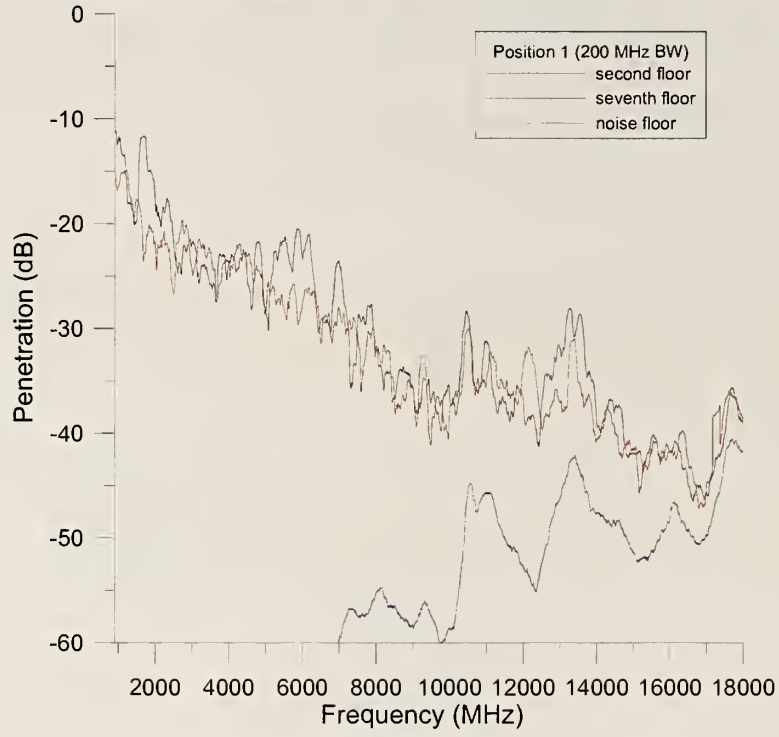

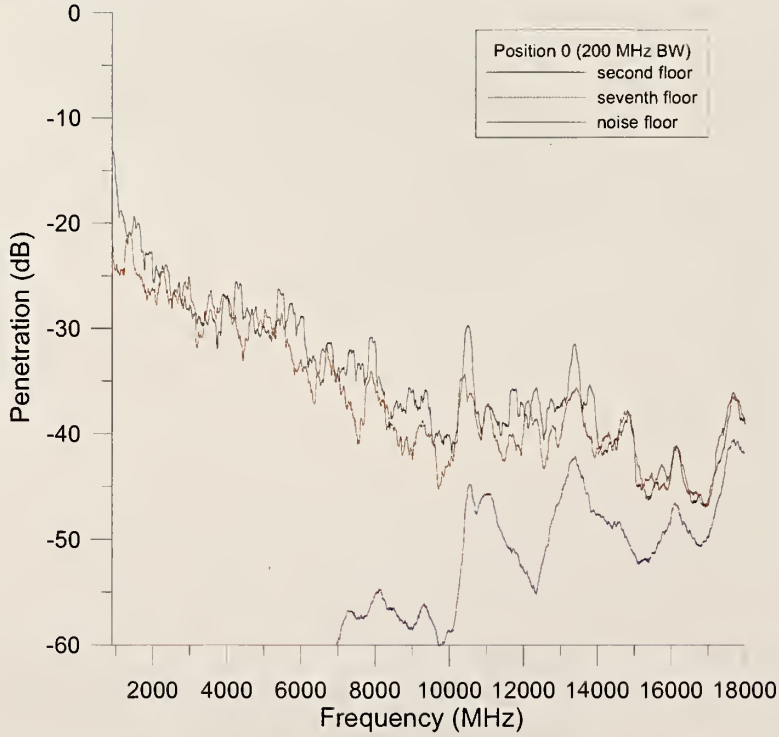

Figure E.2: Excess path loss from 1 GHz to 18 GHz in an 11-story apartment building at locations 1 and 0 on the second (black) and seventh (red) floors. The blue line at the lower part of the graph represents the noise floor.

Wideband Excess Path Loss: Apartment Building

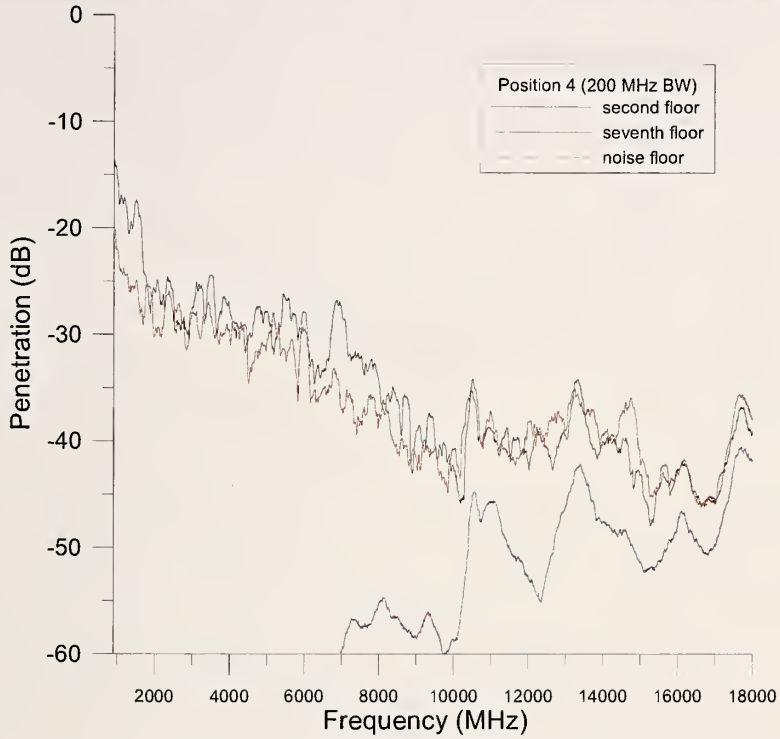

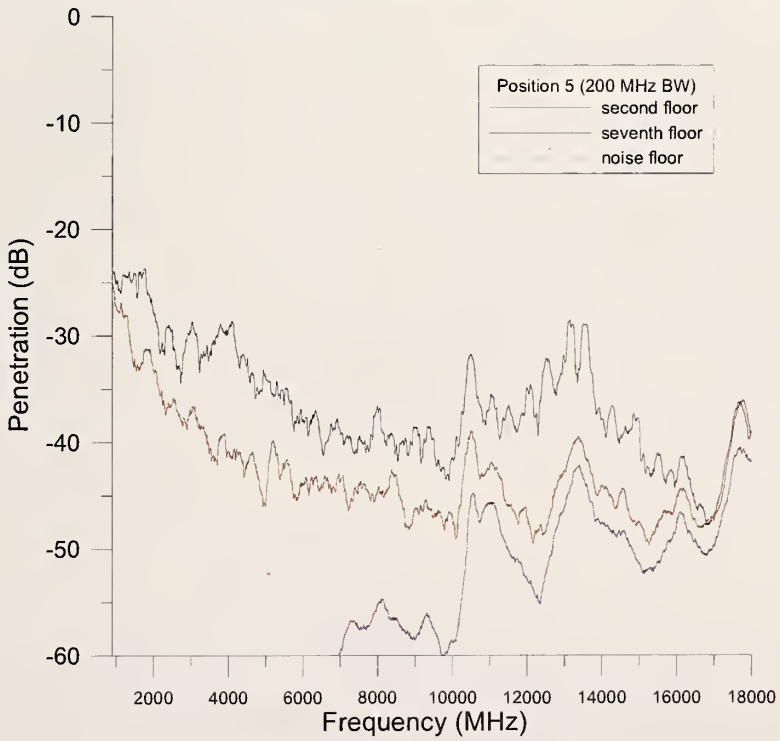

Figure E.3: Excess path loss from 1 GHz to 18 GHz in an 11-story apartment building at locations 4 and 5 on the second (black) and seventh (red) floors. The blue line at the lower part of the graph represents the noise floor.

Wideband Excess Path Loss: Apartment Building

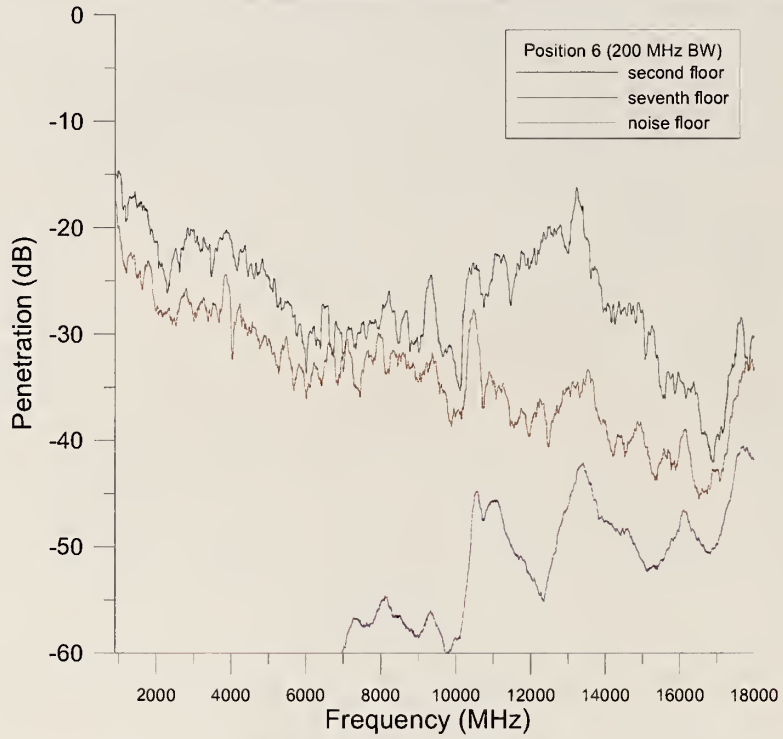

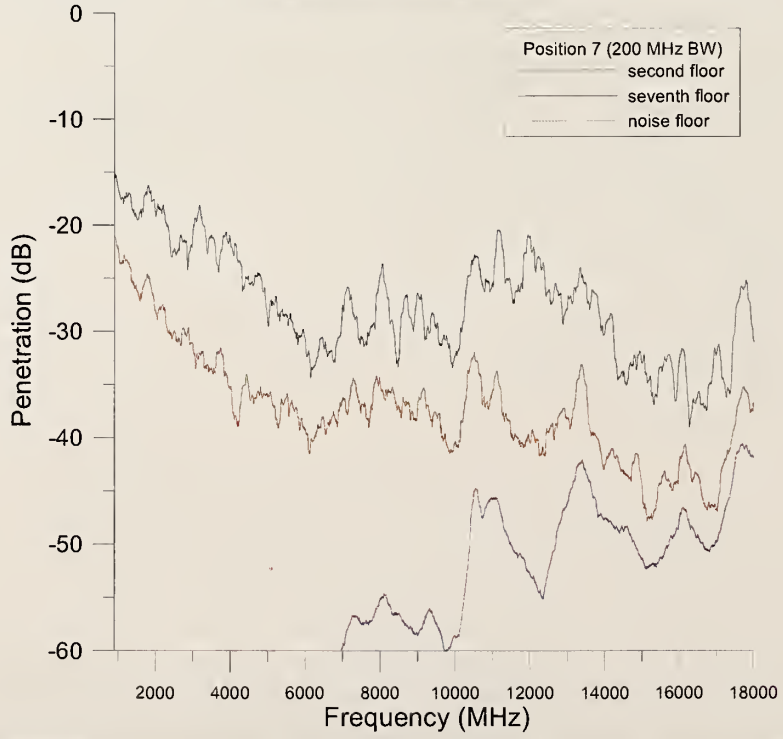

Figure E.4: Excess path loss from 1 GHz to 18 GHz in an 11-story apartment building at locations 6 and 7 on the second (black) and seventh (red) floors. The blue line at the lower part of the graph represents the noise floor.

Wideband Excess Path Loss: Apartment Building

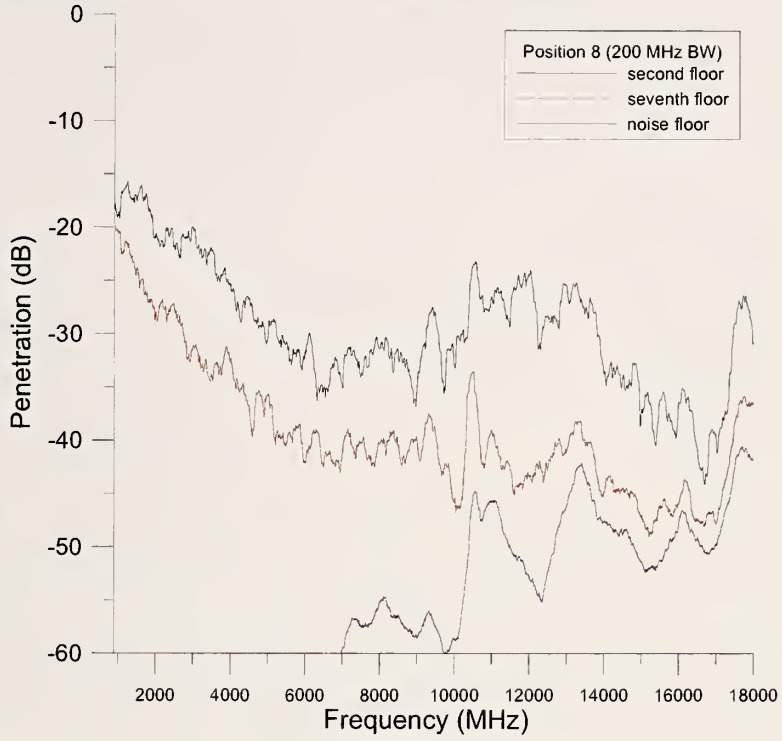

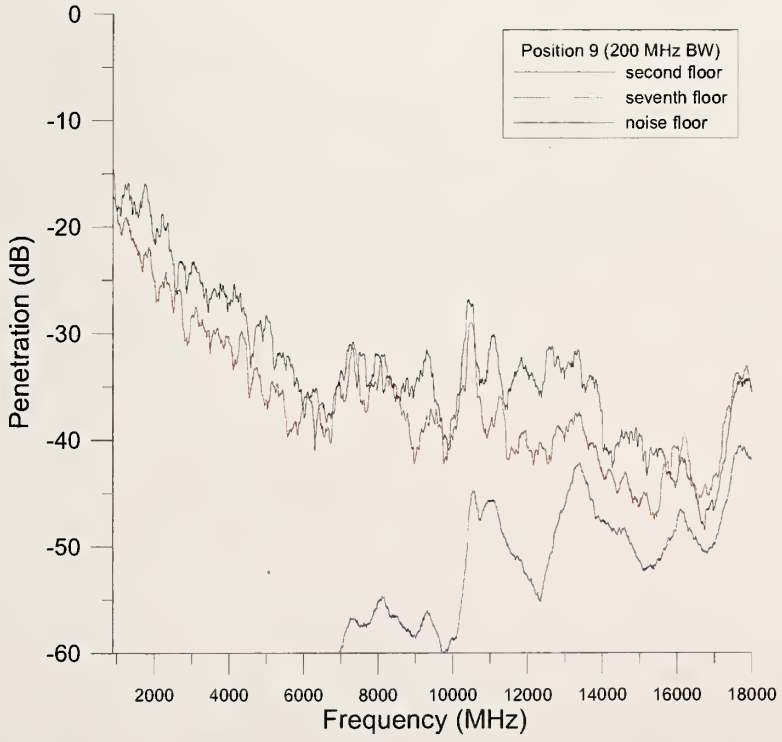

Figure E.5: Excess path loss from 1 GHz to 18 GHz in an 11-story apartment building at locations 8 and 9 on the second (black) and seventh (red) floors. The blue line at the lower part of the graph represents the noise floor.

Wideband Excess Path Loss: Apartment Building

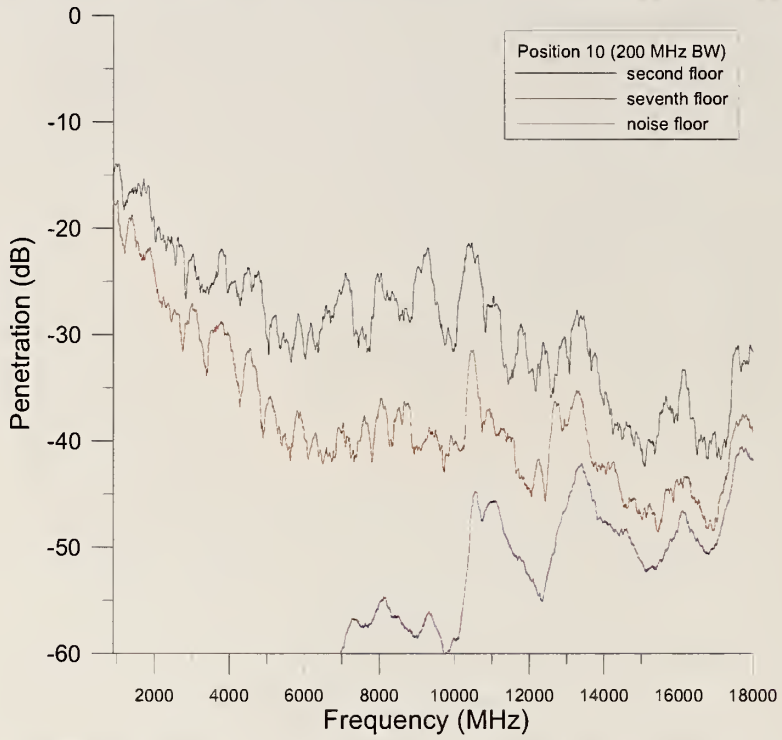

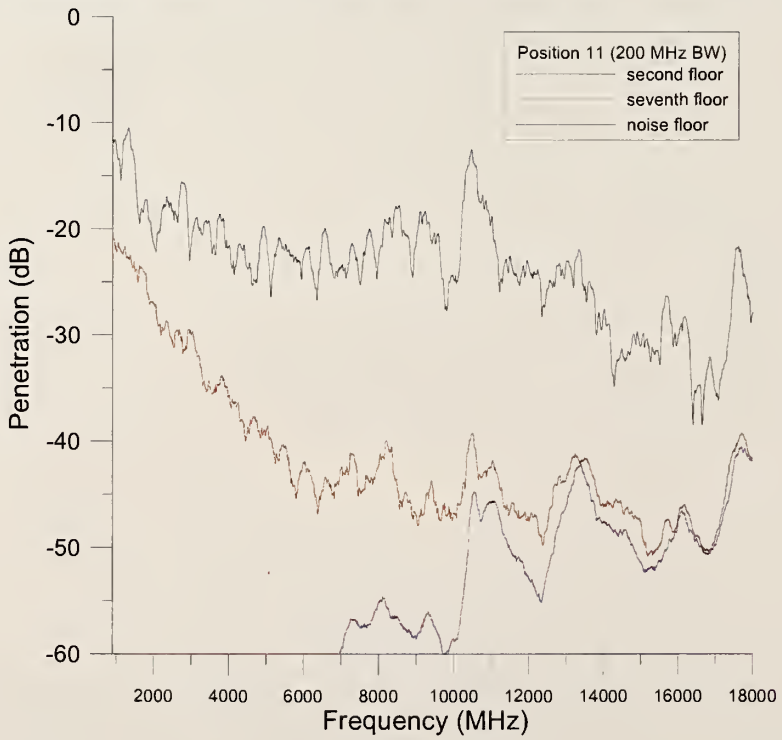

Figure E.6: Excess path loss from 1 GHz to 18 GHz in an 11-story apartment building at locations 10 and 11 on the second (black) and seventh (red) floors. The blue line at the lower part of the graph represents the noise floor.

Wideband Excess Path Loss: Apartment Building

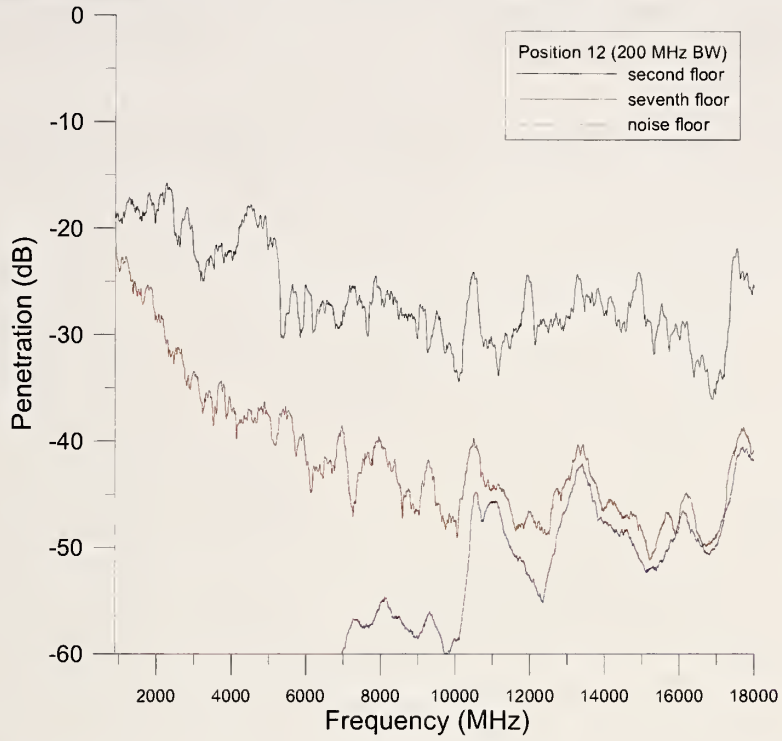

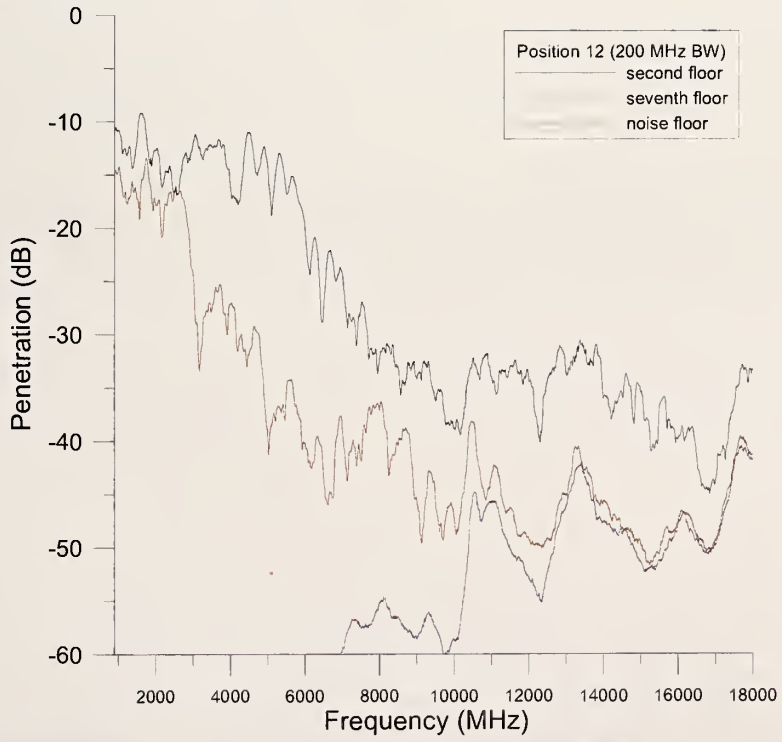

Figure E.7: Excess path loss from 1 GHz to 18 GHz in an 11-story apartment building at locations 12 and 13 on the second (black) and seventh (red) floors. The blue line at the lower part of the graph represents the noise floor.

Appendix F: Wideband Excess Path Loss Measured With a Synthetic-Pulse Vector-Network-Analyzer-Based System: Office Corridor

The following pages contain the complete set of measured data for the office corridor (Section 4.3).

Wideband Excess Path Loss: Office Hallway Corridor

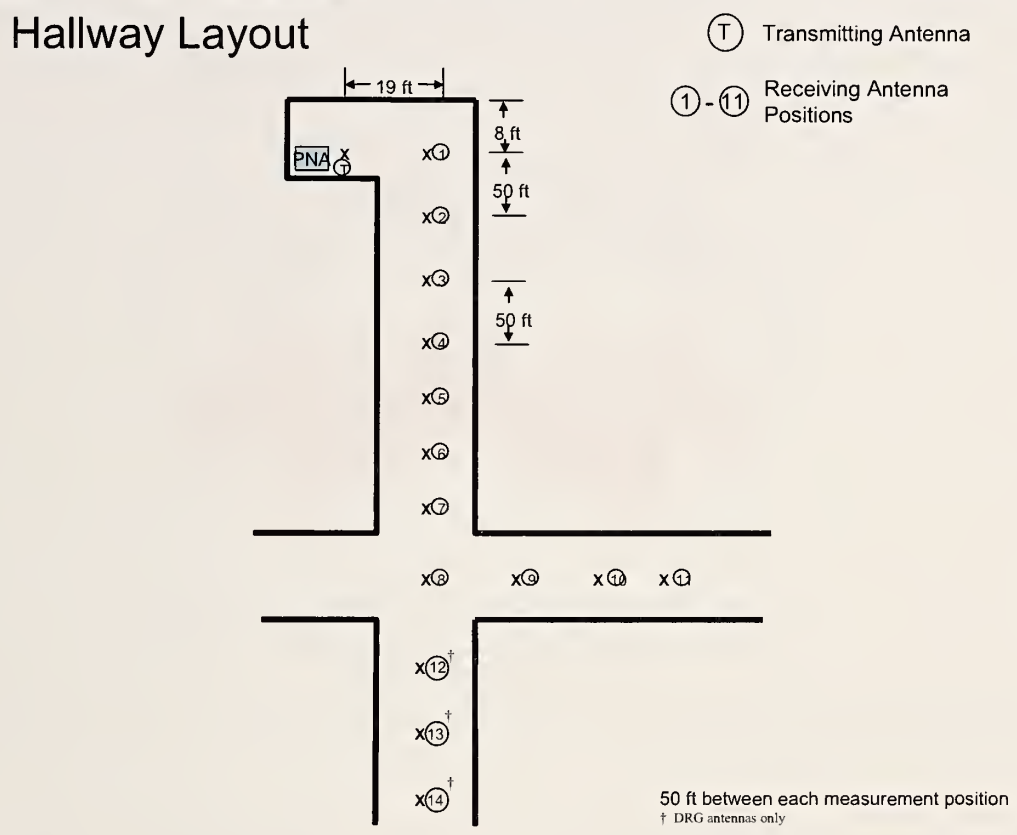

Figure F.1: UWB synthetic pulse measurements were carried out at specific test locations indicated on the outline. The transmitter was located inside the building but in a non-line-of-sight condition. We use the conversion 8 ft ≅ 2.4 m and 50 ft. ≅ 15.25 m.

Wideband Excess Path Loss: Office Hallway Corridor

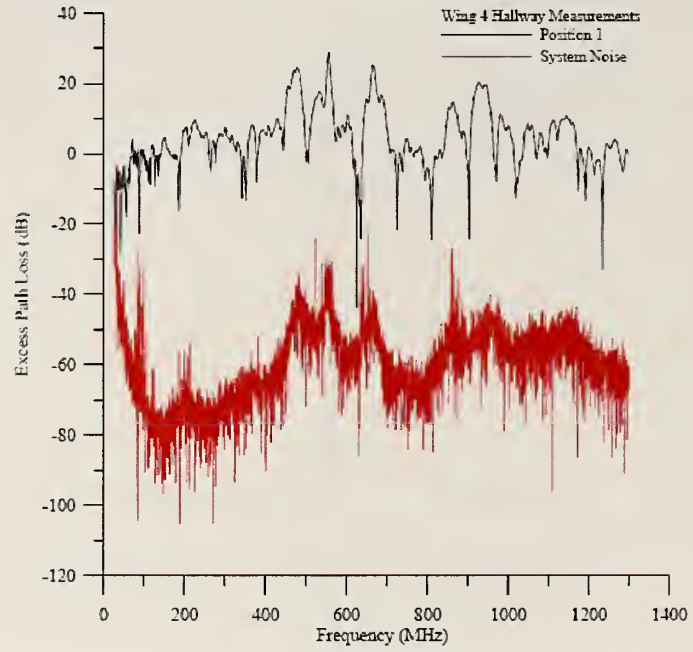

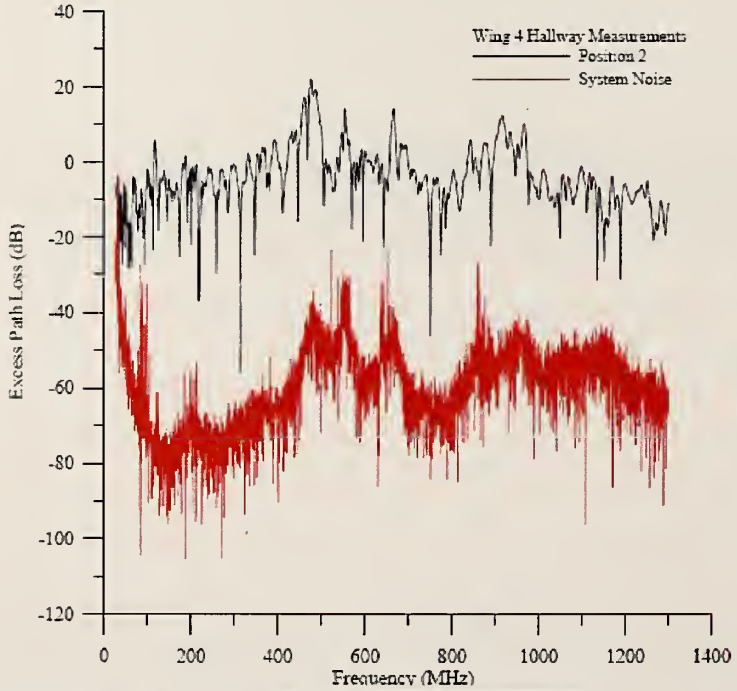

Figure F.2: Excess path loss data from 25 MHz to 1.3 GHz in the Wing 4 hallway. Omnidirectional antennas were used. Distance down the corridor is D = 2.40 m (top) and D = 17.65 m (bottom).

Wideband Excess Path Loss: Office Hallway Corridor

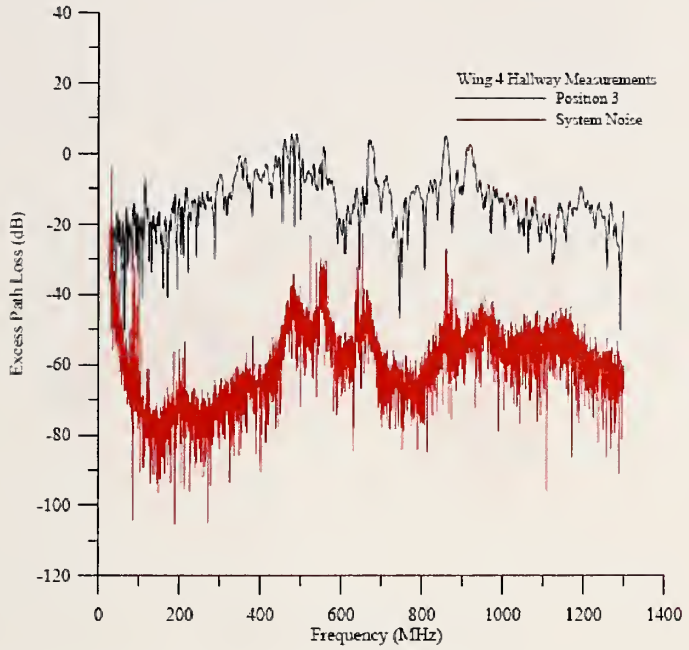

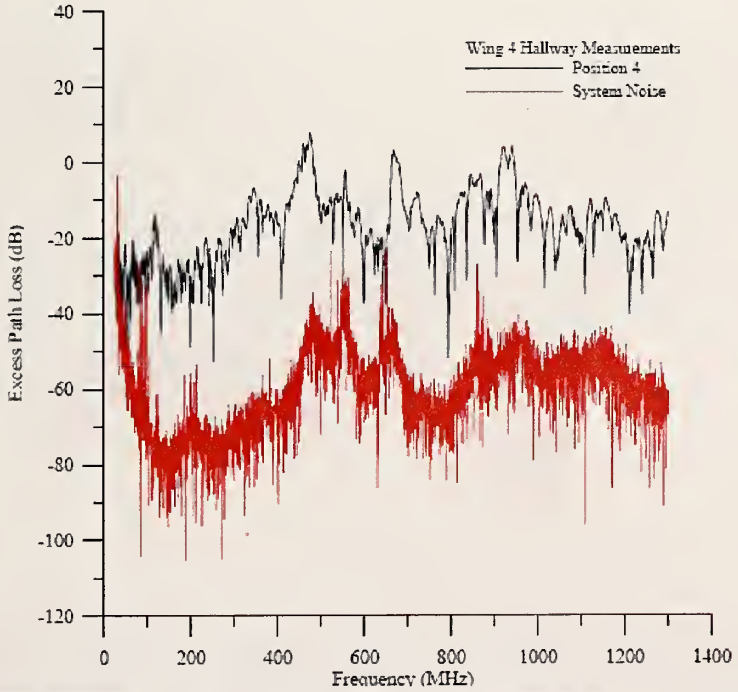

Figure F.3: Excess path loss data from 25 MHz to 1.3 GHz in the Wing 4 hallway. Omnidirectional antennas were used. Distance down the corridor is D = 32.90 m (top) and D = 48.15 m (bottom).

Wideband Excess Path Loss: Office Hallway Corridor

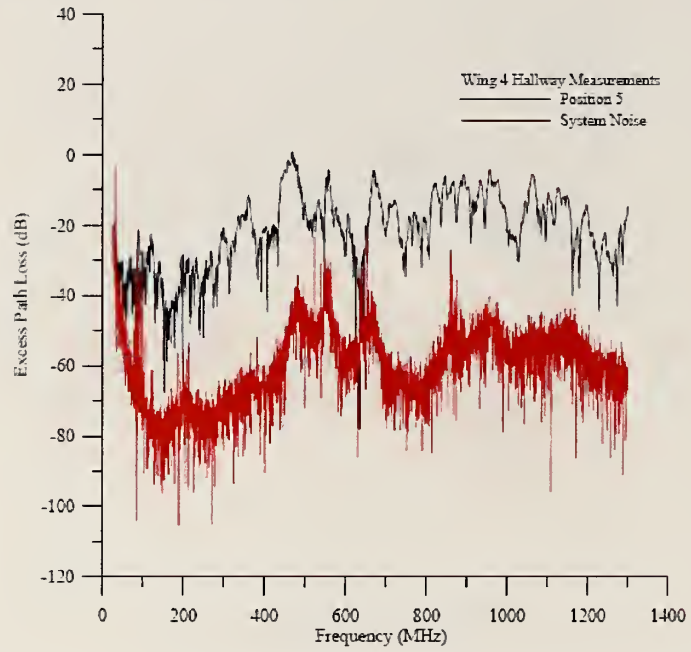

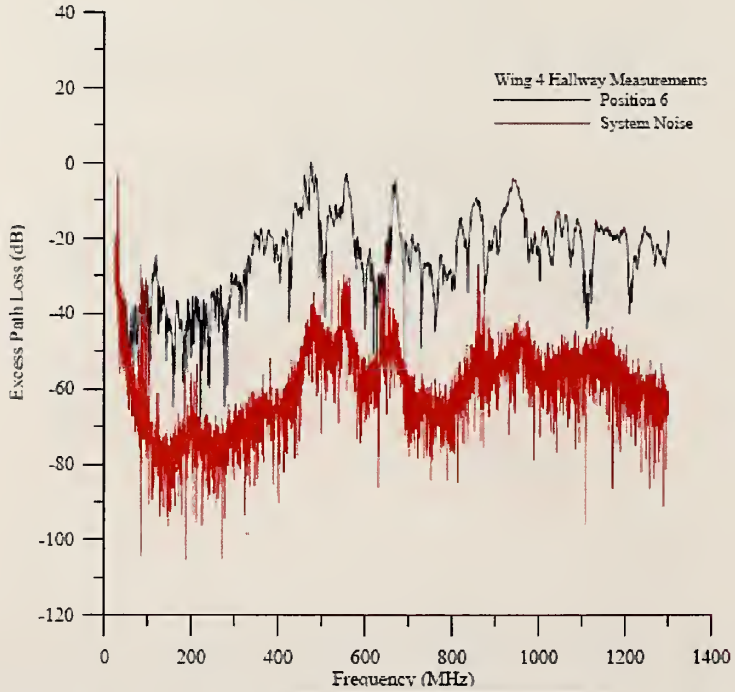

Figure F.4: Excess path loss data from 25 MHz to 1.3 GHz in the Wing 4 hallway. Omnidirectional antennas were used. Distance down the corridor is D = 63.40 m (top) and D = 78.65 m (bottom).

Wideband Excess Path Loss: Office Hallway Corridor

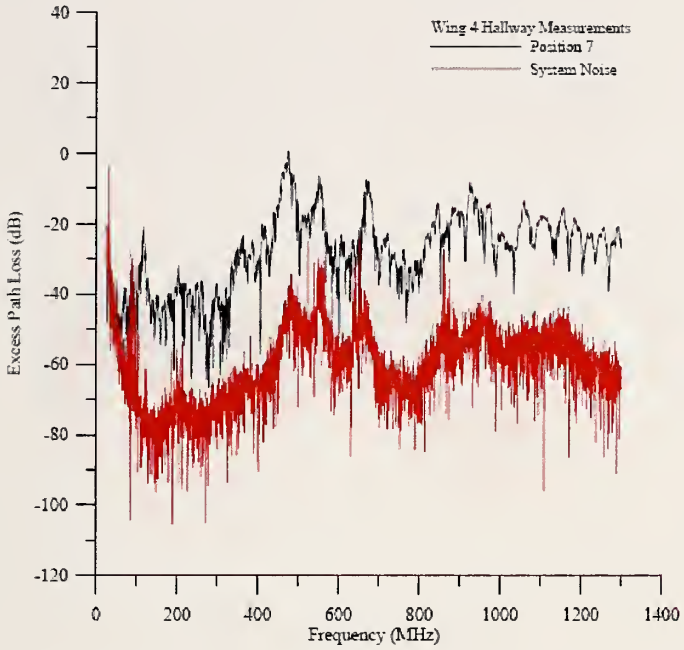

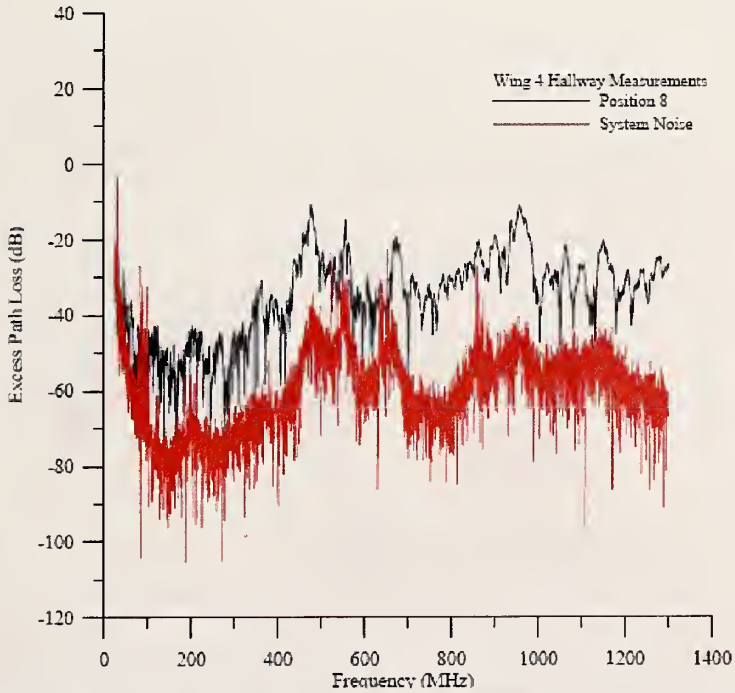

Figure F.5: Excess path loss data from 25 MHz to 1.3 GHz in the Wing 4 hallway. Omnidirectional antennas were used. Distance down the corridor is D = 93.90 m (top) and D = 109.15 m (bottom).

Wideband Excess Path Loss: Office Hallway Corridor

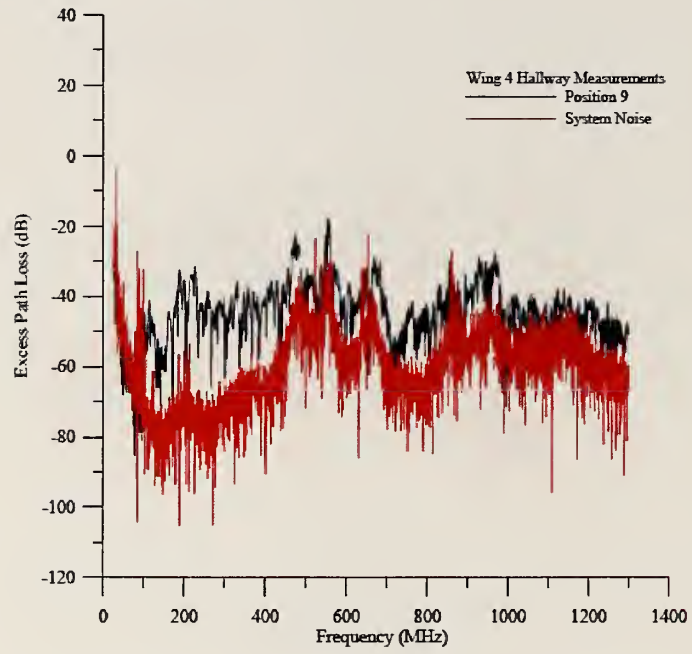

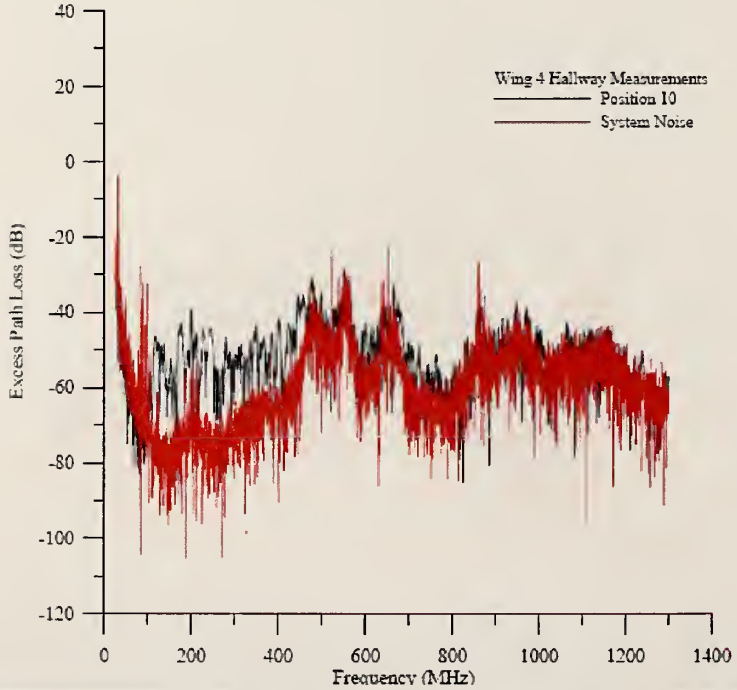

Figure F.6: Excess path loss data from 25 MHz to 1.3 GHz in the Wing 4 hallway. Omnidirectional antennas were used. Distance down the corridor is D = 124.40 m (top) and D = 139.65 m (bottom).

Wideband Excess Path Loss: Office Hallway Corridor

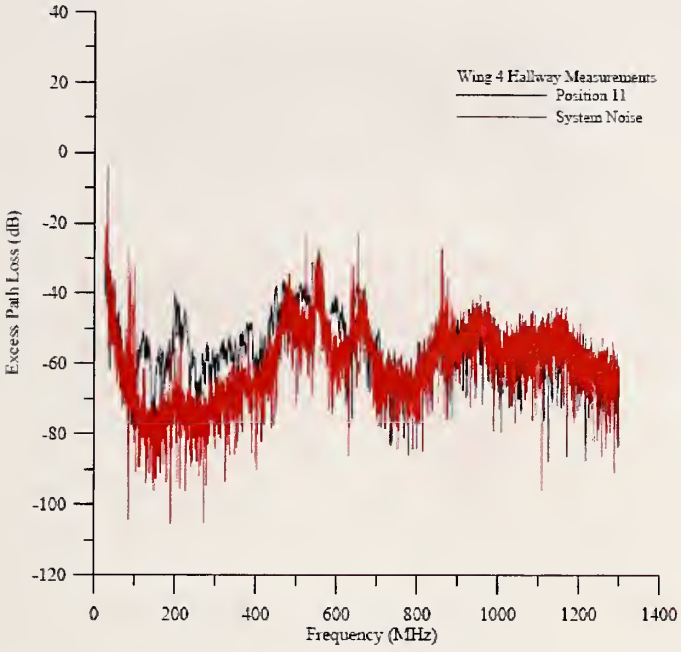

RMS Delay Spread – Diamond Biconicals

Position	Mean Delay (ns)	RMS Delay Spread (ns)
1	20.6	27.9
2	58.6	55.9
3	70.8	76.4
4	84.7	93.1
5	79.9	98.0
6	77.8	84.4
7	103.3	89.3
8	96.4	134.7
9	99.3	66.9
10	[illegible]	[illegible]
11	96.1	[illegible]

Figure F.7: Excess path loss data and RMS delay spread from 25 MHz to 1.3 GHz in the Wing 4 hallway. Omnidirectional antennas were used. Distance down the corridor is D = 154.90 m (top). RMS delay spread (bottom).

Wideband Excess Path Loss: Office Hallway Corridor

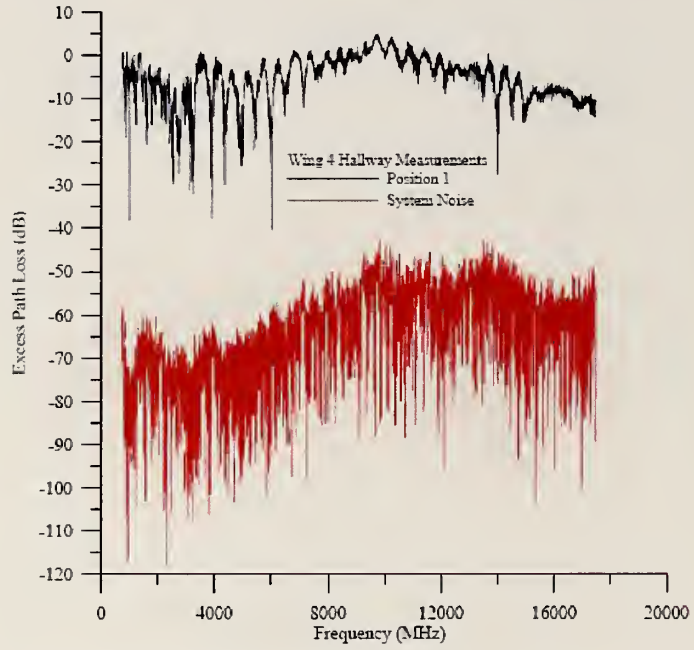

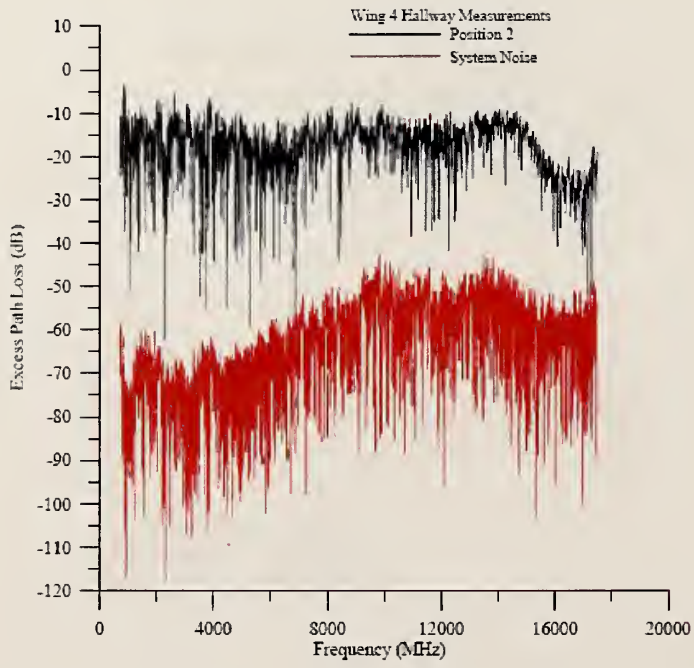

Figure F.8: Excess path loss data from 70 MHz to 18 GHz in the Wing 4 hallway. Directional antennas were used. Distance down the corridor is D = 2.40 m (top) and D = 17.65 m (bottom).

Wideband Excess Path Loss: Office Hallway Corridor

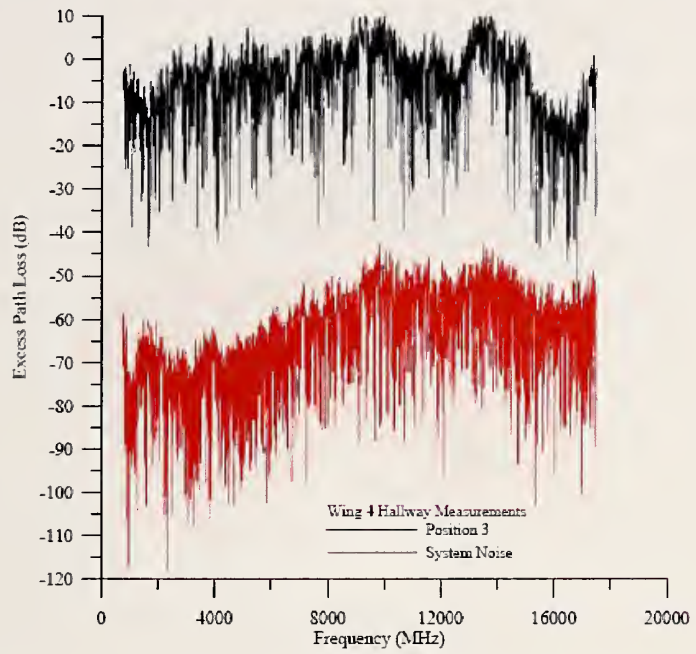

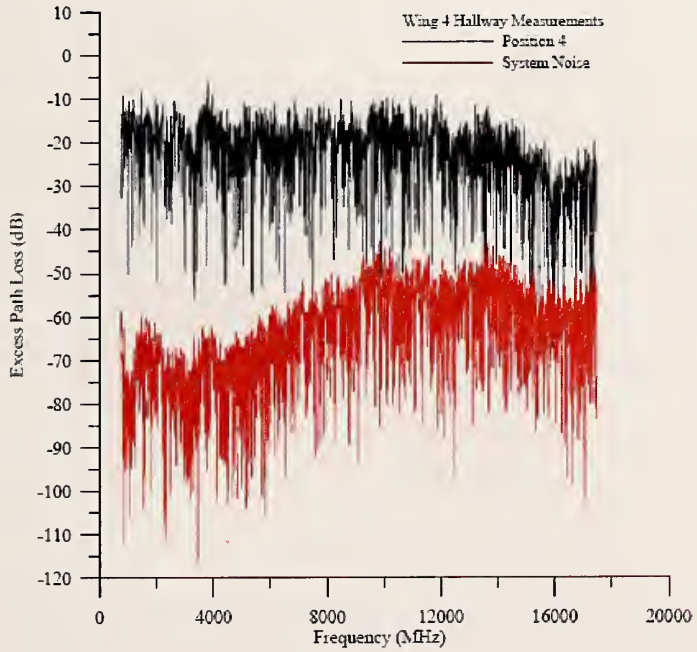

Figure F.9: Excess path loss data from 70 MHz to 18 GHz in the Wing 4 hallway. Directional antennas were used. Distance down the corridor is D = 32.90 m (top) and D = 48.15 m (bottom).

Wideband Excess Path Loss: Office Hallway Corridor

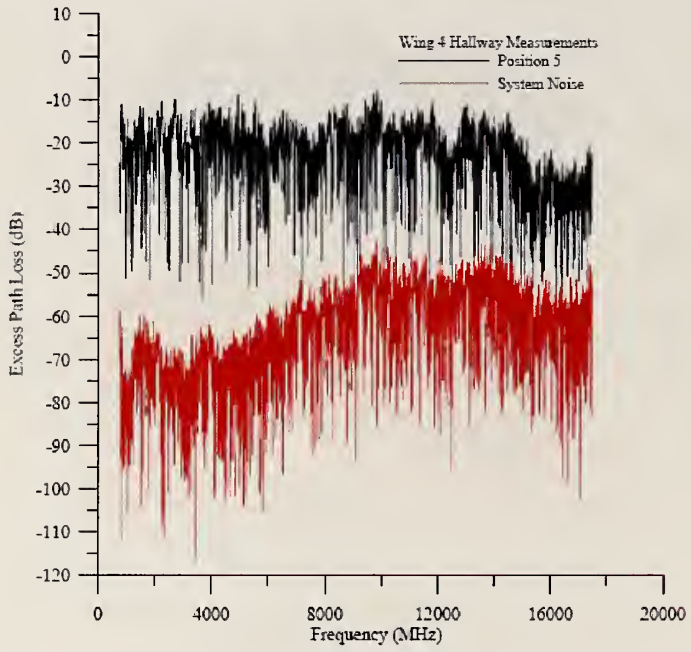

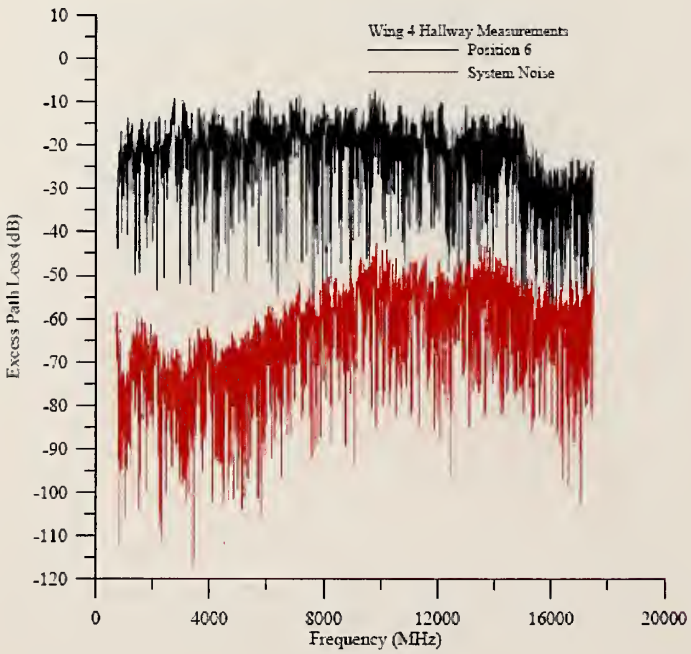

Figure F.10: Excess path loss data from 70 MHz to 18 GHz in the Wing 4 hallway. Directional antennas were used. Distance down the corridor is D = 63.40 m (top) and D = 78.65 m (bottom).

Wideband Excess Path Loss: Office Hallway Corridor

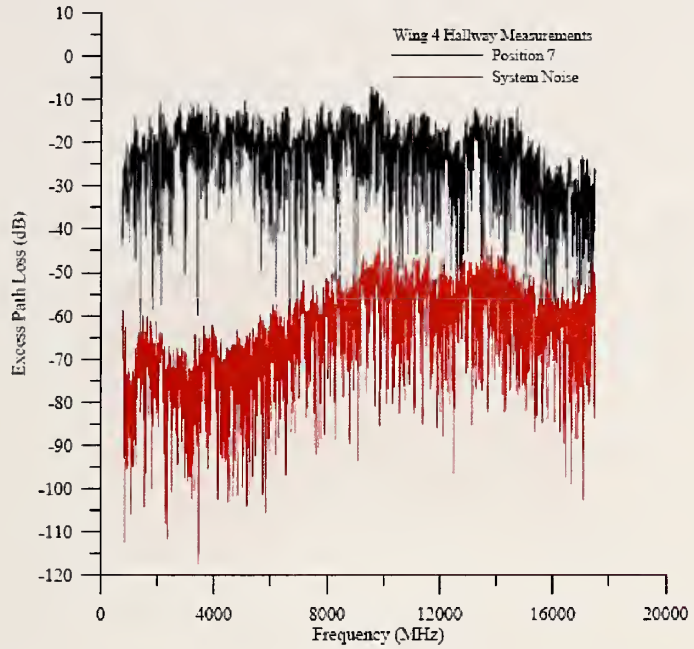

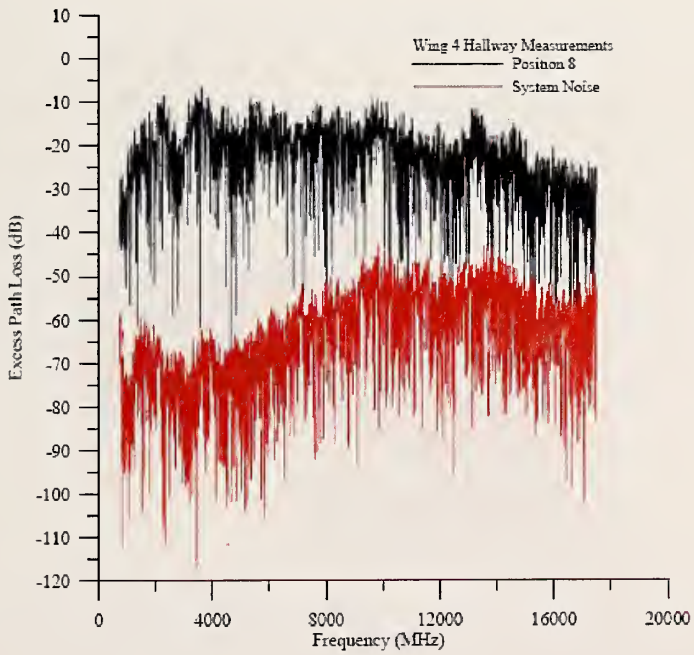

Figure F.11: Excess path loss data from 70 MHz to 18 GHz in the Wing 4 hallway. Directional antennas were used. Distance down the corridor is D = 93.90 m (top) and D = 109.15 m (bottom).

Wideband Excess Path Loss: Office Hallway Corridor

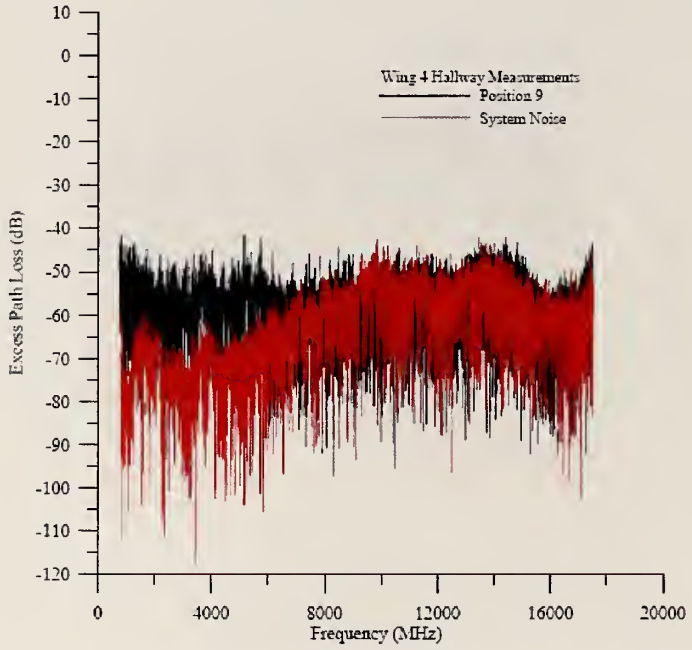

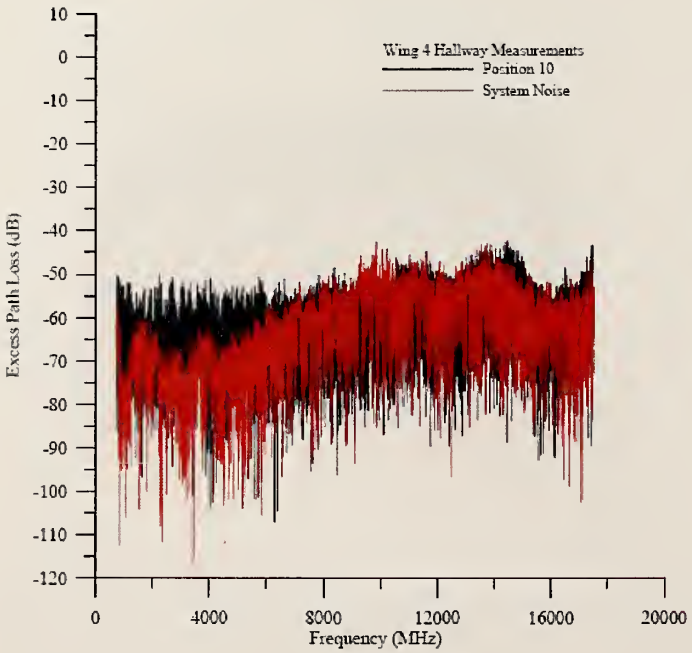

Figure F.12: Excess path loss data from 70 MHz to 18 GHz in the Wing 4 hallway. Directional antennas were used. Distance down the corridor is D = 124.40 m (top) and D = 139.65 m (bottom).

Wideband Excess Path Loss: Office Hallway Corridor

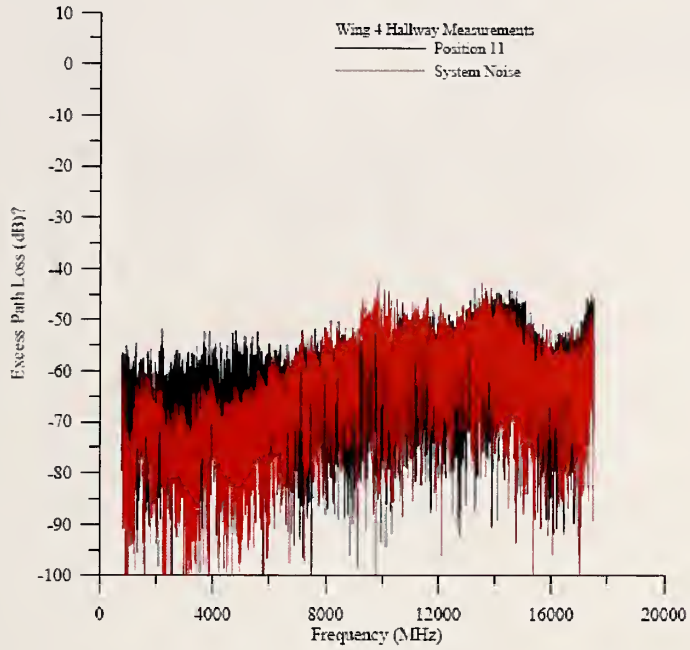

RMS Delay Spread – 3115 DRG Antennas

Position	Mean Delay (ns)	RMS Delay Spread (ns)
1	19.4	8.8
2	25.5	16.7
3	29.8	16.6
4	28.6	17.5
5	27.6	18.0
6	21.4	18.6
7	20.1	20.4
8	17.5	19.6
9	Noise	Noise
10	Noise	Noise
11	Noise	Noise
12	20.9	18.5
13	18.0	17.8
14	16.2	20.2

Figure F.13: Excess path loss and time-delay spread covering 70 MHz to 18 GHz in the Wing 4 hallway. Directional antennas were used. Distance down the corridor is D = 154.90 m (top). RMS delay spread (bottom).

Wideband Excess Path Loss: Office Hallway Corridor

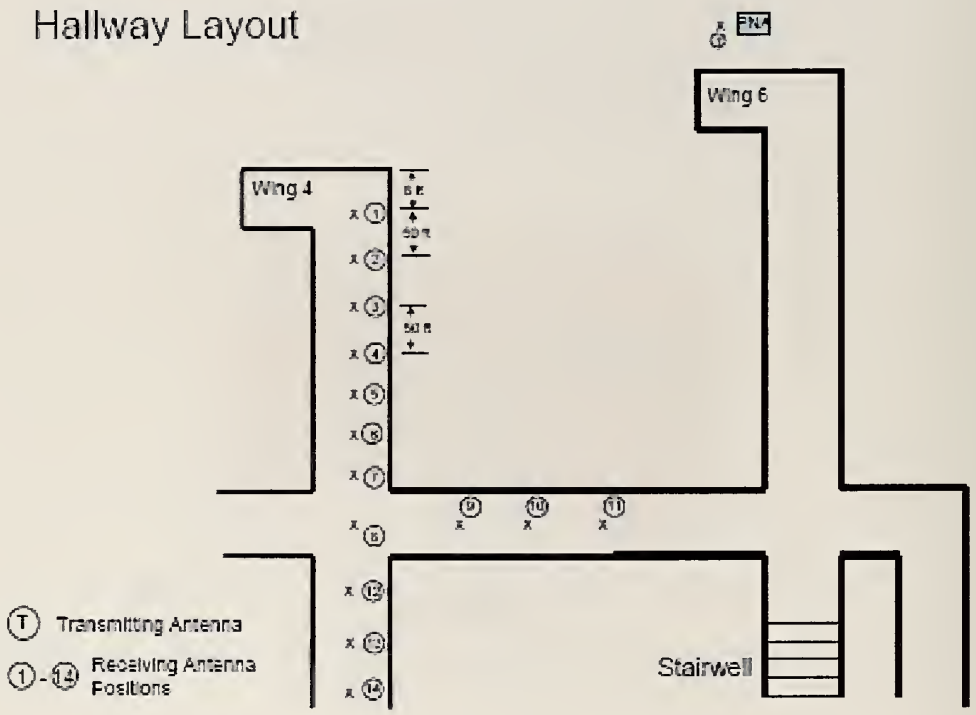

Figure F.14: Building penetration measurements were carried out at specific test locations indicated on the outline. The Wing 4 corridor is lined with offices having windows to the outside, thus indoor-to-outdoor coupling can be expected.

Wideband Excess Path Loss: Office Hallway Corridor

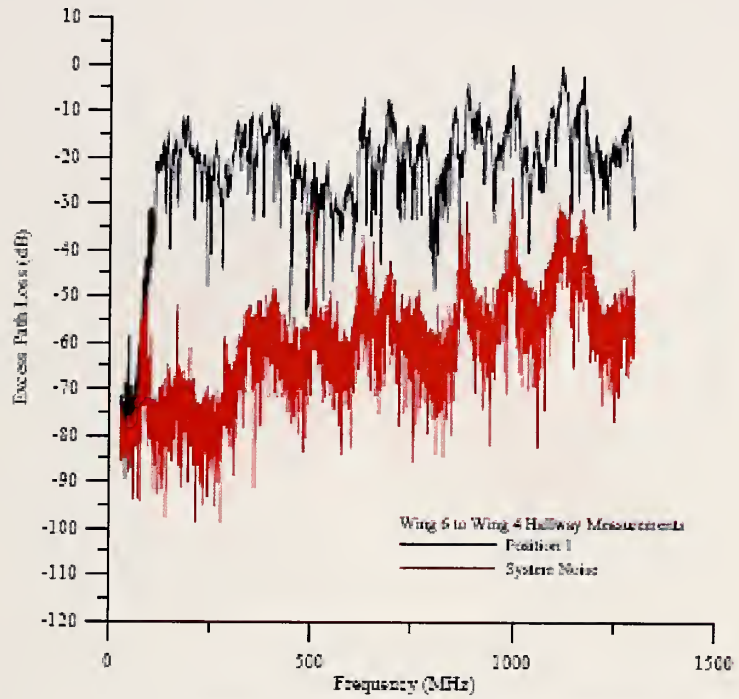

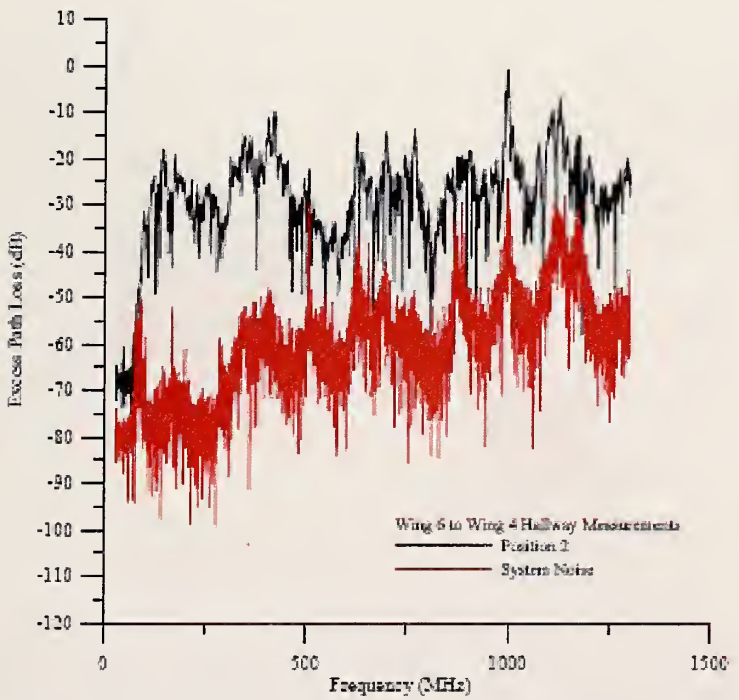

Figure F.15: Excess path loss data from 25 MHz to 1.3 GHz for a path that includes building penetration found using data into the Wing 4 hallway. Omnidirectional antennas were used. Distance down the corridor is D = 2.40 m (top) and D = 17.65 m (bottom).

Wideband Excess Path Loss: Office Hallway Corridor

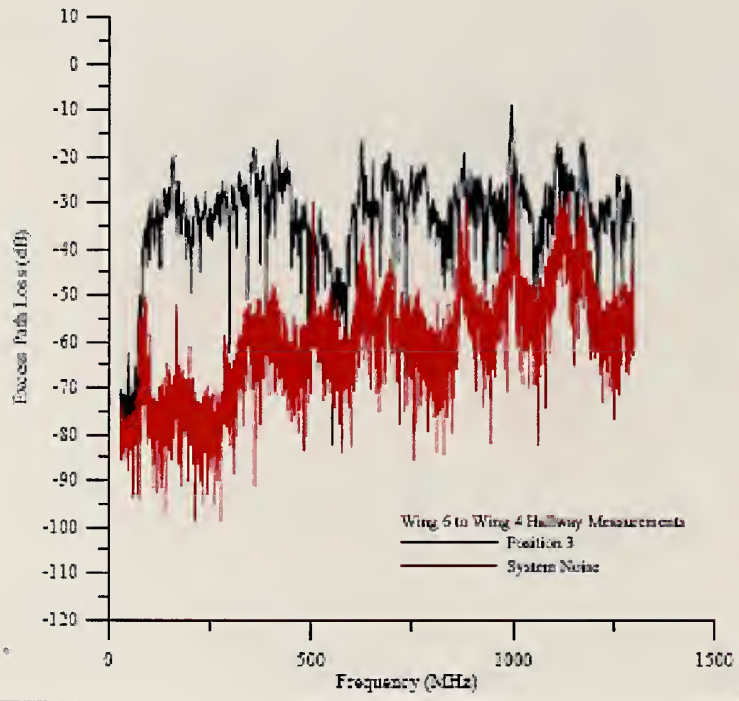

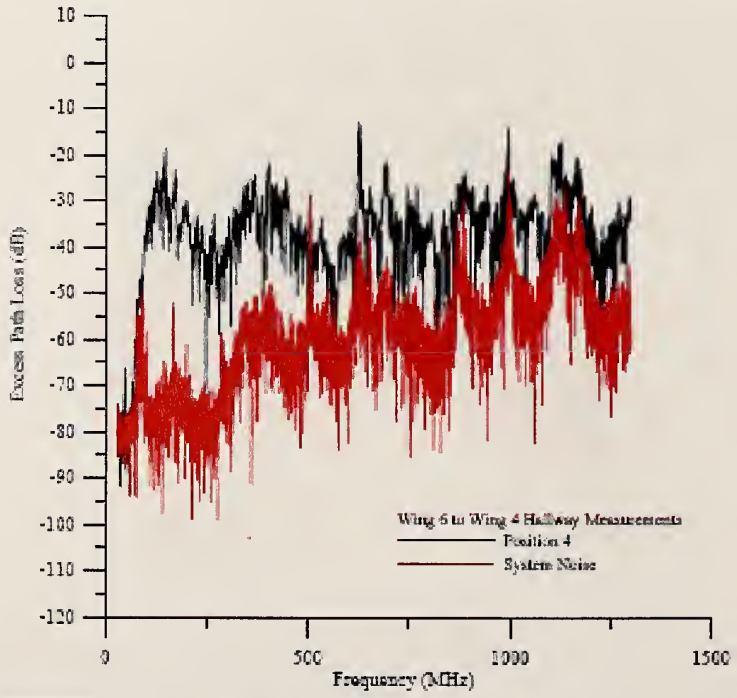

Figure F.16: Excess path loss data from 25 MHz to 1.3 GHz for a path that includes building penetration found using data into the Wing 4 hallway. Omnidirectional antennas were used. Distance down the corridor is D = 32.90 m (top) and D = 48.15 m (bottom).

Wideband Excess Path Loss: Office Hallway Corridor

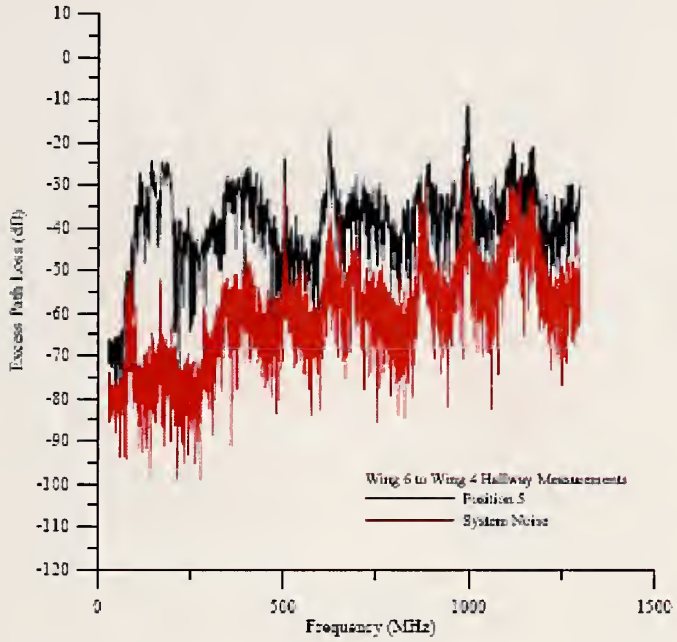

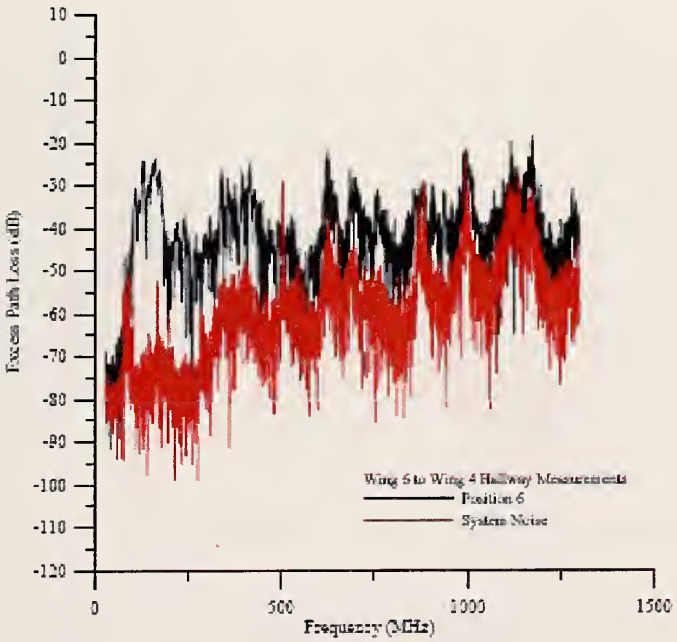

Figure F.17: Excess path loss data from 25 MHz to 1.3 GHz for a path that includes building penetration found using data into the Wing 4 hallway. Omnidirectional antennas were used. Distance down the corridor is D = 63.40 m (top) and D = 78.65 m (bottom).

Wideband Excess Path Loss: Office Hallway Corridor

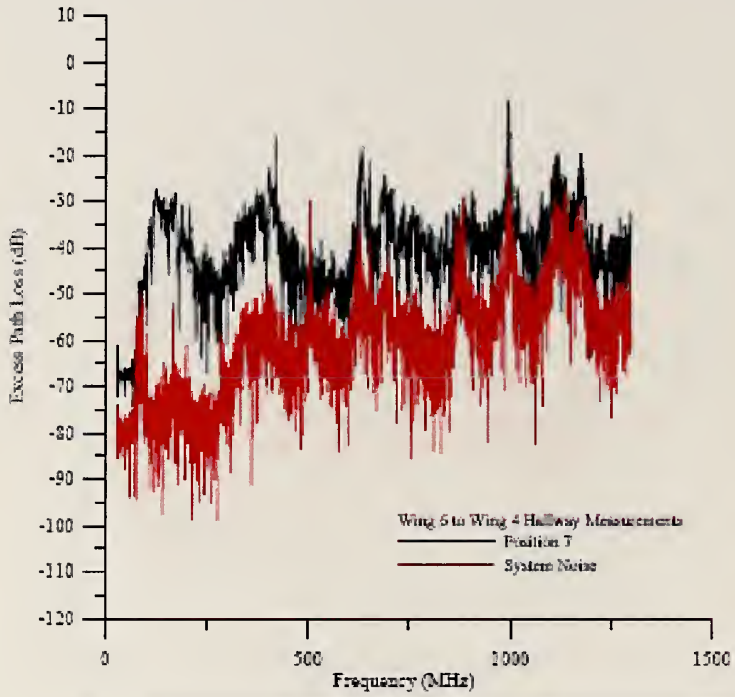

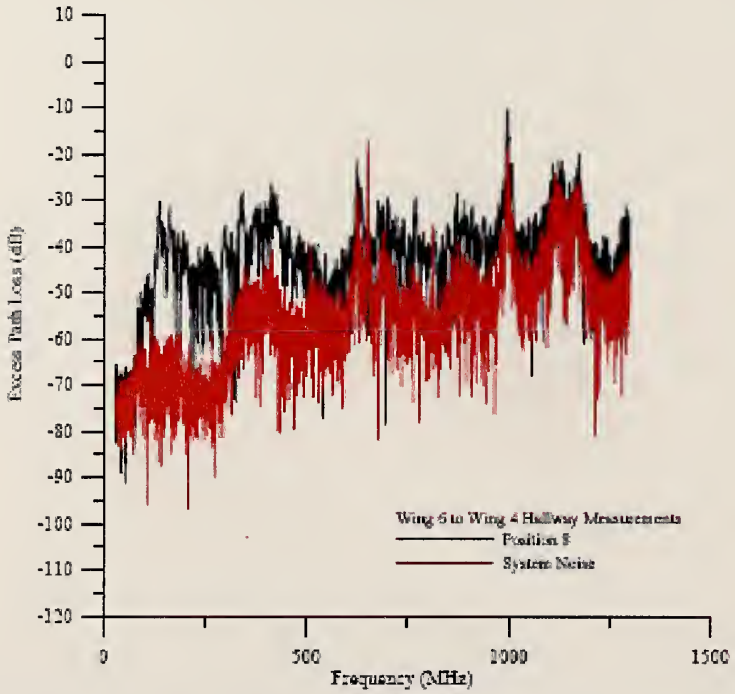

Figure F.18: Excess path loss data from 25 MHz to 1.3 GHz for a path that includes building penetration found using data into the Wing 4 hallway. Omnidirectional antennas were used. Distance down the corridor is D = 93.90 m (top) and D = 109.15 m (bottom).

Wideband Excess Path Loss: Office Hallway Corridor

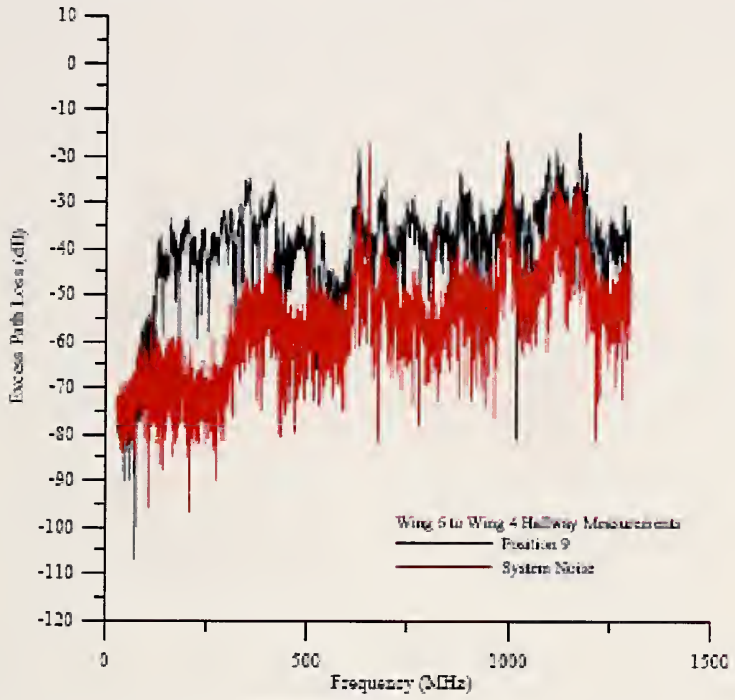

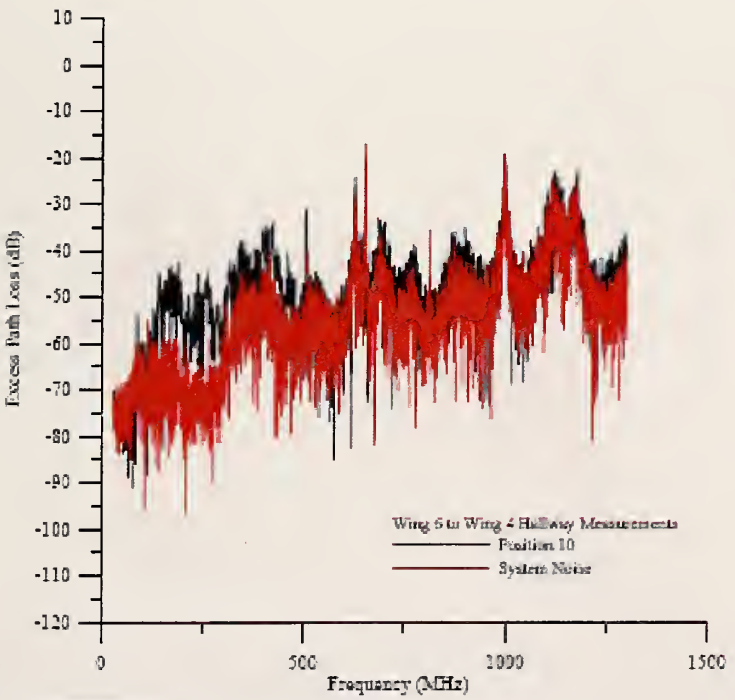

Figure F.19: Excess path loss data from 25 MHz to 1.3 GHz for a path that includes building penetration found using data into the Wing 4 hallway. Omnidirectional antennas were used. Distance down the corridor is D = 124.4 m (top) and D = 139.65 m (bottom).

Wideband Excess Path Loss: Office Hallway Corridor

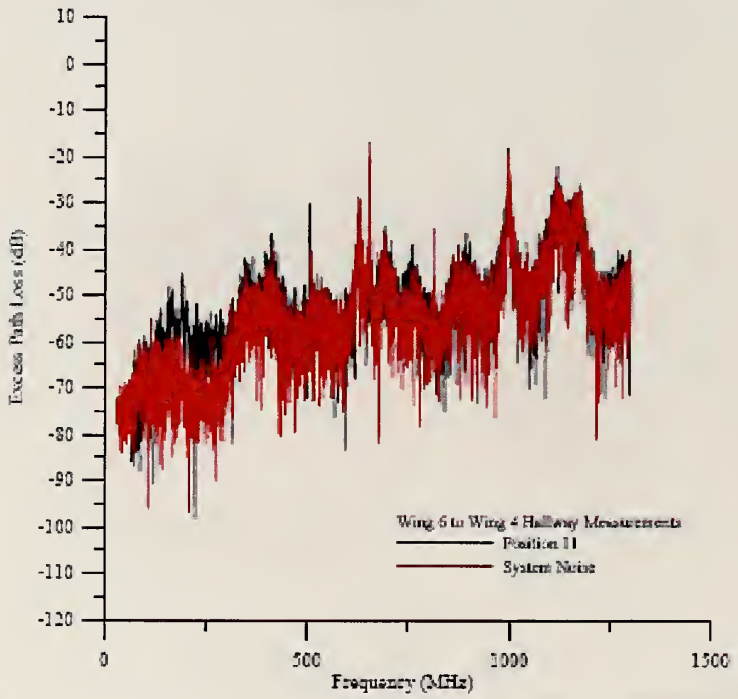

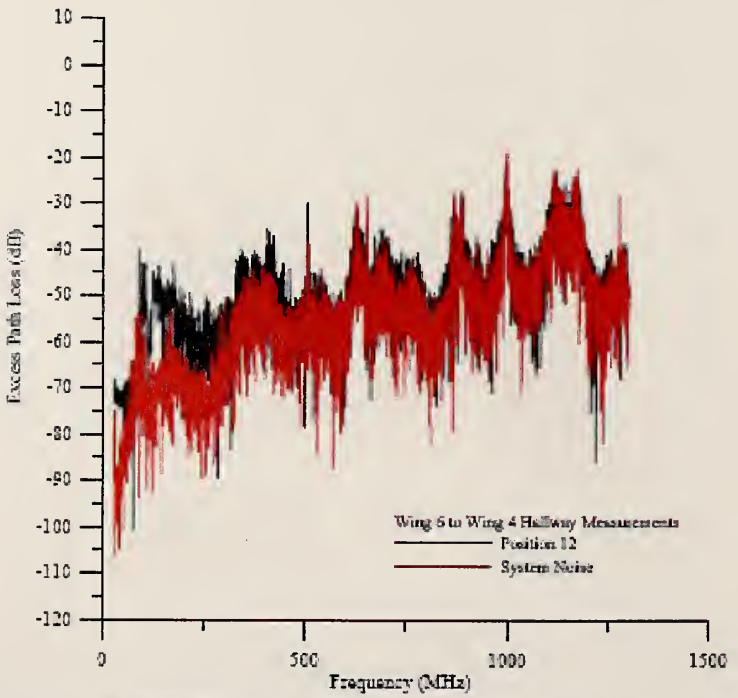

Figure F.20: Excess path loss data from 25 MHz to 1.3 GHz for a path that includes building penetration found using data into the Wing 4 hallway. Omnidirectional antennas were used. Distance down the corridor is D = 154.9 m (top) and D = 170.15 m (bottom).

Wideband Excess Path Loss: Office Hallway Corridor

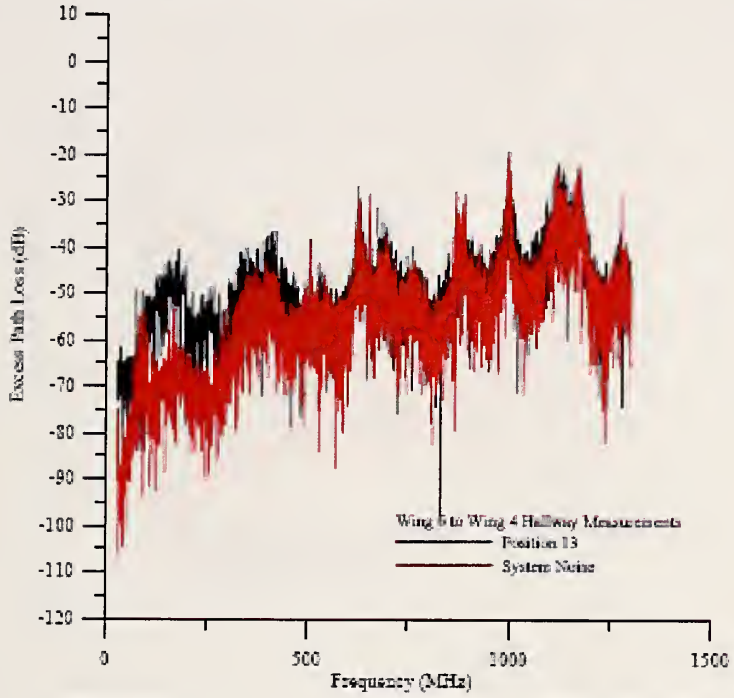

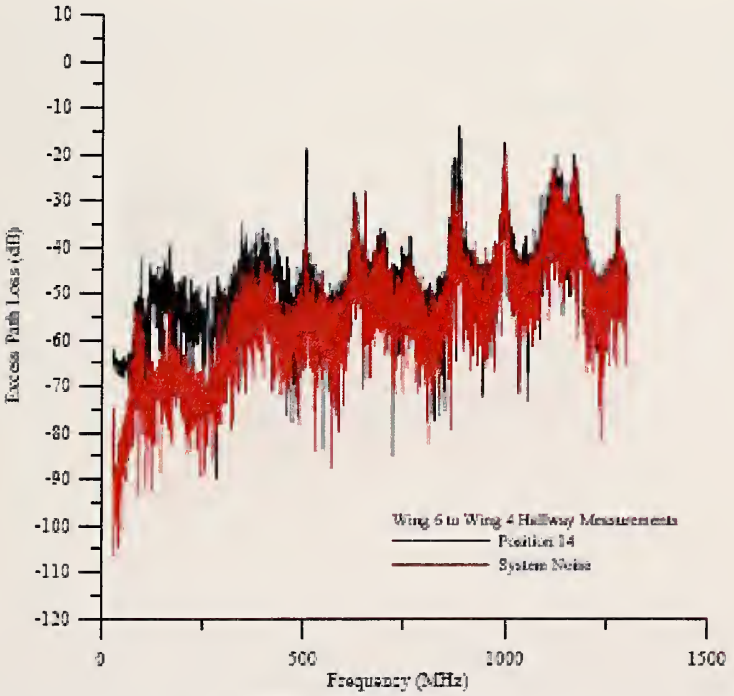

Figure F.21: Excess path loss data from 25 MHz to 1.3 GHz for a path that includes building penetration found using data into the Wing 4 hallway. Omnidirectional antennas were used. Distance down the corridor is D = 185.40 m (top) and D = 200.65 m (bottom).

Wideband Excess Path Loss: Office Hallway Corridor

RMS Delay Spread – Diamond Biconicals

Position	Mean Delay (ns)	RMS Delay Spread (ns)
1	16.9	16.4
2	20.1	21.1
3	35.3	18.0
4	65.1	36.0
5	43.2	26.8
6	35.7	37.4
7	69.6	54.8
8	56.7	44.9
9	53.4	23.4
10	65.9	41.5
11	-*	-*
12	-*	-*
13	-*	-*
14	-*	-*

* These signals are in the noise, but it looks like they have multiple scattering points-long time signature

Figure F.22: Time delay spread found from data covering 25 MHz to 1.3 GHz for a path that includes building penetration found using data into the Wing 4 hallway.

Wideband Excess Path Loss: Office Hallway Corridor

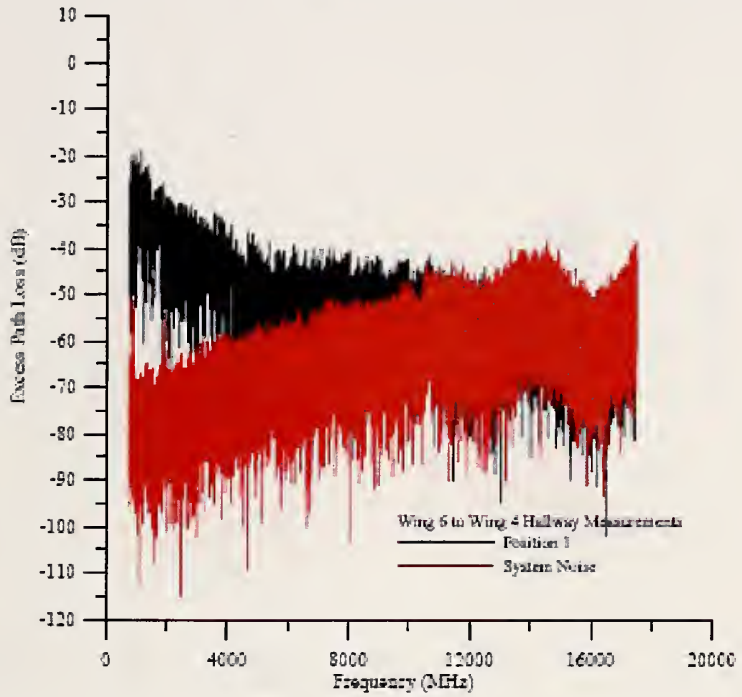

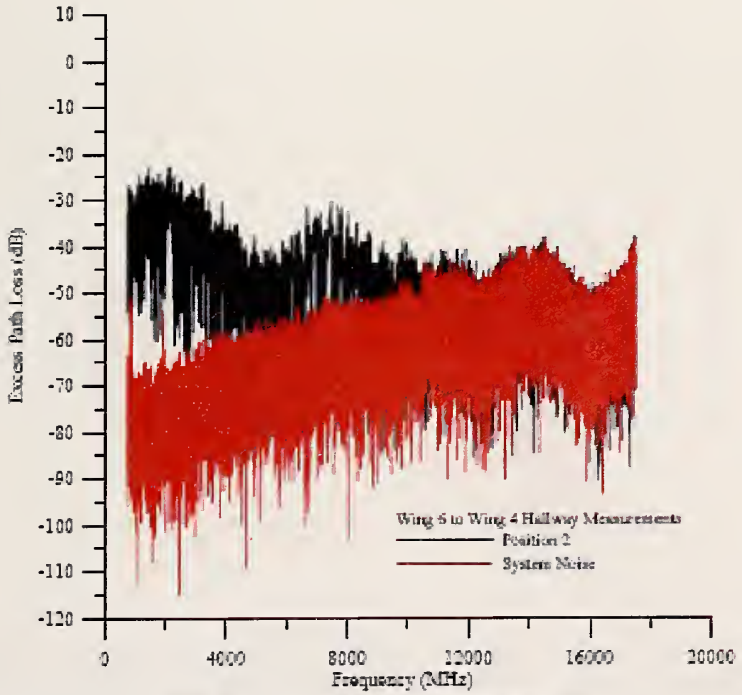

Figure F.23: Excess path loss data from 750 MHz to 18 GHz for a path that includes building penetration found using data into the Wing 4 hallway. Directional antennas were used. Distance down the corridor is D = 2.40 m (top) and D = 17.65 m (bottom).

Wideband Excess Path Loss: Office Hallway Corridor

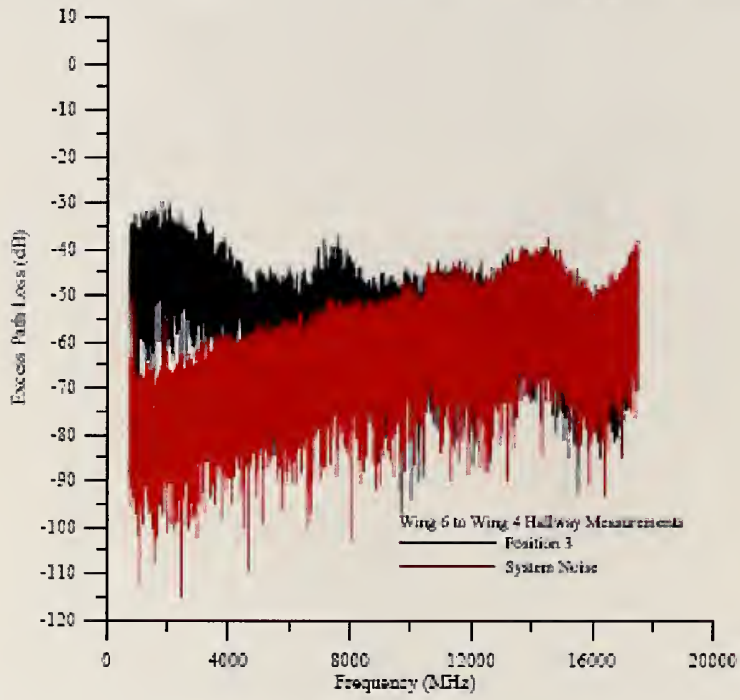

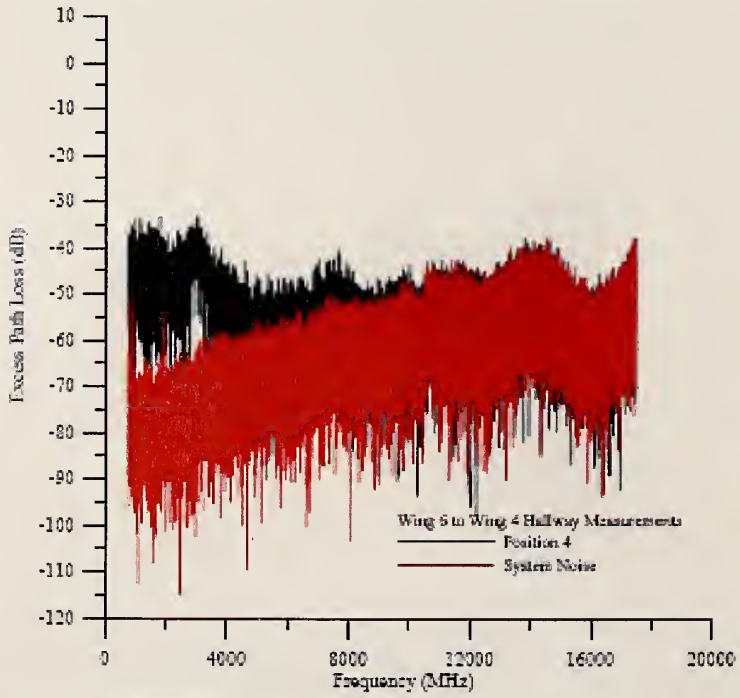

Figure F.24: Excess path loss data from 750 MHz to 18 GHz for a path that includes building penetration found using data into the Wing 4 hallway. Directional antennas were used. Distance down the corridor is D = 32.90 m (top) and D = 48.15 m (bottom).

Wideband Excess Path Loss: Office Hallway Corridor

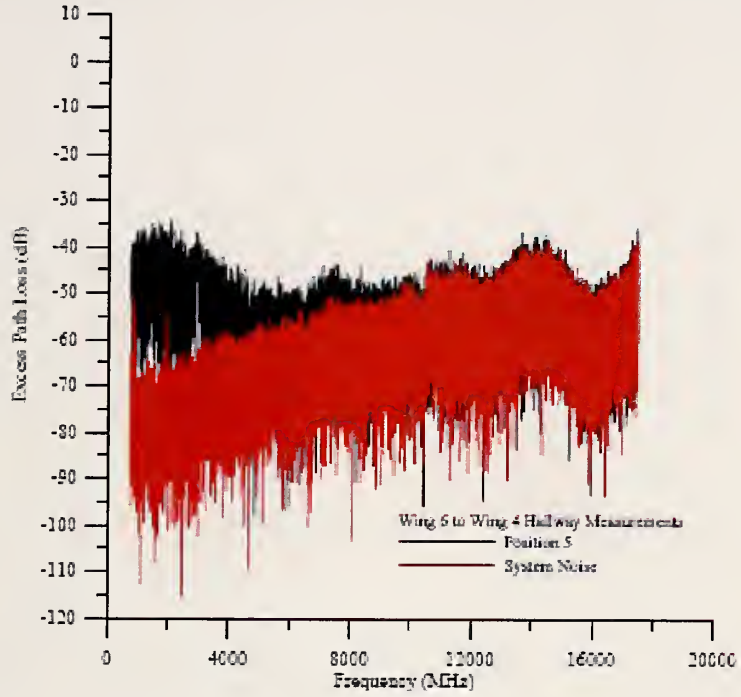

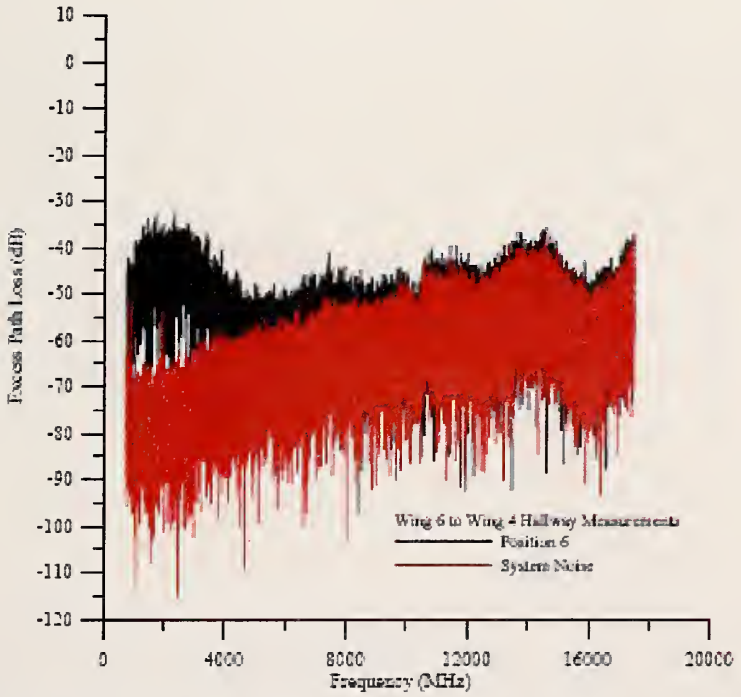

Figure F.25: Excess path loss data from 750 MHz to 18 GHz for a path that includes building penetration found using data into the Wing 4 hallway. Directional antennas were used. Distance down the corridor is D = 63.40 m (top) and D = 78.65 m (bottom).

Wideband Excess Path Loss: Office Hallway Corridor

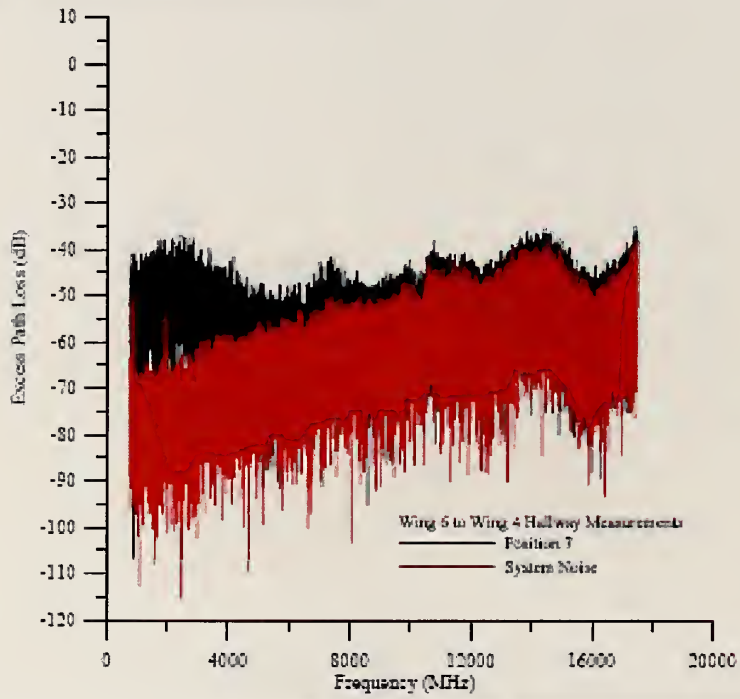

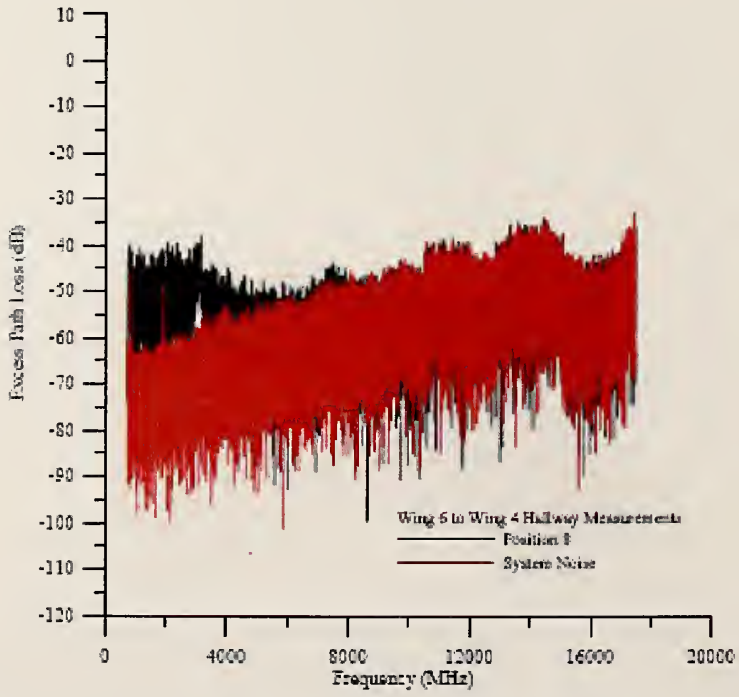

Figure F.26: Excess path loss data from 750 MHz to 18 GHz for a path that includes building penetration found using data into the Wing 4 hallway. Directional antennas were used. Distance down the corridor is D = 93.90 m (top) and D = 109.15 m (bottom).

Wideband Excess Path Loss: Office Hallway Corridor

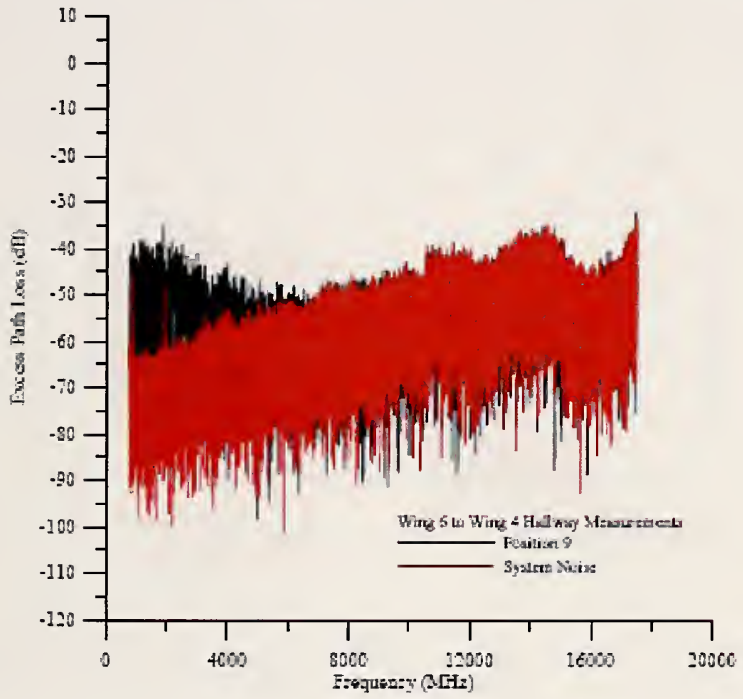

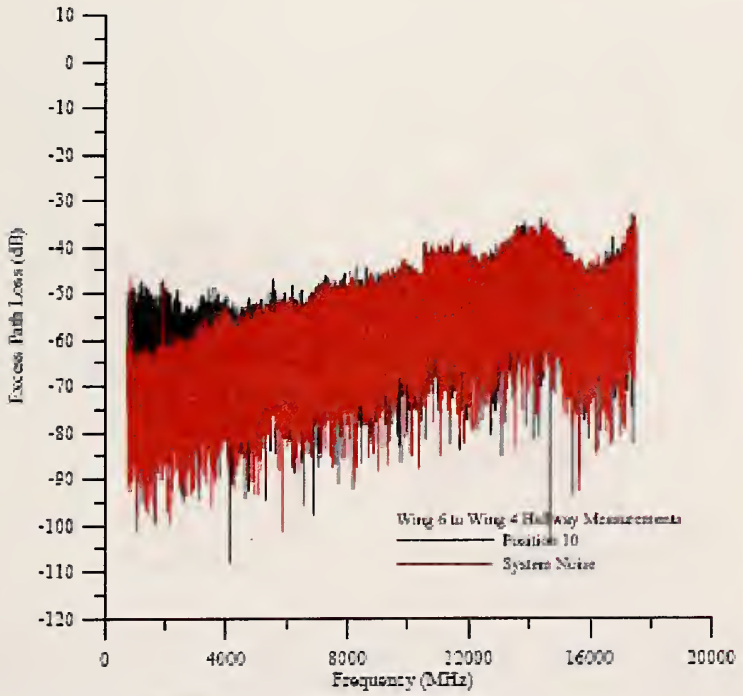

Figure F.27: Excess path loss data from 750 MHz to 18 GHz for a path that includes building penetration found using data into the Wing 4 hallway. Directional antennas were used. Distance down the corridor is D = 124.40 m (top) and D = 139.65 m (bottom).

Wideband Excess Path Loss: Office Hallway Corridor

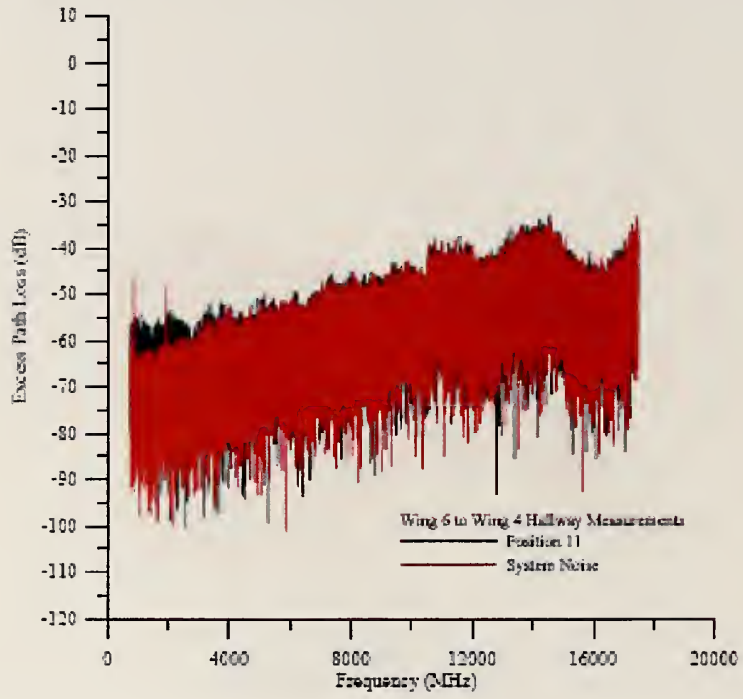

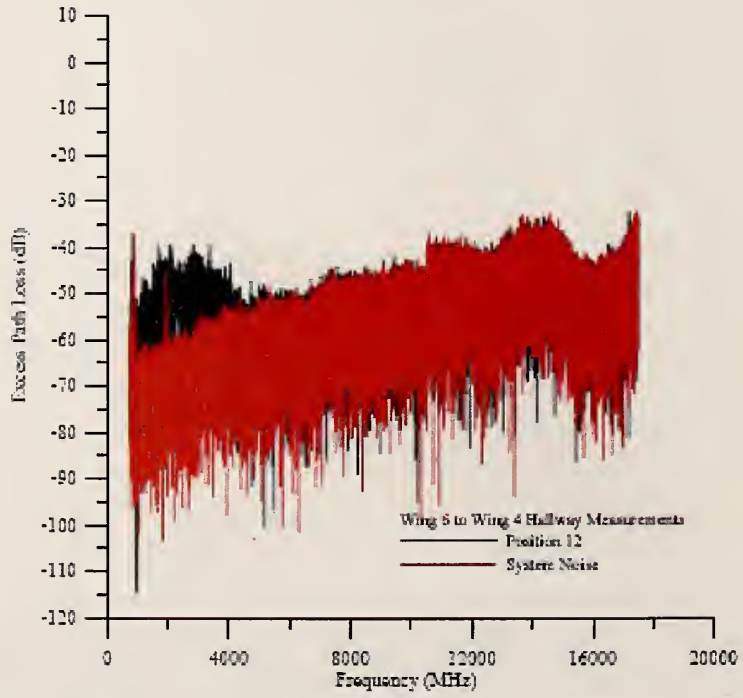

Figure F.28: Excess path loss data from 750 MHz to 18 GHz for a path that includes building penetration found using data into the Wing 4 hallway. Directional antennas were used. Distance down the corridor is D = 154.90 m (top) and D = 170.15 m (bottom).

Wideband Excess Path Loss: Office Hallway Corridor

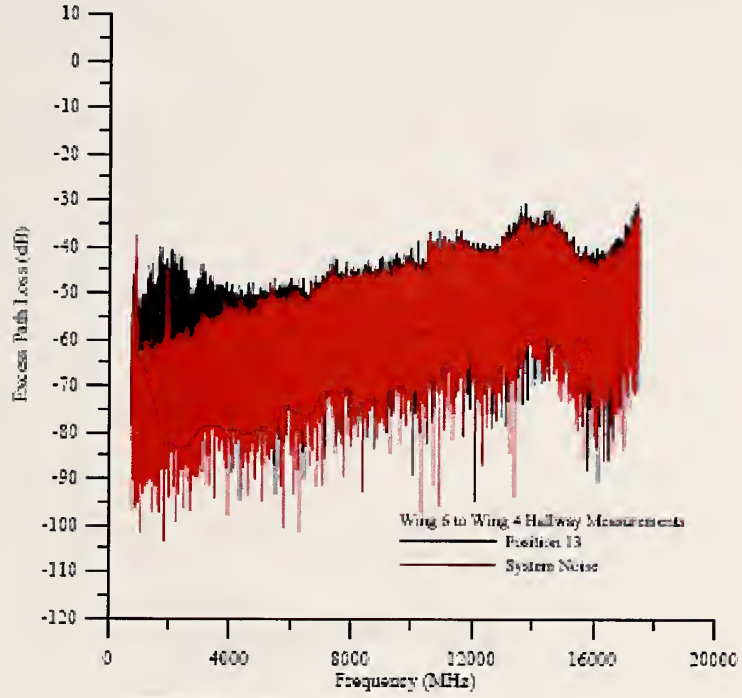

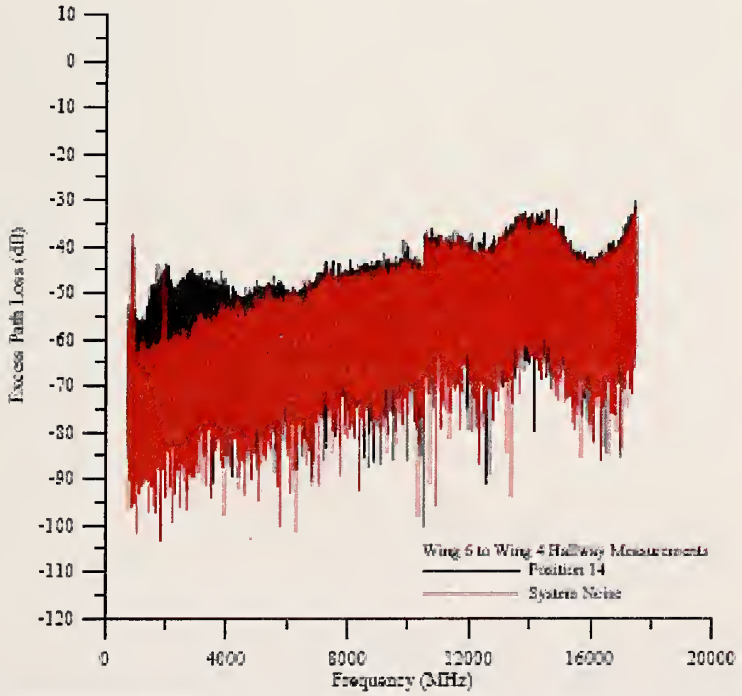

Figure F.29: Excess path loss data from 750 MHz to 18 GHz for a path that includes building penetration found using data into the Wing 4 hallway. Directional antennas were used. Distance down the corridor is D = 185.40 m (top) and D = 200.65 m (bottom).

Wideband Excess Path Loss: Office Hallway Corridor

RMS Delay Spread –
3115 DRG Antennas

Position	Mean Delay (ns)	RMS Delay Spread (ns)
1	18.5	19.8
2	13.1	25.2
3	70.9	37.2
4	91.7	26.2
5	98.3	29.7
6	110.0	26.0
7	113.0	27.0
8	113.7	43.4
9	61.0	24.4
10	71.1	33.9
11		23.1
12		14.3
13	52.0	11.0
14	51.1	13.8

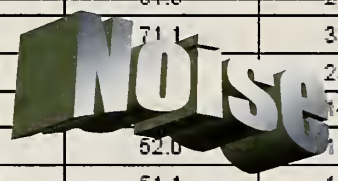

Figure F.30: Time delay spread found from data covering 750 MHz to 18 GHz for a path that includes building penetration found using data into the Wing 4 hallway. Directional antennas were used.

Appendix G: Wideband Excess Path Loss Measured With a Synthetic-Pulse Vector-Network-Analyzer-Based System: Oil Refinery

The following pages contain the complete set of measured data for the oil refinery (Section 5.3).

Wideband Excess Path Loss: Oil Refinery

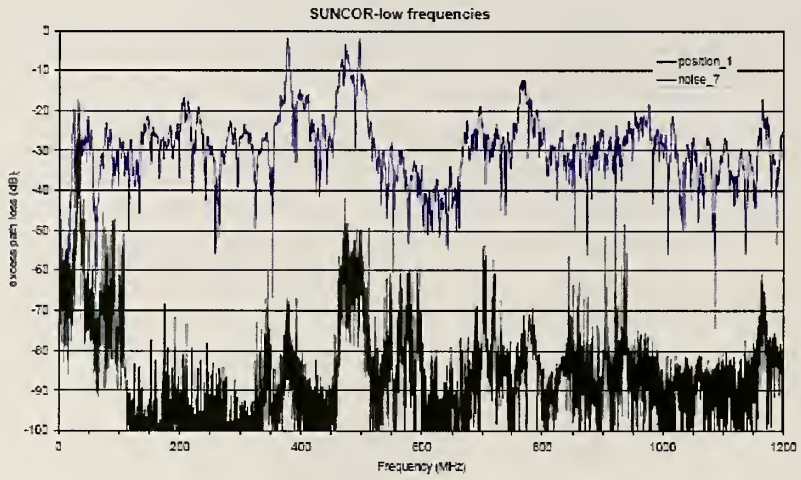

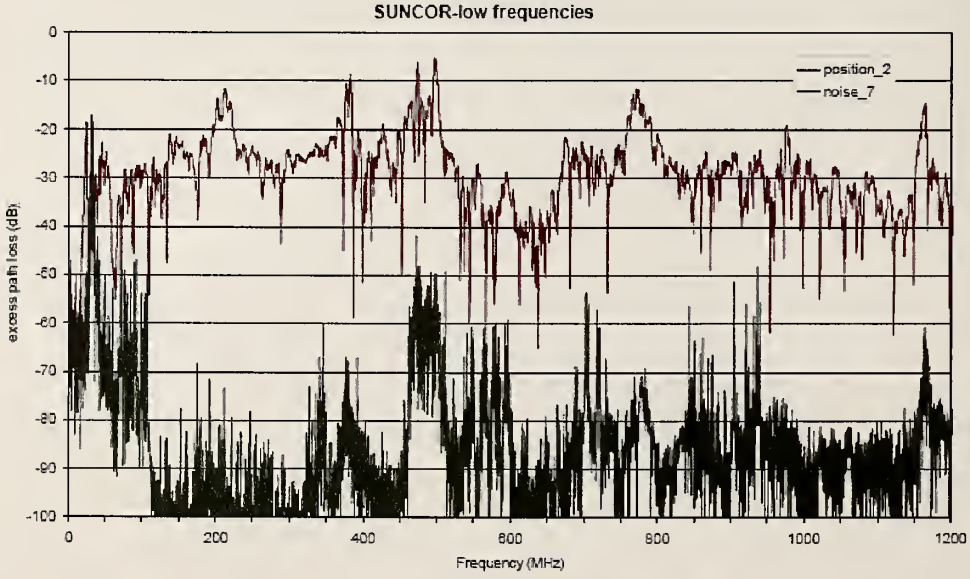

Figure G.1: Excess path loss data from 25 MHz to 1.2 GHz at an oil refinery along a path underneath extensive piping. Distance from the transmitting antenna to the receiving antenna is D = 20.6 m (top) and D = 26.5 m (bottom).

Wideband Excess Path Loss: Oil Refinery

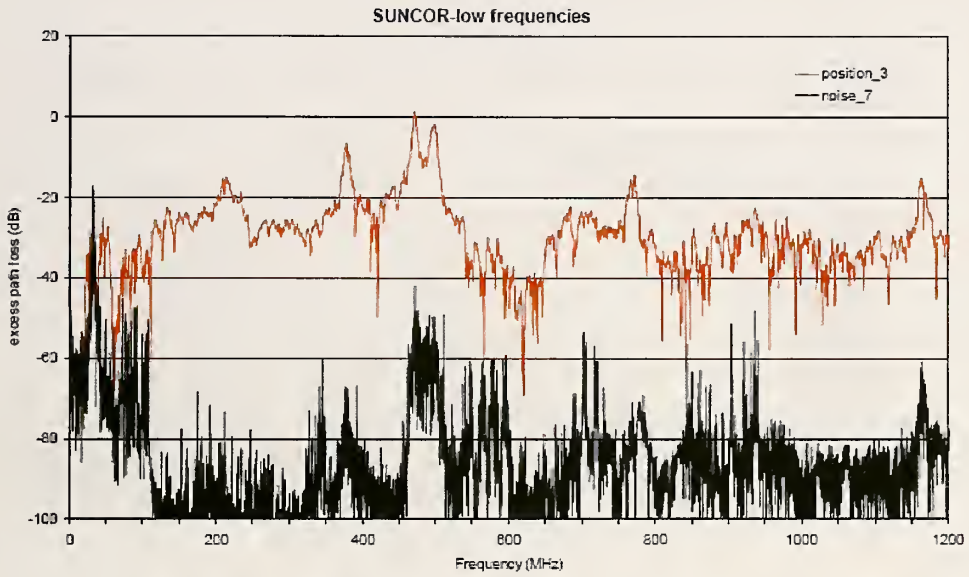

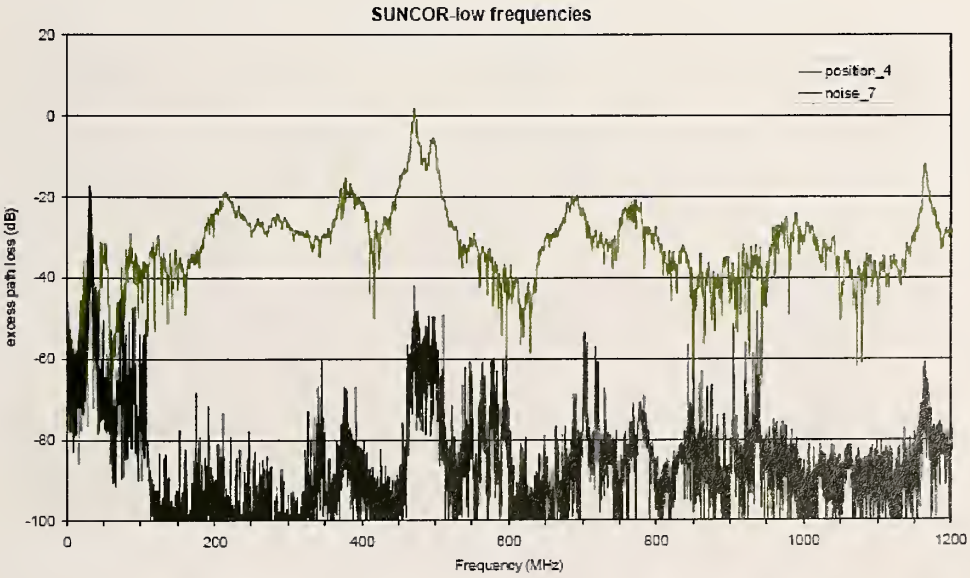

Figure G.2: Excess path loss data from 25 MHz to 1.2 GHz at an oil refinery along a path underneath extensive piping. Distance from the transmitting antenna to the receiving antenna is D = 32.4 m (top) and D = 40.5 m (bottom).

Wideband Excess Path Loss: Oil Refinery

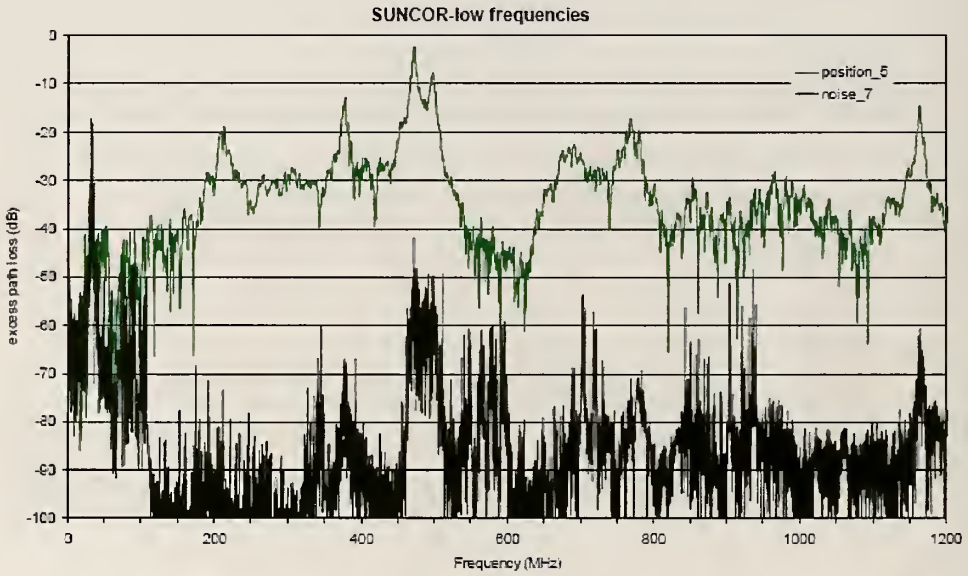

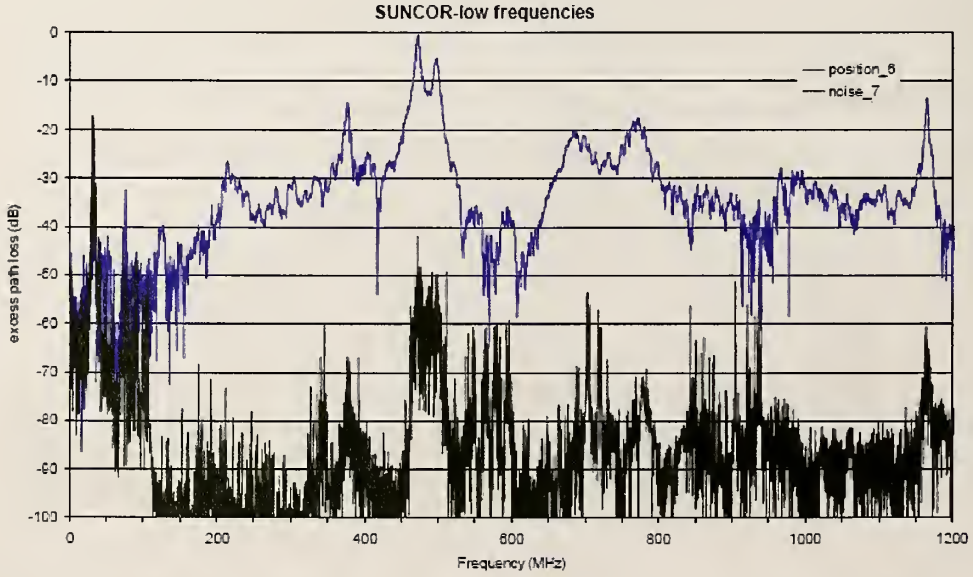

Figure G.3: Excess path loss data from 25 MHz to 1.2 GHz at an oil refinery along a path underneath extensive piping. Distance from the transmitting antenna to the receiving antenna is D = 48.6 m (top) and D = 54.1 m (bottom).

Wideband Excess Path Loss: Oil Refinery

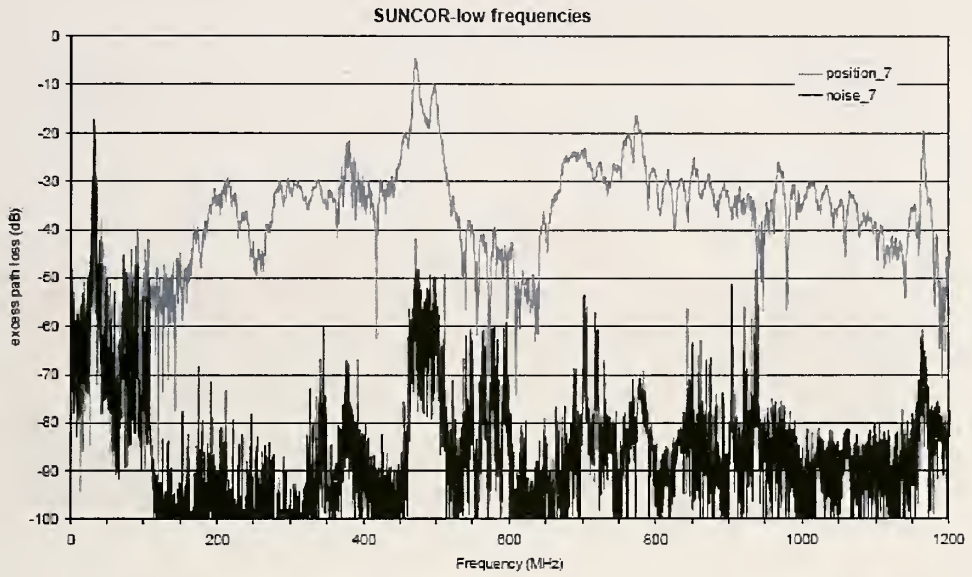

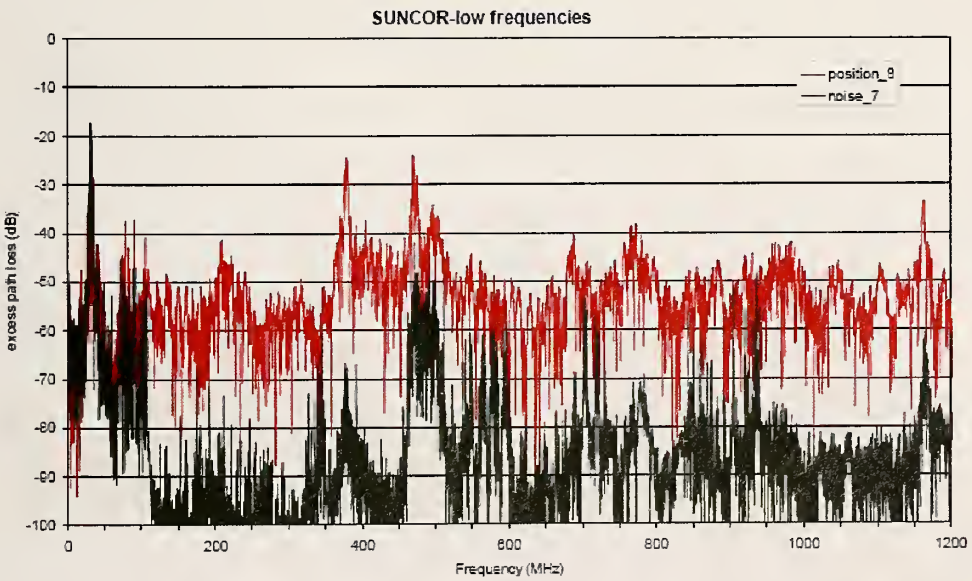

Figure G.4: Excess path loss data from 25 MHz to 1.2 GHz at an oil refinery along a path underneath extensive piping. Distance from the transmitting antenna to the receiving antenna is D = 62.8 m (top) and D = 65.9 m (bottom).

Wideband Excess Path Loss: Oil Refinery

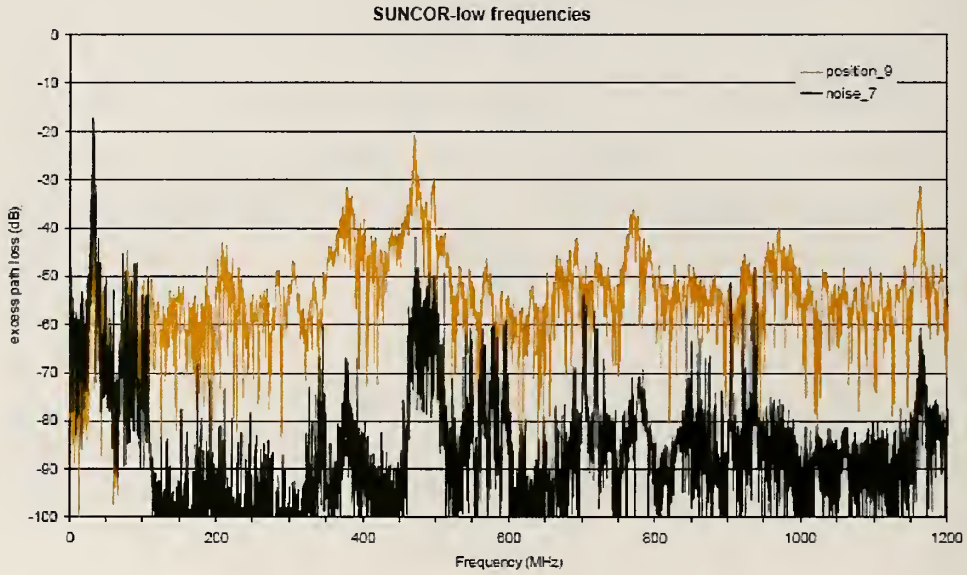

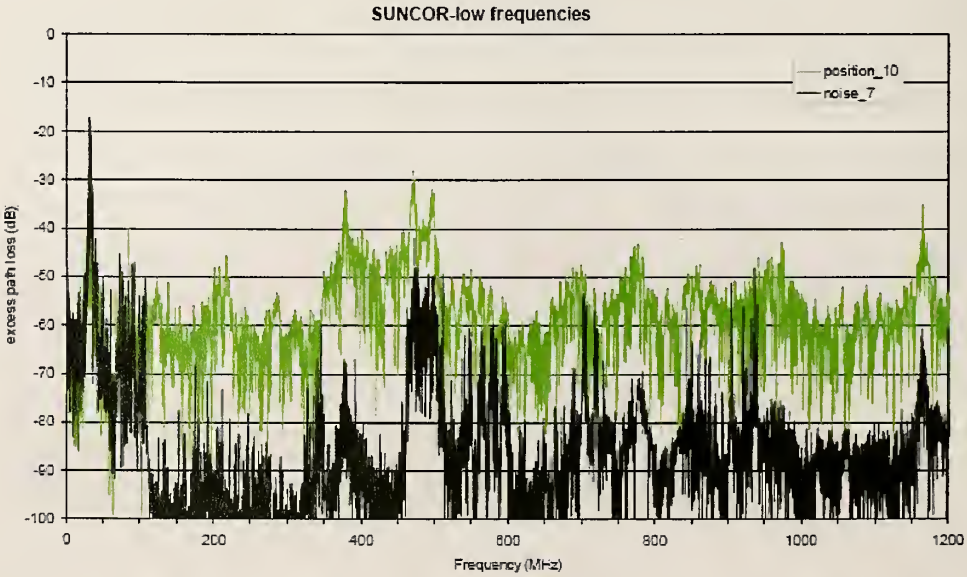

Figure G.5: Excess path loss data from 25 MHz to 1.2 GHz at an oil refinery along a path underneath extensive piping. Distance from the transmitting antenna to the receiving antenna is D = 73.6 m (top) and D = 81.7 m (bottom).

Wideband Excess Path Loss: Oil Refinery

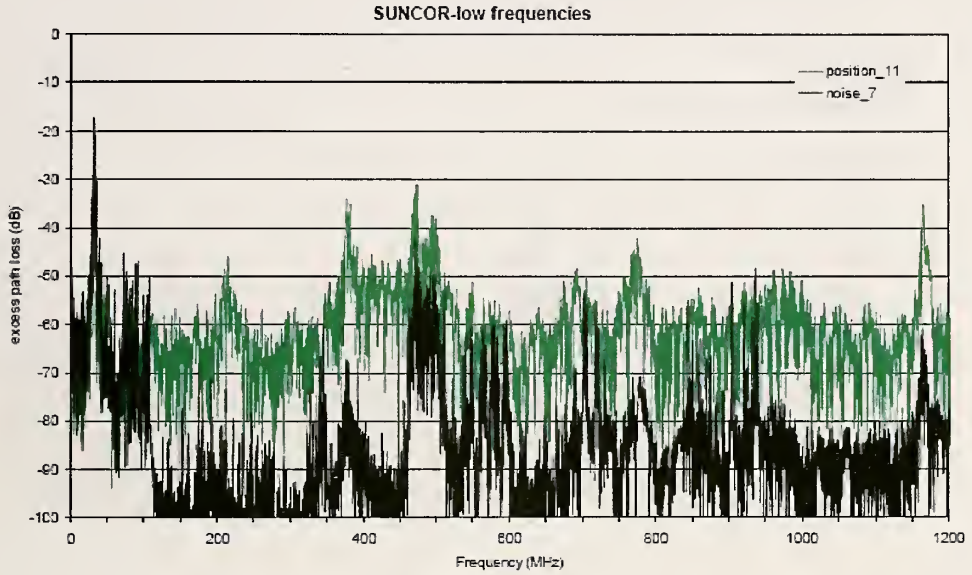

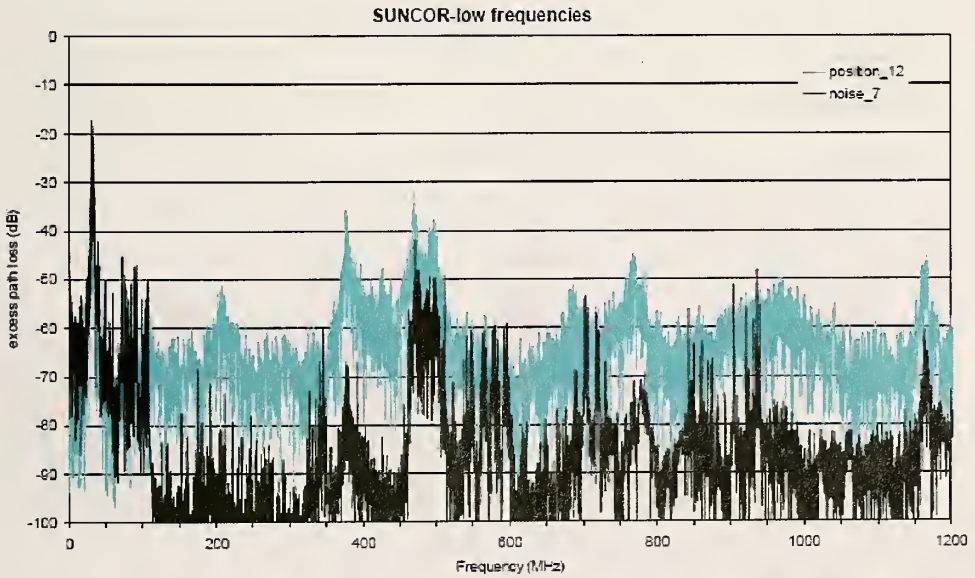

Figure G.6: Excess path loss data from 25 MHz to 1.2 GHz at an oil refinery along a path underneath extensive piping. Distance from the transmitting antenna to the receiving antenna is D = 87.6 m (top) and D = 96.2 m (bottom).

Wideband Excess Path Loss: Oil Refinery

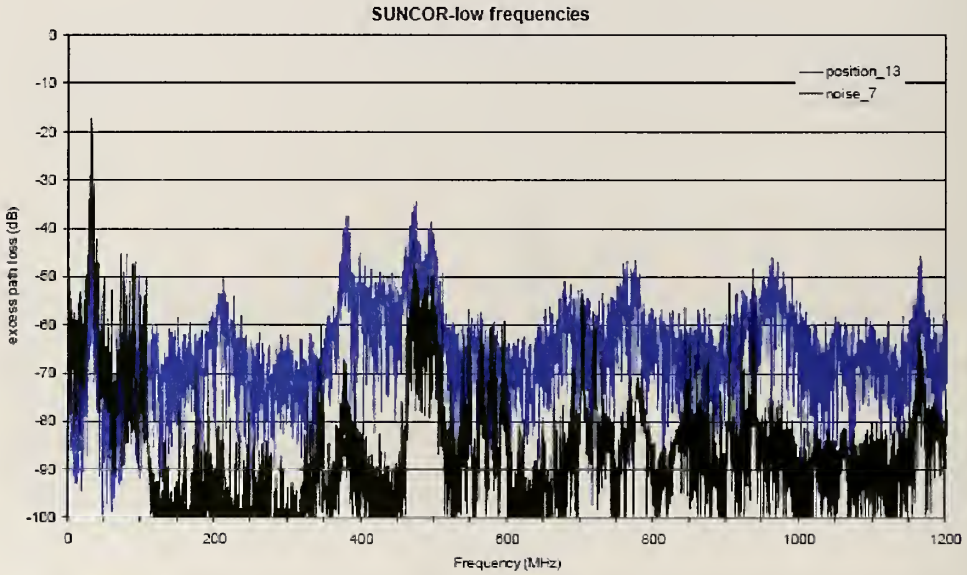

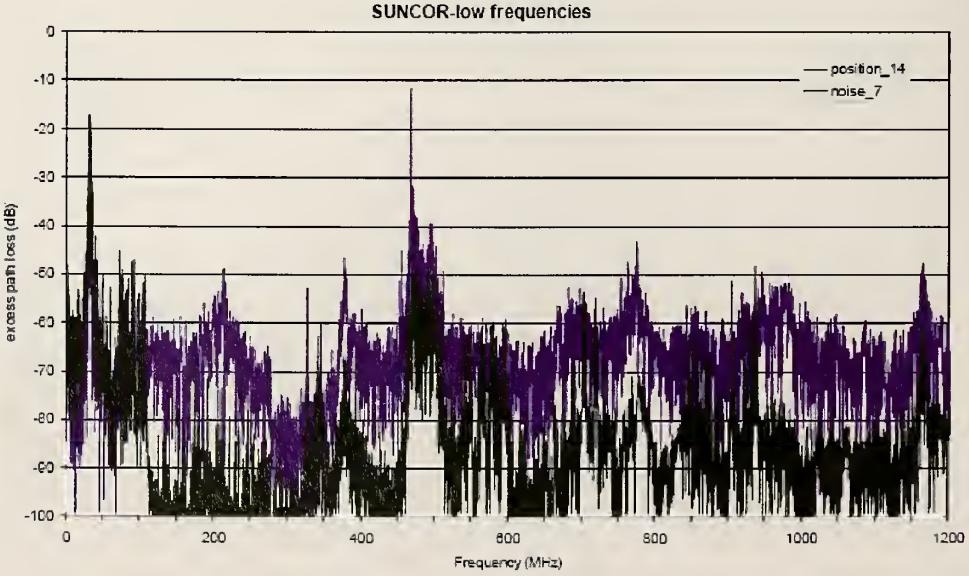

Figure G.7: Excess path loss data from 25 MHz to 1.2 GHz at an oil refinery along a path underneath extensive piping. Distance from the transmitting antenna to the receiving antenna is approx. D = 104 m (top) and D = 112 m (bottom). We assume 8 m separation between test points (this was not measured).

Wideband Excess Path Loss: Oil Refinery

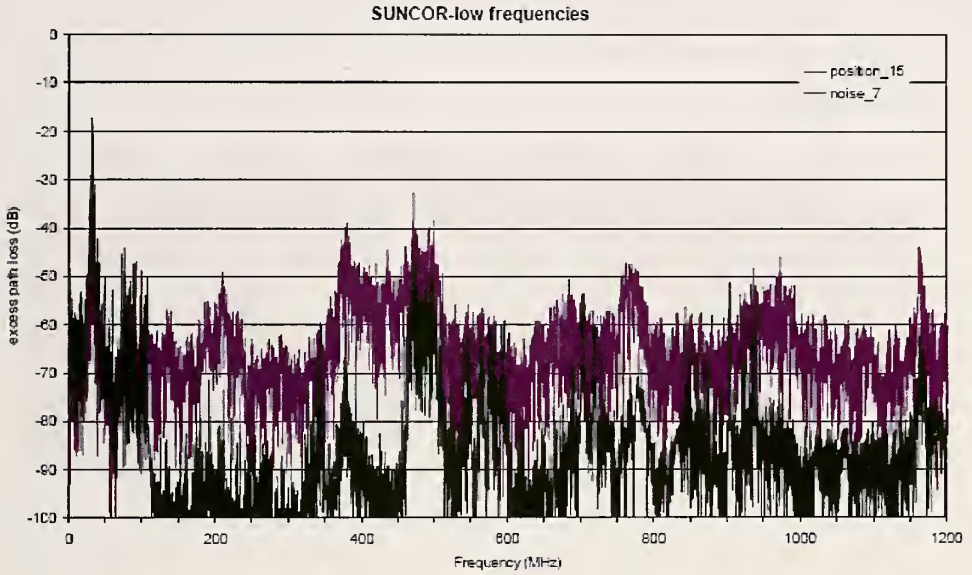

Figure G.8: Excess path loss data from 25 MHz to 1.2 GHz at an oil refinery along a path underneath extensive piping. Distance from the transmitting antenna to the receiving antenna is D = 120 m. We assume 8 m separation between test points (this was not measured).

Wideband Excess Path Loss: Oil Refinery

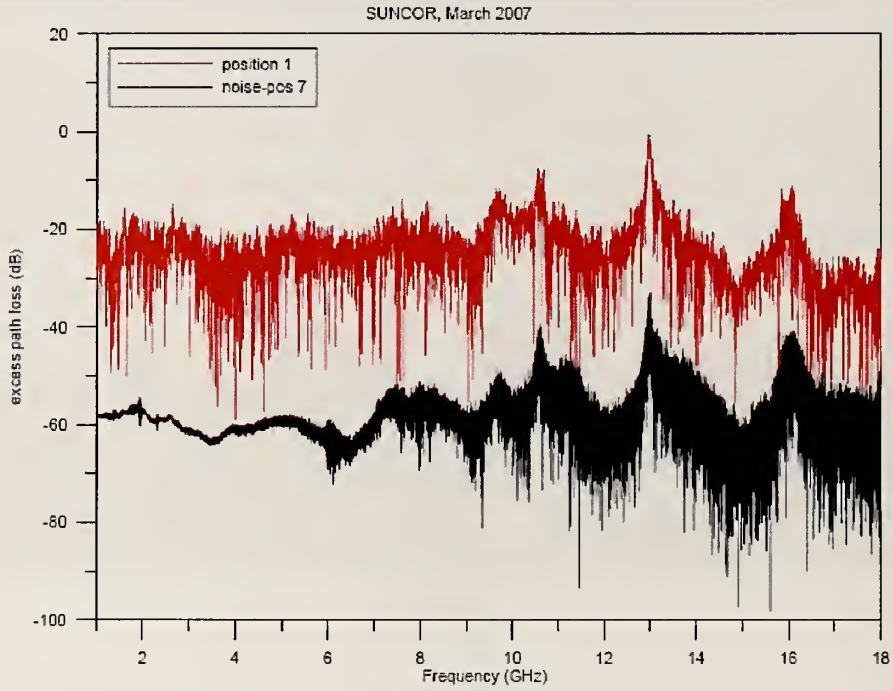

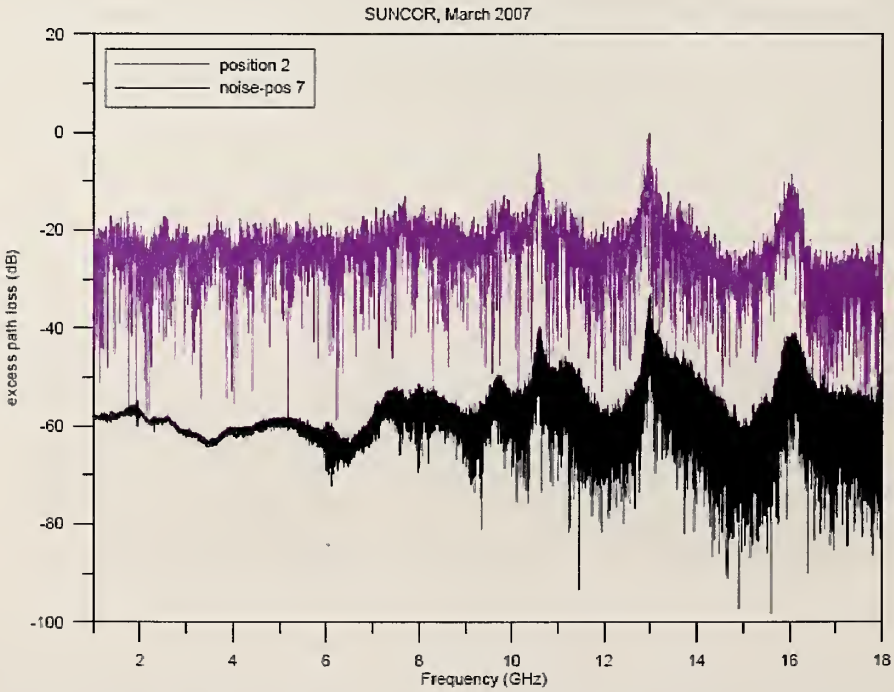

Figure G.9: Excess path loss data from 1 to 18 GHz at an oil refinery along a path underneath extensive piping. Distance from the transmitting antenna to the receiving antenna is D = 20.6 m (top) and D = 26.5 m (bottom).

Wideband Excess Path Loss: Oil Refinery

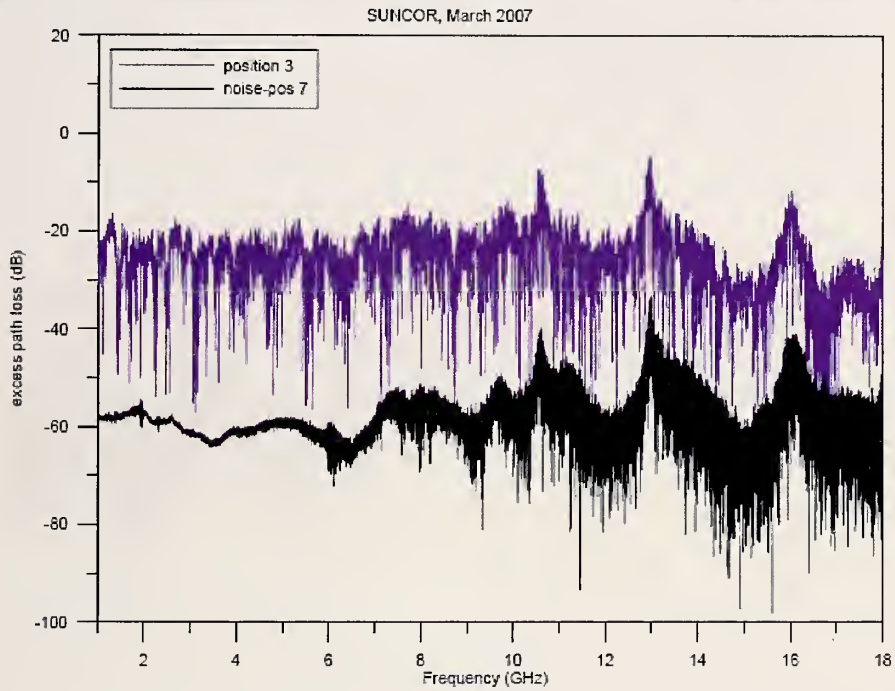

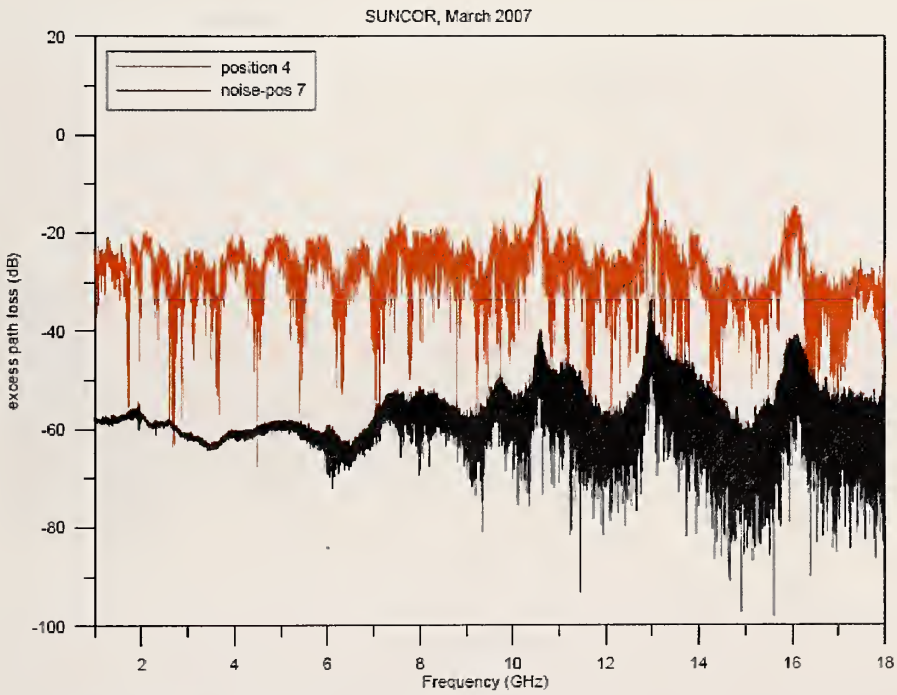

Figure G.10: Excess path loss data from 1 to 18 GHz at an oil refinery along a path underneath extensive piping. Distance from the transmitting antenna to the receiving antenna is D = 32.4 m (top) and D = 40.5 m (bottom).

Wideband Excess Path Loss: Oil Refinery

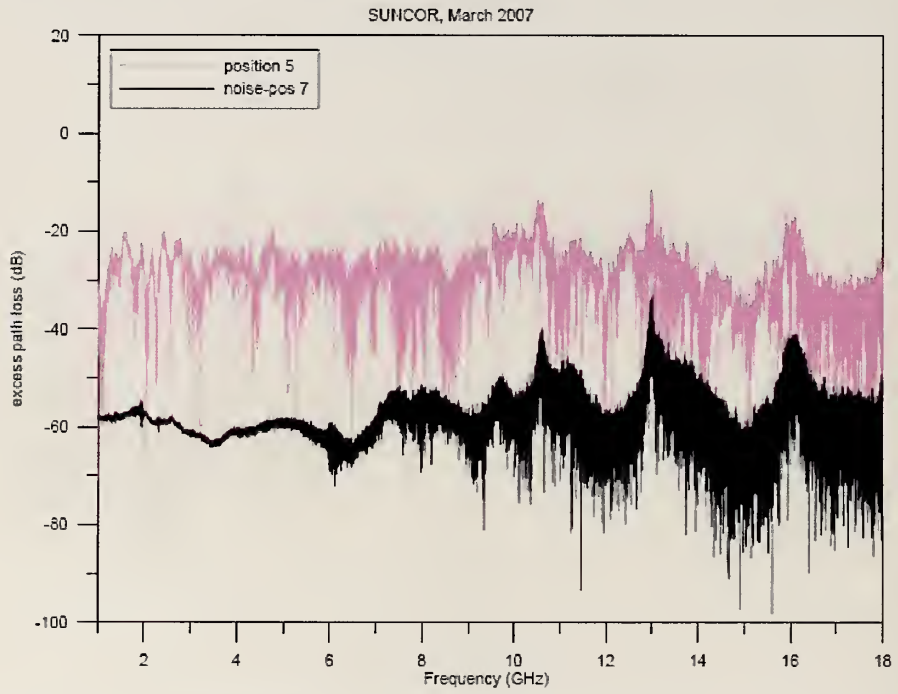

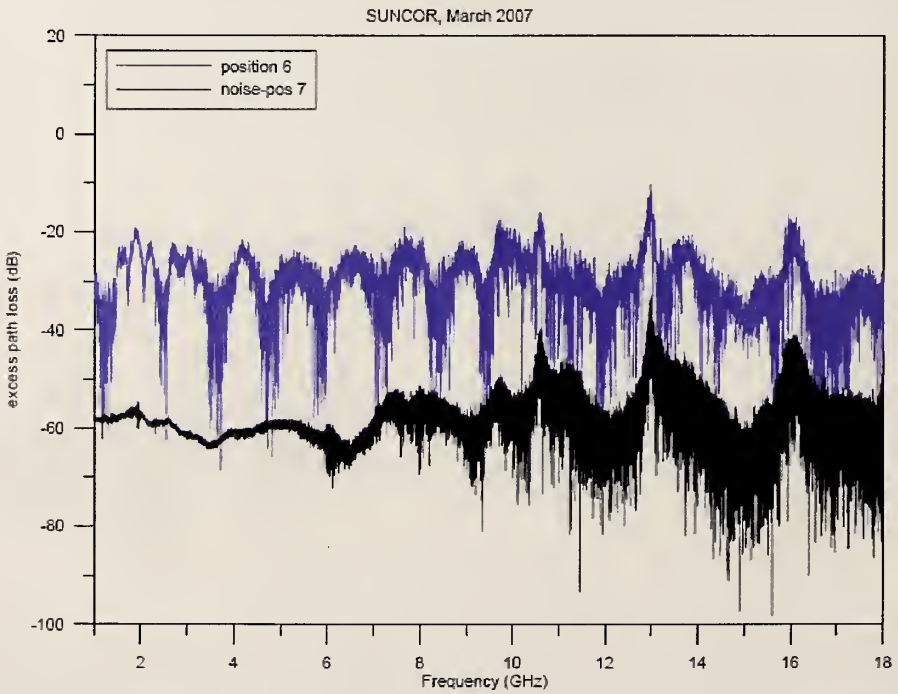

Figure G.11: Excess path loss data from 1 to 18 GHz at an oil refinery along a path underneath extensive piping. Distance from the transmitting antenna to the receiving antenna is D = 48.6 m (top) and D = 54.1 m (bottom).

Wideband Excess Path Loss: Oil Refinery

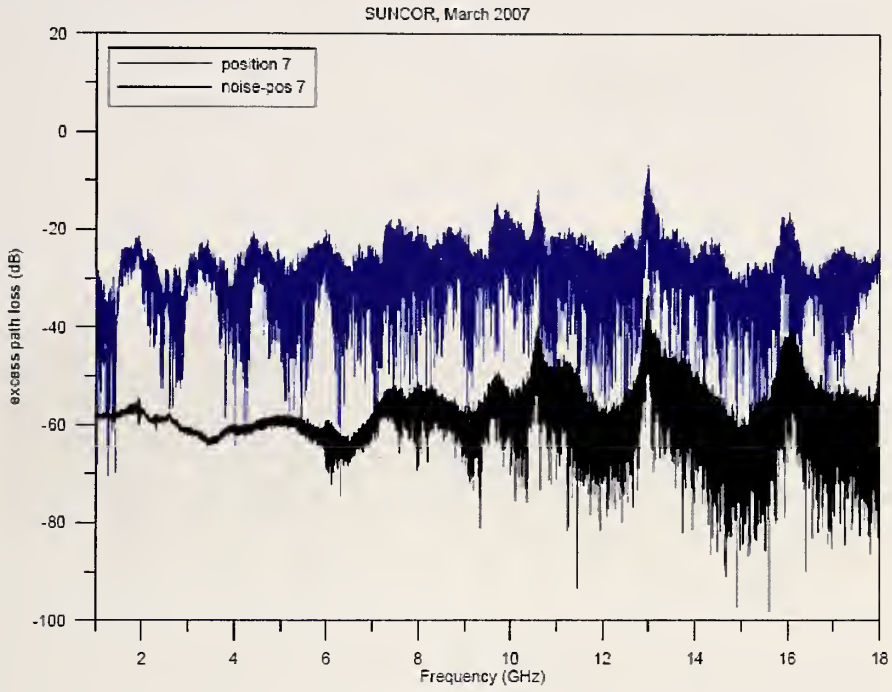

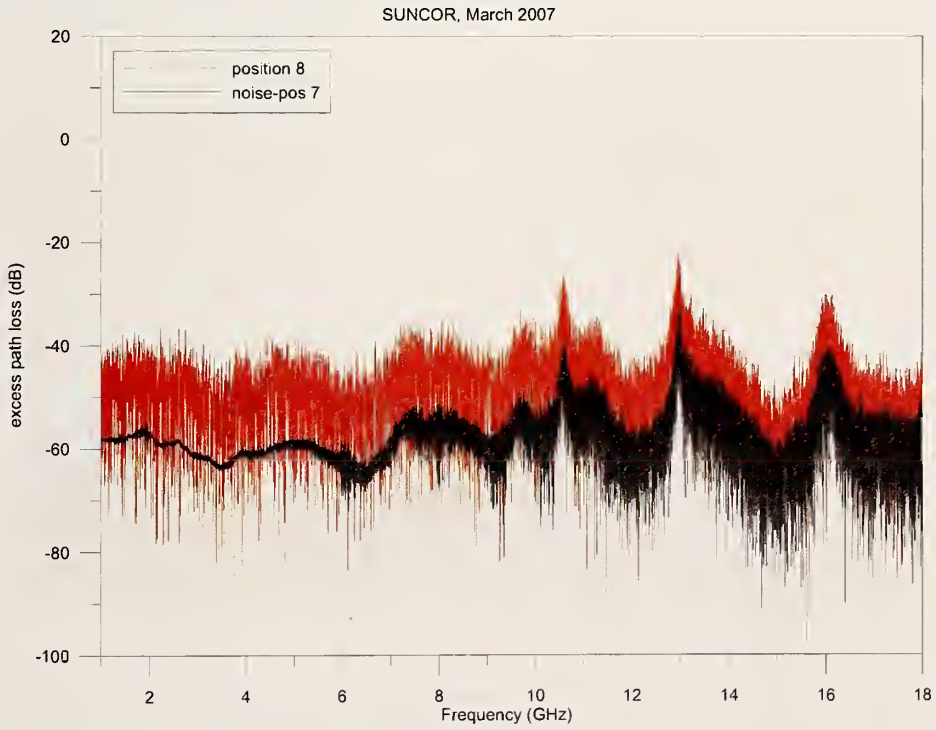

Figure G.12: Excess path loss data from 1 to 18 GHz at an oil refinery along a path underneath extensive piping. Distance from the transmitting antenna to the receiving antenna is D = 62.8 m (top) and D = 65.9 m (bottom).

Wideband Excess Path Loss: Oil Refinery

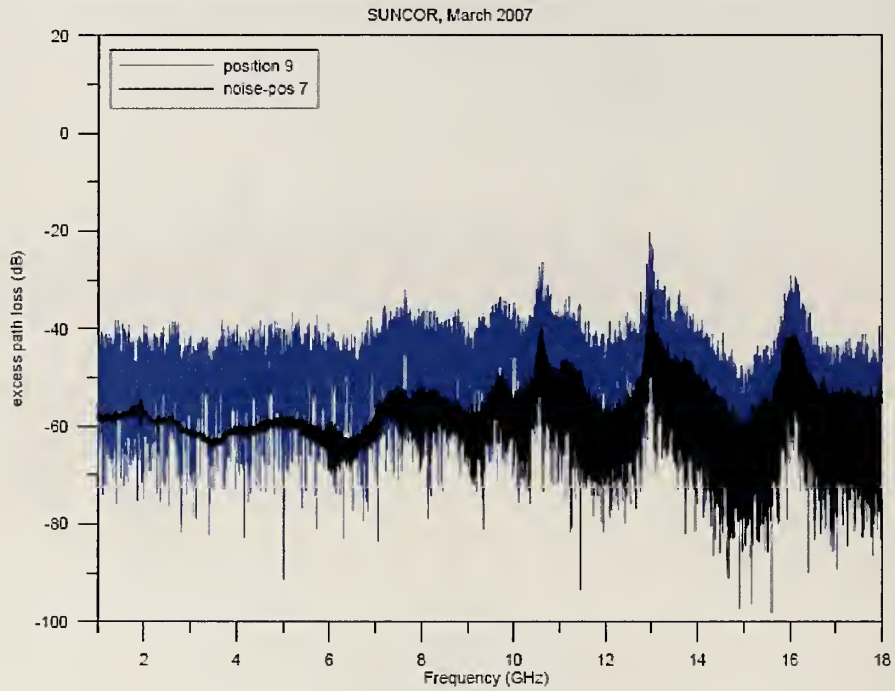

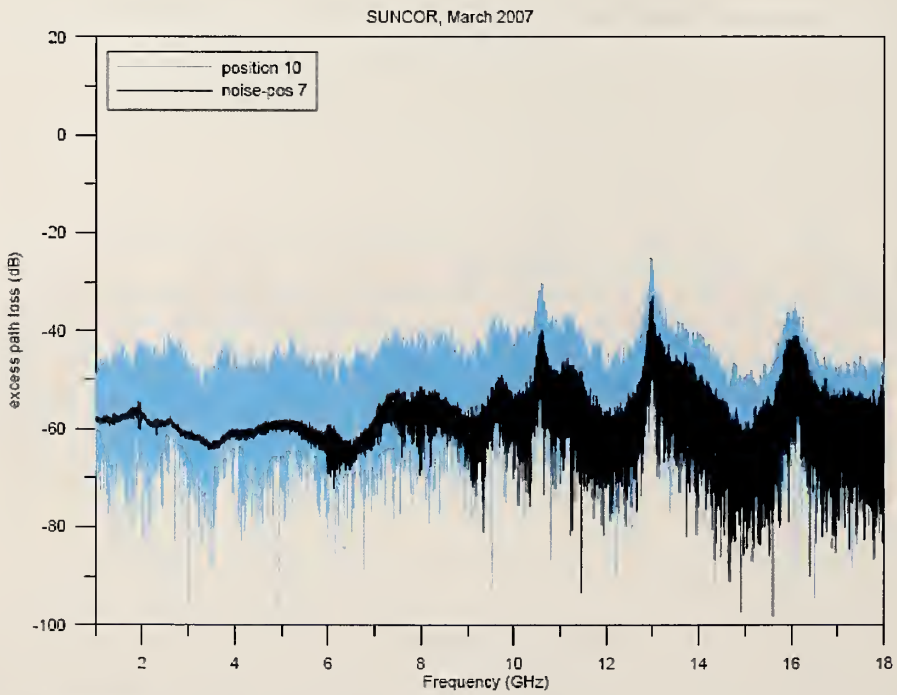

Figure G.13: Excess path loss data from 1 to 18 GHz at an oil refinery along a path underneath extensive piping. Distance from the transmitting antenna to the receiving antenna is D = 73.6 m (top) and D = 81.7 m (bottom).

Wideband Excess Path Loss: Oil Refinery

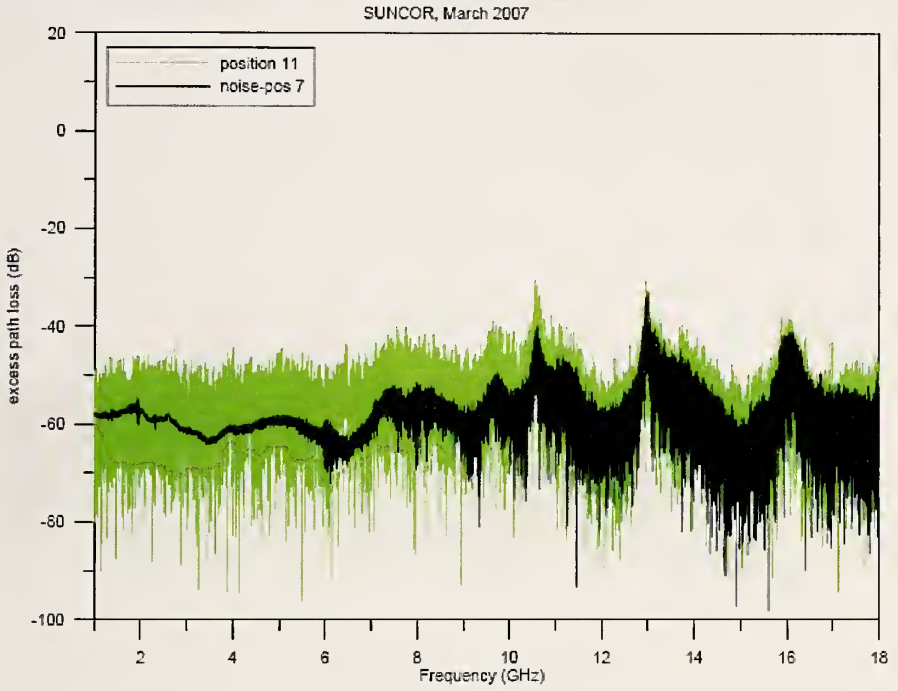

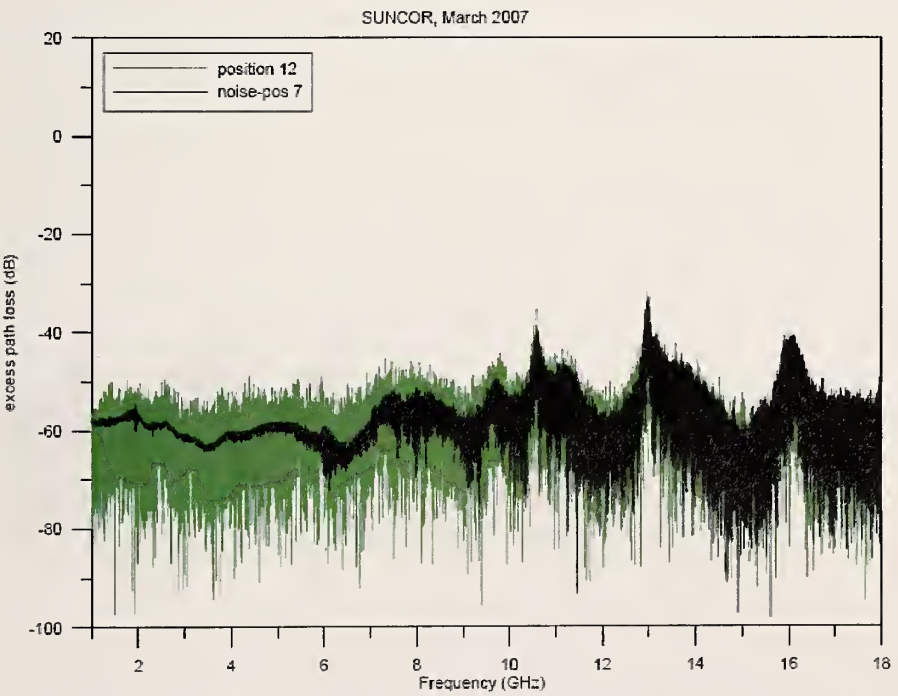

Figure G.14: Excess path loss data from 1 to 18 GHz at an oil refinery along a path underneath extensive piping. Distance from the transmitting antenna to the receiving antenna is D = 87.6 m (top) and D = 96.2 m (bottom).

Wideband Excess Path Loss: Oil Refinery

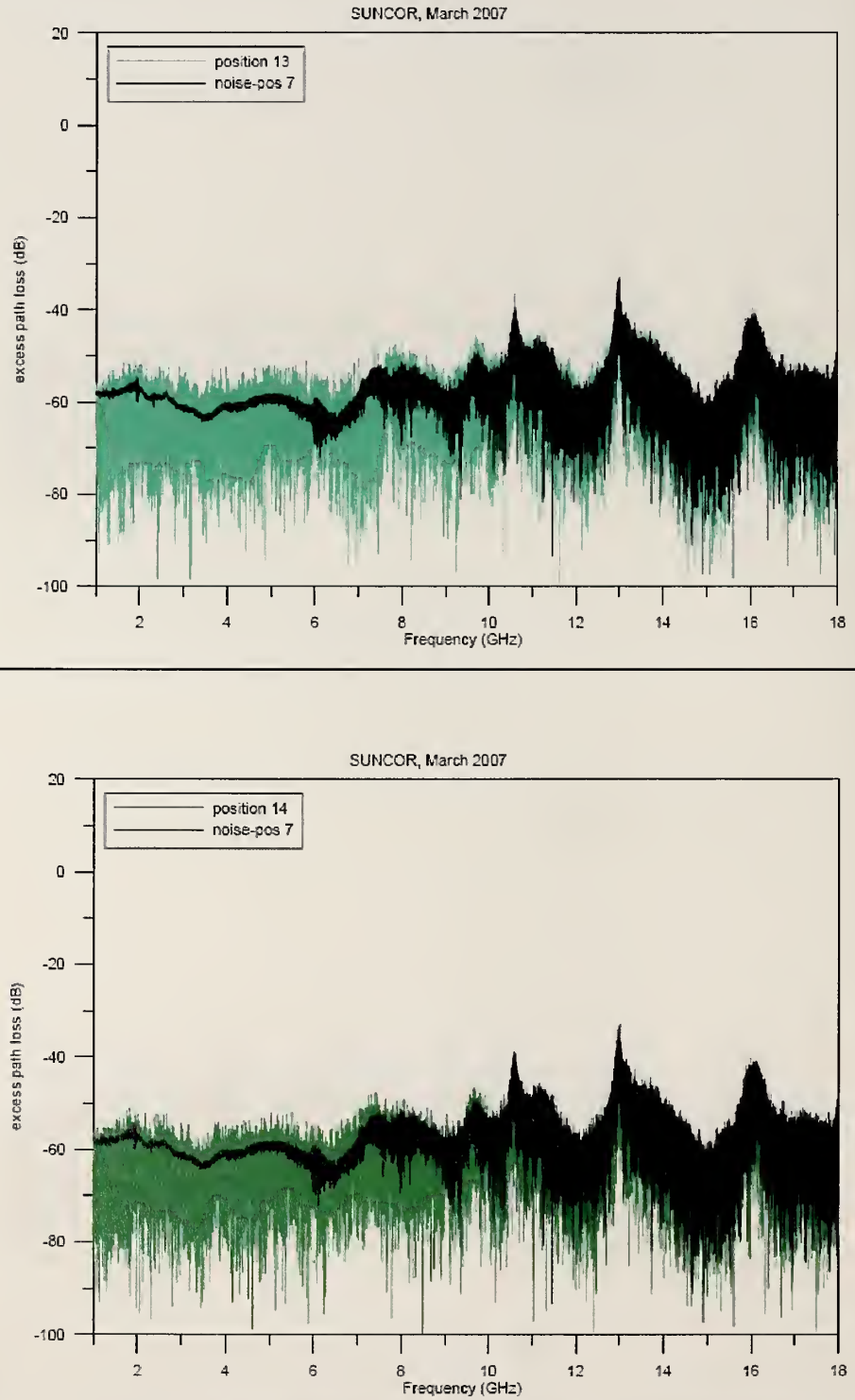

Figure G.15: Excess path loss data from 1 to 18 GHz at an oil refinery along a path underneath extensive piping. Distance from the transmitting antenna to the receiving antenna is approximately D = 107 m (top) and D = 17 m (bottom).

Wideband Excess Path Loss: Oil Refinery

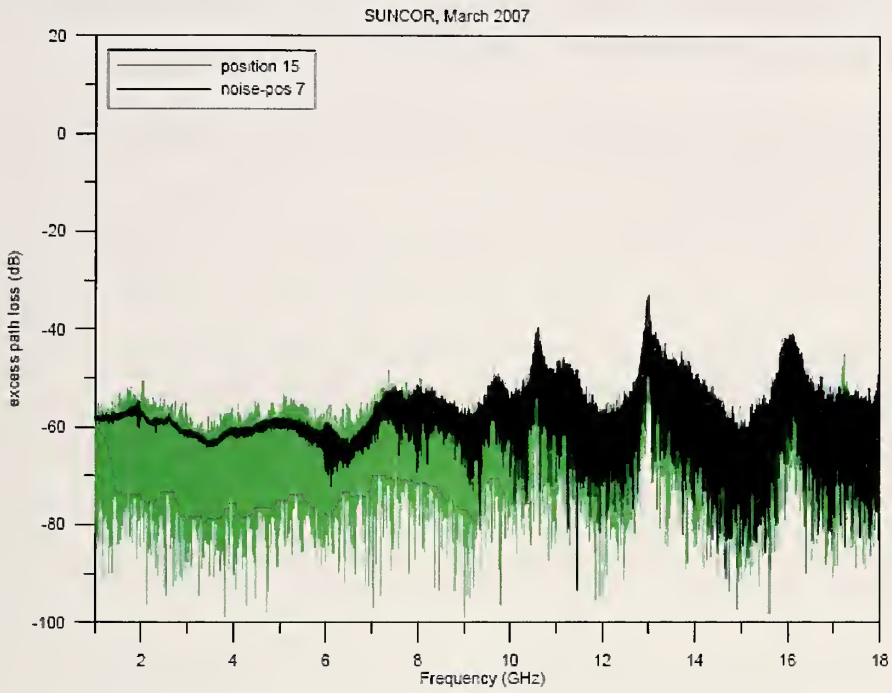

Figure G.16: Excess path loss data from 1 to 18 GHz at an oil refinery along a path underneath extensive piping. Distance from the transmitting antenna to the receiving antenna is approximately D = 130 m.

Appendix H: Wideband Excess Path Loss Measured With a Synthetic-Pulse Vector-Network-Analyzer-Based System: Subterranean Tunnels

The following pages contain the complete set of measured data for the subterranean tunnels (Section 6.3).

Wideband Excess Path Loss: Subterranean Tunnels

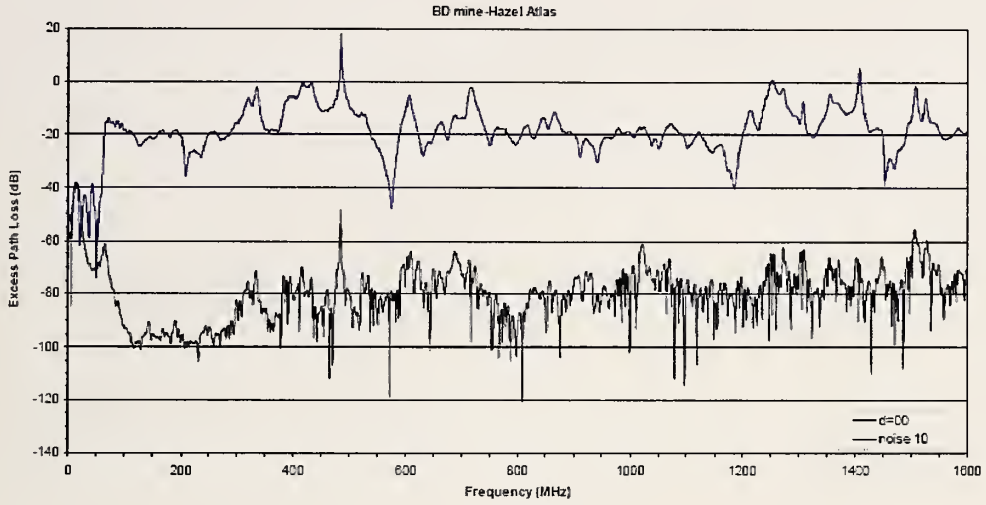

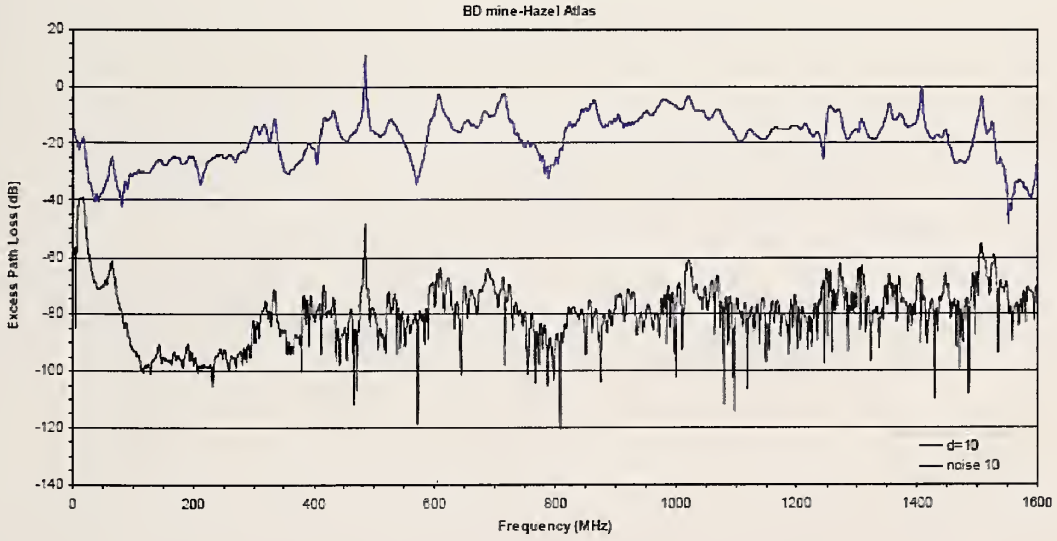

Figure H.1: Excess path loss data from 25 MHz to 1.6 GHz from the Hazel-Atlas tunnel. Distance from the transmitting antenna to the receiving antenna is D = 0 m (top) and D = 10 m (bottom).

Wideband Excess Path Loss: Subterranean Tunnels

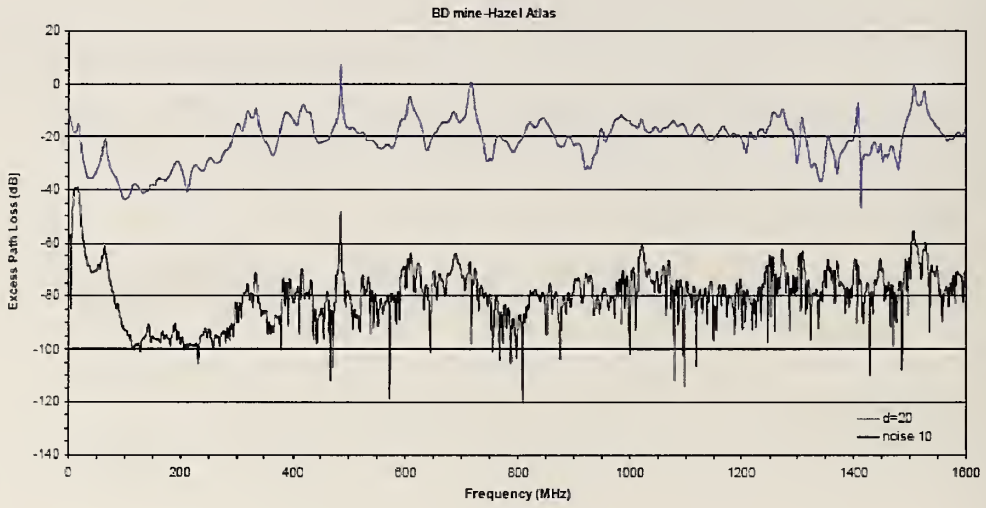

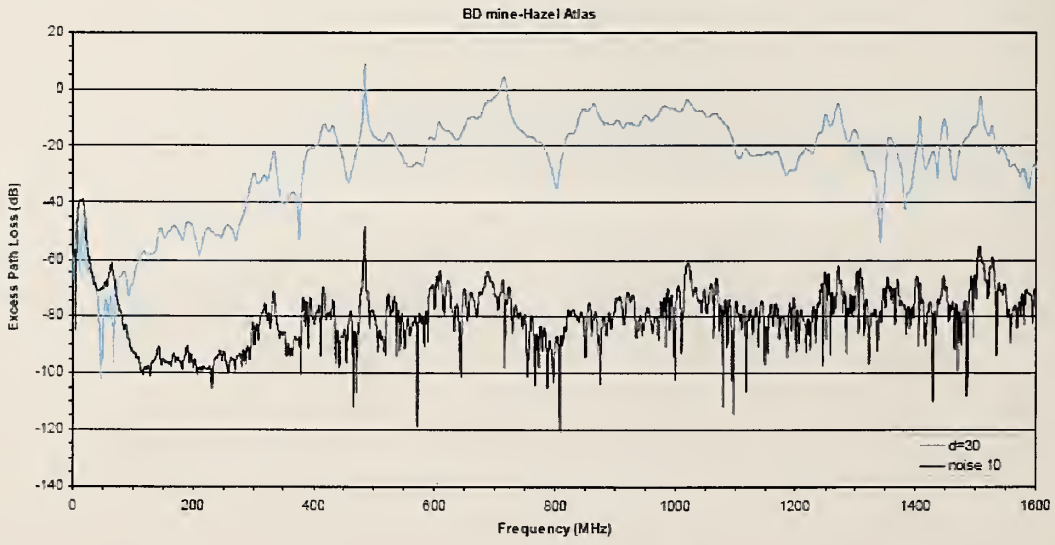

Figure H.2: Excess path loss data from 25 MHz to 1.6 GHz from the Hazel-Atlas tunnel. Distance from the transmitting antenna to the receiving antenna is D = 20 m (top) and D = 30 m (bottom).

Wideband Excess Path Loss: Subterranean Tunnels

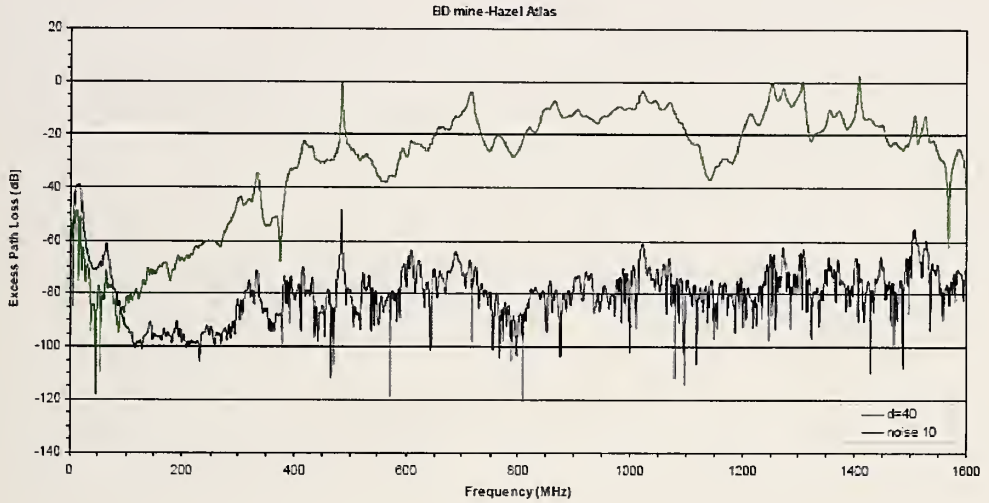

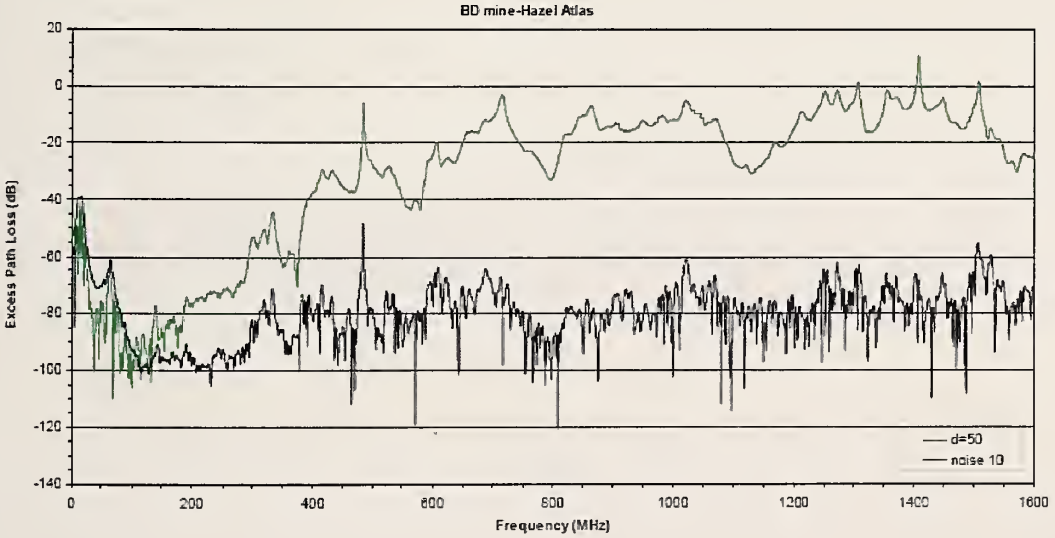

Figure H.3: Excess path loss data from 25 MHz to 1.6 GHz from the Hazel-Atlas tunnel. Distance from the transmitting antenna to the receiving antenna is D = 40 m (top) and D = 50 m (bottom).

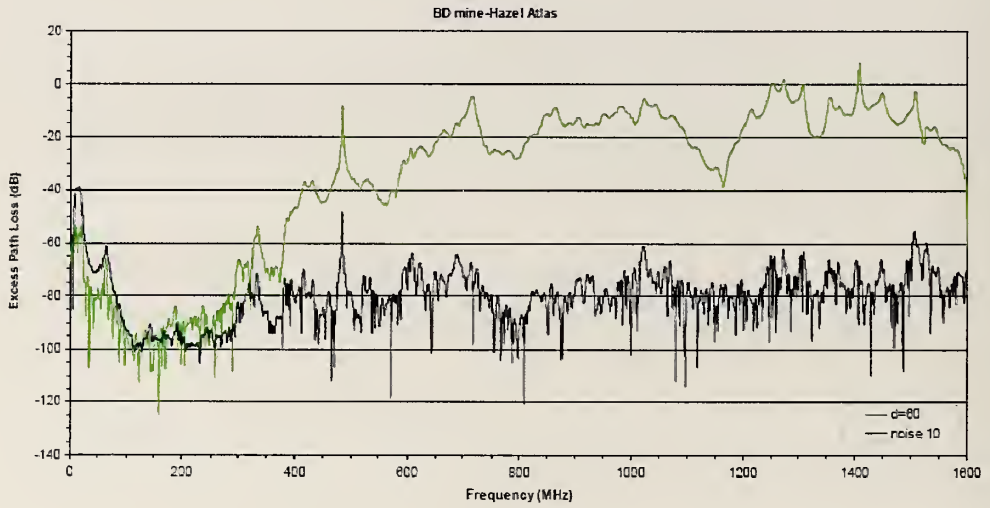

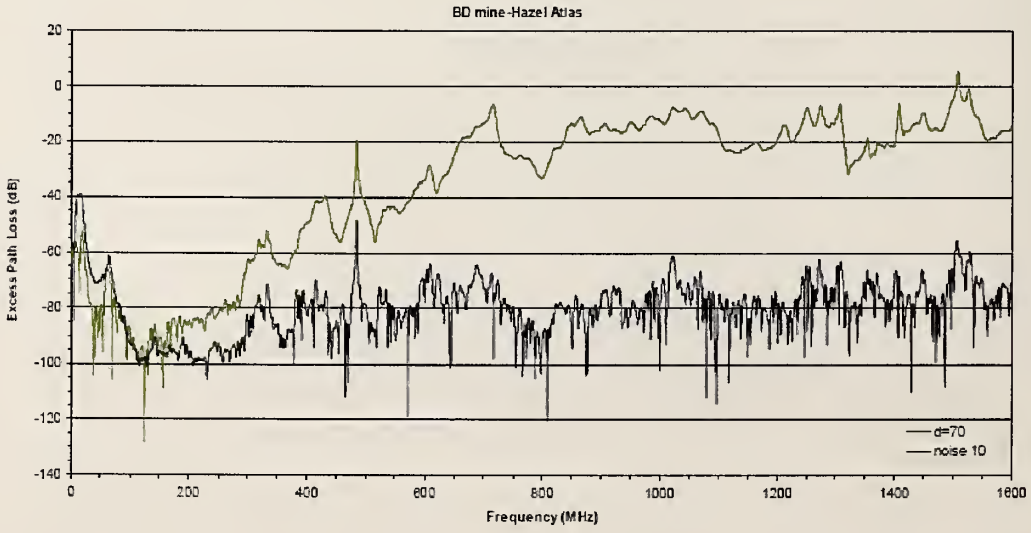

Figure H.4: Excess path loss data from 25 MHz to 1.6 GHz from the Hazel-Atlas tunnel. Distance from the transmitting antenna to the receiving antenna is D = 60 m (top) and D = 70 m (bottom).

Wideband Excess Path Loss: Subterranean Tunnels

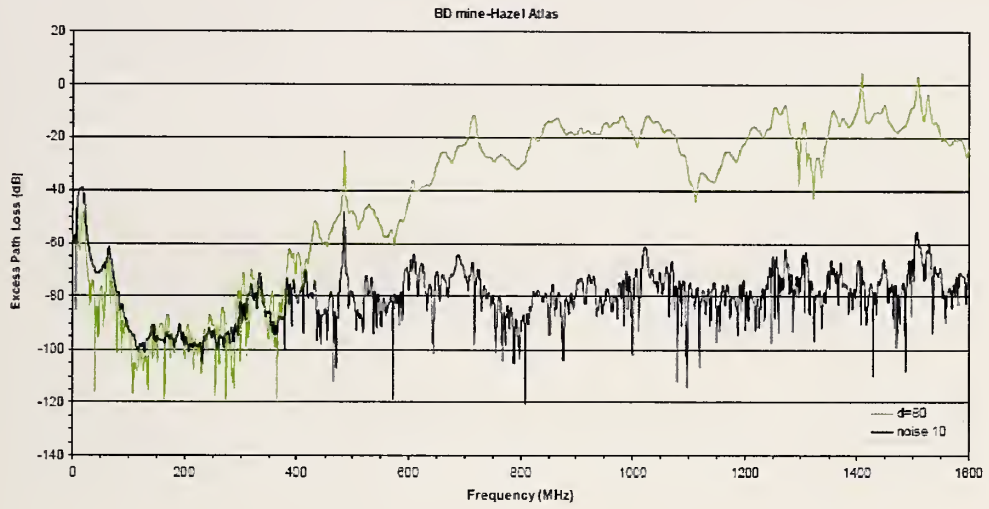

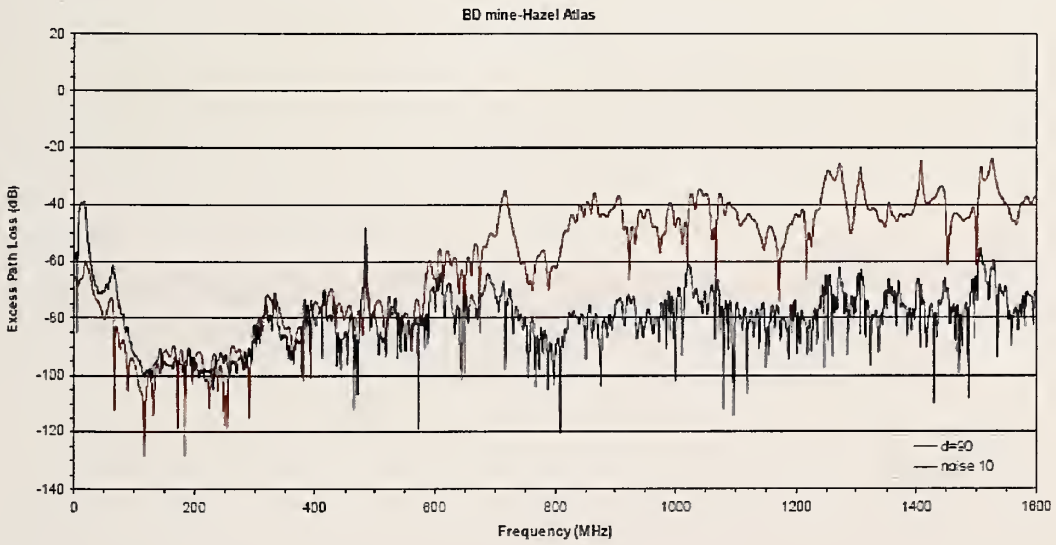

Figure H.5: Excess path loss data from 25 MHz to 1.6 GHz from the Hazel-Atlas tunnel. Distance from the transmitting antenna to the receiving antenna is D = 80 m (top) and D = 90 m (bottom).

Wideband Excess Path Loss: Subterranean Tunnels

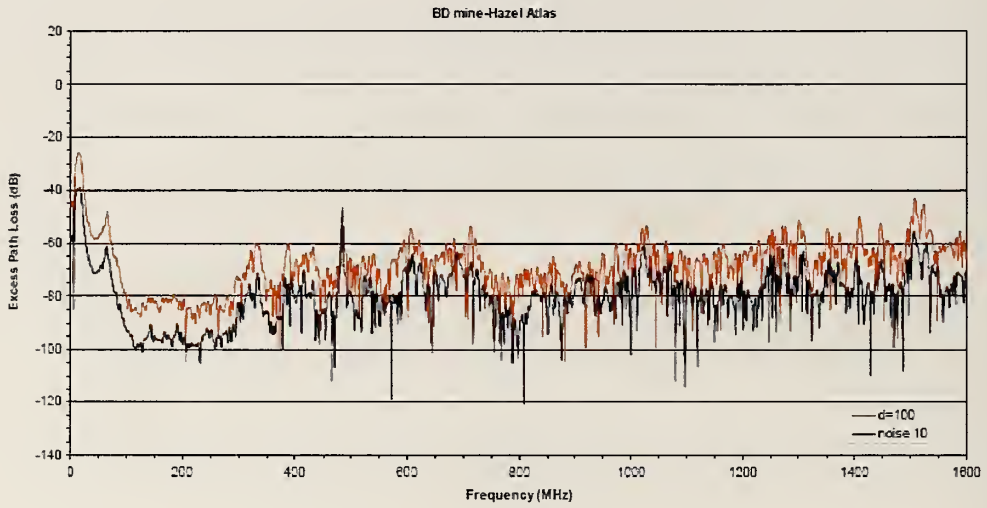

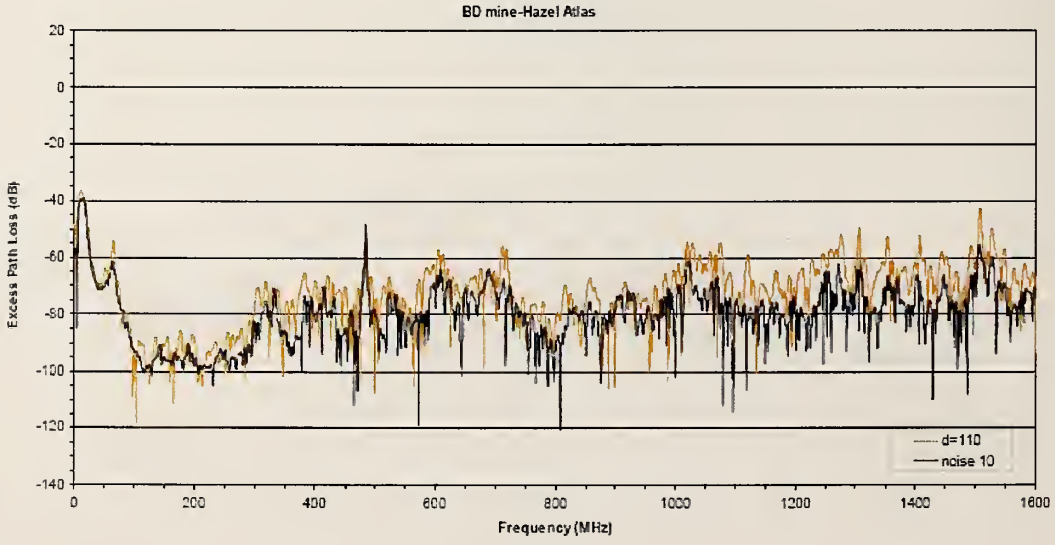

Figure H.6: Excess path loss data from 25 MHz to 1.6 GHz from the Hazel-Atlas tunnel. Distance from the transmitting antenna to the receiving antenna is D = 100 m (top) and D = 110 m (bottom).

Wideband Excess Path Loss: Subterranean Tunnels

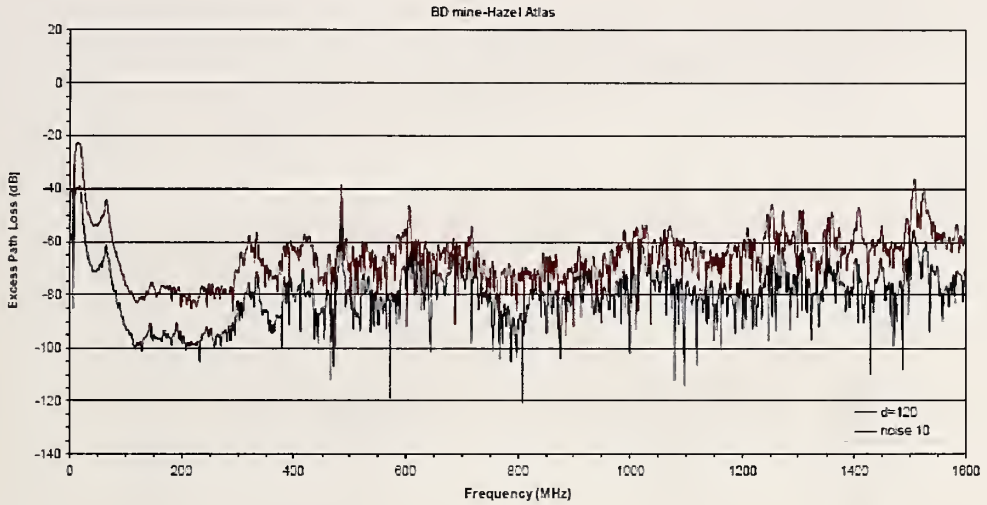

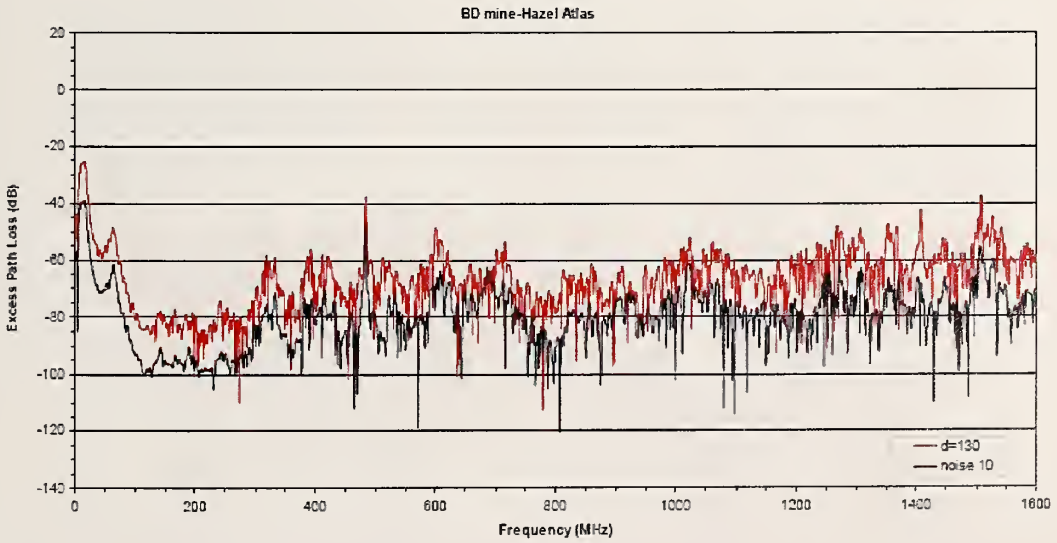

Figure H.7: Excess path loss data from 25 MHz to 1.6 GHz from the Hazel-Atlas tunnel. Distance from the transmitting antenna to the receiving antenna is D = 120 m (top) and D = 130 m (bottom).

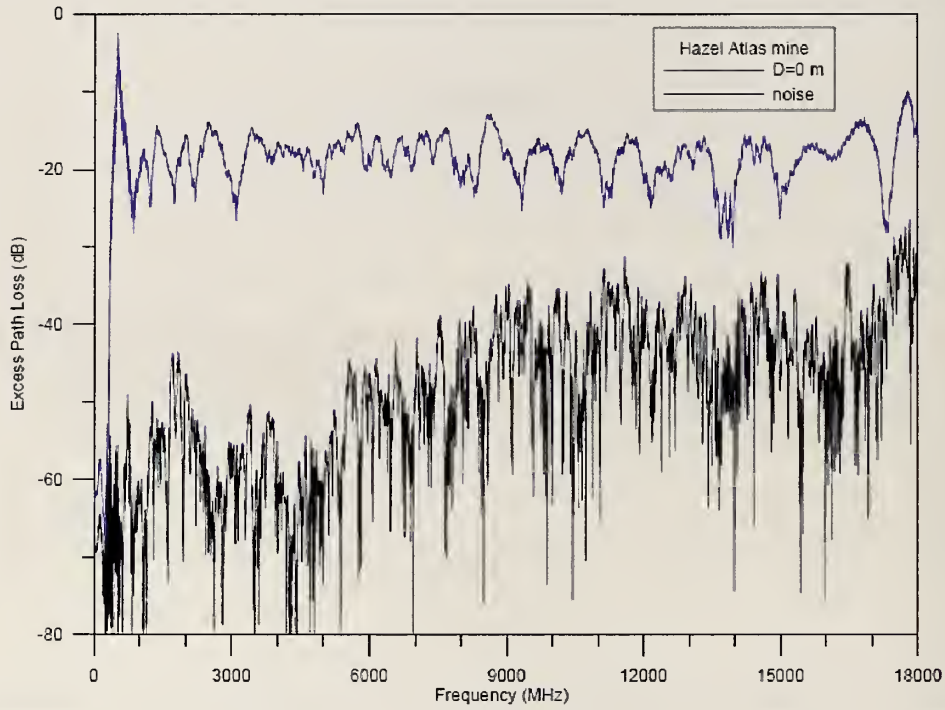

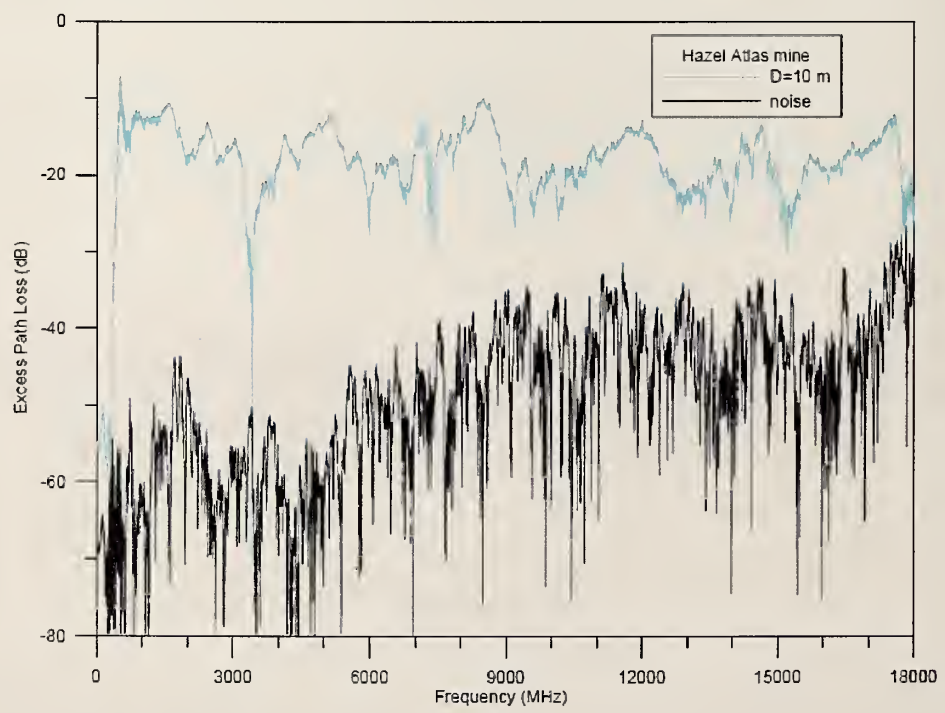

Figure H.8: Excess path loss data from 1 GHz to 18 GHz from the Hazel-Atlas tunnel. Distance from the transmitting antenna to the receiving antenna is D = 0 m (top) and D = 10 m (bottom).

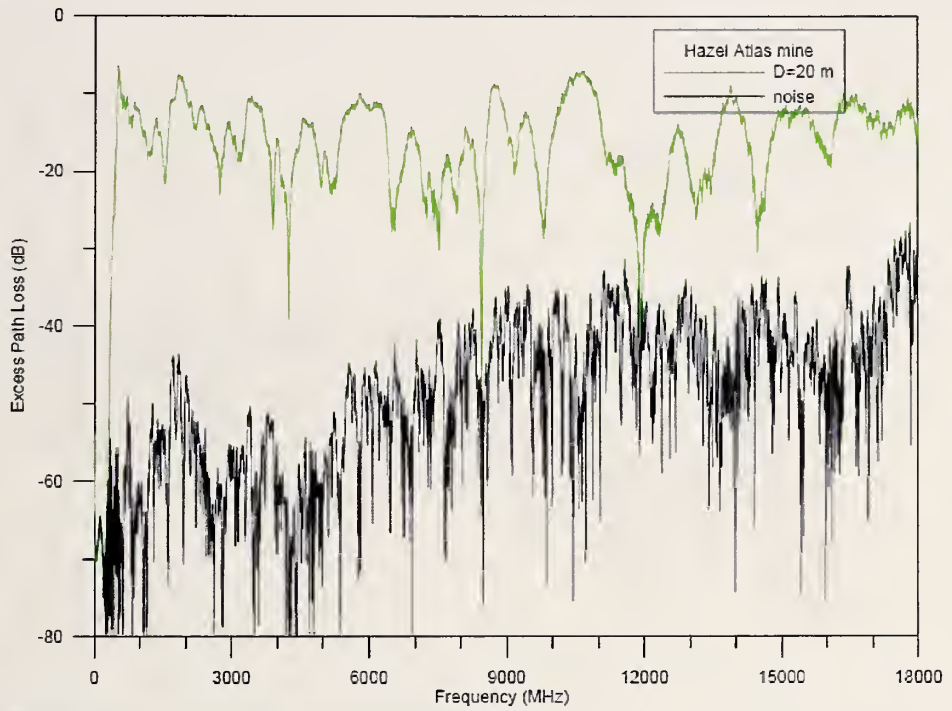

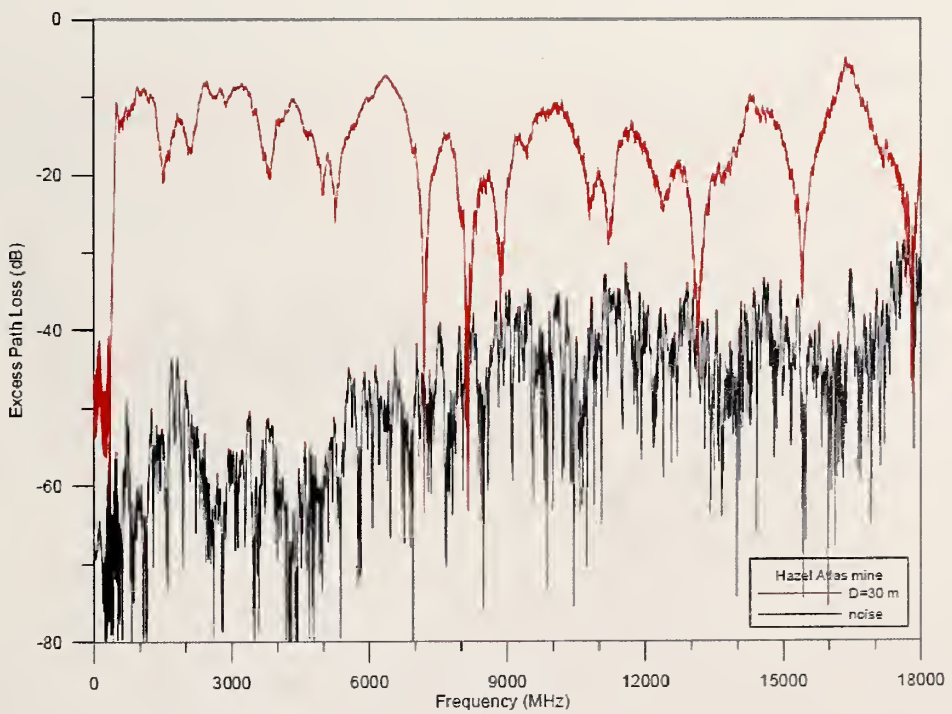

Figure H.9: Excess path loss data from 1 GHz to 18 GHz from the Hazel-Atlas tunnel. Distance from the transmitting antenna to the receiving antenna is D = 20 m (top) and D = 30 m (bottom).

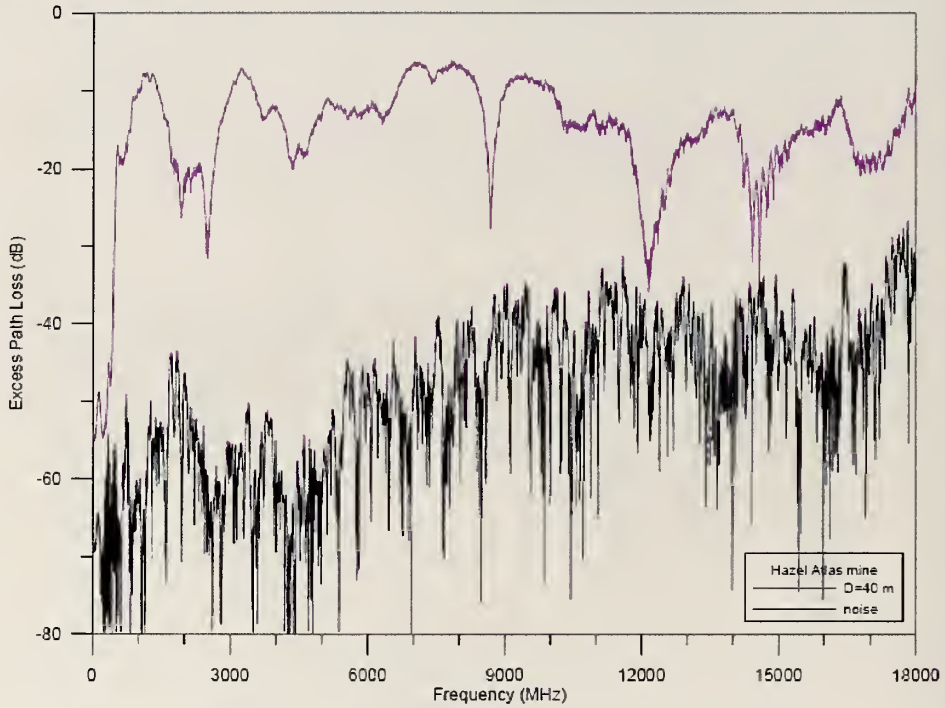

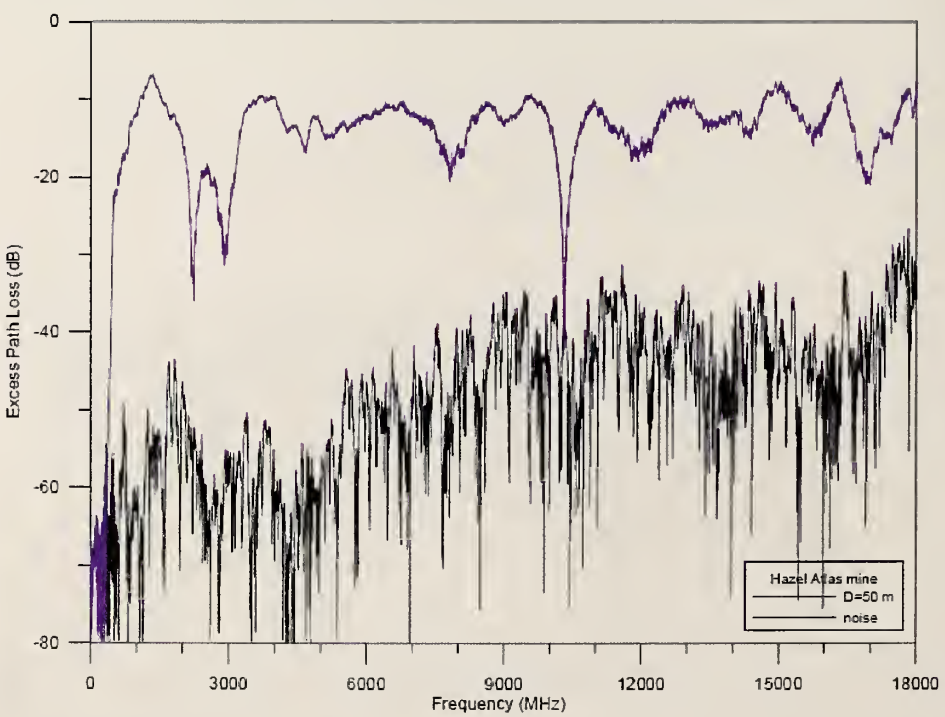

Figure H.10: Excess path loss data from 1 GHz to 18 GHz from the Hazel-Atlas tunnel. Distance from the transmitting antenna to the receiving antenna is D = 40 m (top) and D = 50 m (bottom).

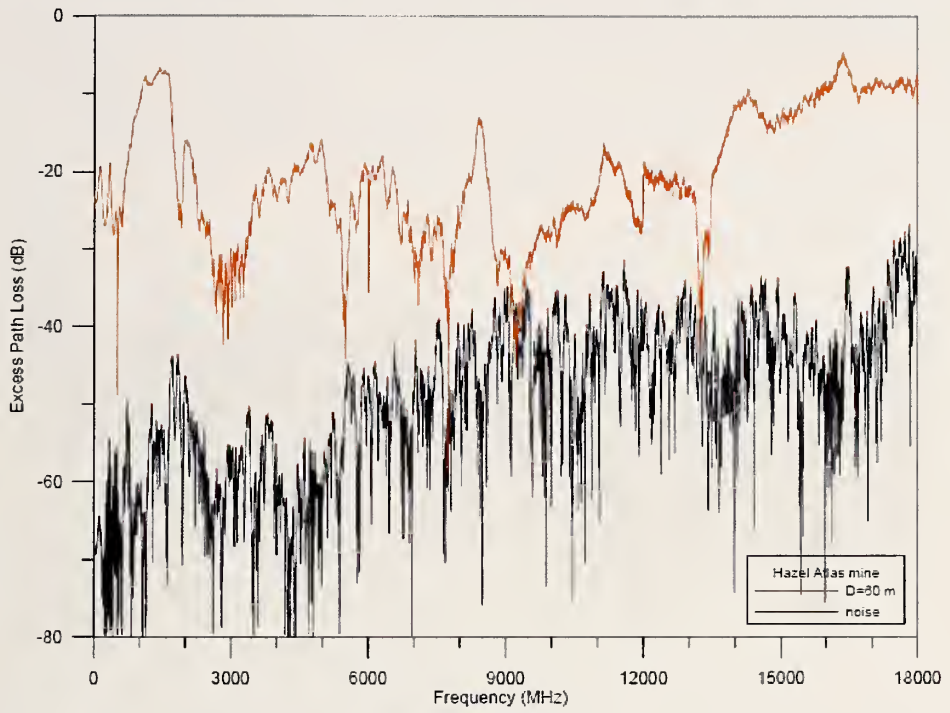

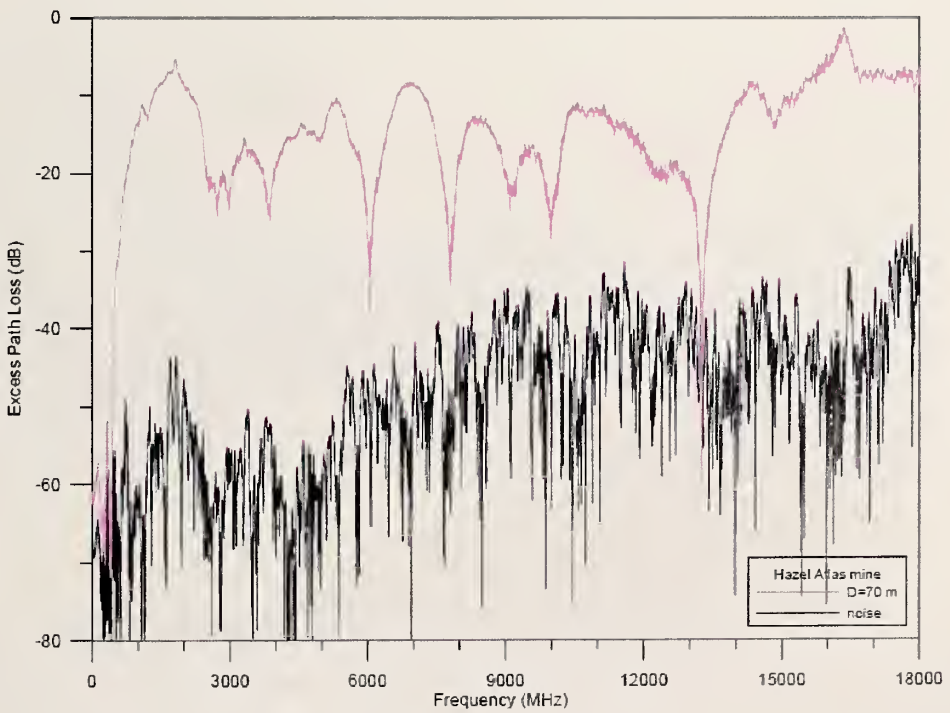

Figure H.11: Excess path loss data from 1 GHz to 18 GHz from the Hazel-Atlas tunnel. Distance from the transmitting antenna to the receiving antenna is D = 60 m (top) and D = 70 m (bottom).

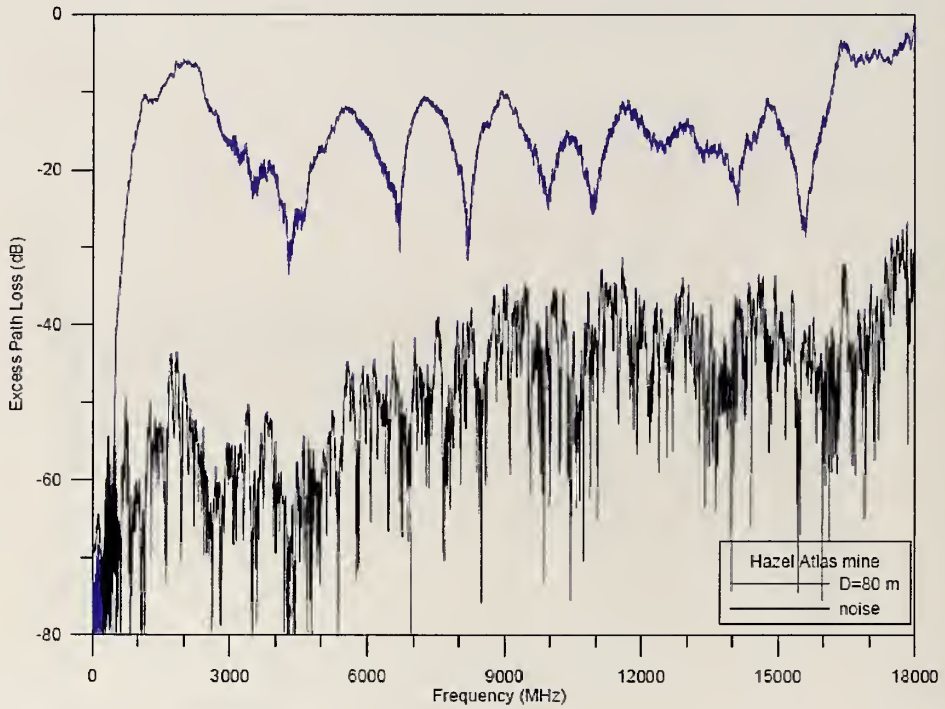

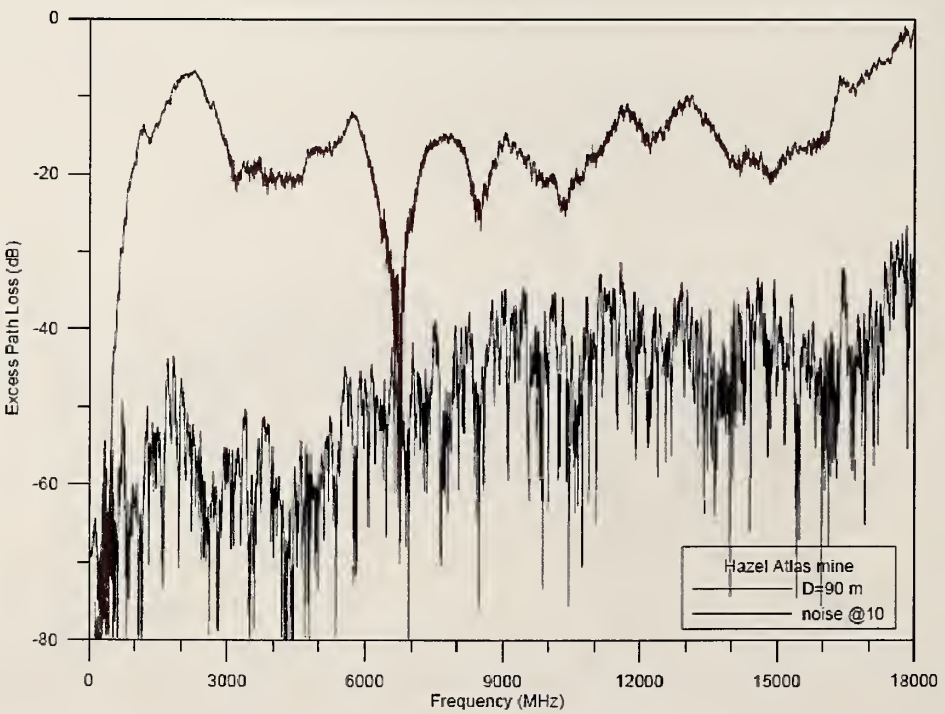

Figure H.12: Excess path loss data from 1 GHz to 18 GHz from the Hazel-Atlas tunnel. Distance from the transmitting antenna to the receiving antenna is D = 80 m (top) and D = 90 m (bottom).

Wideband Excess Path Loss: Subterranean Tunnels

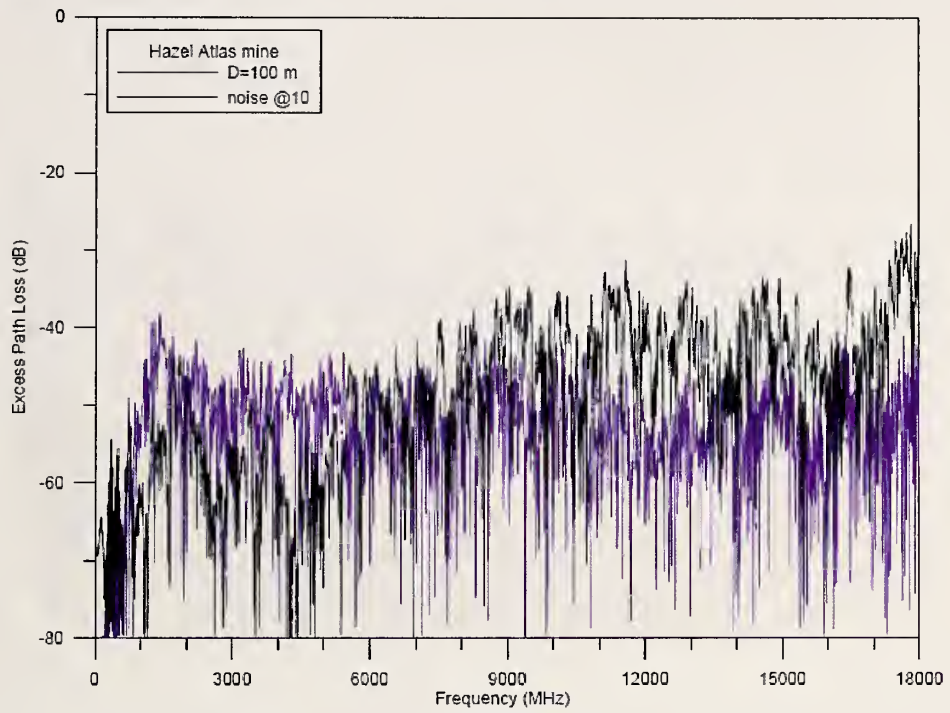

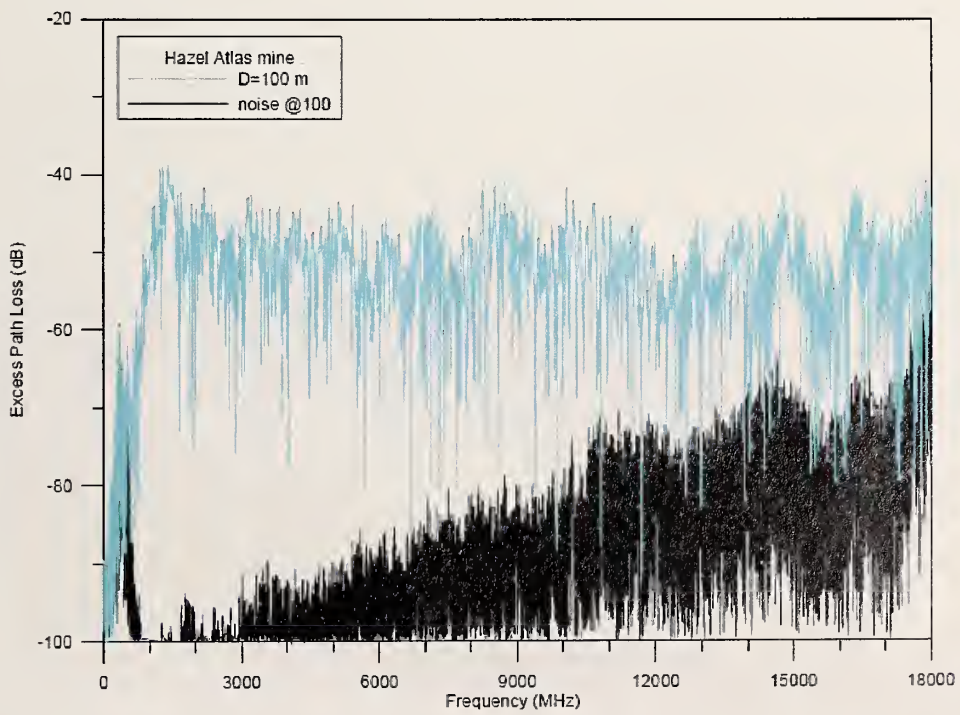

Figure H.13: Excess path loss data from 1 GHz to 18 GHz from the Hazel-Atlas tunnel. Distance from the transmitting antenna to the receiving antenna is D = 100 m (top) and (bottom), with a noise reference at 100 m for increased range.

Wideband Excess Path Loss: Subterranean Tunnels

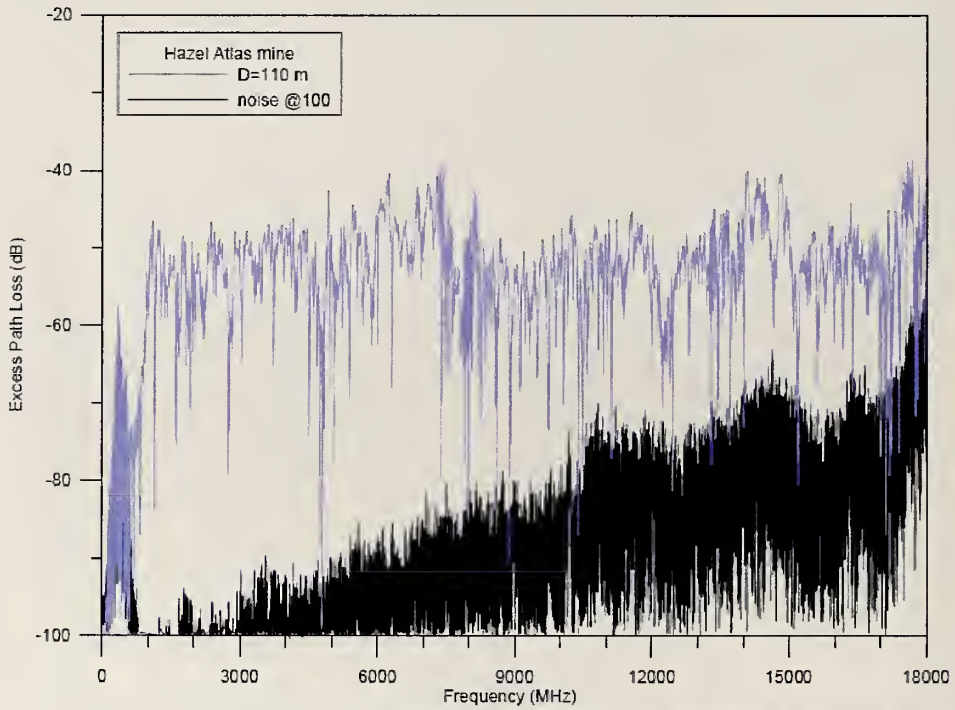

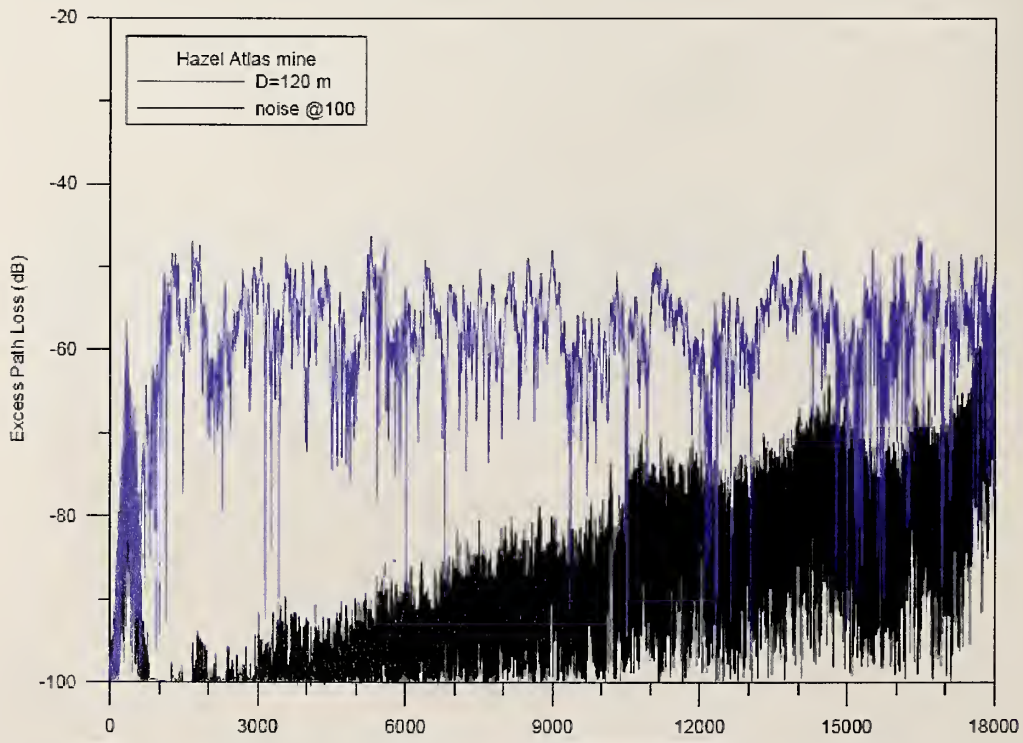

Figure H.14: Excess path loss data from 1 GHz to 18 GHz from the Hazel-Atlas tunnel. Distance from the transmitting antenna to the receiving antenna is D = 110 m (top) and D = 120 m (bottom).

Wideband Excess Path Loss: Subterranean Tunnels

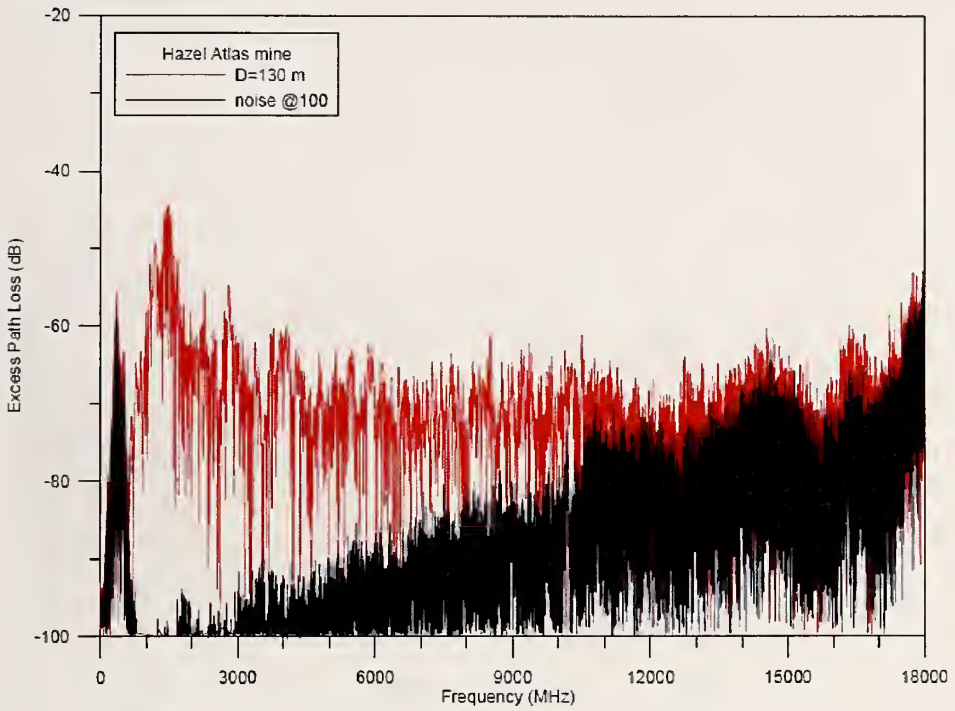

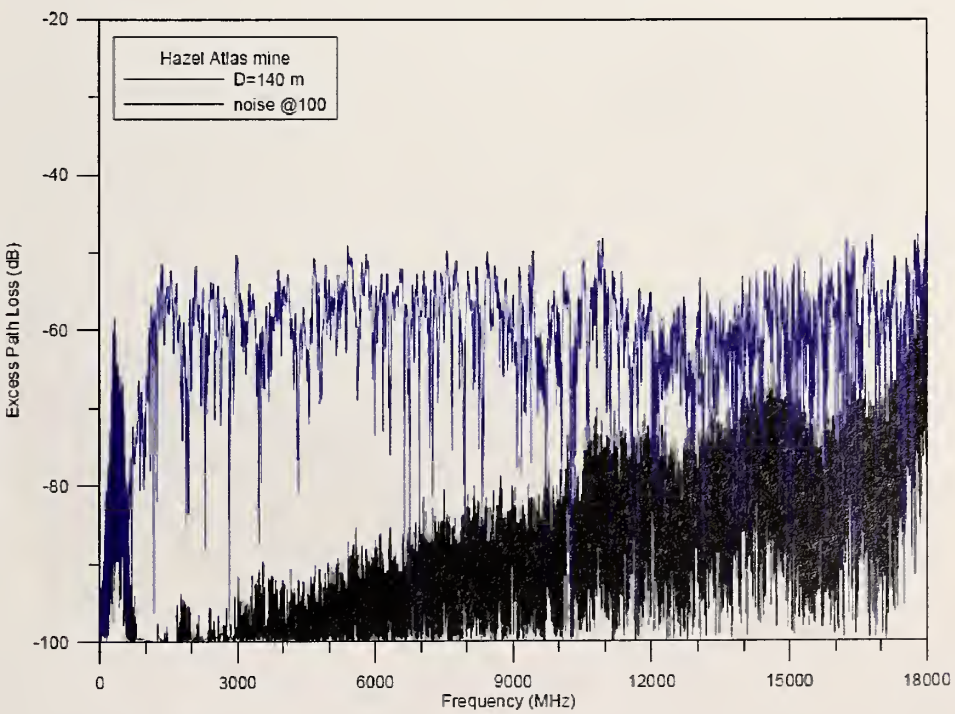

Figure H.15: Excess path loss data from 1 GHz to 18 GHz from the Hazel-Atlas tunnel. Distance from the transmitting antenna to the receiving antenna is D = 130 m (top) and D = 140 m (bottom).

Wideband Excess Path Loss: Subterranean Tunnels

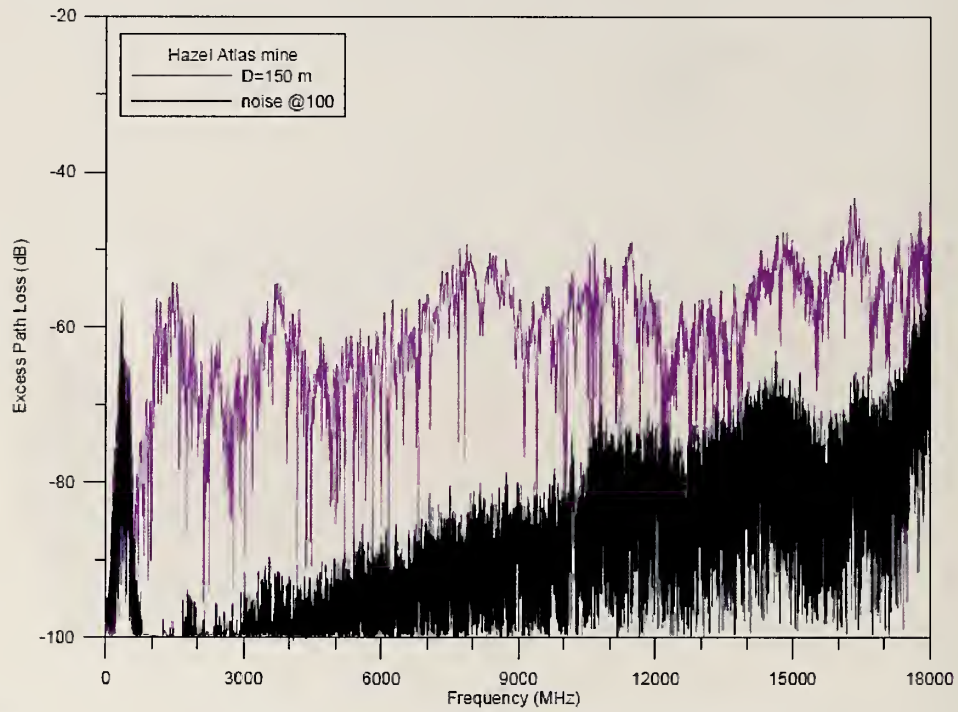

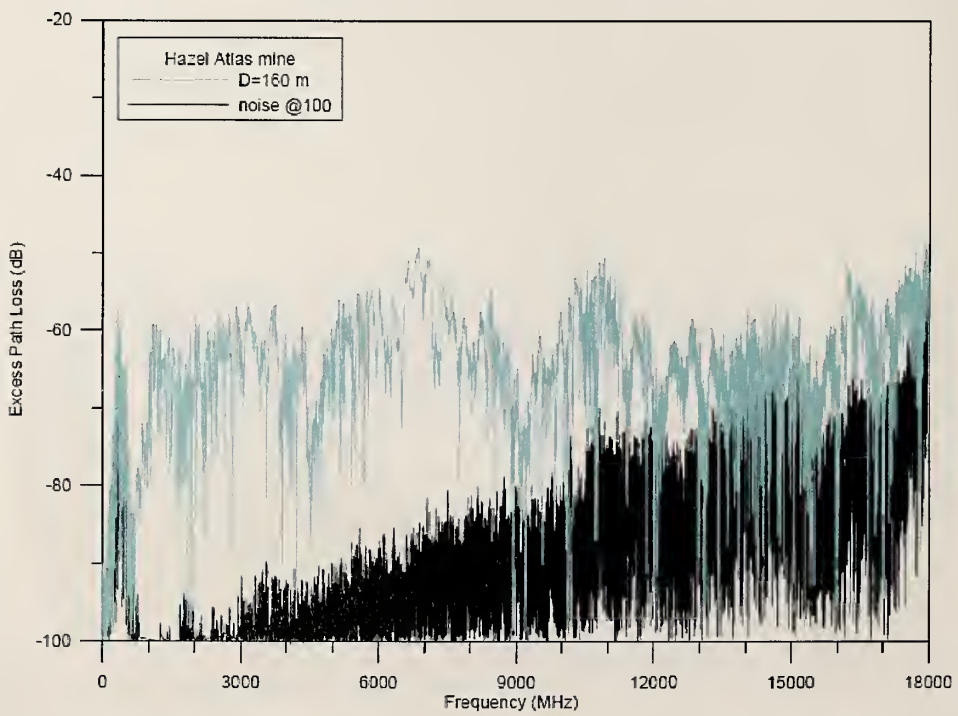

Figure H.16: Excess path loss data from 1 GHz to 18 GHz from the Hazel-Atlas tunnel. Distance from the transmitting antenna to the receiving antenna is D = 150 m (top) and D = 160 m (bottom).

Wideband Excess Path Loss: Subterranean Tunnels

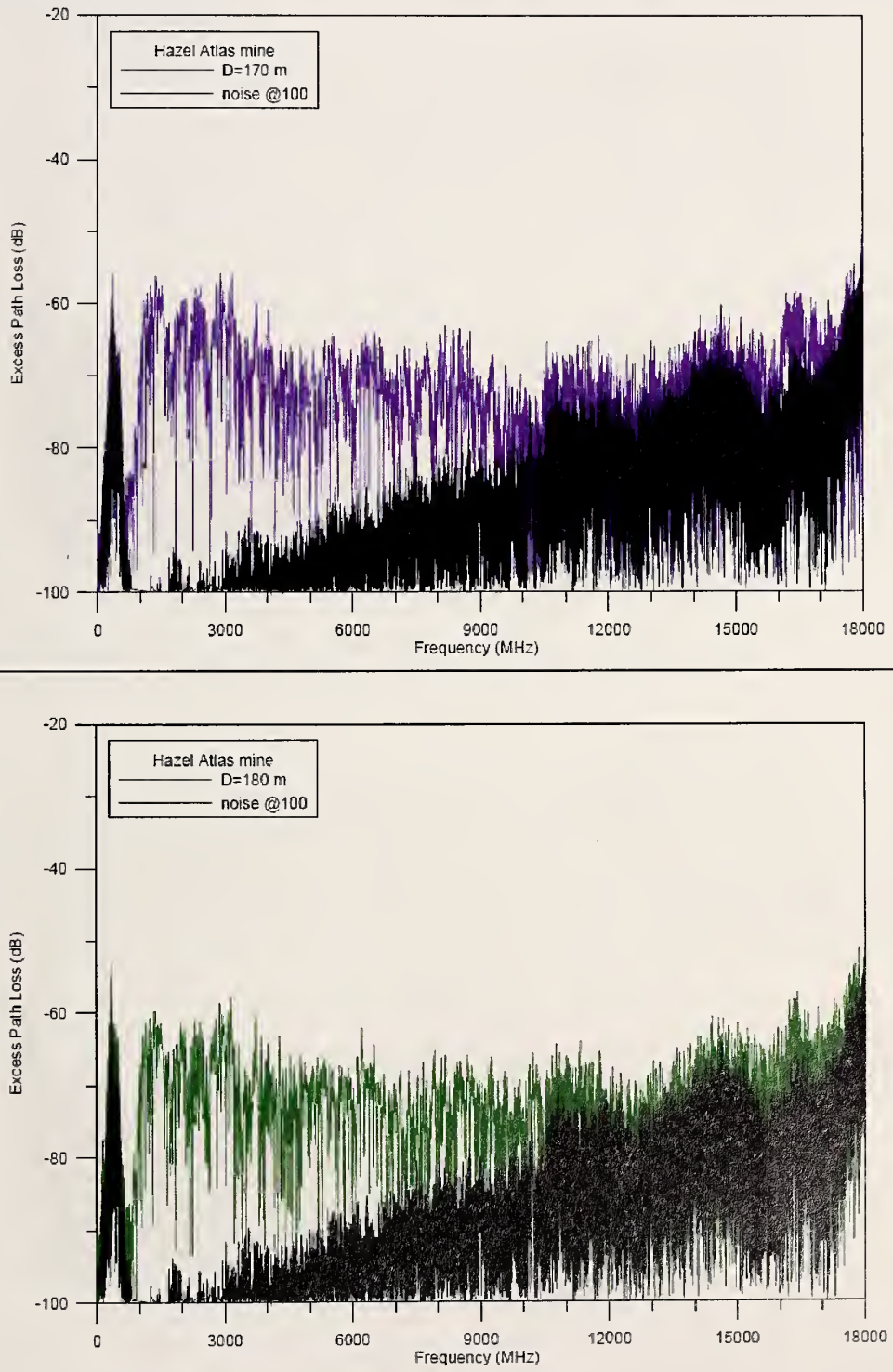

Figure H.17: Excess path loss data from 1 GHz to 18 GHz from the Hazel-Atlas tunnel. Distance from the transmitting antenna to the receiving antenna is D = 170 m (top) and D = 180 m (bottom).

Wideband Excess Path Loss: Subterranean Tunnels

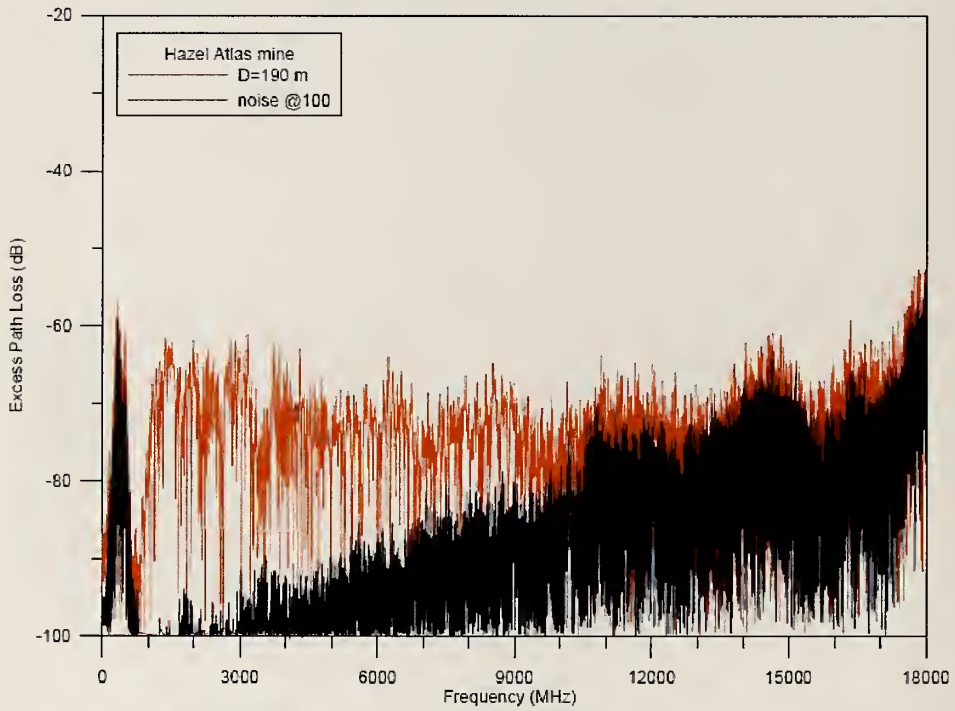

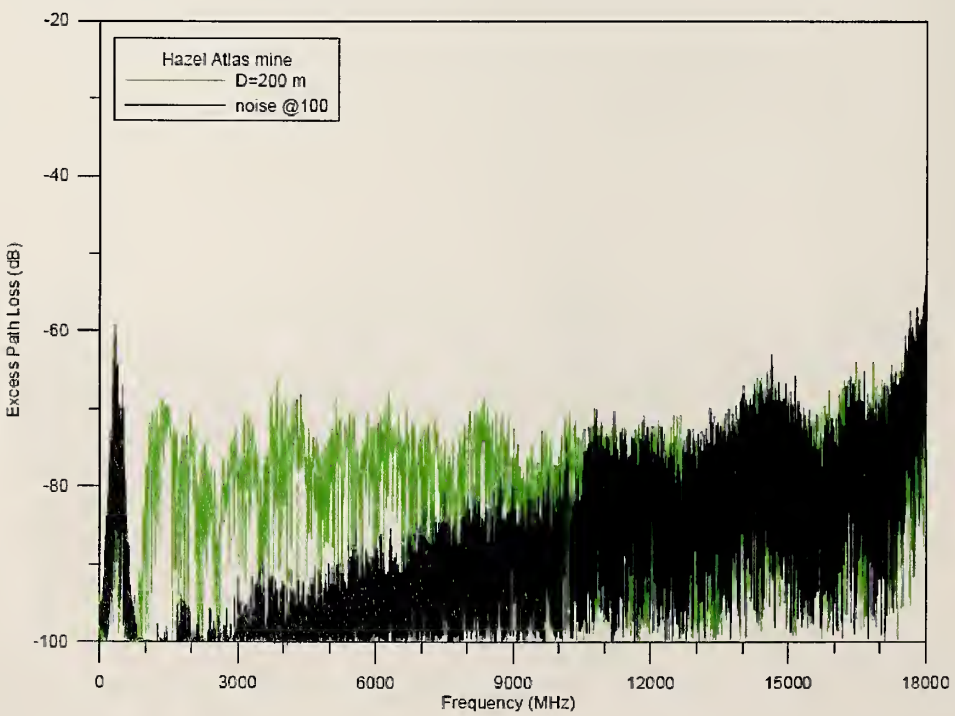

Figure H.18: Excess path loss data from 1 GHz to 18 GHz from the Hazel-Atlas tunnel. Distance from the transmitting antenna to the receiving antenna is D = 190 m (top) and D = 200 m (bottom).

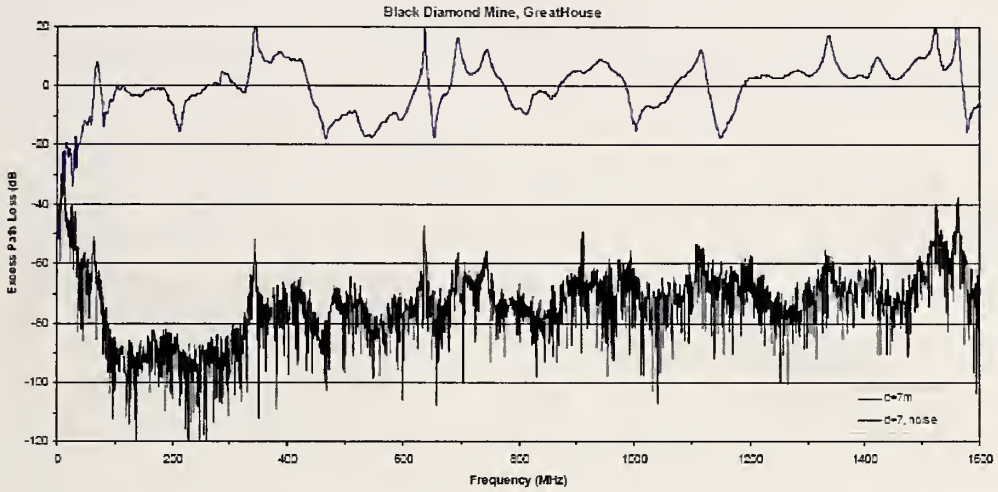

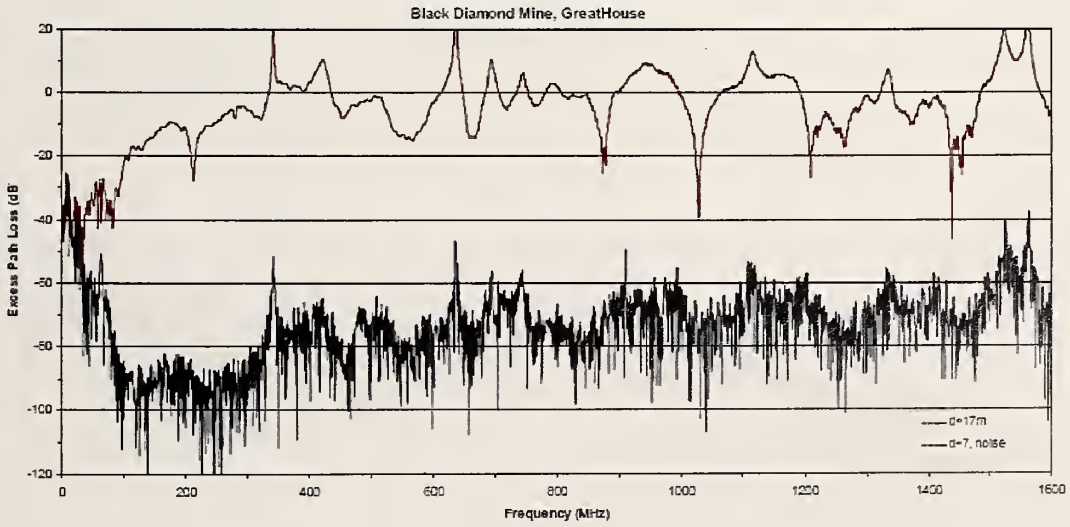

Figure H.19: Excess path loss data from 25 MHz to 1.6 GHz from the Greathouse tunnel. Distance from the transmitting antenna to the receiving antenna is D = 7 m (top) and D = 17 m (bottom).

Wideband Excess Path Loss: Subterranean Tunnels

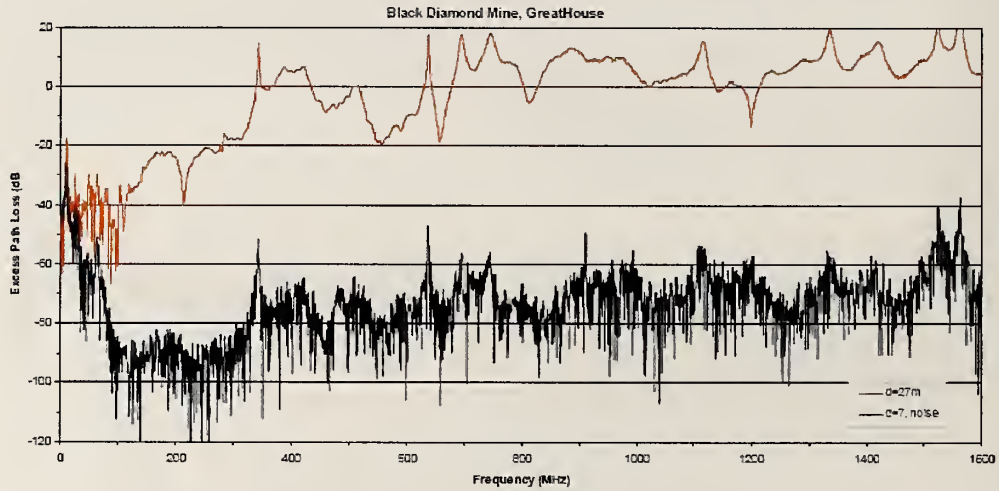

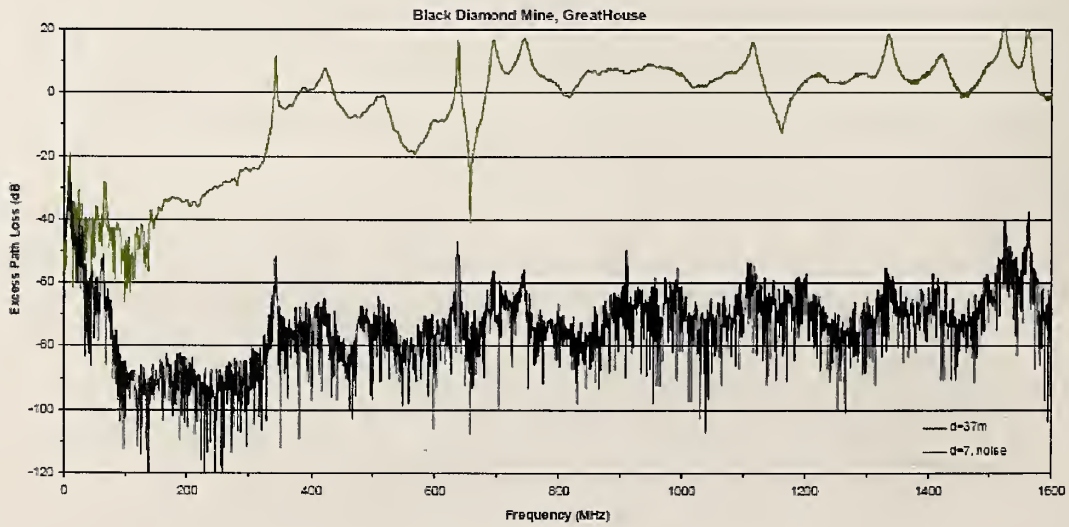

Figure H.20: Excess path loss data from 25 MHz to 1.6 GHz from the Greathouse tunnel. Distance from the transmitting antenna to the receiving antenna is D = 27 m (top) and D = 37 m (bottom).

Wideband Excess Path Loss: Subterranean Tunnels

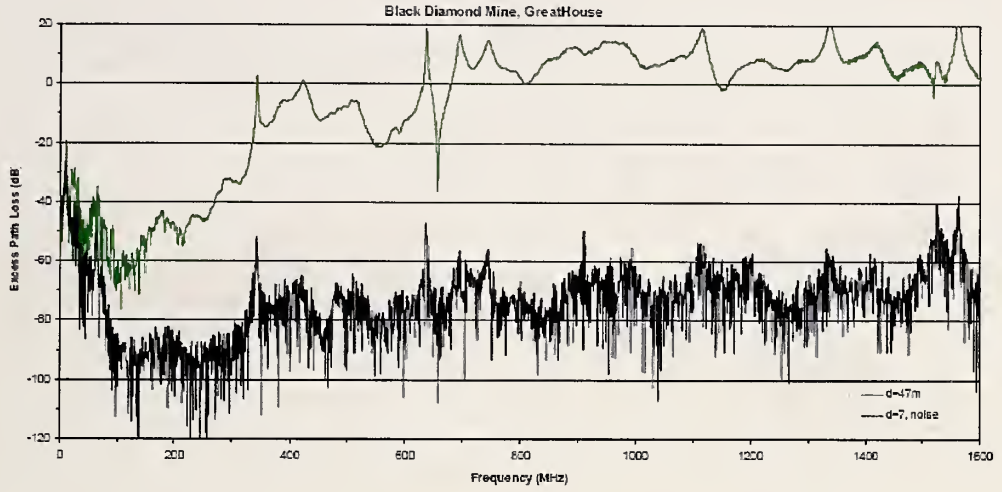

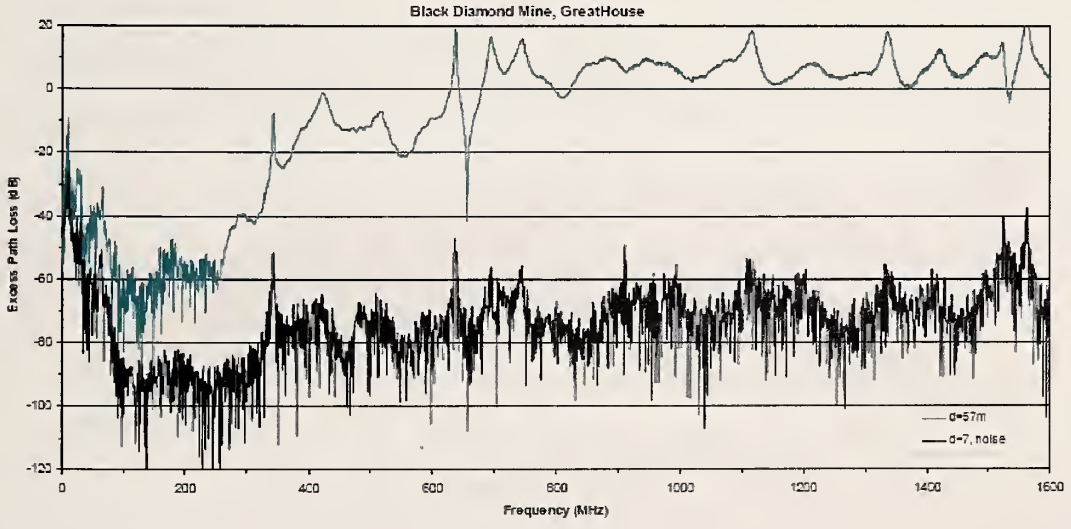

Figure H.21: Excess path loss data from 25 MHz to 1.6 GHz from the Greathouse tunnel. Distance from the transmitting antenna to the receiving antenna is D = 47 m (top) and D = 57 m (bottom).

Wideband Excess Path Loss: Subterranean Tunnels

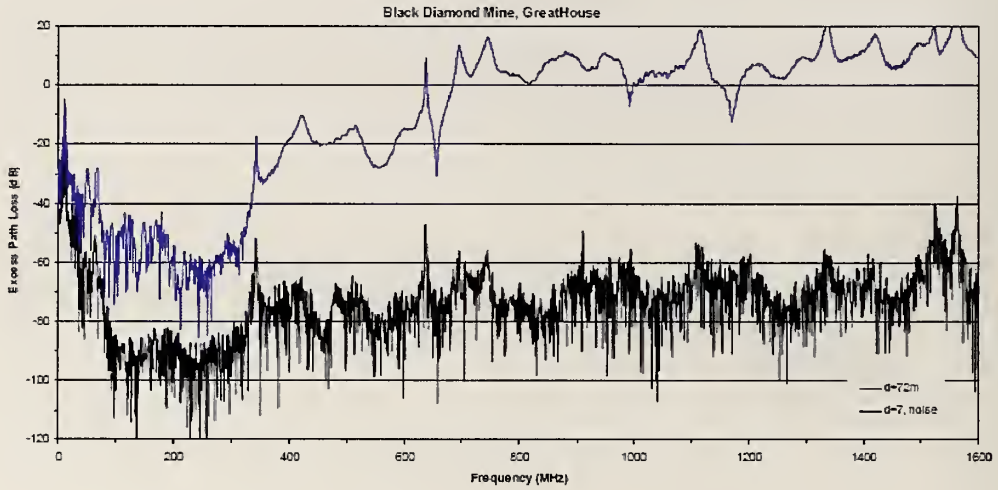

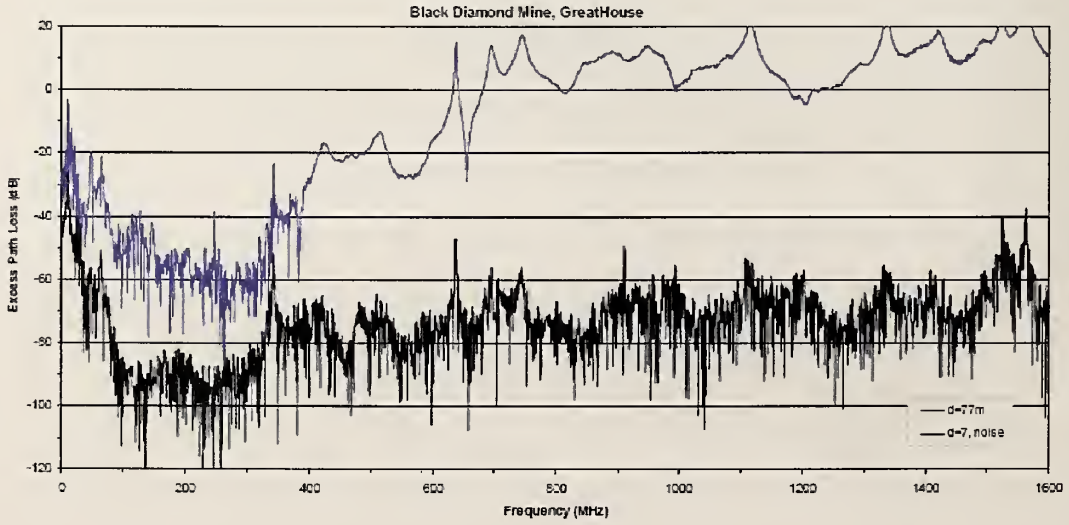

Figure H.22: Excess path loss data from 25 MHz to 1.6 GHz from the Greathouse tunnel. Distance from the transmitting antenna to the receiving antenna is D = 72 m (top) and D = 77 m (bottom).

Wideband Excess Path Loss: Subterranean Tunnels

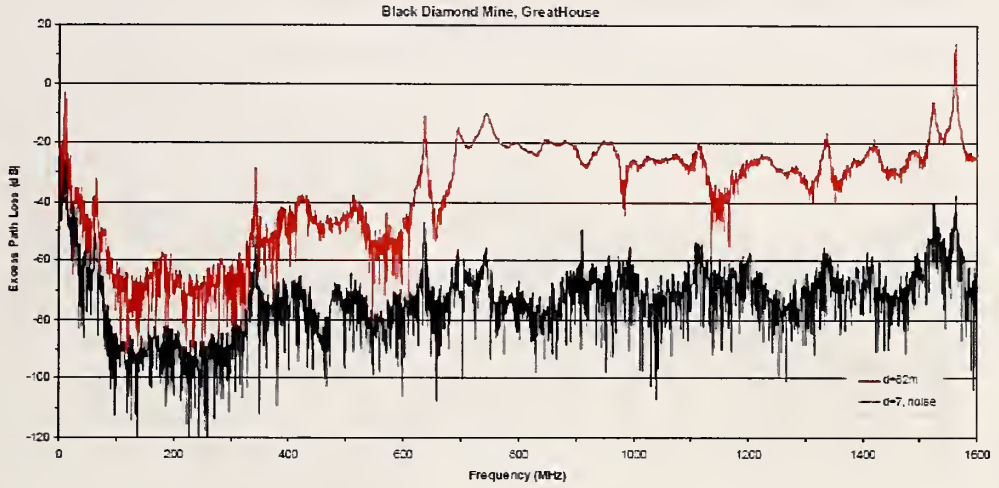

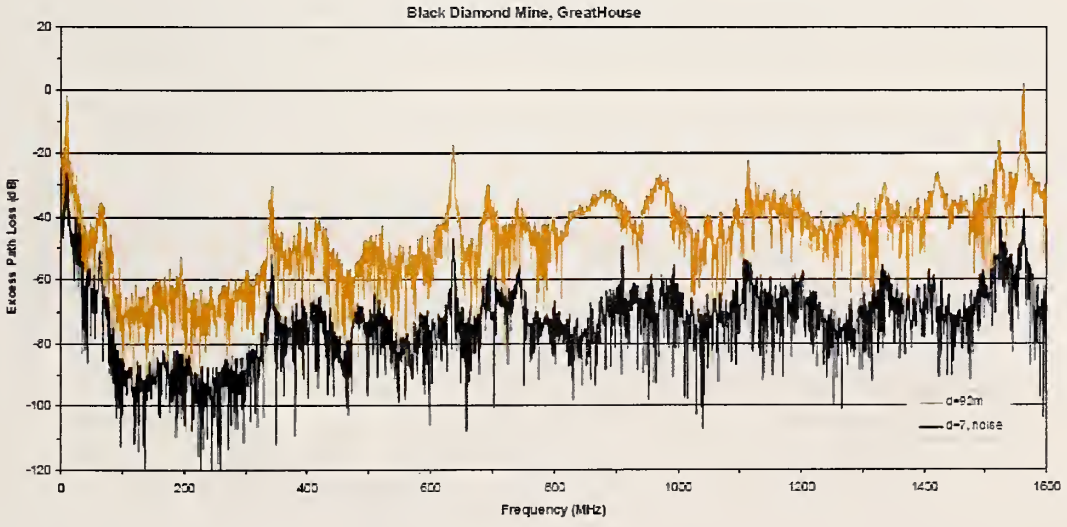

Figure H.23: Excess path loss data from 25 MHz to 1.6 GHz from the Greathouse tunnel. Distance from the transmitting antenna to the receiving antenna is D = 82 m (top) and D = 92 m (bottom).

Wideband Excess Path Loss: Subterranean Tunnels

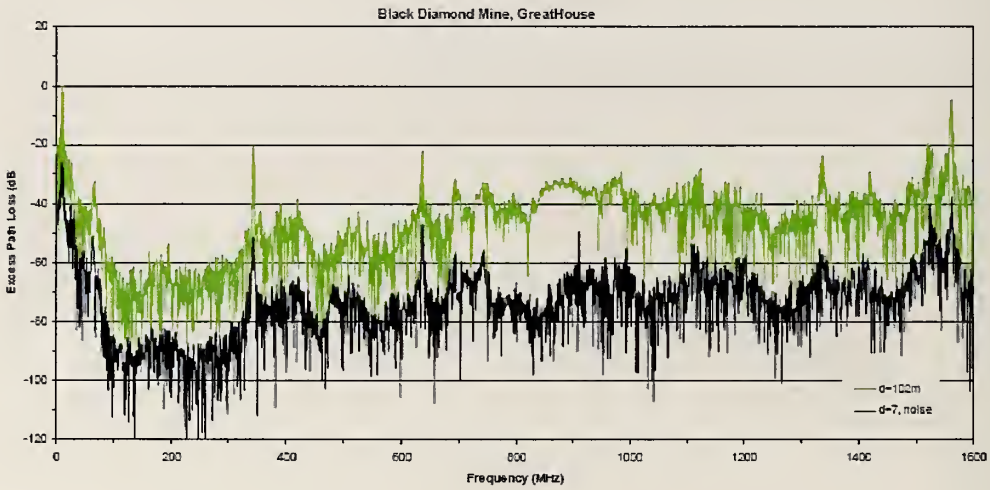

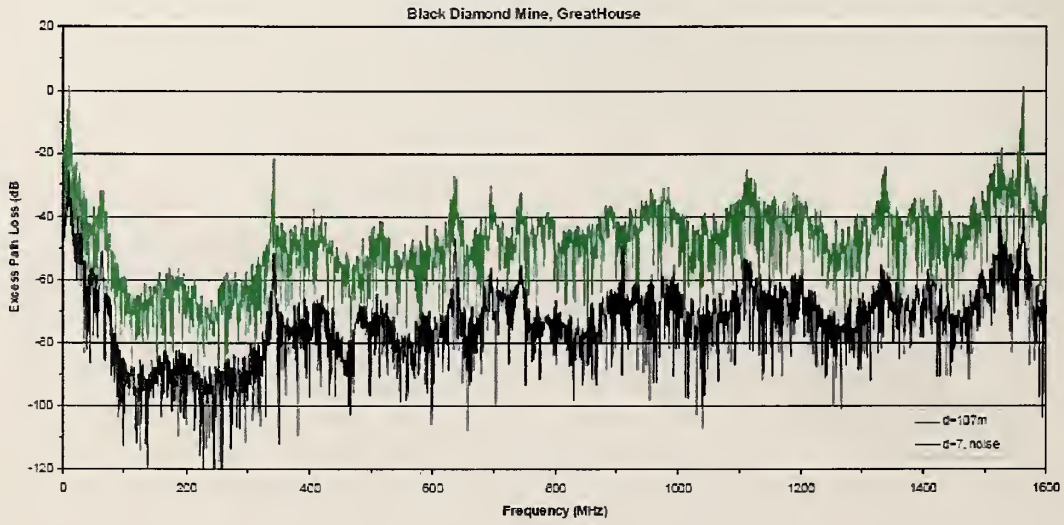

Figure H.24: Excess path loss data from 25 MHz to 1.6 GHz from the Greathouse tunnel. Distance from the transmitting antenna to the receiving antenna is D = 102 m (top) and D = 107 m (bottom).

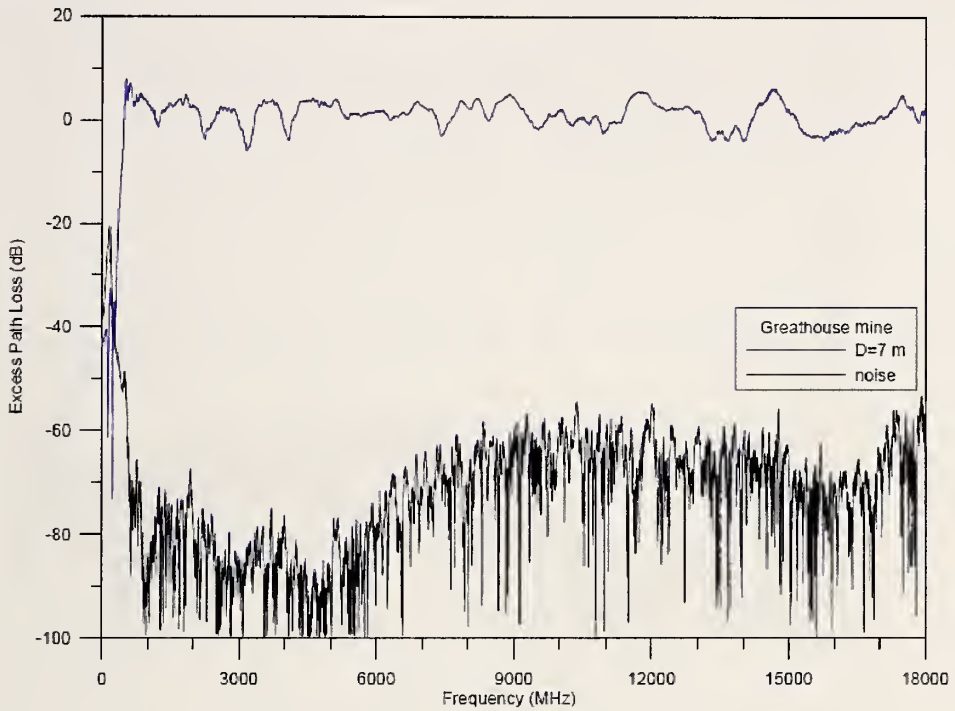

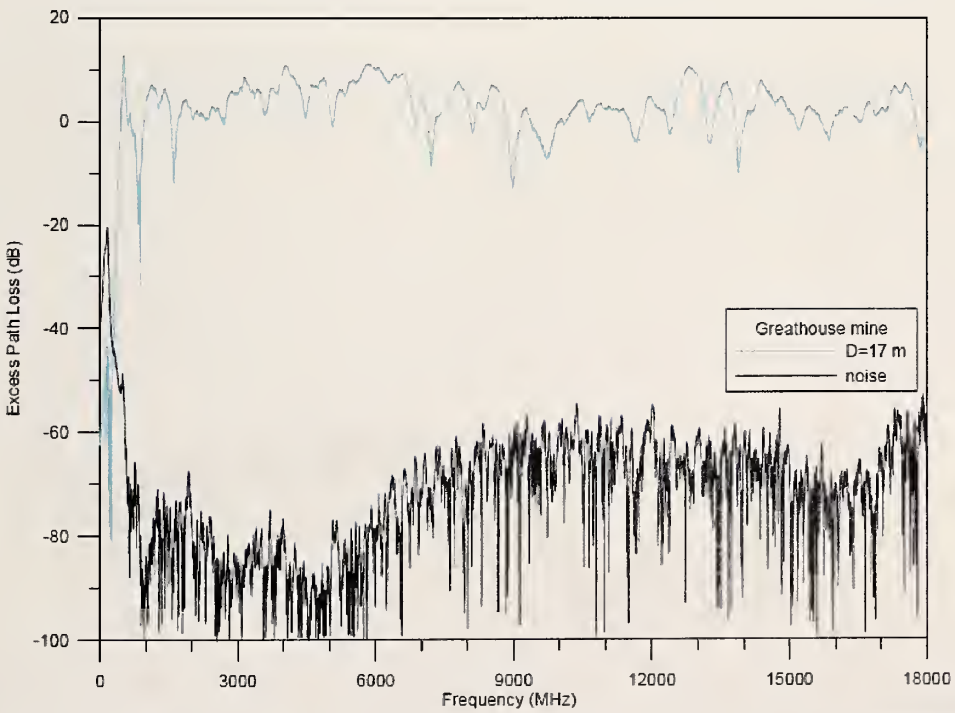

Figure H.25: Excess path loss data from 1 GHz to 18 GHz from the Greathouse tunnel. Distance from the transmitting antenna to the receiving antenna is D = 7 m (top) and D = 17 m (bottom).

Wideband Excess Path Loss: Subterranean Tunnels

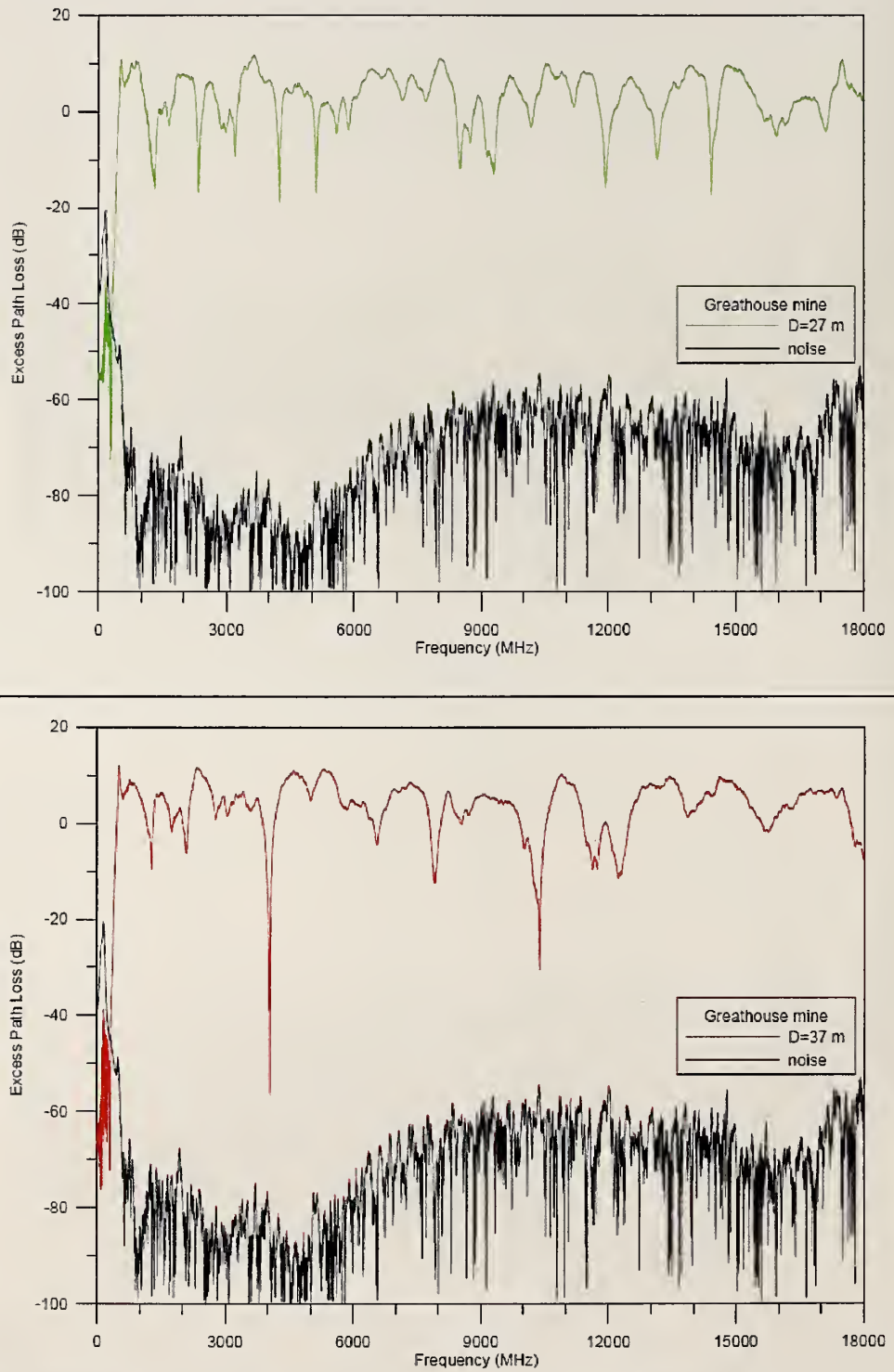

Figure H.26: Excess path loss data from 1 GHz to 18 GHz from the Greathouse tunnel. Distance from the transmitting antenna to the receiving antenna is D = 27 m (top) and D = 37 m (bottom).

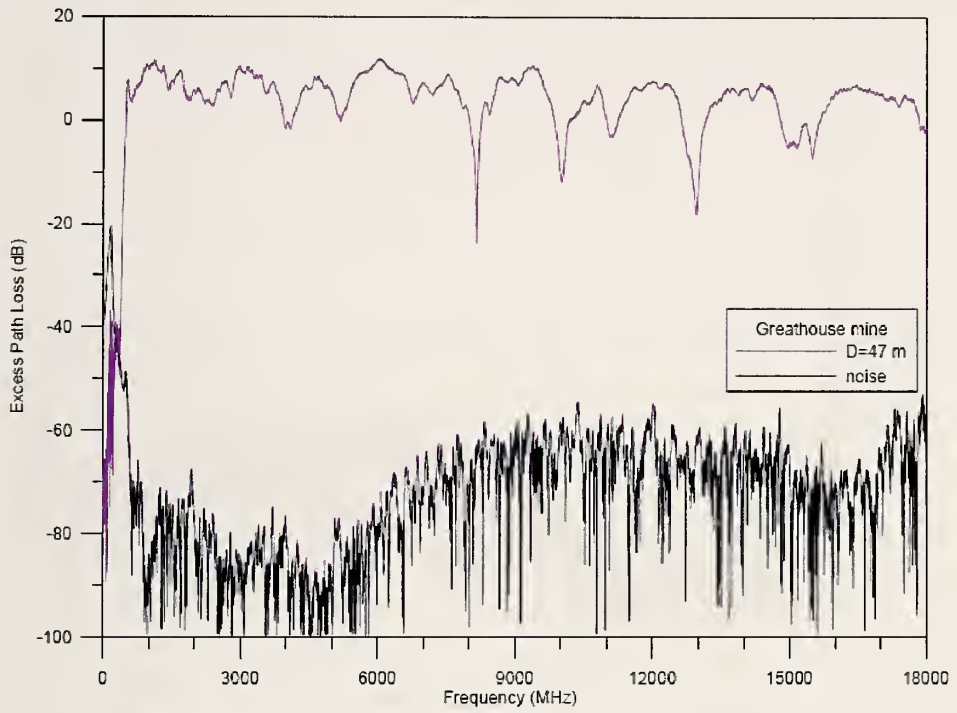

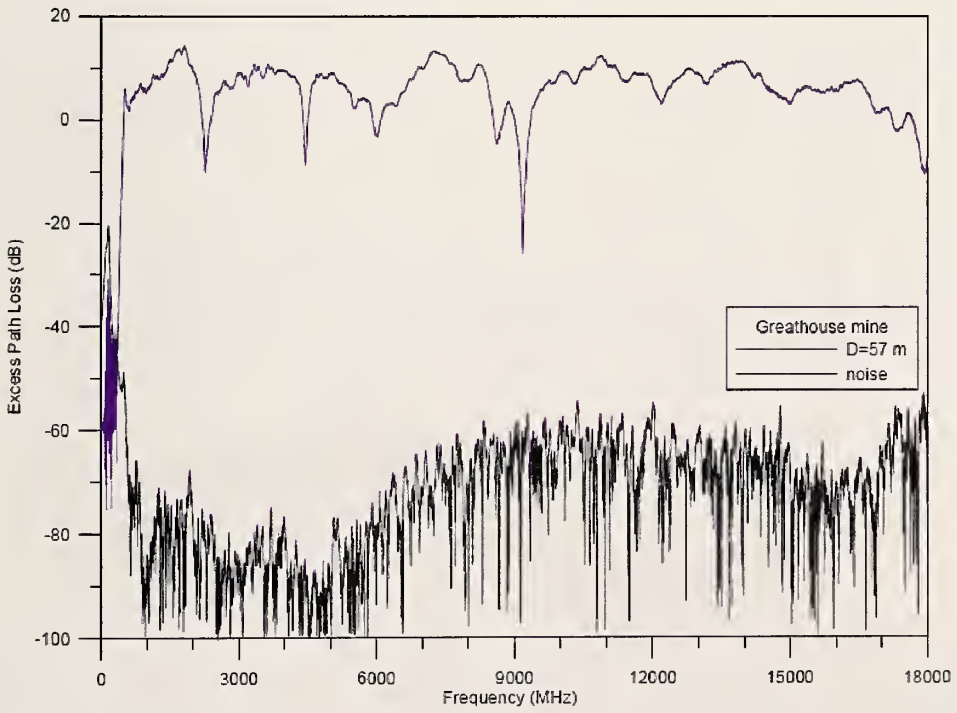

Figure H.27: Excess path loss data from 1 GHz to 18 GHz from the Greathouse tunnel. Distance from the transmitting antenna to the receiving antenna is D = 47 m (top) and D = 57 m (bottom).

Wideband Excess Path Loss: Subterranean Tunnels

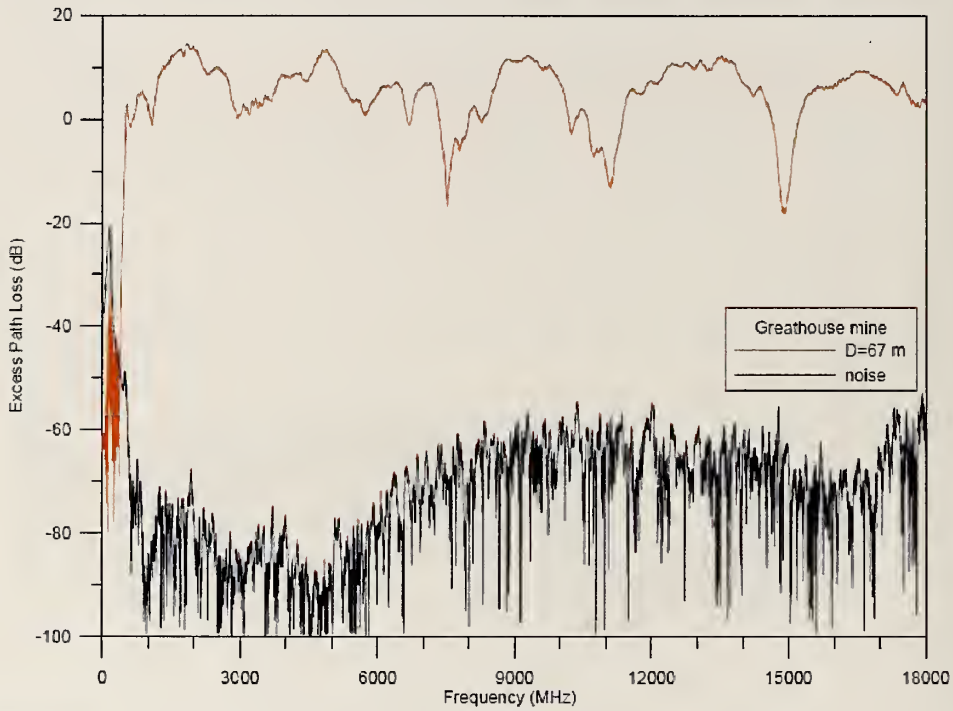

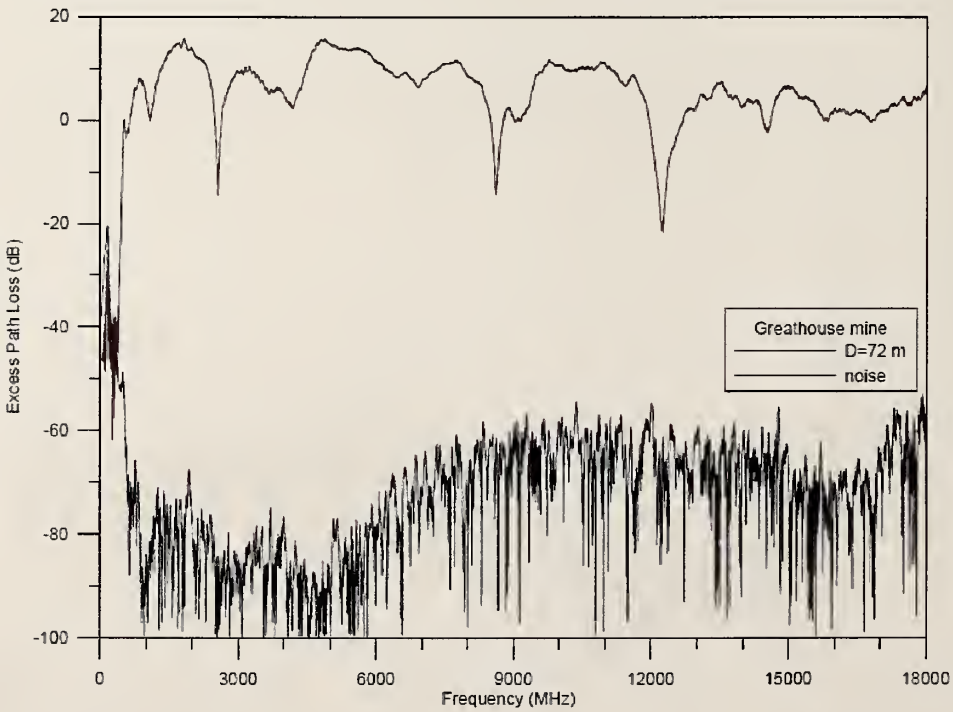

Figure H.28: Excess path loss data from 1 GHz to 18 GHz from the Greathouse tunnel. Distance from the transmitting antenna to the receiving antenna is D = 67 m (top) and D = 72 m (bottom).

Wideband Excess Path Loss: Subterranean Tunnels

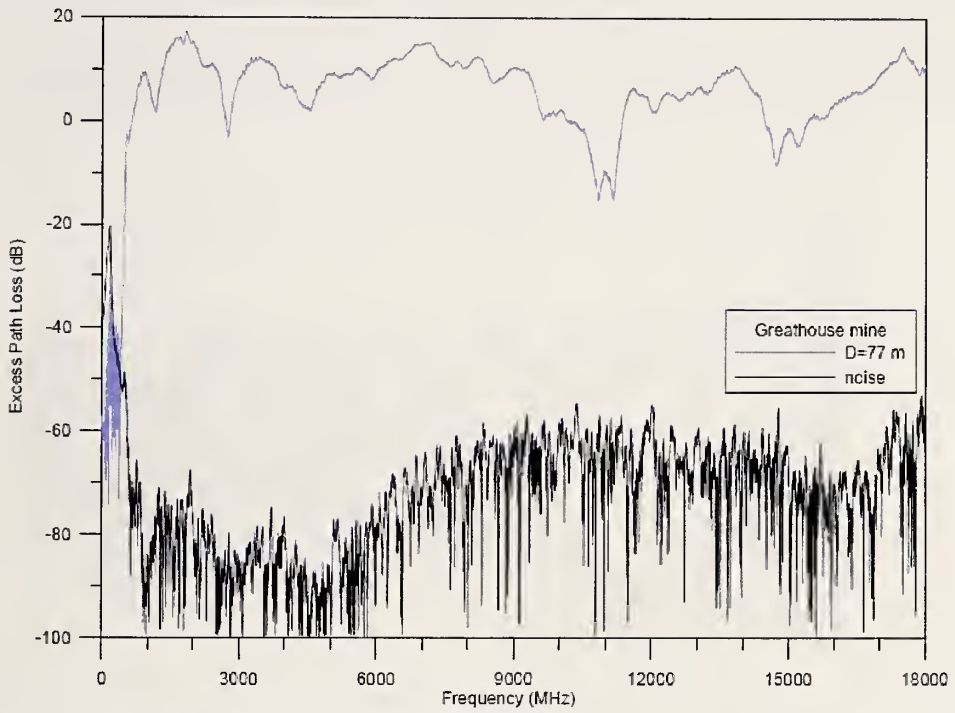

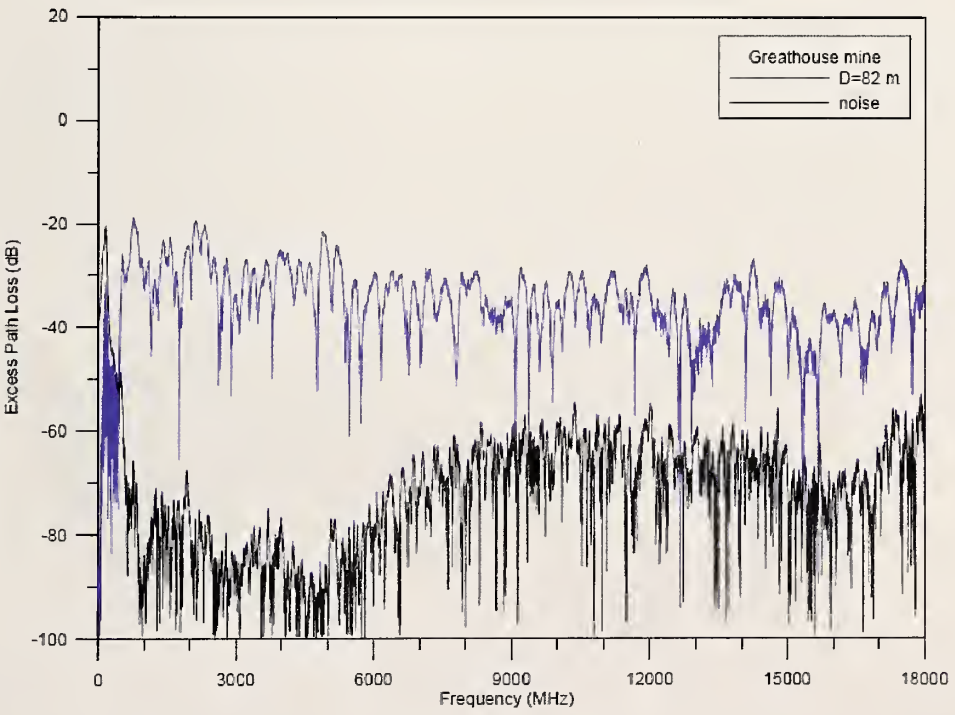

Figure H.29: Excess path loss data from 1 GHz to 18 GHz from the Greathouse tunnel. Distance from the transmitting antenna to the receiving antenna is D = 77 m (top) and D = 82 m (bottom).

Wideband Excess Path Loss: Subterranean Tunnels

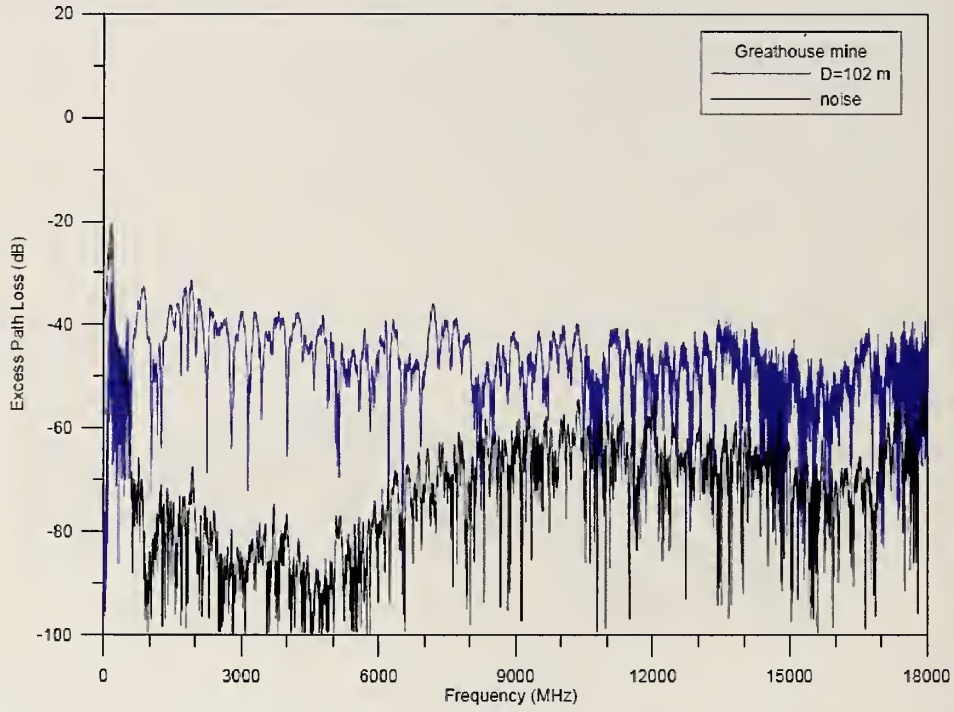

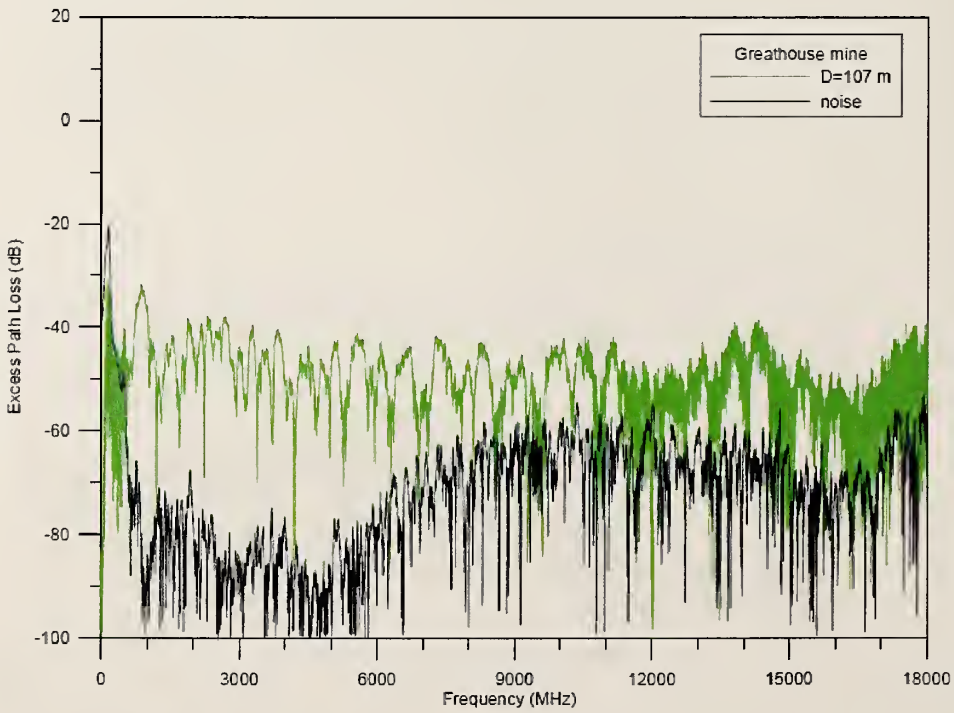

Figure H.30: Excess path loss data from 1 GHz to 18 GHz from the Greathouse tunnel. Distance from the transmitting antenna to the receiving antenna is D = 102 m (top) and D = 107 m (bottom).

Appendix I: Modulated-Signal Spectra Measured With a Vector-Signal Analyzer: Apartment Building

The following pages contain the complete set of measured data for the apartment building (Section 3.4).

Modulated-Signal Spectra: Apartment Building

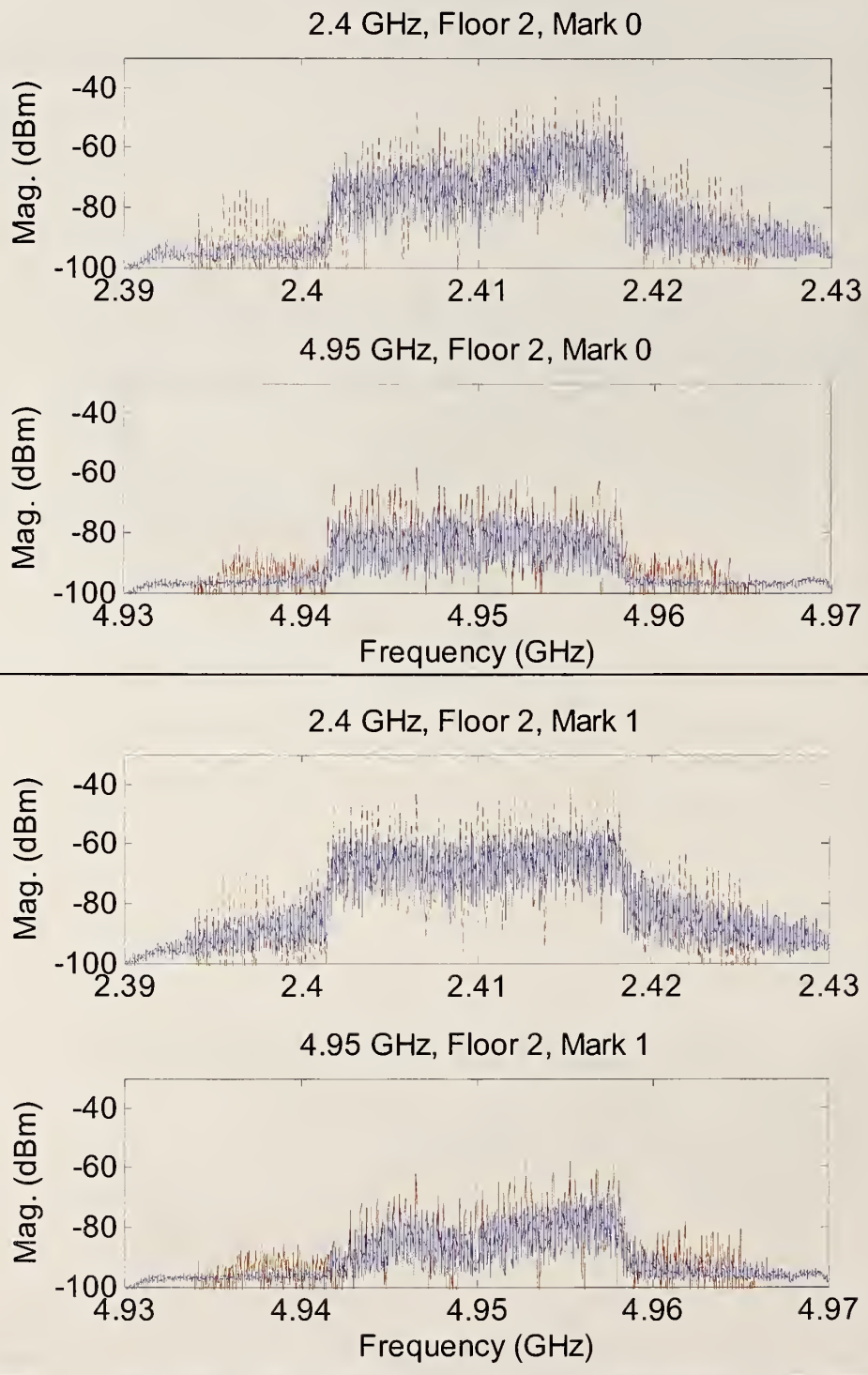

Figure I.1: Bandpass measurements for carrier frequencies of 2.41 GHz and 4.95 GHz for a QPSK-modulated OFDM signal (solid) and a multisine designed to simulate it (dashed). Floor 2, position 0 (top) and position 1 (bottom).

Modulated-Signal Spectra: Apartment Building

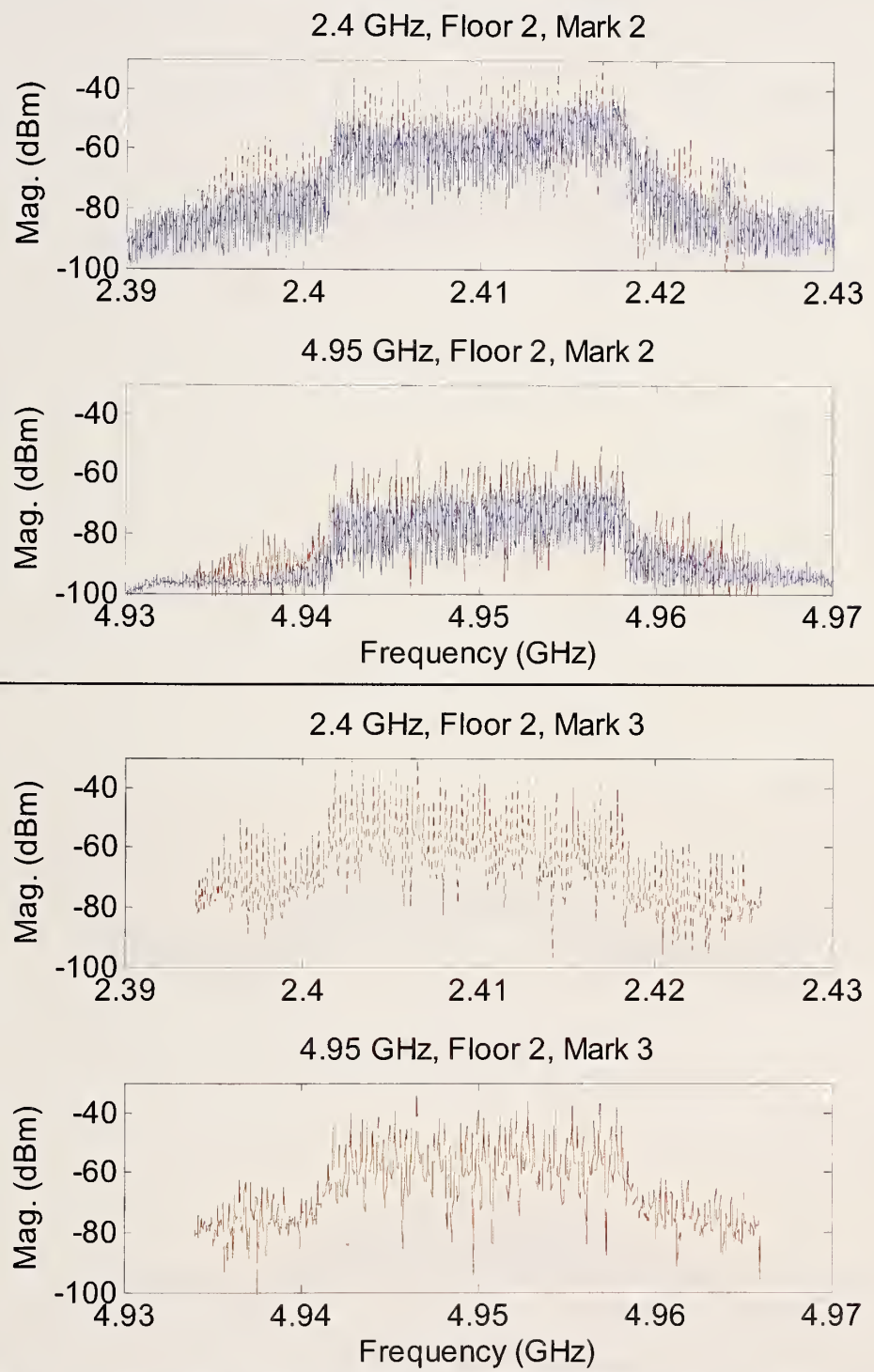

Figure I.2: Bandpass measurements for carrier frequencies of 2.41 GHz and 4.95 GHz for a QPSK-modulated OFDM signal (solid) and a multisine designed to simulate it (dashed). Floor 2, position 2 (top) and position 3 (bottom). The data for the digitally modulated signal were corrupted at position 3.

Modulated-Signal Spectra: Apartment Building

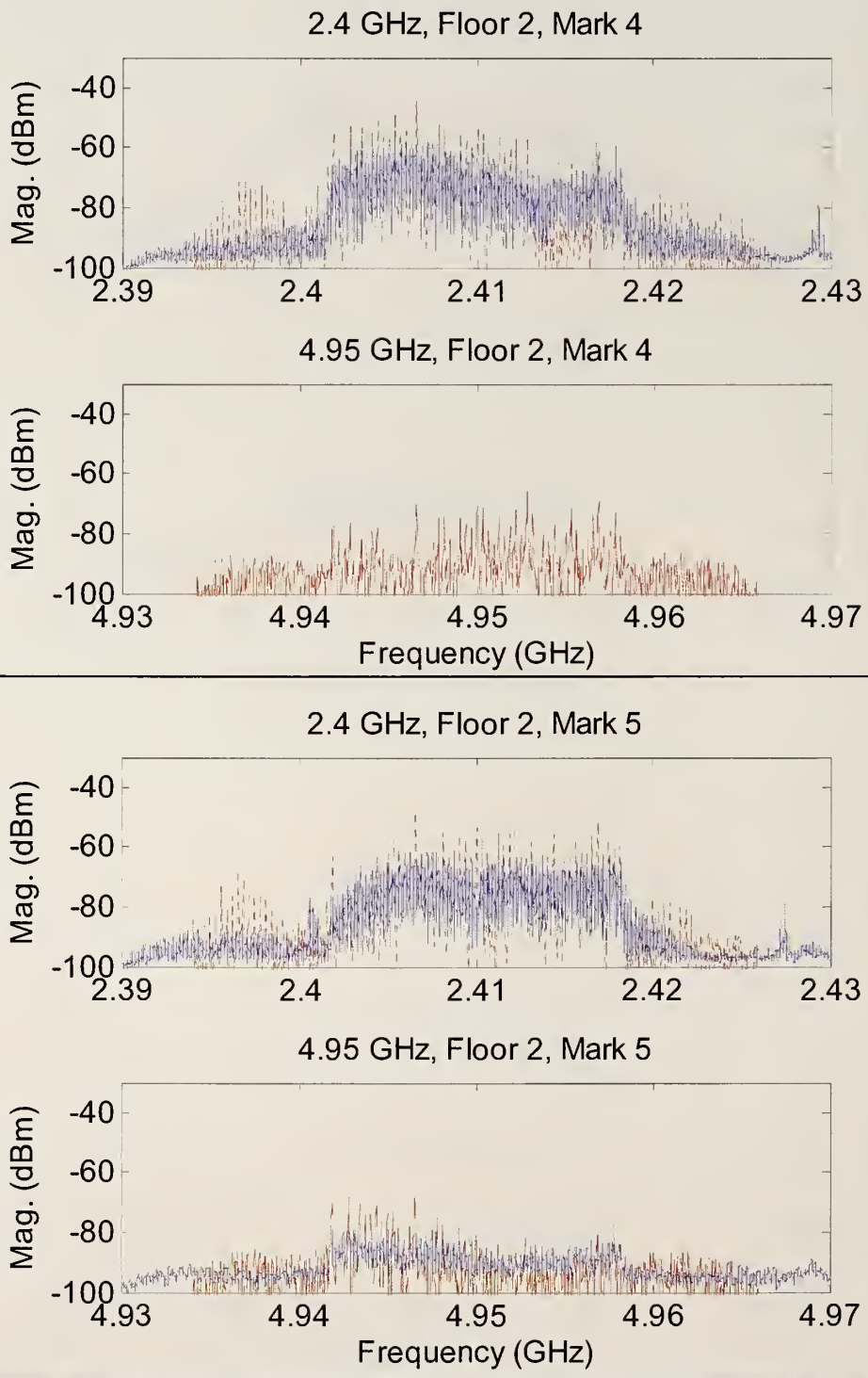

Figure I.3: Bandpass measurements for carrier frequencies of 2.41 GHz and 4.95 GHz for a QPSK-modulated OFDM signal (solid) and a multisine designed to simulate it (dashed). Floor 2, position 4 (top) and position 5 (bottom).

Modulated-Signal Spectra: Apartment Building

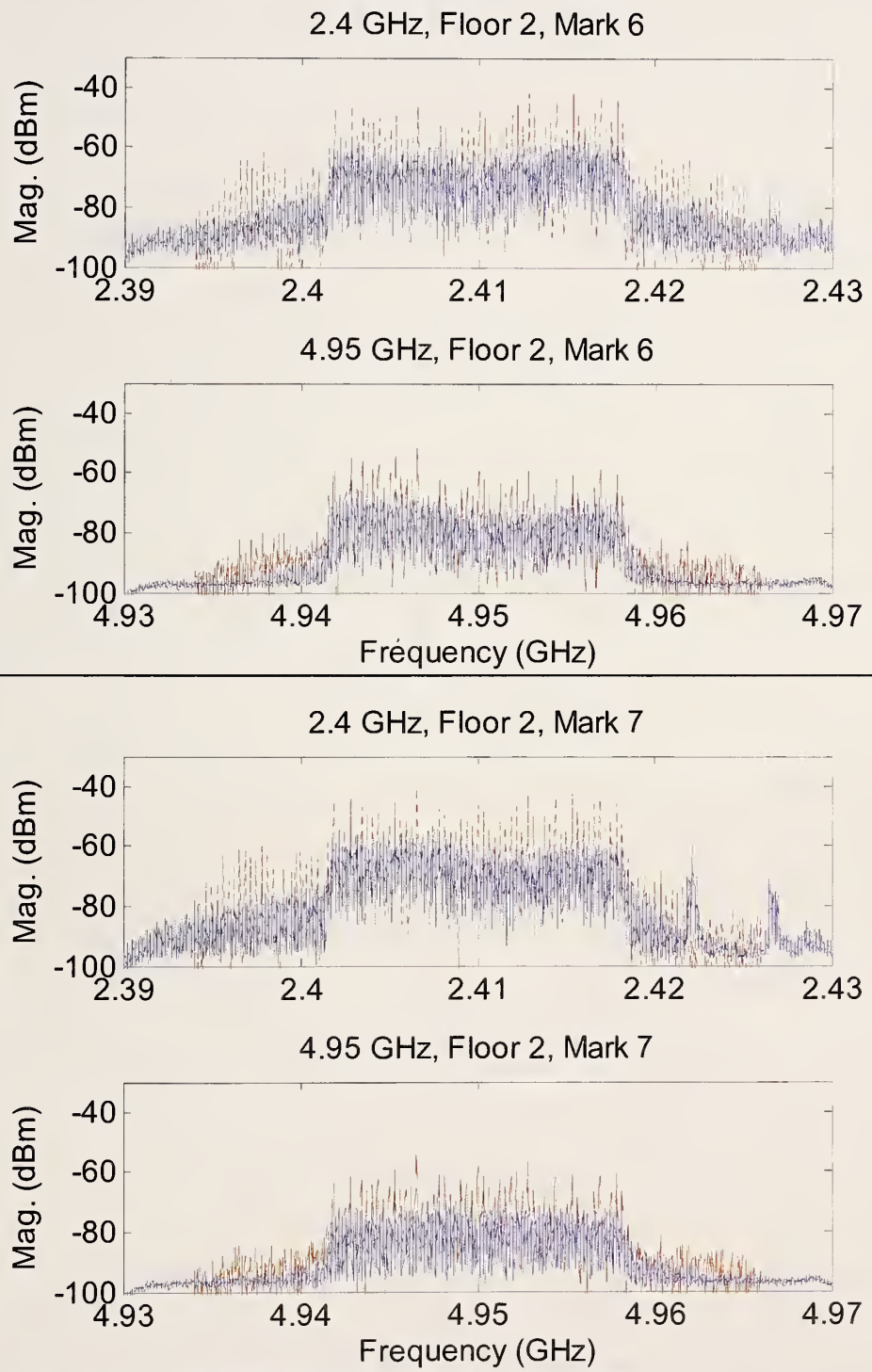

Figure I.4: Bandpass measurements for carrier frequencies of 2.41 GHz and 4.95 GHz for a QPSK-modulated OFDM signal (solid) and a multisine designed to simulate it (dashed). Floor 2, position 6 (top) and position 7 (bottom).

Modulated-Signal Spectra: Apartment Building

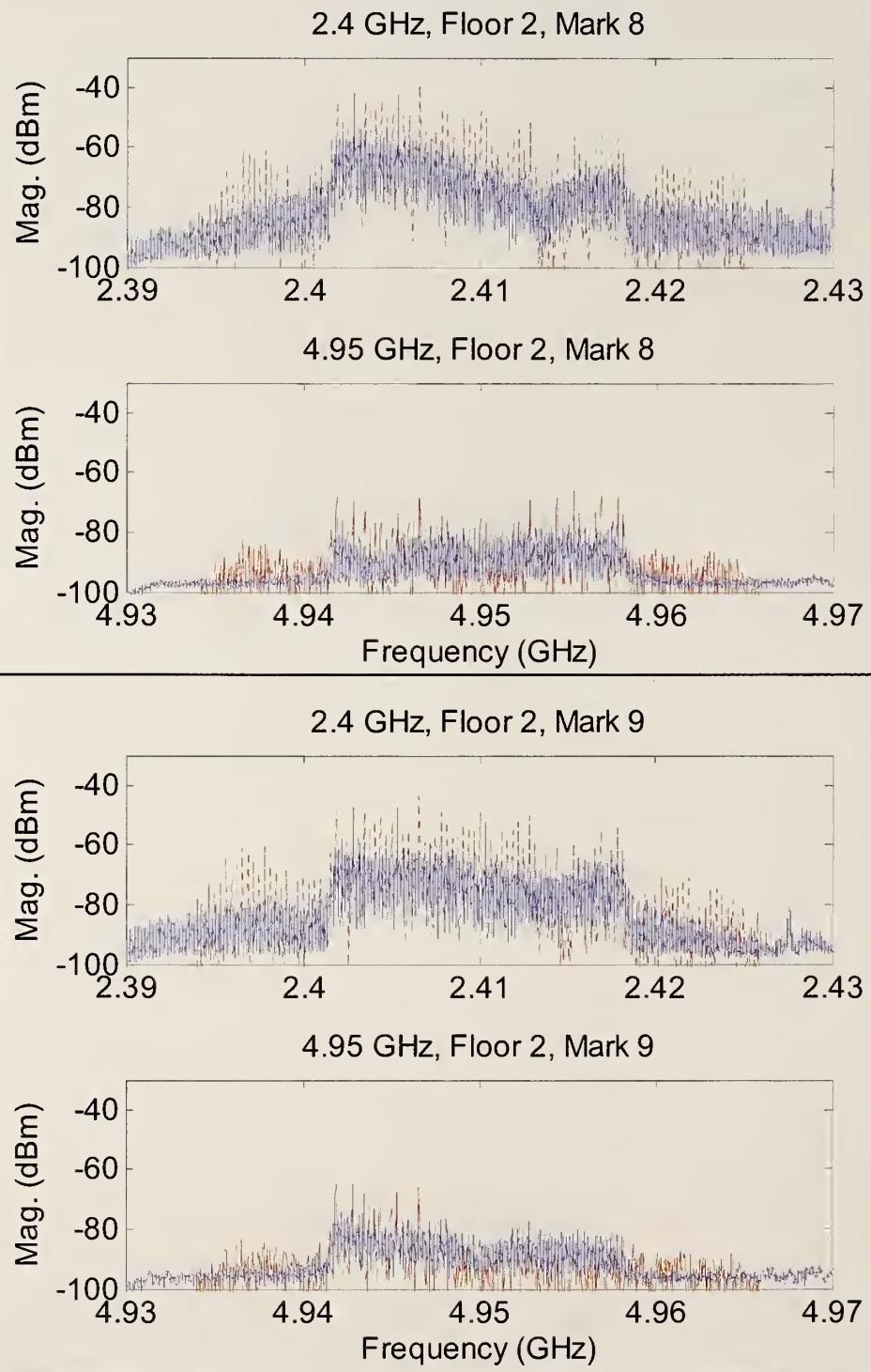

Figure I.5: Bandpass measurements for carrier frequencies of 2.41 GHz and 4.95 GHz for a QPSK-modulated OFDM signal (solid) and a multisine designed to simulate it (dashed). Floor 2, position 8 (top) and position 9 (bottom).

Modulated-Signal Spectra: Apartment Building

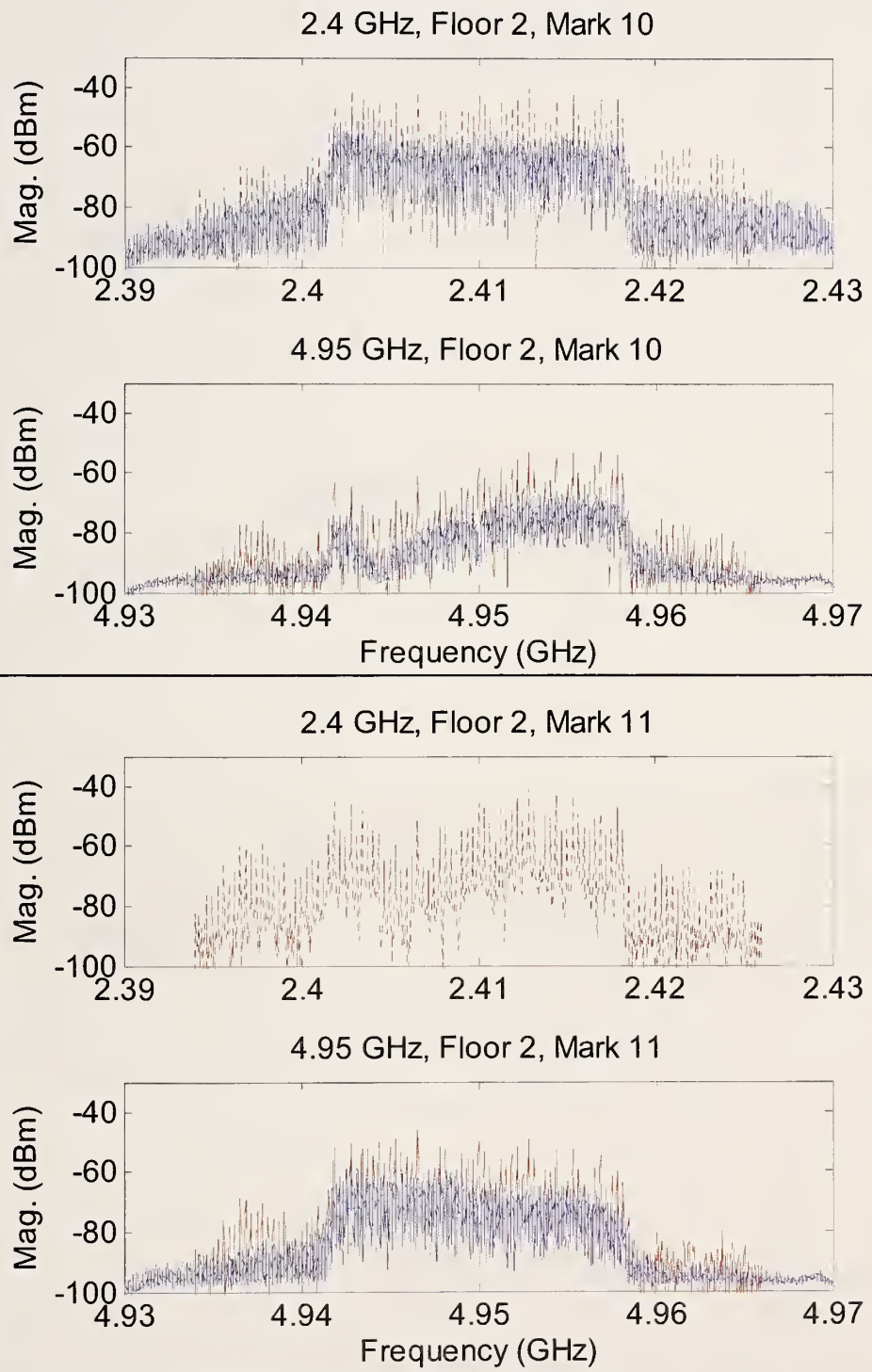

Figure I.6: Bandpass measurements for carrier frequencies of 2.41 GHz and 4.95 GHz for a QPSK-modulated OFDM signal (solid) and a multisine designed to simulate it (dashed). Floor 2, position 10 (top) and position 11 (bottom).

Modulated-Signal Spectra: Apartment Building

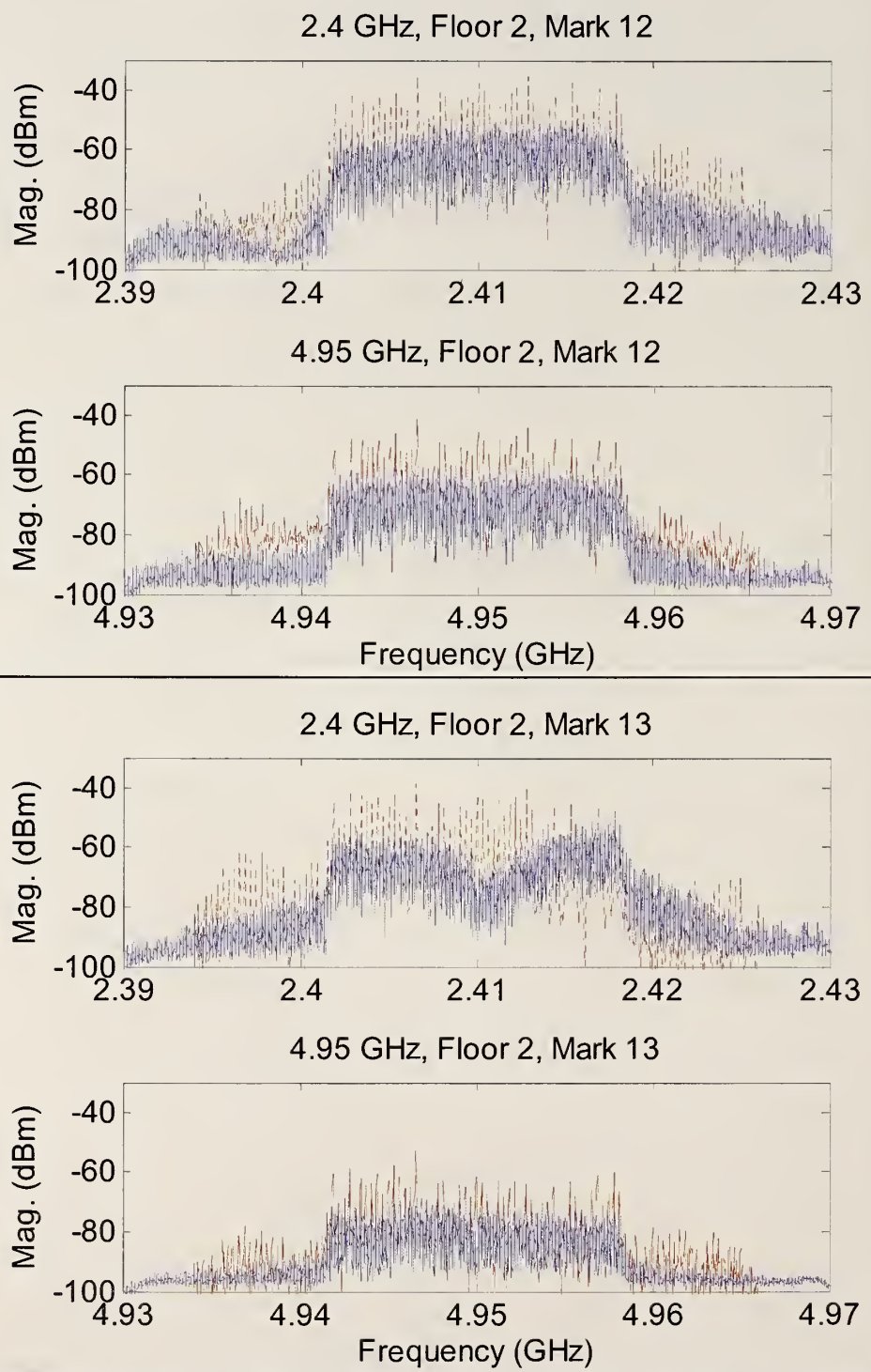

Figure I.7: Bandpass measurements for carrier frequencies of 2.41 GHz and 4.95 GHz for a QPSK-modulated OFDM signal (solid) and a multisine designed to simulate it (dashed). Floor 2, position 12 (top) and position 13 (bottom).

Modulated-Signal Spectra: Apartment Building

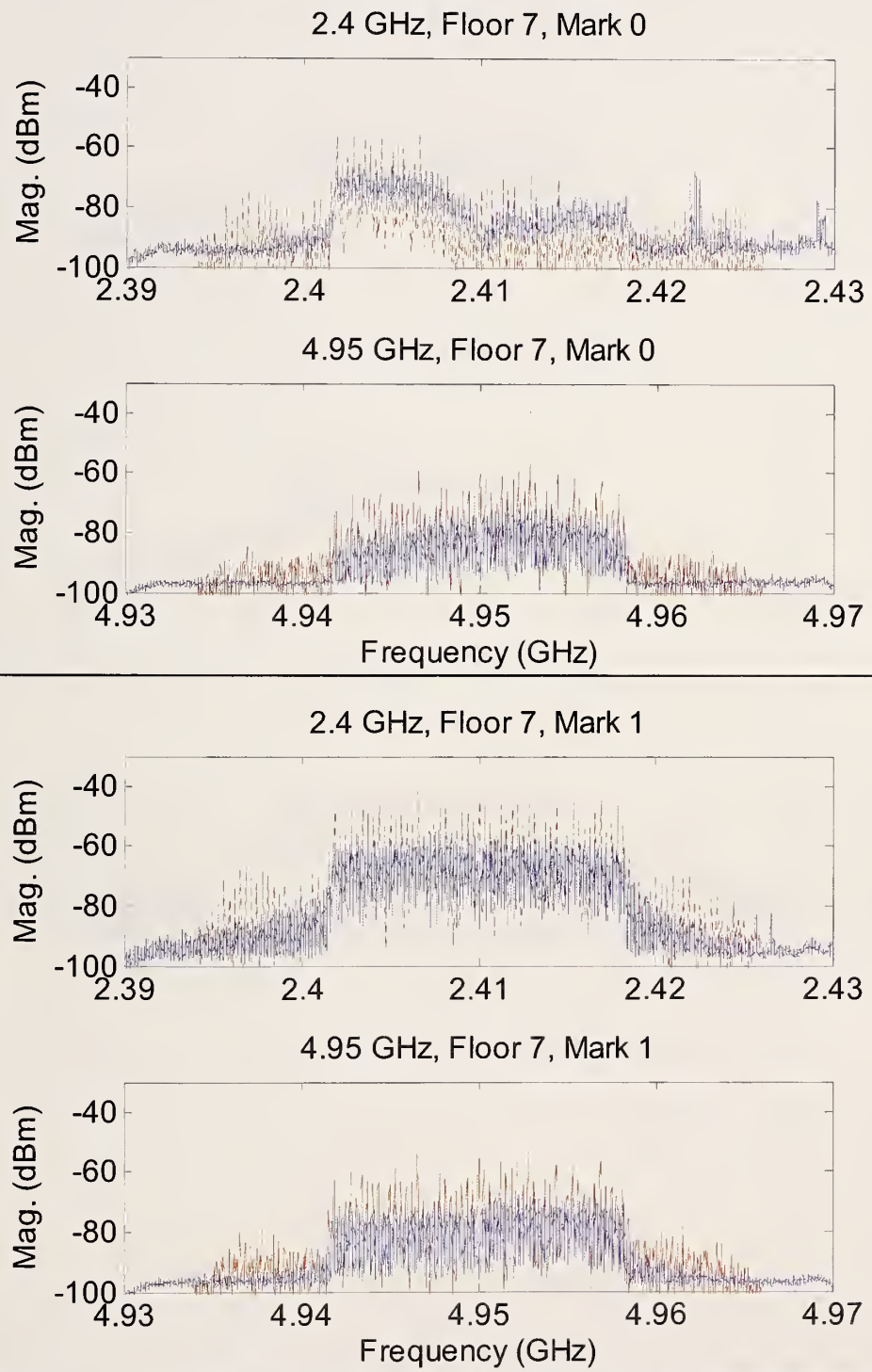

Figure I.8: Bandpass measurements for carrier frequencies of 2.41 GHz and 4.95 GHz for a QPSK-modulated OFDM signal (solid) and a multisine designed to simulate it (dashed). Floor 7, position 0 (top) and position 1 (bottom).

Modulated-Signal Spectra: Apartment Building

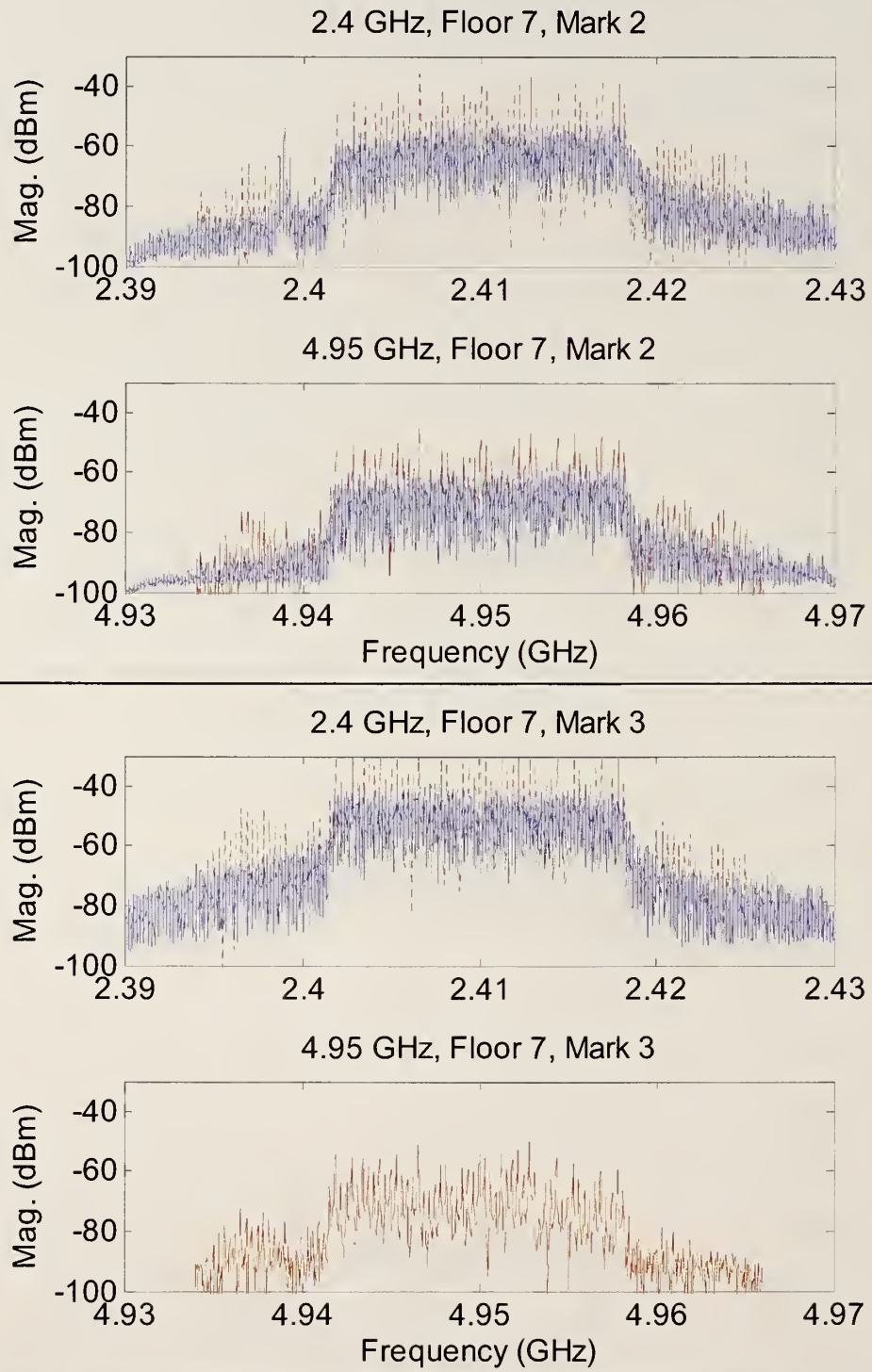

Figure I.9: Bandpass measurements for carrier frequencies of 2.41 GHz and 4.95 GHz for a QPSK-modulated OFDM signal (solid) and a multisine designed to simulate it (dashed). Floor 7, position 2 (top) and position 3 (bottom).

Modulated-Signal Spectra: Apartment Building

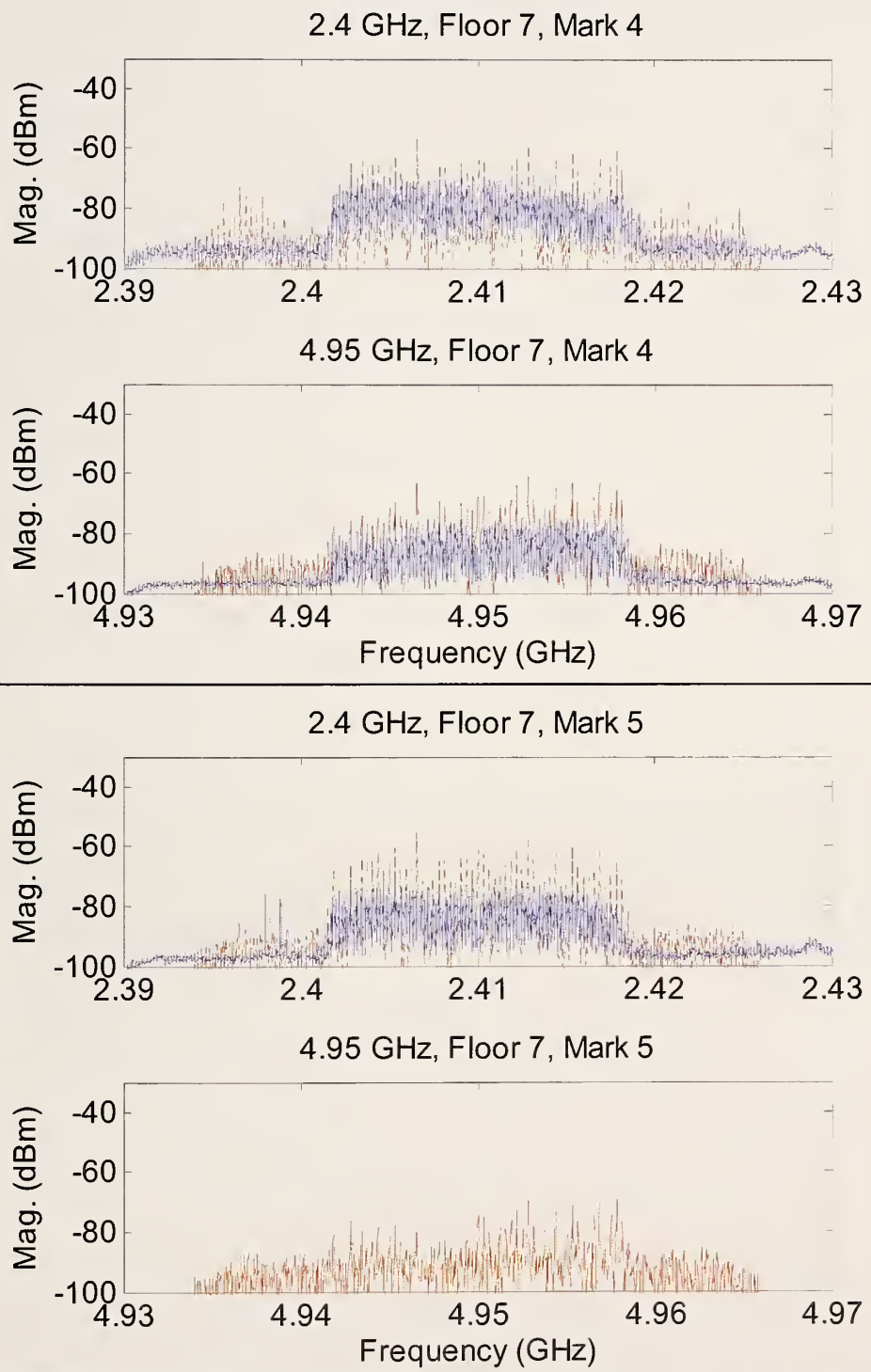

Figure I.10: Bandpass measurements for carrier frequencies of 2.41 GHz and 4.95 GHz for a QPSK-modulated OFDM signal (solid) and a multisine designed to simulate it (dashed). Floor 7, position 4 (top) and position 5 (bottom).

Modulated-Signal Spectra: Apartment Building

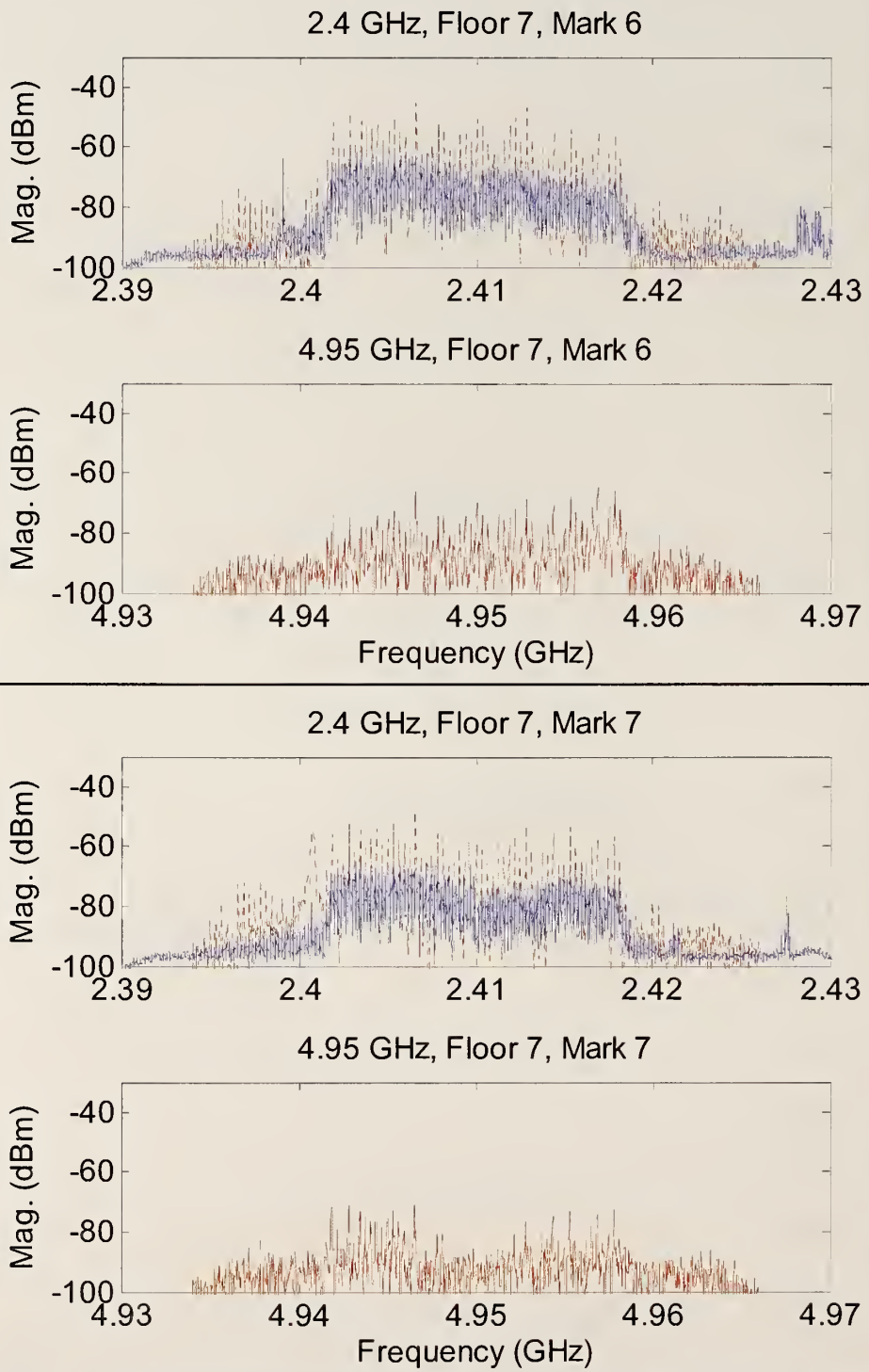

Figure I.11: Bandpass measurements for carrier frequencies of 2.41 GHz and 4.95 GHz for a QPSK-modulated OFDM signal (solid) and a multisine designed to simulate it (dashed). Floor 7, position 6 (top) and position 7 (bottom).

Modulated-Signal Spectra: Apartment Building

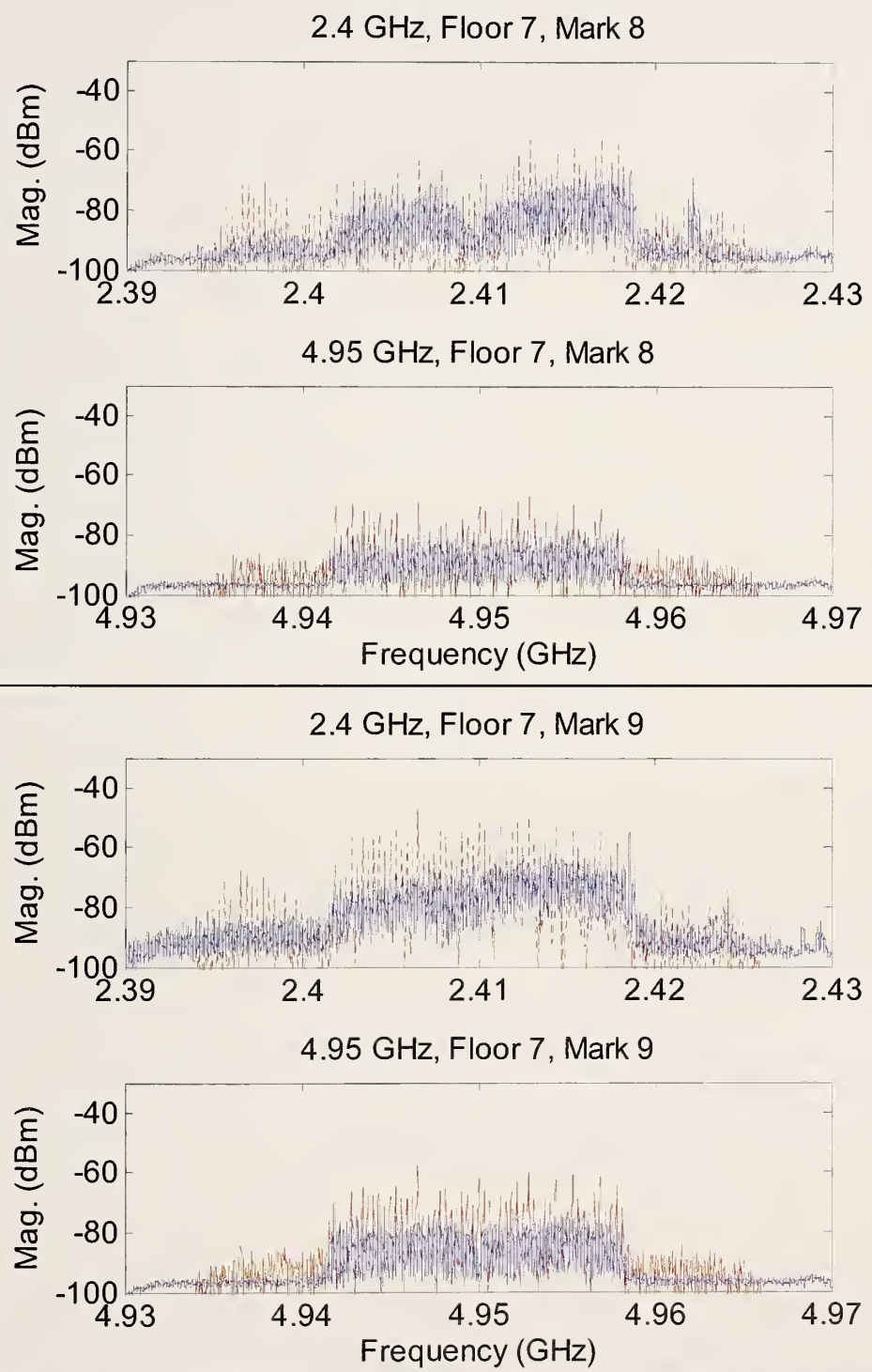

Figure I.12: Bandpass measurements for carrier frequencies of 2.41 GHz and 4.95 GHz for a QPSK-modulated OFDM signal (solid) and a multisine designed to simulate it (dashed). Floor 7, position 8 (top) and position 9 (bottom).

Modulated-Signal Spectra: Apartment Building

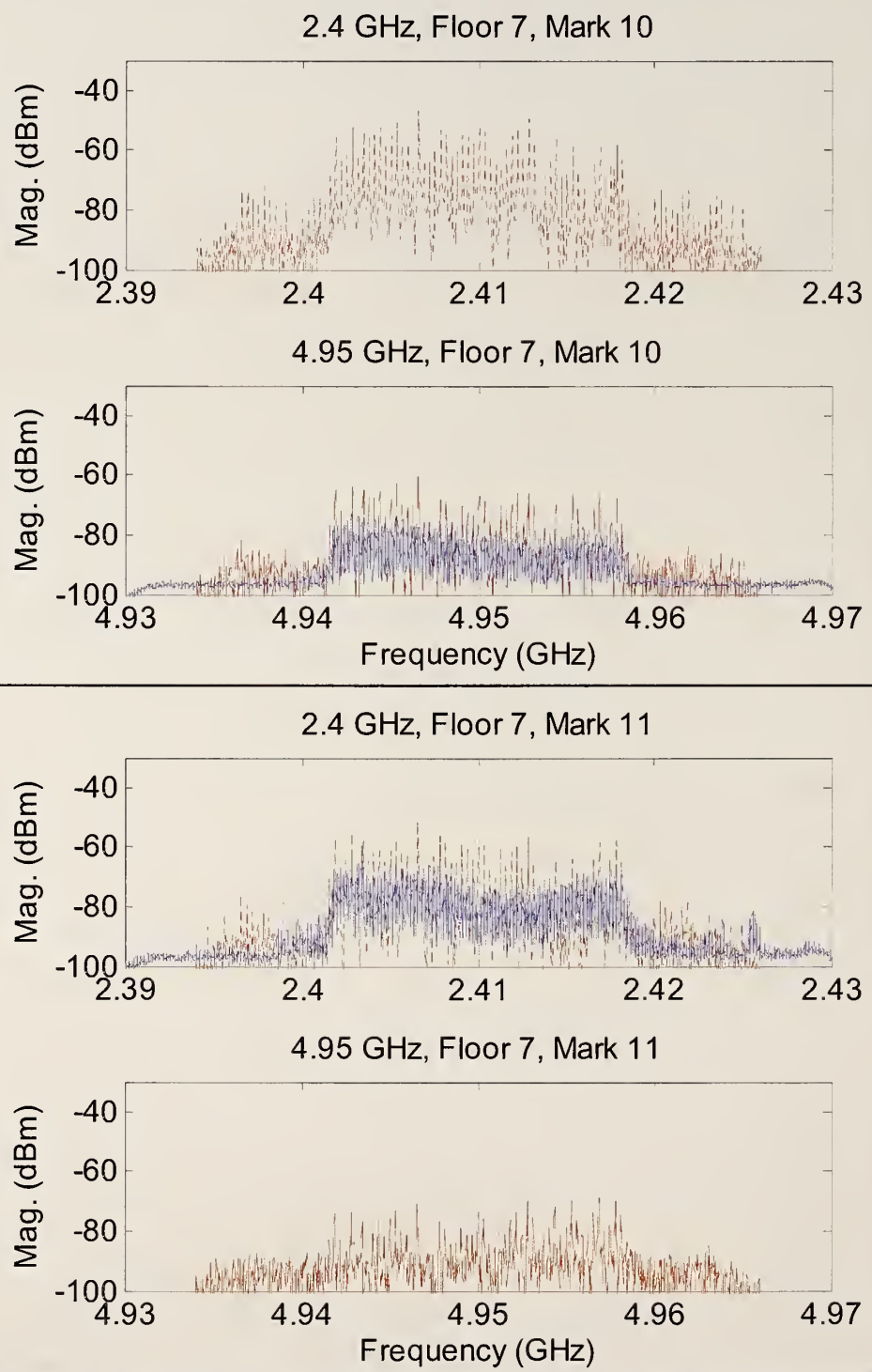

Figure I.13: Bandpass measurements for carrier frequencies of 2.41 GHz and 4.95 GHz for a QPSK-modulated OFDM signal (solid) and a multisine designed to simulate it (dashed). Floor 2, position 10 (top) and position 11 (bottom).

Modulated-Signal Spectra: Apartment Building

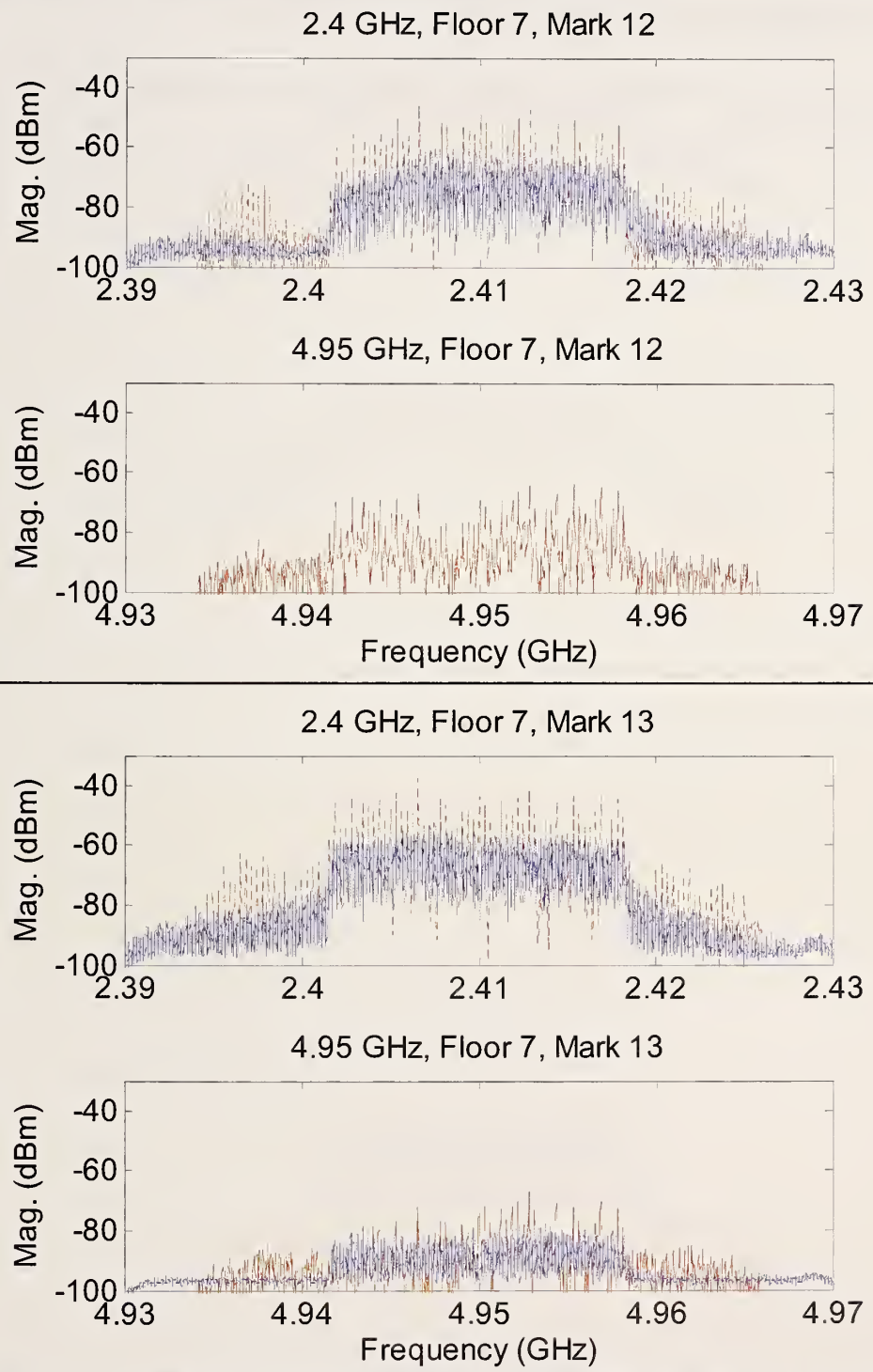

Figure I.14: Bandpass measurements for carrier frequencies of 2.41 GHz and 4.95 GHz for a QPSK-modulated OFDM signal (solid) and a multisine designed to simulate it (dashed). Floor 7, position 12 (top) and position 13 (bottom).

Appendix J: Modulated-Signal Spectra Measured With a Vector-Signal Analyzer: Office Corridor

The following pages contain the complete set of measured data for the office corridor (Section 4.4).

Modulated-Signal Spectra: Office Corridor

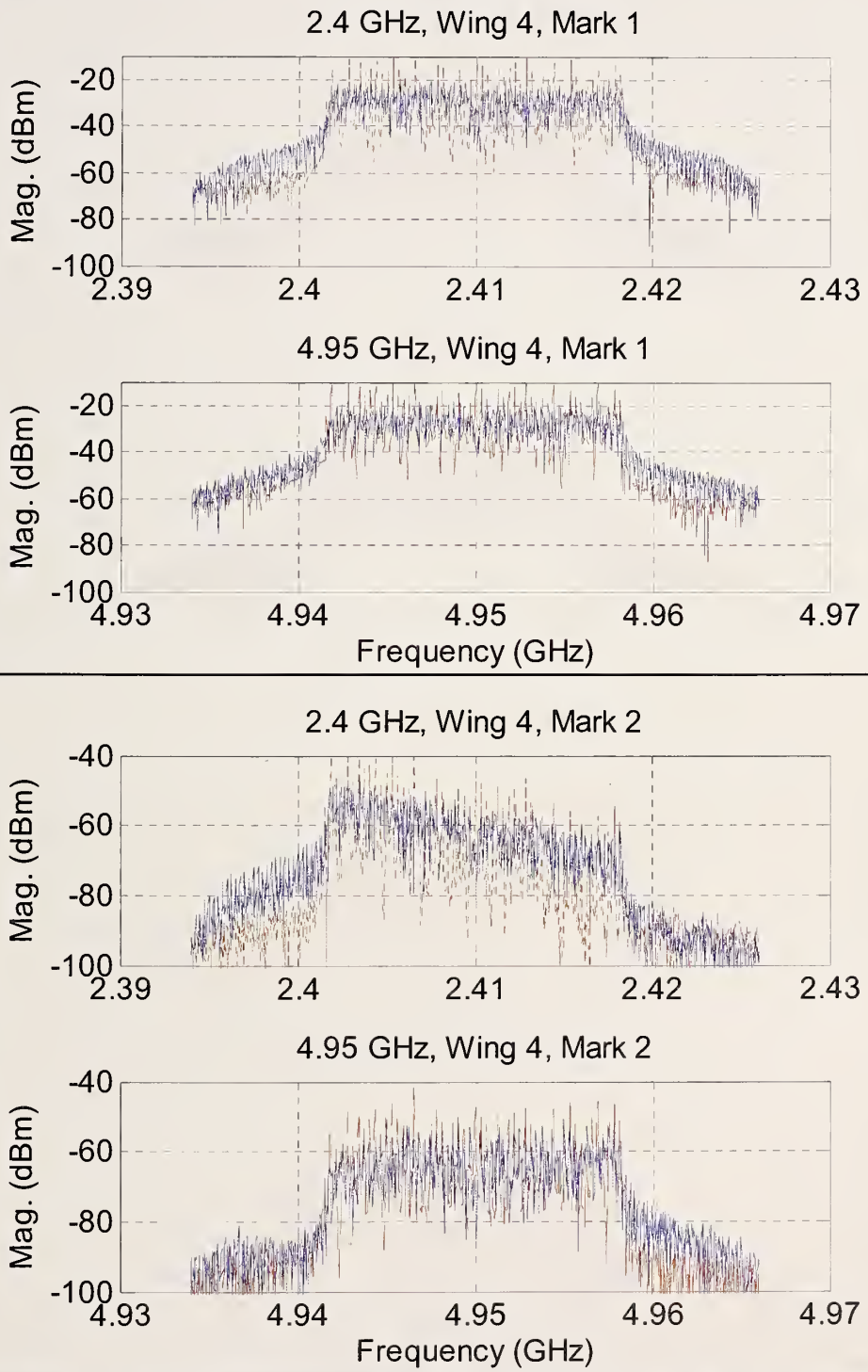

Figure J.1: Bandpass measurements for carrier frequencies of 2.41 GHz and 4.95 GHz for a QPSK-modulated OFDM signal (solid) and a multisine designed to simulate it (dashed). Position 1 (top) and position 2 (bottom).

Modulated-Signal Spectra: Office Corridor

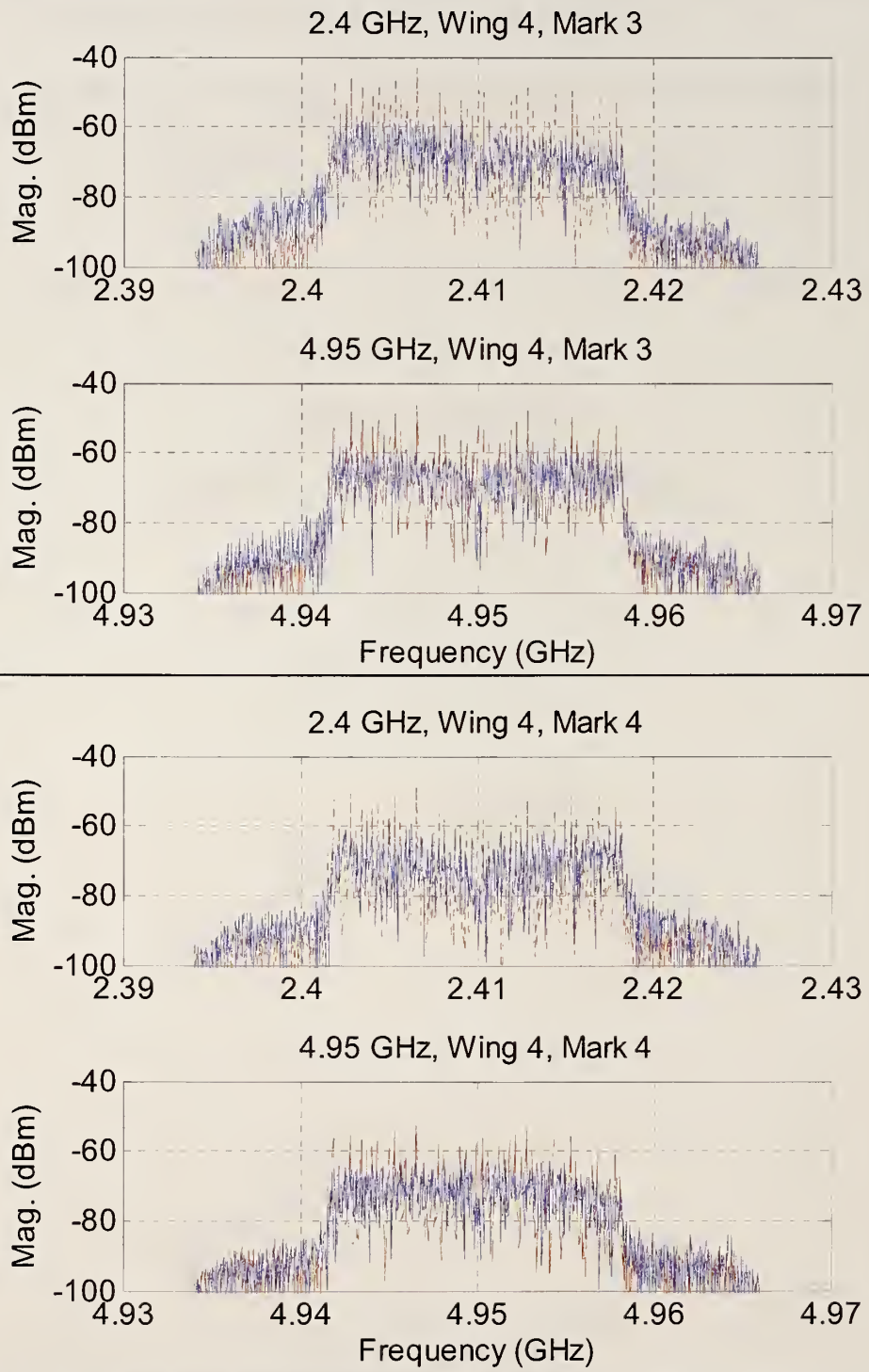

Figure J.2: Bandpass measurements for carrier frequencies of 2.41 GHz and 4.95 GHz for a QPSK-modulated OFDM signal (solid) and a multisine designed to simulate it (dashed). Position 3 (top) and position 4 (bottom).

Modulated-Signal Spectra: Office Corridor

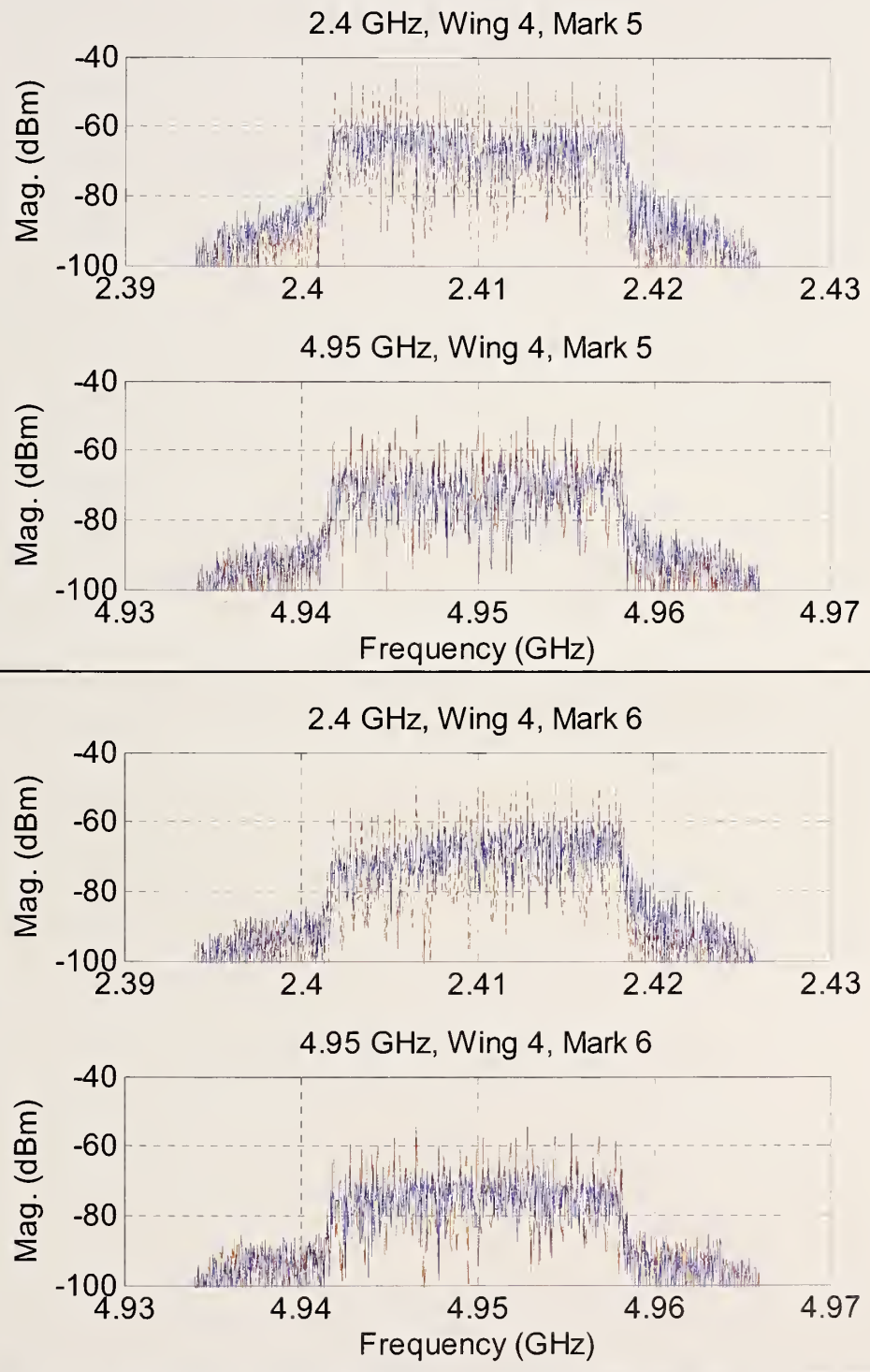

Figure IJ3: Bandpass measurements for carrier frequencies of 2.41 GHz and 4.95 GHz for a QPSK-modulated OFDM signal (solid) and a multisine designed to simulate it (dashed). Floor 2, position 5 (top) and position 6 (bottom).

Modulated-Signal Spectra: Office Corridor

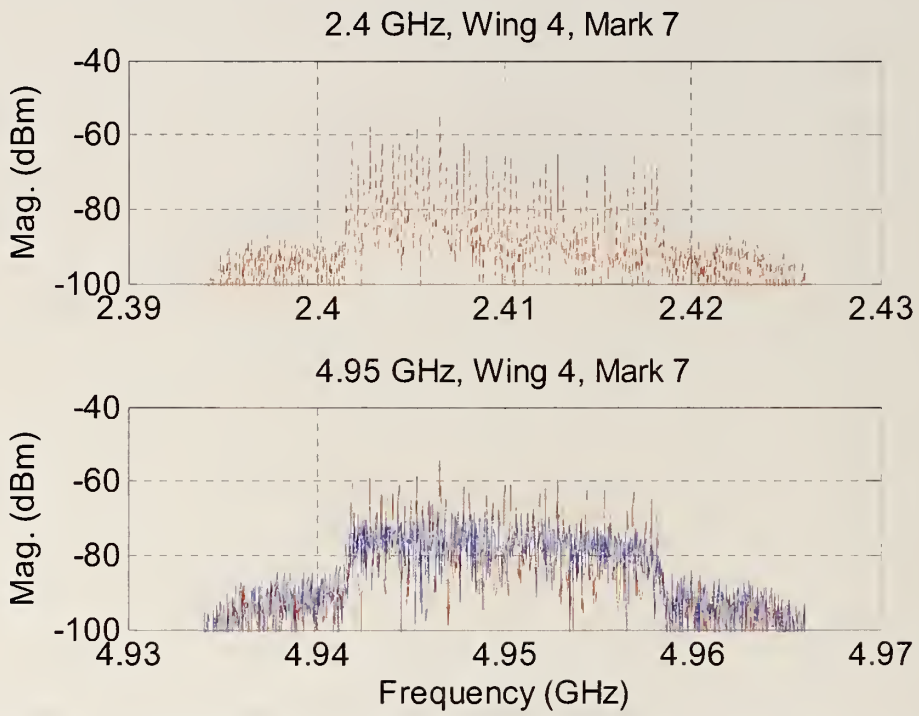

Figure J.4: Bandpass measurements for carrier frequencies of 2.41 GHz and 4.95 GHz for a QPSK-modulated OFDM signal (solid) and a multisine designed to simulate it (dashed). Position 7.

Modulated-Signal Spectra: Office Corridor

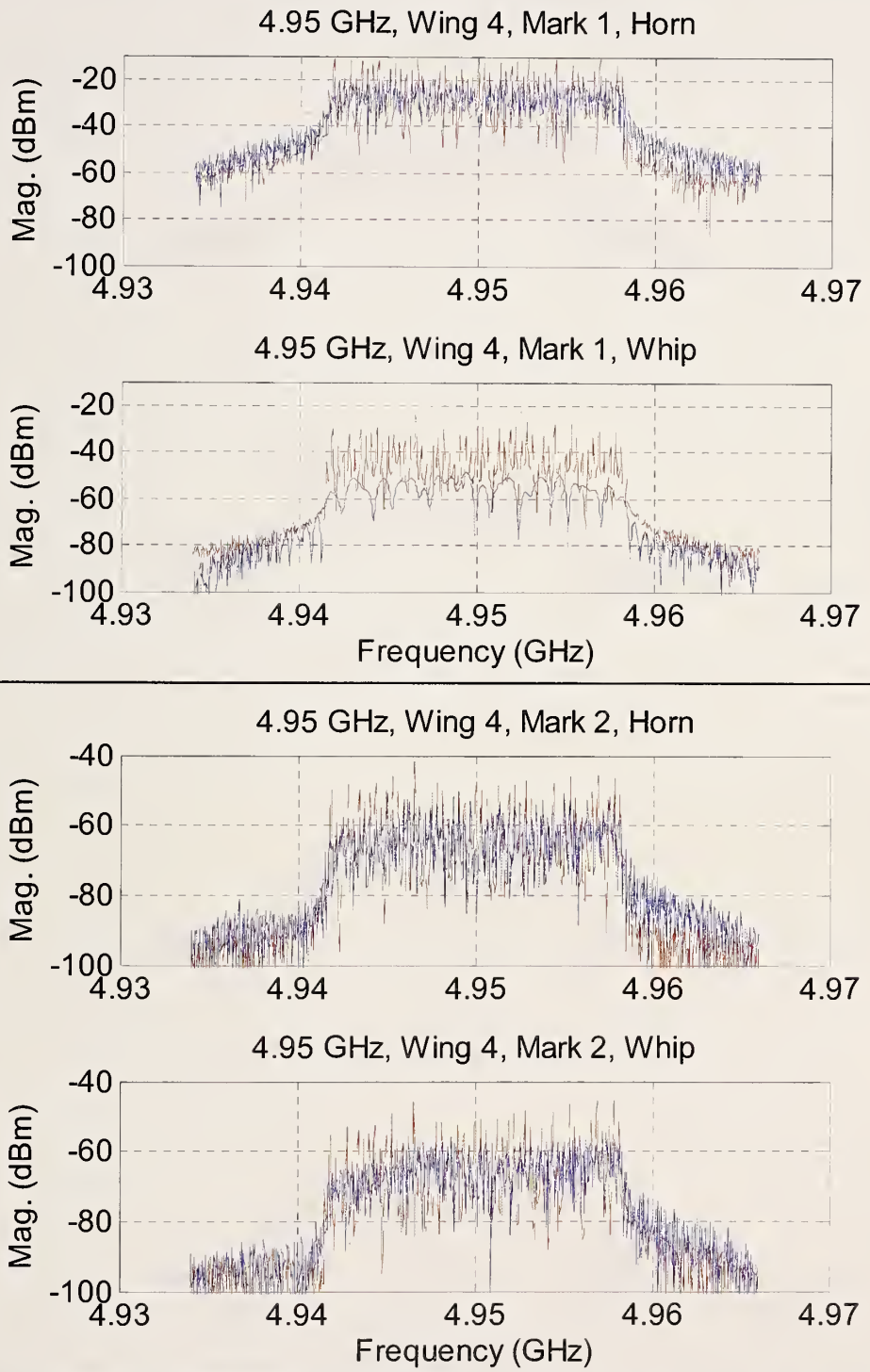

Figure J.5: Bandpass measurements for a carrier frequency of 4.95 GHz for a QPSK-modulated OFDM signal (solid) and a multisine designed to simulate it (dashed). Position 1 (top) and position 2 (bottom). In each graph: directional antenna (top), omnidirectional antenna (bottom).

Modulated-Signal Spectra: Office Corridor

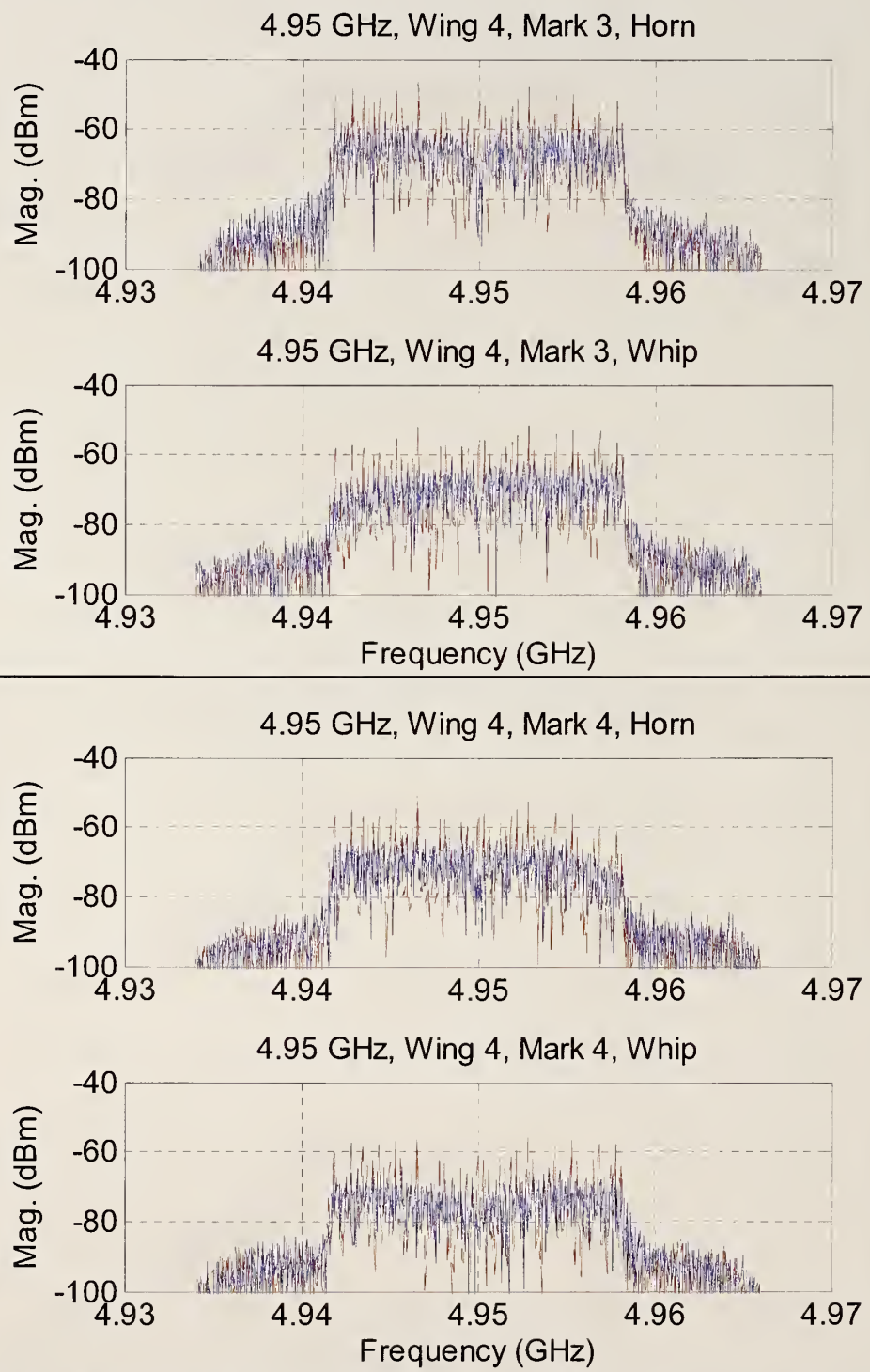

Figure J.6: Bandpass measurements for a carrier frequency of 4.95 GHz for a QPSK-modulated OFDM signal (solid) and a multisine designed to simulate it (dashed). Position 3 (top) and position 4 (bottom). In each graph: directional antenna (top), omnidirectional antenna (bottom).

Appendix K: Modulated-Signal Spectra Measured With a Vector-Signal Analyzer: Oil Refinery

The following pages contain the complete set of measured data for the oil refinery (Section 5.4).

Modulated-Signal Spectra: Oil Refinery

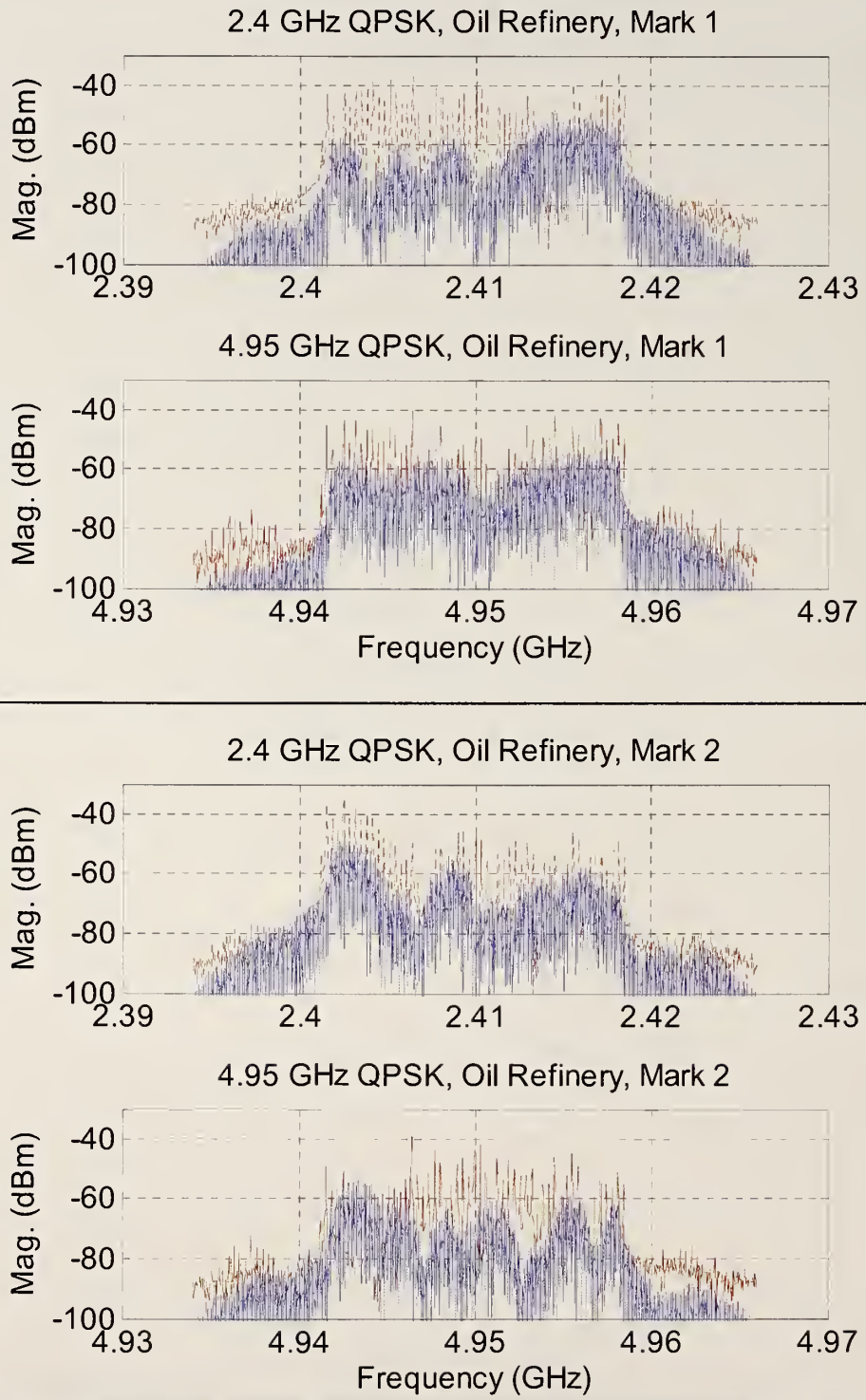

Figure K.1: Bandpass measurements of a QPSK-modulated OFDM signal (solid) and a multisine designed to simulate it (dashed). Distance from the transmitting antenna to the receiving antenna is D = 20.6 m (top) and D = 26.5 m (bottom).

Modulated-Signal Spectra: Oil Refinery

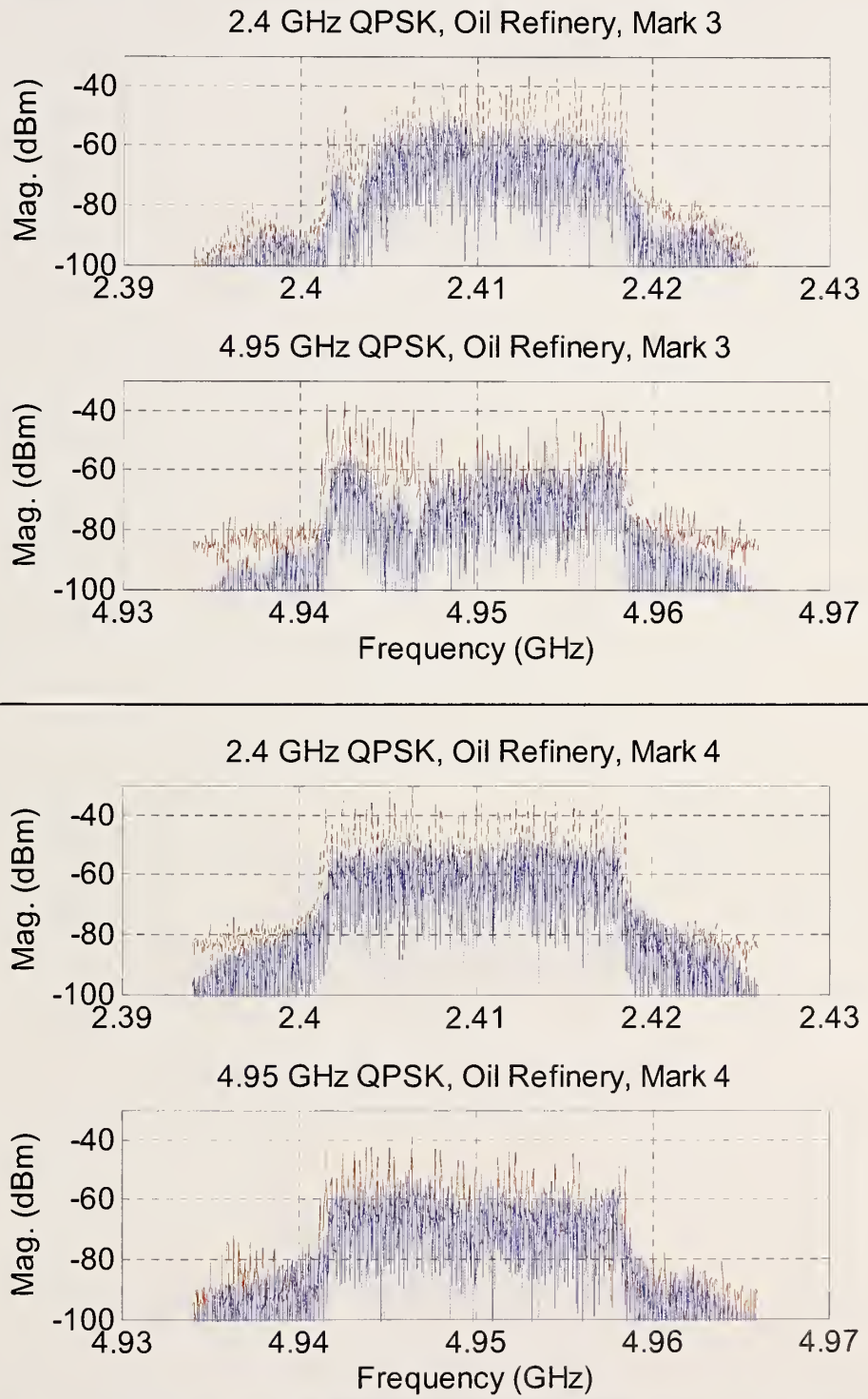

Figure K.2: Bandpass measurements of a QPSK-modulated OFDM signal (solid) and a multisine designed to simulate it (dashed). Distance from the transmitting antenna to the receiving antenna is D = 32.4 m (top) and D = 40.5 m (bottom).

Modulated-Signal Spectra: Oil Refinery

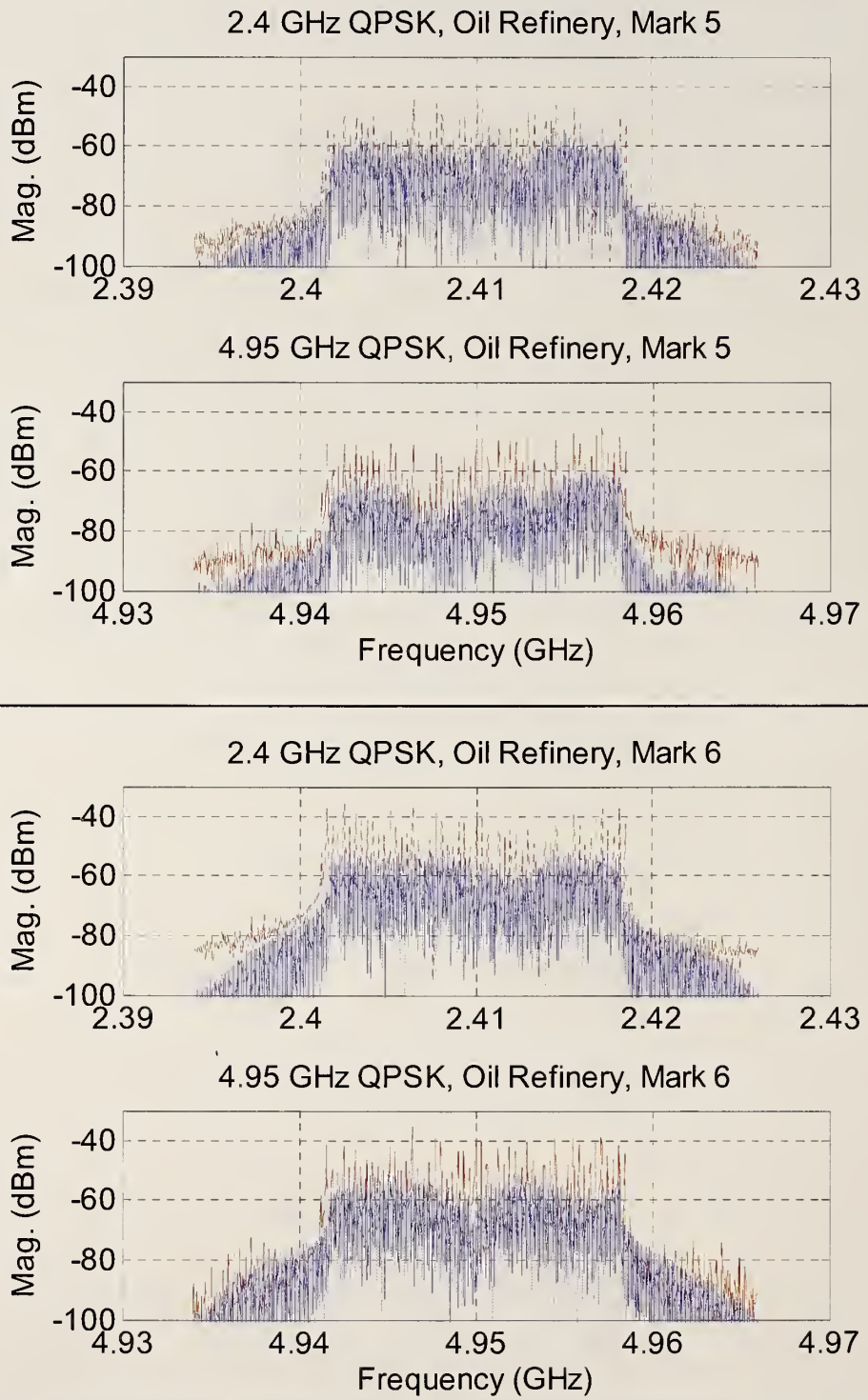

Figure K.3: Bandpass measurements of a QPSK-modulated OFDM signal (solid) and a multisine designed to simulate it (dashed). Distance from the transmitting antenna to the receiving antenna is D = 48.6 m (top) and D = 54.1 m (bottom).

Modulated-Signal Spectra: Oil Refinery

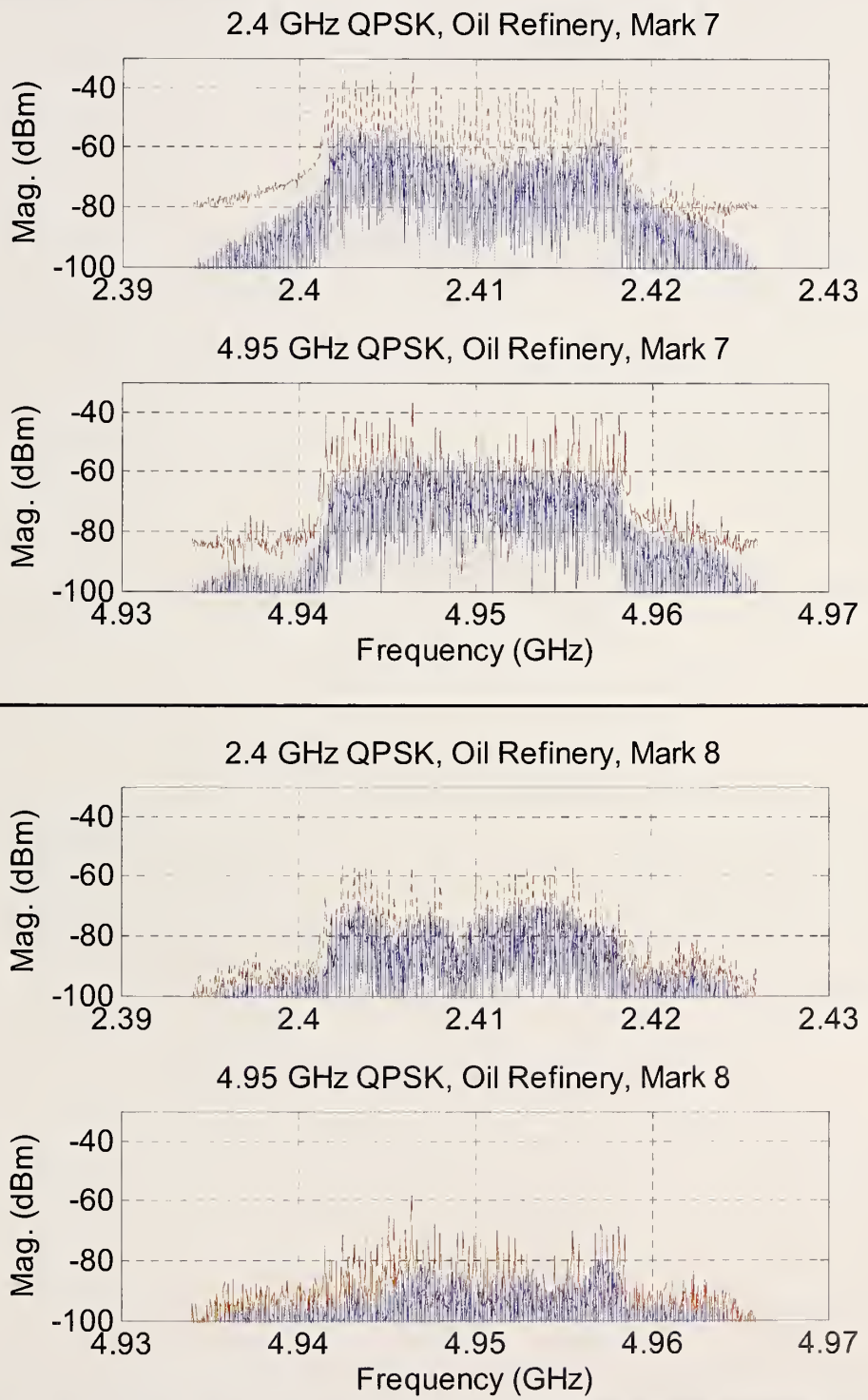

Figure K.4: Bandpass measurements of a QPSK-modulated OFDM signal (solid) and a multisine designed to simulate it (dashed). Distance from the transmitting antenna to the receiving antenna is D = 62.8 m (top) and D = 65.9 m (bottom).

Modulated-Signal Spectra: Oil Refinery

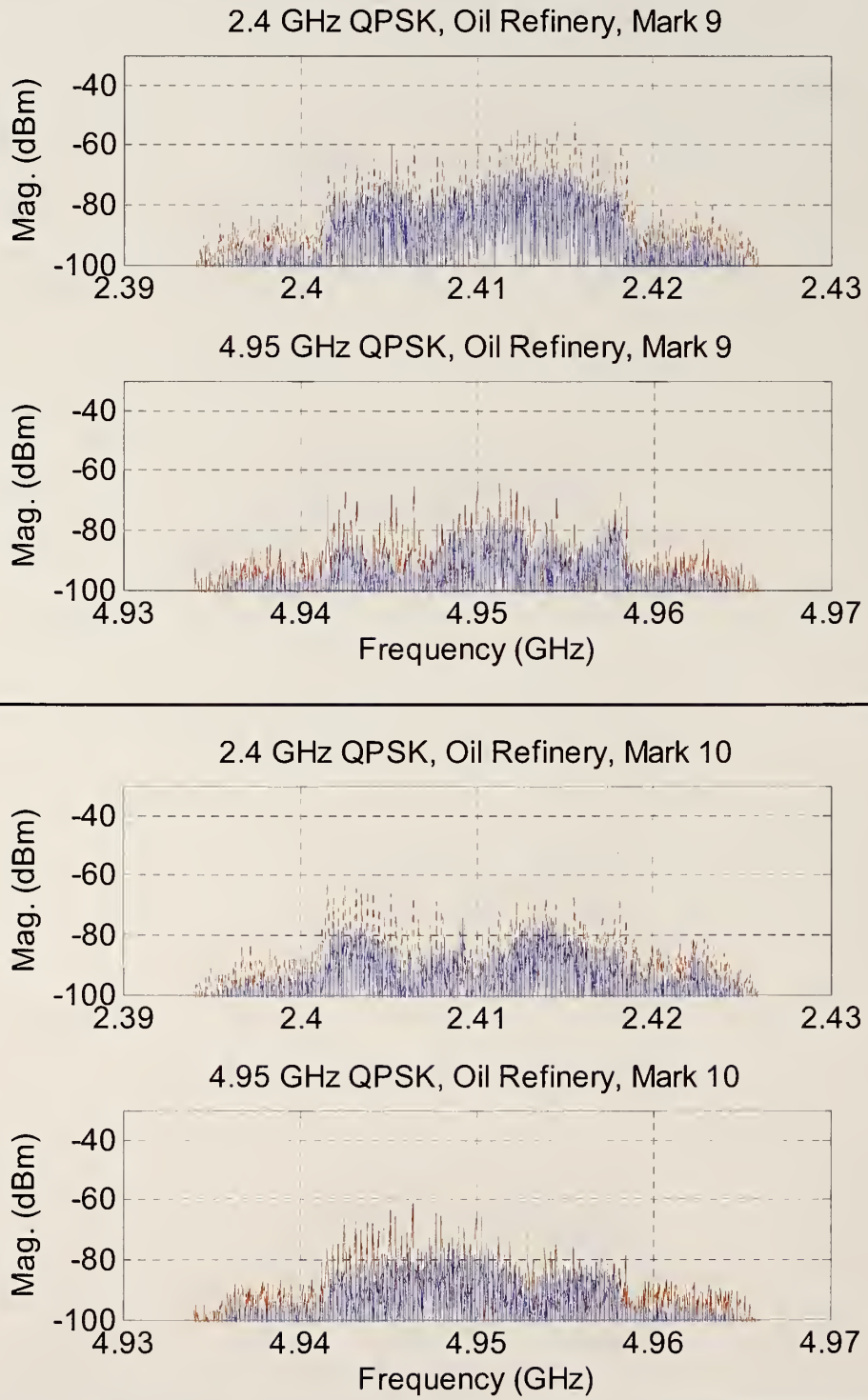

Figure K.5: Bandpass measurements of a QPSK-modulated OFDM signal (solid) and a multisine designed to simulate it (dashed). Distance from the transmitting antenna to the receiving antenna is D = 73.6 m (top) and D = 81.7 m (bottom).

Modulated-Signal Spectra: Oil Refinery

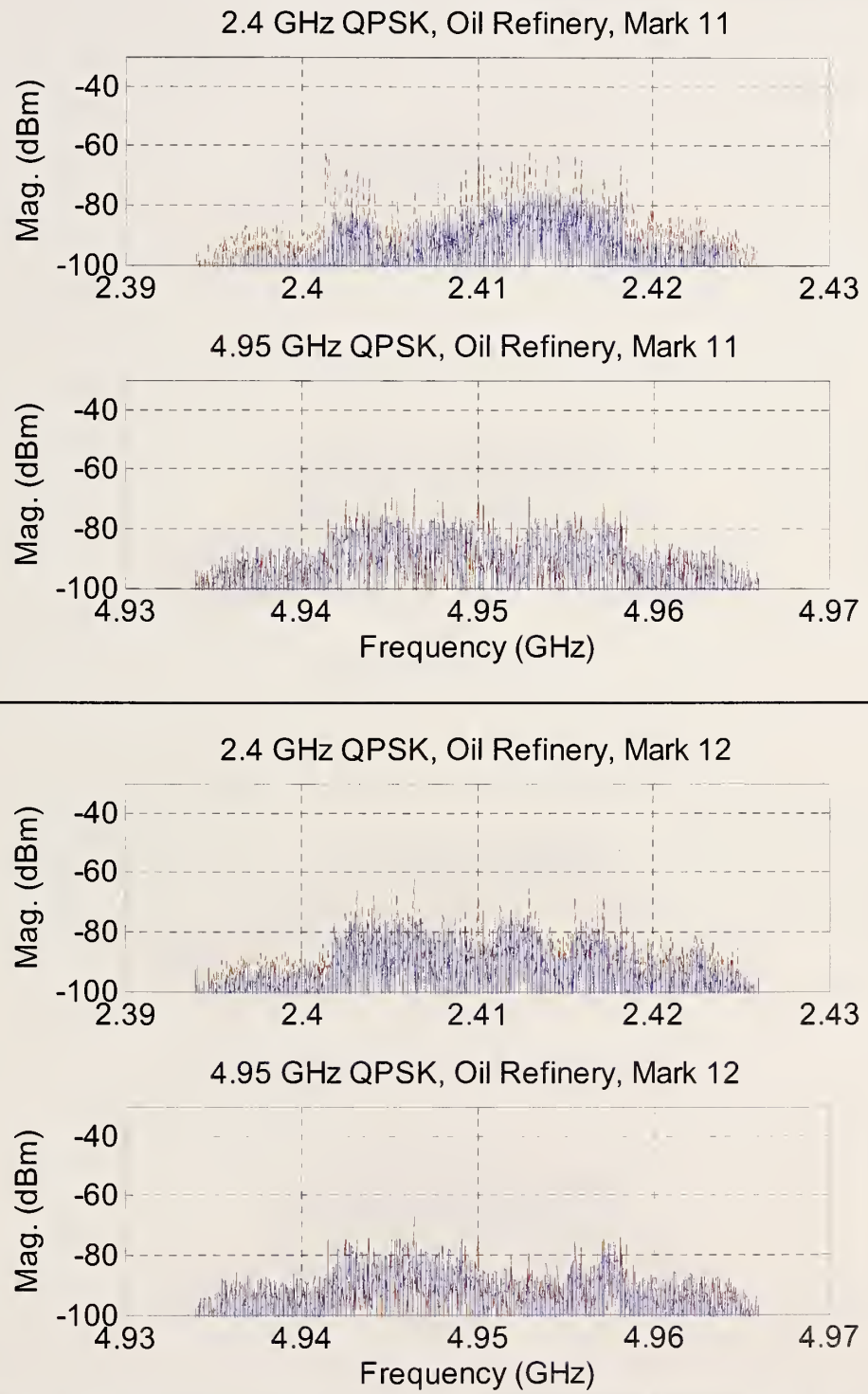

Figure K.6: Bandpass measurements of a QPSK-modulated OFDM signal (solid) and a multisine designed to simulate it (dashed). Distance from the transmitting antenna to the receiving antenna is D = 87.6 m (top) and D = 96.2 m (bottom).

Modulated-Signal Spectra: Oil Refinery

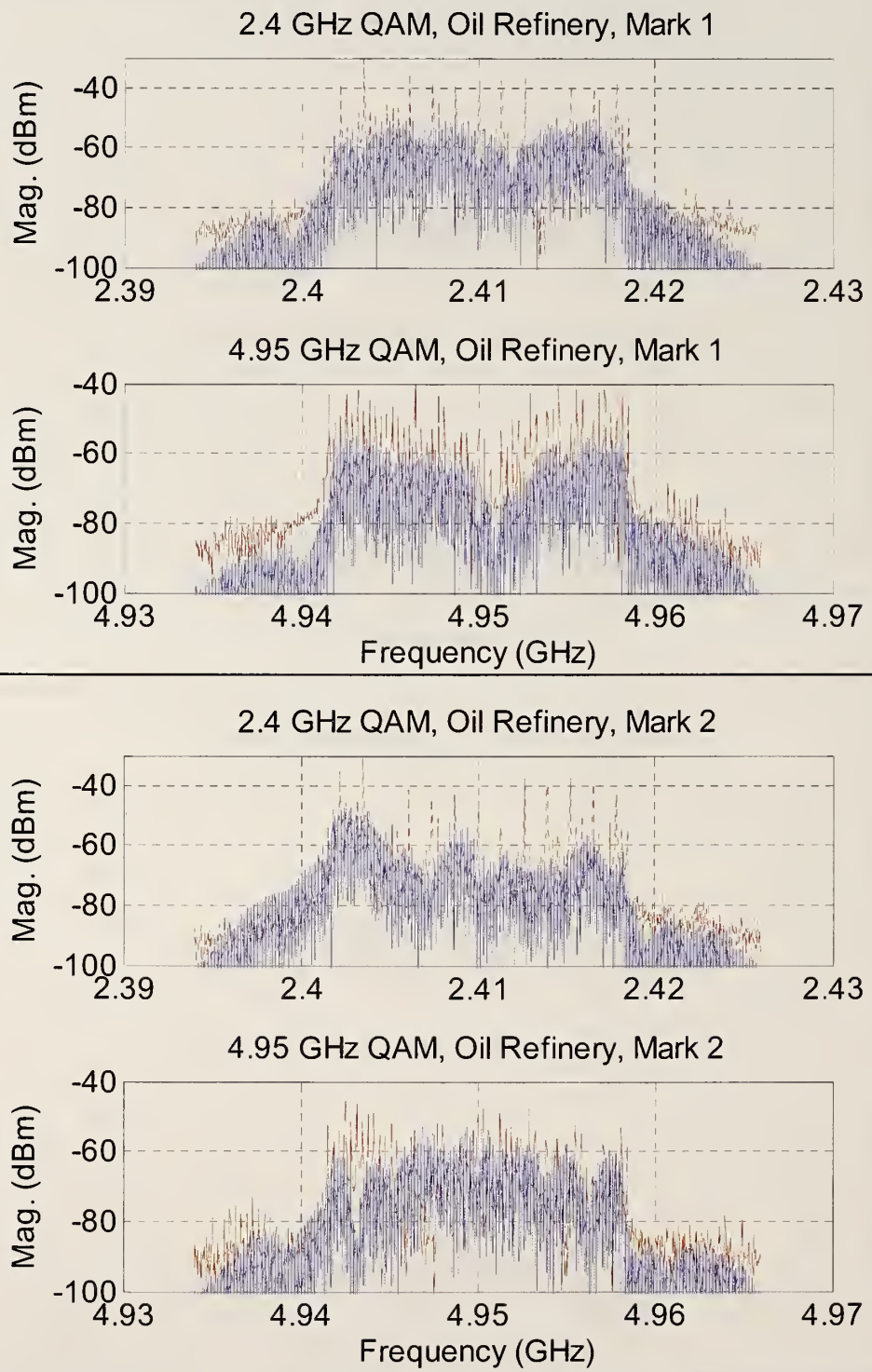

Figure K.7: Bandpass measurements of a QAM-modulated OFDM signal (solid) and a multisine designed to simulate it (dashed). Distance from the transmitting antenna to the receiving antenna is D = 20.6 m (top) and D = 26.5 m (bottom).

Modulated-Signal Spectra: Oil Refinery

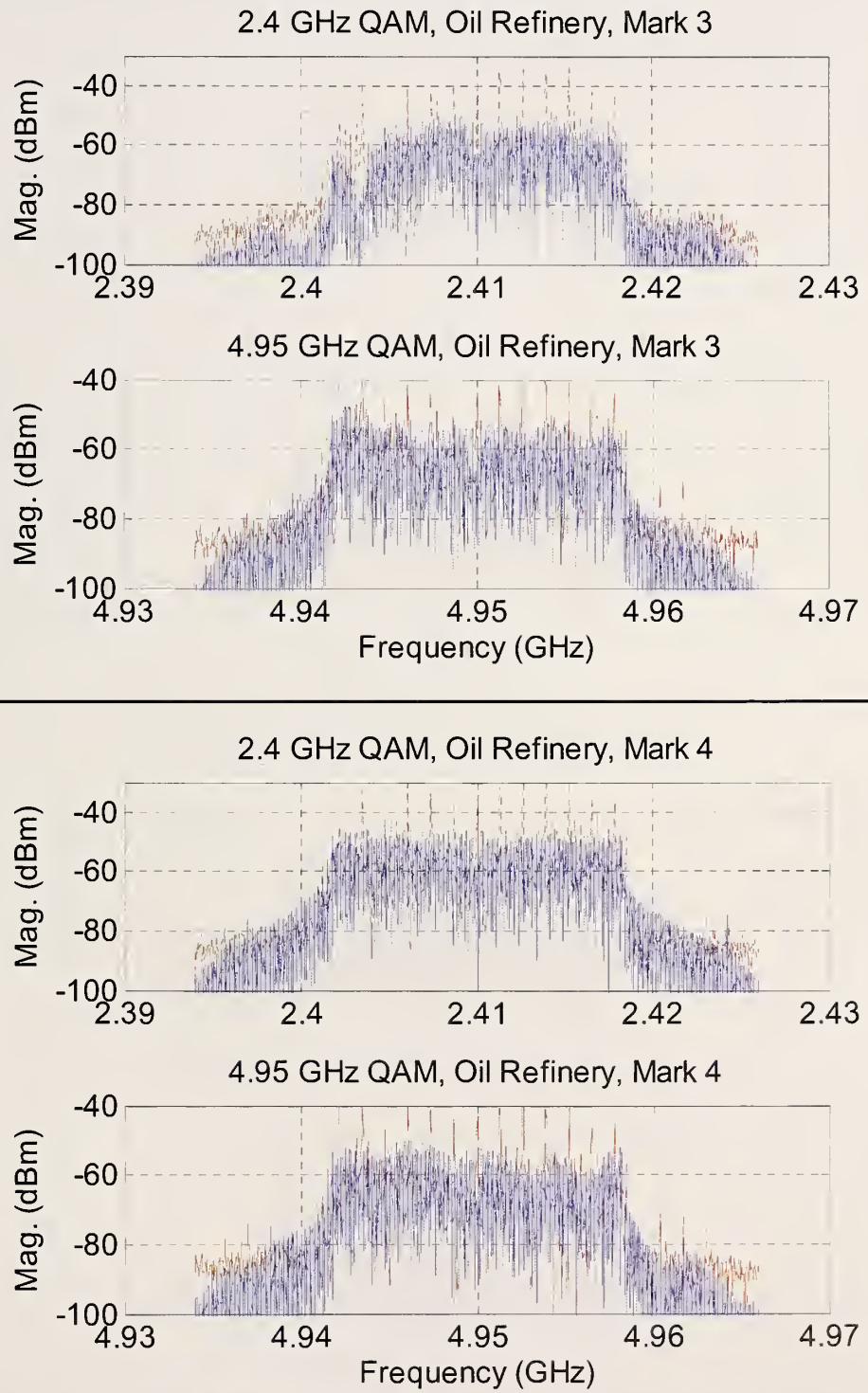

Figure K.8: Bandpass measurements of a QAM-modulated OFDM signal (solid) and a multisine designed to simulate it (dashed). Distance from the transmitting antenna to the receiving antenna is D = 32.4 m (top) and D = 40.5 m (bottom).

Modulated-Signal Spectra: Oil Refinery

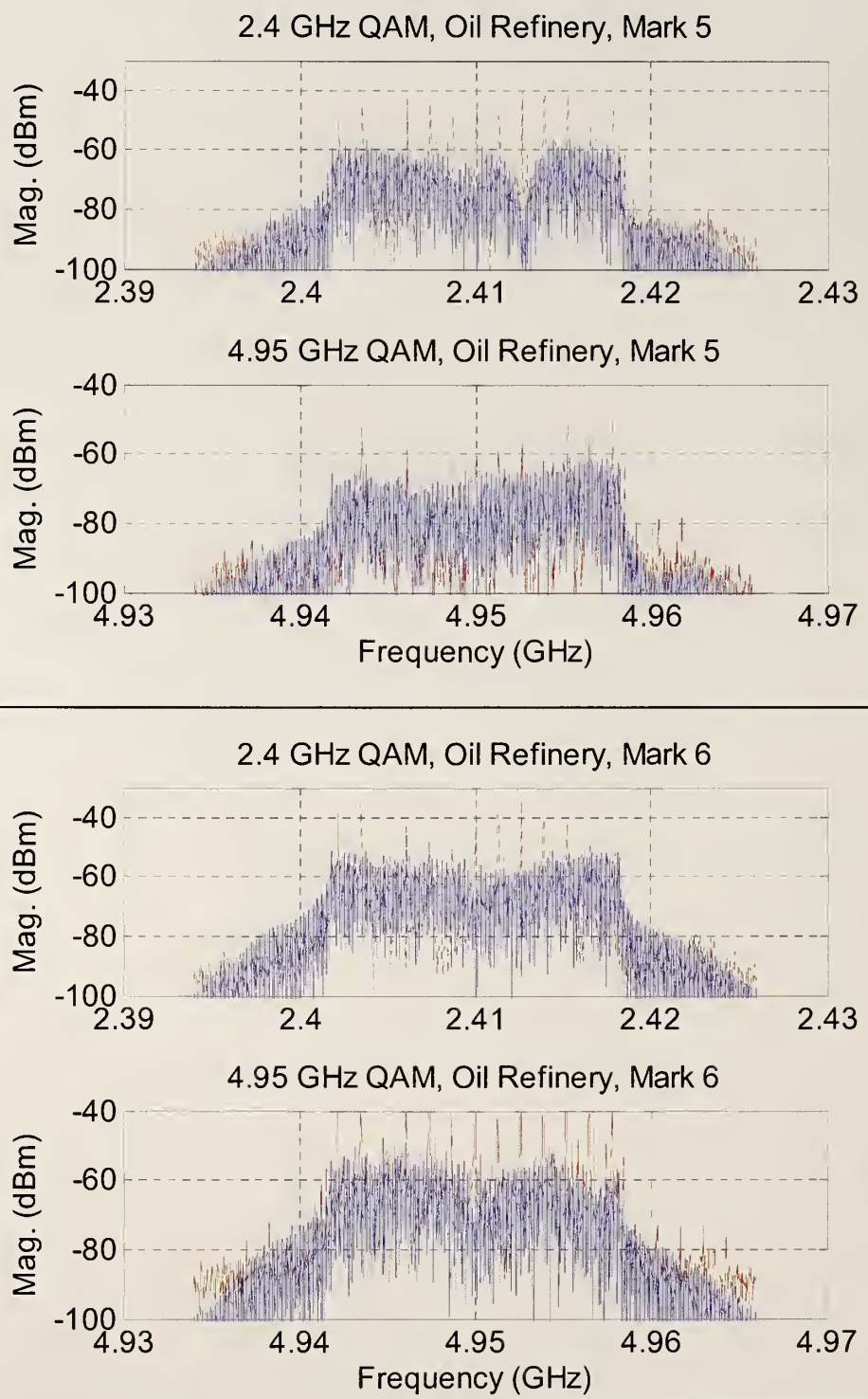

Figure K.9: Bandpass measurements of a QAM-modulated OFDM signal (solid) and a multisine designed to simulate it (dashed). Distance from the transmitting antenna to the receiving antenna is D = 48.6 m (top) and D = 54.1 m (bottom).

Modulated-Signal Spectra: Oil Refinery

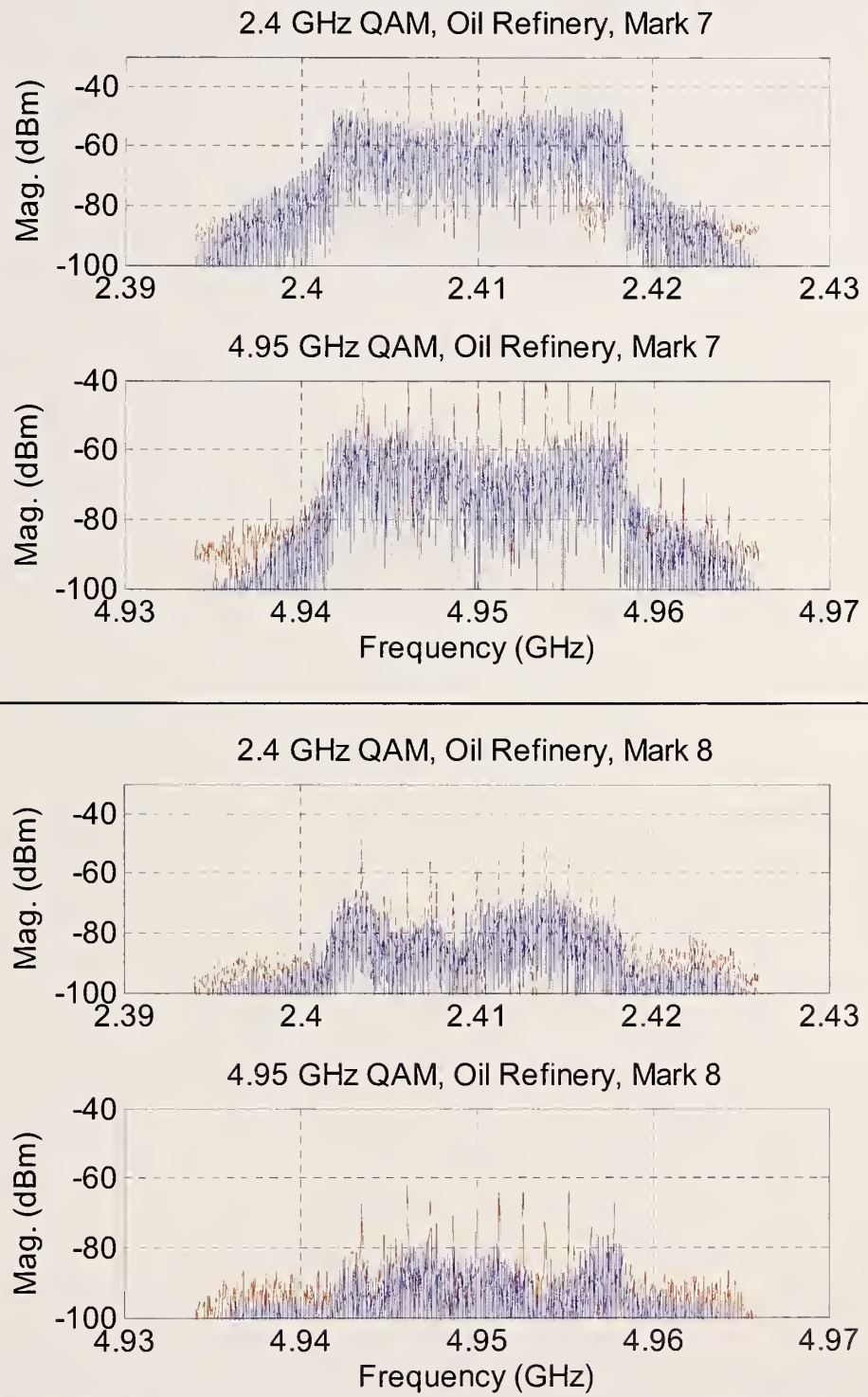

Figure K.10: Bandpass measurements of a QAM-modulated OFDM signal (solid) and a multisine designed to simulate it (dashed). Distance from the transmitting antenna to the receiving antenna is D = 62.8 m (top) and D = 65.9 m (bottom).

Modulated-Signal Spectra: Oil Refinery

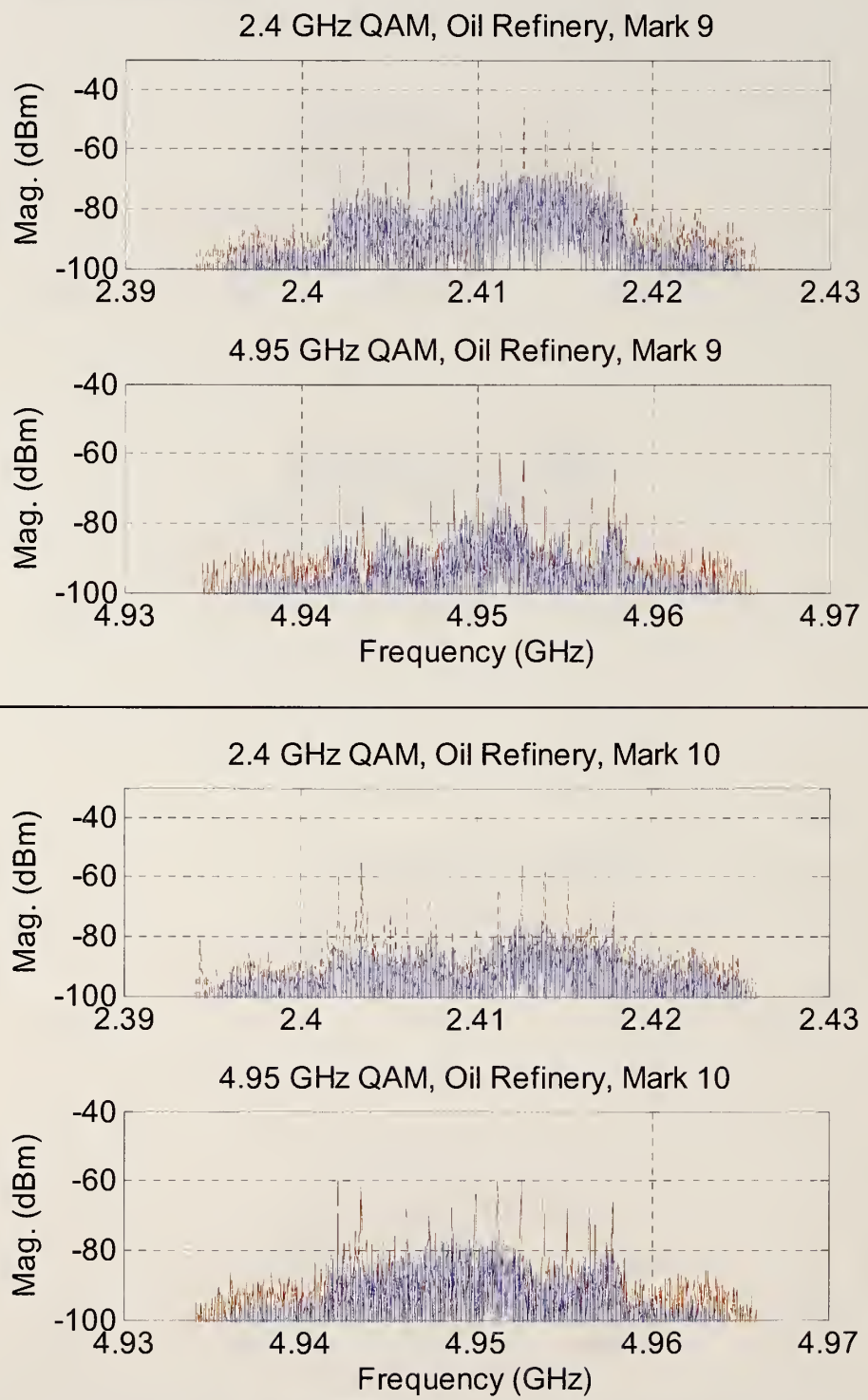

Figure K.11: Bandpass measurements of a QAM-modulated OFDM signal (solid) and a multisine designed to simulate it (dashed). Distance from the transmitting antenna to the receiving antenna is D = 73.6 m (top) and D = 81.7 m (bottom).

Modulated-Signal Spectra: Oil Refinery

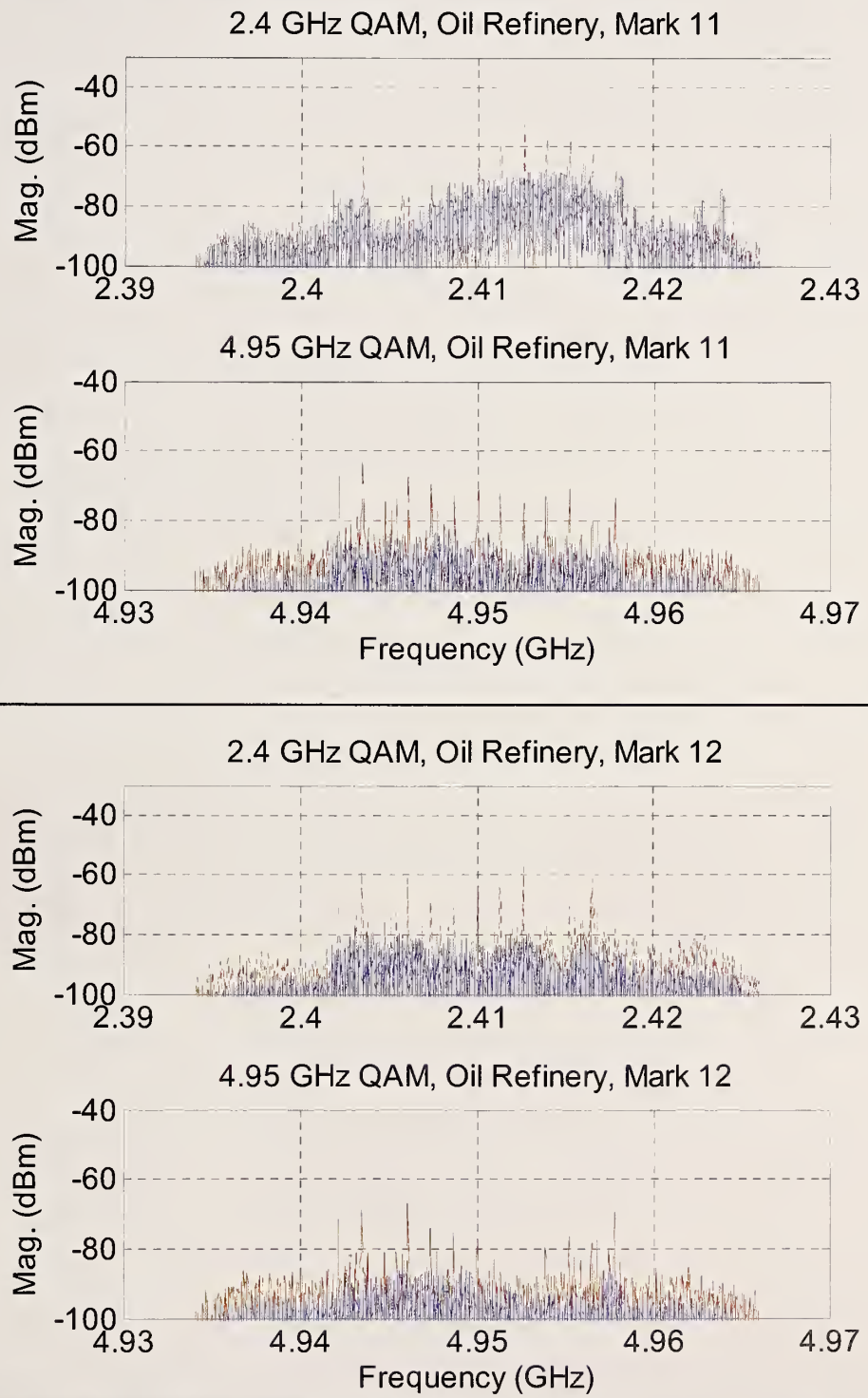

Figure K.12: Bandpass measurements of a QAM-modulated OFDM signal (solid) and a multisine designed to simulate it (dashed). Distance from the transmitting antenna to the receiving antenna is D = 87.6 m (top) and D = 96.2 m (bottom).

NIST Technical Publications

Periodical

Journal of Research of the National Institute of Standards and Technology—Reports NIST research and development in metrology and related fields of physical science, engineering, applied mathematics, statistics, biotechnology, and information technology. Papers cover a broad range of subjects, with major emphasis on measurement methodology and the basic technology underlying standardization. Also included from time to time are survey articles on topics closely related to the Institute's technical and scientific programs. Issued six times a year.

Nonperiodicals

Monographs—Major contributions to the technical literature on various subjects related to the Institute's scientific and technical activities.
Handbooks—Recommended codes of engineering and industrial practice (including safety codes) devel- oped in cooperation with interested industries, professional organizations, and regulatory bodies.
Special Publications—Include proceedings of conferences sponsored by NIST, NIST annual reports, and other special publications appropriate to this grouping such as wall charts, pocket cards, and bibliographies.
National Standard Reference Data Series—Provides quantitative data on the physical and chemical properties of materials, compiled from the world's literature and critically evaluated. Developed under a worldwide program coordinated by NIST under the authority of the National Standard Data Act (Public Law 90-396). NOTE: The Journal of Physical and Chemical Reference Data (JPCRD) is published bimonthly for NIST by the American Institute of Physics (AIP). Subscription orders and renewals are available from AIP, P.O. Box 503284, St. Louis, MO 63150-3284.
Building Science Series—Disseminates technical information developed at the Institute on building materials, components, systems, and whole structures. The series presents research results, test methods, and performance criteria related to the structural and environmental functions and the durability and safety characteristics of building elements and systems.
Technical Notes—Studies or reports which are complete in themselves but restrictive in their treatment of a subject. Analogous to monographs but not so comprehensive in scope or definitive in treatment of the subject area. Often serve as a vehicle for final reports of work performed at NIST under the sponsorship of other government agencies.
Voluntary Product Standards—Developed under procedures published by the Department of Commerce in Part 10, Title 15, of the Code of Federal Regulations. The standards establish nationally recognized requirements for products, and provide all concerned interests with a basis for common understanding of the characteristics of the products. NIST administers this program in support of the efforts of private-sector standardizing organizations.

*Order the **following** NIST publications—FIPS and NISTIRs—from the National Technical Information Service, Springfield, VA 22161.*

Federal Information Processing Standards Publications (FIPS PUB)—Publications in this series collectively constitute the Federal Information Processing Standards Register. The Register serves as the official source of information in the Federal Government regarding standards issued by NIST pursuant to the Federal Property and Administrative Services Act of 1949 as amended, Public Law 89-306 (79 Stat. 1127), and as implemented by Executive Order 11717 (38 FR 12315, dated May 11,1973) and Part 6 of Title 15 CFR (Code of Federal Regulations).
NIST Interagency or Internal Reports (NISTIR)—The series includes interim or final reports on work performed by NIST for outside sponsors (both government and nongovernment). In general, initial distribution is handled by the sponsor; public distribution is handled by sales through the National Technical Information Service, Springfield, VA 22161, in hard copy, electronic media, or microfiche form. NISTIR's may also report results of NIST projects of transitory or limited interest, including those that will be published subsequently in more comprehensive form.

U.S. Department of Commerce
National Bureau of Standards and Technology
325 Broadway
Boulder, CO 80305-3328